Wheel-rail Contact Force Measurement Based on LC Resonance Sensing

Changrong Yang

A doctoral thesis submitted for the degree of Doctor of Philosophy

School of Engineering, Newcastle University

Date of submission: 07/01/2025

This page is intentionally left blank.

CERTIFICATE OF ORIGINALITY

This is to certify that the thesis entitled “Wheel-rail Contact Force Measurement Based on LC Resonance Sensing” and the work presented has been generated by me as my own original research. I confirm that:

- This work has been done for a research degree at Newcastle University.
- Where I have cited from the work of others, the source is always given.
- I have acknowledged all main sources of help.
- The research contributions presented in Chapter 3, 4, and 6 were published and listed in the list of the publication page.

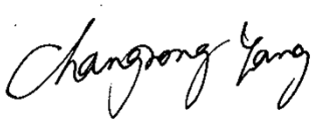

……. (Signed)

07/01/2025

……. (Date)

This page is intentionally left blank.

Abstract

Railway transportation has become a popular means for passenger travel and goods delivery. Wheel-rail contact forces are important parameters in rolling stock, which determine the running safety and stability. Therefore, it is significant to take measures to measure them. The conventional approach is to employ strain gauges with wired connection to measure these forces which has strict requirements for the installation of strain gauges and signal transmission. Exploring wireless measurement methods is beneficial to replace the traditional way to lower the measurement complexity. Although methods such as gap sensors and digital image correlation (DIC) have been investigated, there remains a need to explore new approaches that are low-cost, wireless, and capable of multi-parameter measurement to extend the range of alternative techniques for wheel-rail contact force measurement.

This thesis aims to investigate inductor-capacitor (LC) resonance-based sensing for wireless force measurement (WFM), which ultimately contribute to advancements in wheel-rail contact force measurement (WRCFM). The contributions of this work are summarized as follows:

The first study is to investigate WFM using a rectangular LC resonance sensor and the LDC1614-based resonant frequency measurement system. The comparison with a strain gauge and aspect ratio of the inductance coil were studied. The results revealed that the rectangular LC resonance sensor realized the wireless force measurement with good repeatability and linear relationship between the resonant frequency (f_{res}) and the loaded force, and a smaller aspect ratio caused greater directivity to enlarge the response range.

The second work addresses the overlap challenge of the lift-off and force in sensor output, which can lead to misinterpretation, an orthogonal LC resonance sensor was designed alongside a multi-parameter measurement system based on the LDC1101-ESP32S3 that provided two resonant frequencies and two equivalent parallel resistances (R_p). By analysing their independence in response to lift-off and force changes, an 8-node coordinate transformation algorithm was proposed to effectively separate the lift-off and force. Validation results showed that the maximum relative error of 22.61% for forces and 1.66% for lift-offs, confirming the accuracy and robustness of the proposed system.

The third investigation involves the enhancement in lift-off and sensitivity in WFM by integrating semiconductor strain gauge (SSG), magnetic resonance coupling (MRC), and an LDC1101-ESP32S3 based measurement system. By investigating parallel-parallel (PP) and series-parallel (SP) topologies under various lift-offs and SSGs, the approach achieved a sensitivity 5.5 Ω/kN at a lift-off of 33 mm for the PP topology with a 350 Ω SSG and

demonstrated stable sensitivity near the critical coupling region. These advancements enable WFM with improved robustness and extend the operational range to lift-offs of tens of millimetres.

The fourth research applies advancements from the third work to a rotating testing platform, focusing on signal stability against electromagnetic interference (EMI) and temperature fluctuations, as well as signal readout and analysis of signal characteristics. A differential LC resonator configuration combined with Kalman filter (KF) and moving average algorithm (MAA) significantly reduced the impact of temperature changes and EMI noise. According to the enhancement in hardware and software, a rotating testing platform was established to perform the signal readout and characteristic analysis at various lift-offs and R_{var} (the simulated change in SSG). Results demonstrated that the changes in lift-off affected both ΔR_p (the difference between the measured R_p and the reference R_p) and Δf_{res} (the difference between the measured f_{res} and the reference f_{res}) while R_{var} primarily altered ΔR_p, demonstrating a proportional relation between the negative peak of R_{var} and ΔR_p with Δf_{res} remaining stable. These findings highlight the potential of Δf_{res} to measure lift-off and compensate for shifts in ΔR_p, enabling improved performance in dynamic scenario.

The research achievements for WFM presented in this thesis provide alternative approaches for WRCFM, offering the advantages of low cost, wireless sensing, and high sensitivity. Future work will conduct the actual testing in a wheel-rail system. The installation positions of LC resonators and the measurement system will be optimized according to stress distributions on the wheel, identifying the most susceptible areas. The sensing structure of LC resonators will be further developed into a double-D configuration to achieve uniform and concentrated eddy currents, enhancing sensing capability in terms of directivity and resolution. Additionally, the system will be integrated with an internet of things (IoT) platform and artificial intelligence to enable real-time feature extraction, data visualization, and monitoring of wheel-rail forces.

Acknowledgements

I am excited to see myself reaching the final stage of my PhD studies at Newcastle University. These four years have been a journey of immense learning and growth. First and foremost, I would like to express my heartfelt gratitude to my supervisors, Prof. Guiyun Tian and Prof. Mark Robinson, for their invaluable guidance and unwavering support throughout my PhD journey. Prof. Guiyun Tian introduced me to the fascinating field of electromagnetic NDT&E and sensing, providing me with professional training in critical thinking, project management, and academic research. His encouragement and support have been instrumental in helping me reach this stage. Prof. Mark Robinson has been a source of inspiration and guidance, particularly in honing my academic presentation and writing skills. His patience and kindness have left a lasting impression on me.

I would also like to extend my sincere appreciation to my colleagues and collaborators. A special thanks to Emmanuel Ibrahim from Nigeria, who has been more than a colleague – he has been like an elder brother. Starting the project together, we spent countless hours in the lab and beyond. His continuous encouragement, support, and patience have not only helped me professionally but also significantly improved my English-speaking abilities. I am also grateful to Dr. Qiuping Ma, who graduated last year, for her thoughtful guidance and invaluable advice on scientific research.

To my group members – Dr. Jummah Abdulwali, Mr. Thomas McDonald, Dr. Lawal Umar Daura, Dr. Qiuji Yi, Mr. Peilin Hui, Mr. Wenjie Li, and Mr. Lei Zhang – thank you for your collaboration, suggestions, and shared moments during this journey. I am also deeply grateful to Prof. Bin Gao, Prof. Hailin Cao, and Dr. Xiaolong Lu for their insightful guidance and suggestions. My sincere thanks to my panel members for their constructive feedback and to the technical team, particularly Mr. Paul Killan and Mr. Paul Scott, for their professional support in setting up my experiments.

I am fortunate to have had the companionship of wonderful friends and roommates – Peng Jia, Jian Huang, Gailing Ma, Yingxia Jin, Zhiming Feng, Wengbo Wang, and Chao Zhang – who made my time here memorable and enjoyable. Additionally, I extend my gratitude to the China Scholarship Council (CSC) for their financial support, which made my studies possible.

Finally, I would like to express my deepest gratitude to my wife, Mrs. Yongqin Wen, who has been my rock throughout this journey. Her unwavering support, care, and love have been my greatest source of strength. She has stood by me during tough times, prepared meals for me

daily, and ensured my well-being. I am forever grateful to her. To my family, thank you for your love and encouragement – I wish you all good health and happiness.

List of Publications

Journal Papers

1. **C. Yang**, G. Tian, M. Robinson, and E. T. Ibrahim, "Wheel-Rail Force Measurement Based on Wireless LC Resonance Sensing," *IEEE Sensors Journal,* vol. 23, no. 15, pp. 17470-17479, 2023. (Contributing to **Chapter 3**)
2. **C. Yang**, G. Tian, Q. Ma, M. Robinson, and E. T. Ibrahim *et al.*, "Measurement and separation of forces and lift-offs employing an inductance-to-digital converters (LDC)-based orthogonal LC resonance sensor," *NDT & E International,* vol. 144, p.103072, 2024. (Contributing to **Chapter 4**)
3. **C. Yang**, G. Tian, M. Robinson et al., "Novel Impedance Sensing via Semiconductor Strain Gauge and Magnetic Resonant Coupling for Wireless Force Measurement," *IEEE Transactions on Instrumentation and Measurement*, 2025. (Contributing to **Chapter 5**).
4. G. Tian, **C. Yang**, X. Lu, Z. Wang, Z. Liang, and X. Li, "Inductance-to-digital converters (LDC) based integrative multi-parameter eddy current testing sensors for NDT&E," *NDT & E International*, vol. 138, p.102888, 2023.
5. E. T. Ibrahim, **C. Yang**, G. Tian, M. Robinson, Q. Ma, and L. U. Daura, "Pulsed Magnetic Flux Leakage Measurement Using Magnetic Head and Tunnelling Magnetoresistance for Defect Detection," *IEEE Sensors Journal*, vol. 23, no. 17, pp. 19184-19193, 2023.
6. Z. Liang, Z. Wang, **C. Yang**, X. Lu, and G. Tian, "Investigating a defect width identification based on half-peak width for LDC-based eddy current testing," *Nondestructive Testing and Evaluation*, pp. 1-14, 2024.

Conference Papers

1. **C. Yang**, G. Tian, M. Robinson, " Wheel-Rail Contact Force Monitoring Based on Wireless LC Resonance Sensing," The Fifth International Conference on Railway Technology: Research, Development and Maintenance. Montpellier, France, 22-25 August 2022. (Contributing to **Chapter 3**)
2. **C. Yang**, G. Tian, and M. Robinson., "Steel Stress Measurement Using an Orthogonal LC Resonance Sensor and Chip-based Frequency and Impedance System," 2024 IEEE International Instrumentation and Measurement Technology Conference (I2MTC). IEEE, 2024, Glasgow, Scotland, 19-23 May 2024. (Contributing to **Chapter 4**)
3. **C. Yang**, G. Tian, and M. Robinson., "Stability Study of Differential LC Resonant Sensors for Wireless Force Measurement," 2024 Far East NDT New Technology & Application Forum (FENDT), Zhongshan, China, 24-27 Jun 2024. (Contributing to **Chapter 6**)

Table of Contents

List of Abbreviations

ADC	Analog to digital converters
AECC	Apparent eddy current conductivity
AIN	Aluminium nitride
BP	Backpropagation
CMT	Coupled-mode theory
DIC	Digital image correlation
ECT	Eddy current testing
EDA	Electronic design automation
EMI	Electromagnetic interference
ESR	Equivalent series resistance
FEA	Finite element analysis
f_{res}	Resonant frequency
GUI	Graphic user interface
IoT	Internet of Things
KF	Kalman filter
KVL	Kirchhoff's voltage law
LC	Inductor-capacitor
LDC	Inductance-to-digital converters
LF	Low frequency
LOI	Lift-off invariance
LVDT	Linear variable differential transformer
MAA	Moving average algorithm
MBN	Magnetic Barkhausen noise
MEMS	Micromechanical systems
MRC	Magnetic resonance coupling
MWCNT	Multiwalled carbon nanotube
NDT&E	Non-destructive testing & evaluation
NER	Near electrical resonance
PCA	Principal component analysis
PCB	Printed circuit board
PDMS	Polydimethylsiloxane
PECT	Pulsed eddy current testing

PP	Parallel-parallel
PS	Parallel-series
PVDF	Polyvinylidene fluoride
Q	Vertical force
RFEC	Remote field eddy current
RFID	Radio frequency identification
RLT	Reflected load theory
RMS	Root mean square
R_p/R_{Peq}	Equivalent parallel resistance
RPM	Revolution per minute
Rx	Receiver
SG	Strain gauge
SHM	Structural health monitoring
SNR	Signal-to-noise ratio
SP	Series-parallel
SS	Series-series
SSG	Semiconductor strain gauge
STFT	Short-time Fourier transformation
SWR	Standing wave ratio
TF	Time-frequency
Tx	Transmitter
UHF	Ultra-high frequency
UWB	Ultra-wideband
VNA	Vector network analyser
WFM	Wireless force measurement
WPT	Wireless power transfer
WRCFM	Wheel-rail contact forces measurement
Y	Lateral force

List of Figures

List of Tables

Chapter 1. Introduction

In this chapter, the research background on wheel-rail contact force, the existing measurement method, and inductor-capacitor (LC) resonance sensing are presented. The motivations, aim and objectives, methodology, and thesis layout are described. Finally, a summary of this chapter is provided.

1.1 Research Background

Rolling stock plays an important role in high-speed railway vehicles. Due to the long-term operation of railway vehicles, some key components of rolling stock such as gearbox, primary steel coil spring, welded bogie frame and clip of rail fastener may suffer from internal and external excitation and thus fatigue damages occur, which may pose a major threat to the running safety and ride comfort [1]. Thus, it is necessary to inspect or monitor those significant components in rolling stock. The development of non-destructive testing & evaluation (NDT&E) and structural health monitoring (SHM) technology enables offline inspection and on-board monitoring [2-9].

Wheel-rail contact forces, generated by the interaction between wheels and rails during railway vehicle operation, represent the dynamic performance of rolling stock in railway systems and serve as indicators of travelling safety, stability, and ride comfort. Their respective components, lateral forces (Y) and vertical forces (Q), are used to calculate the derailment coefficient (Y/Q) [10]. Therefore, it is crucial to implement measures for accurately measuring wheel-rail contact forces. Presently, strain gauges are the primary approach used for measuring these forces due to advantages of high sensitivity and accuracy, low cost, and a wide variety of forms, such as linear and rosette strain gauges for multi-directional force measurement [10-15]. The measurement procedure involves properly sticking strain gauges to the surface of wheel webs or axles, close to the wheel rims and wheel hubs. This method requires a specially designed wheelset, including drilling holes in the wheel webs to install strain gauges. However, drilling holes may cause the structure damage of wheels, affecting the structural health and integrity. More importantly, the approach relies on wired connection, and signal transmission through telemetry is both complicated and costly. These stringent requirements significantly limit the widespread adoption of this method in real railway vehicles. Although techniques such as gap sensors and the DIC method for wireless measurement have been explored [16, 17] , there remains a need for a non-destructive, wireless, low-cost, and multi-parameter approach to wheel-rail contact force measurement (WRCFM).

Thus, to address the challenges mentioned above, this thesis investigates wireless force measurement (WFM) approaches, ultimately contributing to WRCFM. The research focuses on designing inductor-capacitor (LC) resonance sensors, developing inductance-to-digital converters (LDC)-based measurement systems, separating lift-off and force using isoparametric quadrilateral transformation, and enhancing lift-off and sensitivity through magnetic resonance coupling (MRC).

1.2 Research Motivation

The research work in this paper is part of the International Collaboration and Exchange Project of NSFC between UK and China: Intelligent Sensing and Monitoring of Running Gears (Grant number: 61960206010). This project aims to design and develop a comprehensive sensing and monitoring system of running gears for high-speed railway. It will focus on cross-discipline research of vehicle dynamics, failure mechanism, sensors, monitoring systems, data management, and decision making. In addition to design and development of geometry optical inspection, active and passive RFID sensors and Barkhausen noise stress detection, wireless acoustic and vibrational sensor network for compressed sensing. Specifically, vehicle dynamics and failure mechanism based multiple modality sensors and monitoring integration, data capturing, and fusion, condition-based maintenance and safety management platform will be developed and evaluated via different case studies. It will be compared with rail track high-speed inspection for high-speed railway running gears inspection, monitoring, and safety management.

This thesis has identified the problems of the current approaches for WRCFM and developed new potential solutions. Although the existing methods can achieve WRCFM, they face challenges from sensor installation, signal transmission, expense of measurement system, and signal processing. WFM brings the benefits of easy installation, no contact, and simplicity of the measurement system. Unfortunately, there is no mature method measuring wheel-rail force wirelessly. Eddy current testing (ECT) is a potential solution for WFM because of its non-destructive, non-contact, fast, and low-cost characteristics, and some researchers have made progress using ECT for non-contact measurement. It measures the force based on the change of equivalent inductance due to piezoresistive or inverse magneto-resistive effects. However, ECT has low sensitivity and the distance between the ECT sensor and specimen is very low. LC resonance sensor differs from eddy current sensors which only contain a coil. It has an extra capacitor that forms an LC resonator, causing the improvement in sensitivity owing to the sharp variation in impedance curves. The utilization of LC resonance sensors on WFM contribute to enhancement in measurement sensitivity compared with other non-contact methods.

1.3 Aim and Objectives

The work in this thesis aims to design, develop, and investigate novel LC resonance sensors and integrated LDC-based measurement systems for WFM, coping with the challenges appearing in state-of-the-art technology, such as wiring connection of strain gauges, complicated image processing of DIC technology. The developed WFM approach will be used in future WRCFM in practical railway industry. Figure 1.1 shows the research outline of WRCFM based on LC resonance sensing, which mainly replies on the change in material properties and geometric dimension. The objectives of the work are summarised as the subsequent statements:

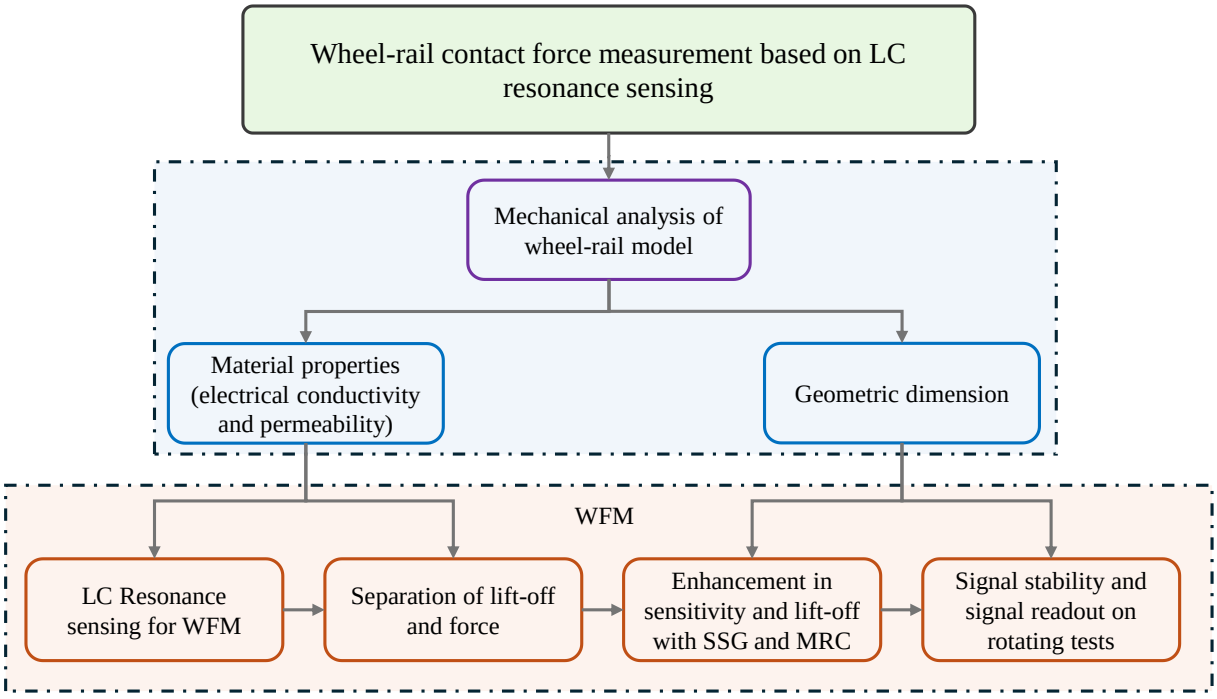

Figure 1.1 Research outline of WRCFM using LC resonance sensing

1. To investigate the measurement principle and signal characteristics of LC resonance sensing for WFM by analysing the mechanism of wheel-rail contact force, studying changes in material properties and geometric dimensions, and simplifying the wheel-rail model.
2. To design LC resonance sensors based on wheel-rail force analysis by determining the sensing direction, inductor coil size, and capacitor value; to develop an LDC1614-based system for resonant frequency measurement system; and to investigate the application of the designed LC resonance sensors and LDC-based systems in the wheel specimen loading tests using the universal testing machines in the laboratory.

3. To investigate the separation of forces and lift-offs by designing an orthogonal LC resonance sensor, developing a multi-parameter measurement system based on the LDC1101, and proposing 8-node isoparametric coordinate transformation algorithms.
4. To study MRC-LDC-based impedance sensing approach for WFM using semiconductor strain gauges (SSG), and series-parallel (SP) and parallel-parallel (PP) topologies, aiming to extend lift-off capabilities and enhance sensitivity.
5. To research the stability of LC resonance sensor outputs under temperature fluctuations by employing differential configurations and software processing algorithms, and to investigate signal readout and signal feature extraction through rotating platform tests.

1.4 Research Methodology

To achieve the aim and objectives outlined above, the work adopts a compressive strategy encompassing the analysis of wheel-rail force, the design of LC resonance sensors, the development of an LDC1614-based system for resonant frequency measurement, the establishment of experimental testing platforms, signal processing, the design of orthogonal LC resonance sensors, the development of a multi-parameter measurement system based on the LDC1101-ESP32S3, separation algorithms of forces and lift-offs, an MRC-LDC based impedance sensing system for extending lift-off and enhancing sensitivity, a data acquisition platform, and a rotating testing platform.

LC resonance sensor design involves the consideration of ranges in resonant frequency and parallel equivalent impedance, dimension of LC resonance sensors, number of inductor coil turns, spacing between coil traces, rotating direction of coil tracks, number of layers, types of inductors and capacitors, package of capacitors, substrate materials, maximum current ratings, and fabrication technique. After determining these parameters, inductor coils and capacitor pads can be designed using Altium Designer, a professional electronic design automation (EDA) software, to create the printed circuit board (PCB) routing and layout. LC resonance sensors are then fabricated on a substrate, such as FR4, with the specified coil structure and capacitor. An impedance analyser Bode 100 is used to measure parameters of the fabricated LC resonance sensors, including its resonant frequency, quality factor, impedance, equivalent parallel resistance. To tune the resonant frequency, the inductance of the inductor coil can be firstly measured, and then different parallel capacitors are selected.

The measurement system is crucial for sensor's operation, stability, accuracy, and anti-electromagnetic interference (EMI) capability. The LD1614-based measurement system, which measures only resonant frequency, consists of an LDC1614 chip that integrates both excitation

and integration modules, an MSP430 MCU for controlling, writing and reading the registers of LDC1614 via the I2C communication protocol, and a LabView-based graphic user interface (GUI) for data visualisation and logging through serial communication.

The experimental platform determines how the test conducts and what specimen is tailored to use. In the laboratory stage, a SHIMADZU Autograph AGS-100kNX tensile testing machine and Instron 3369 are used for loading specimens. Due to the requirement of testing grips, dog-bone specimens made of carbon steel C50, which possesses similar mechanical properties as wheel materials, are designed. During experimental tests, an LC resonance sensor connected to the LDC1614-based system measures the specimen which is loaded by the testing machine. The output of LC resonance sensor-resonant frequency, and the actual loading force on the specimen are imported to MATLAB to perform feature extraction and curve fitting. Thus, the relationship between resonant frequency and force is determined.

The design of orthogonal LC resonance sensors aims to provide multiple parameters which facilitate separation of forces and lift-offs. It uses the similar approach as the previous LC resonance sensor while it has 8 layers with an orthogonal configuration of two LC resonance sensors, increasing sensitivity in unidirectional force measurement and offering lift-off information as well. A 2-channel LDC1101- ESP32S3 based system is specially designed, offering 4 parameters measurement, two resonant frequencies, and two equivalent parallel resistances. A MATLAB-based GUI is devised to meet the requirement of visualizing these 4 parameters in one interface. The separation algorithm of forces and lift-offs considers the output characteristics and combinations of the two LC resonance sensors. An 8-node iso-parametric coordinate transformation algorithm is proposed based on two the independence of the selected characteristics. The algorithm processes the four outputs of the orthogonal LC resonance sensor in MATLAB.

MRC-LDC based impedance sensing is able to enlarge the operational range of lift-offs while maintaining the desired sensitivity. This method utilizes two LC resonators, one SSG, a LDC1101-ESP32S3 based system. A SSG installed on the specimen is connected to an LC resonator, denoted as Rx, while another LC resonator connected to the measurement system, denoted Tx, is used to interact with Rx via magnetic coupling. Any change in SSG resistance incurred by force changes impedance in Rx. This change is magnetically coupled to Tx, represented by reflected impedance, varying the equivalent impedance in Tx which is then measured by the measurement system. There are two topologies for this approach with one referring to SP while the other PP. The influence of topologies on the measurement performance of WFM is simulated via LT-Spice and experimental study.

Rotating testing platform is important to study the signal response between Rx and Tx when the lift-off and SSG varies, offering guide in the future WRCFM. One metallic circular plate is machined and then installed on a motor which drives the plate to spin, simulating running status of wheels.

1.5 Thesis Layout

The layout of this thesis is outlined as follows:

Chapter 1 describes the introduction of the thesis structure, including research background of WRCFM, existing advantages and disadvantages of using strain gauges and other techniques, research motivation based on the identified challenges of using LC resonance sensing for WFM and MRC-LDC based impedance sensing, aim and objectives, and applied methodology.

Chapter 2 presents literature review for state-of-the-art technique in WRCFM. It includes strain gauges, digital image correlation (DIC), RFID-based force sensor, eddy current testing for WFM, LC resonance sensing, wireless power transfer (WPT)-based force detection, and digitalisation and miniaturization of measurement systems. Their principle, measurement system, signal features, and applications are detailed as well.

Chapter 3 explores the conceptual study of using an LC resonance sensor for WFM. It covers the design of the LC resonance sensor, experimental set-up including the specimen preparation, LDC1614-based measurement system, SHIMADZU testing platform, performance tests on the lift-off and aspect ratios of the inductor coil, and results analysis.

Chapter 4 addresses the separation problem of lift-off and force in a LC resonance sensing system for WFM. An orthogonal LC resonance sensor was designed to produce multiple parameters which potentially cover independent characteristics for lift-off and force. A 2-channel LDC1101-ESP32S3 measurement system and MATLAB-based GUI were developed for multiple-parameter measurement, data visualisation and collection. Besides, an 8-node iso-parametric coordinate transformation algorithm was proposed to separate force and lift-off according to their independent features.

Chapter 5 proposes a novel MRC-LDC based impedance sensing approach for WFM. This new method inherits the previous measurement system but introduces MRC with a SSG and an additional LC resonator, aiming to enhancement in lift-off while maintain the sensitivity. Both simulation and experimental studies were conducted to investigate SP/PP topologies, lift-offs, and SSGs for the influence of WFM.

Chapter 6 carries out stability research of the MRC-based impedance sensing over temperature fluctuation through differential configurations and software filtering processing, and rotary test for signal response analysis and feature extraction.

Chapter 7 concludes the overall progress of the research, main contributions in WFM field, limitations of the research, and application exploration using the proposed methods. In addition, future work directs potential challenges in practical applications and underlying solutions, such as combination of artificial intelligence and the proposed physics system.

1.6 Chapter Summary

This chapter mainly describes the overall structure of the thesis. Starting from the background of WRCFM and the limitations of the existing technique, the proposed solution is introduced, followed by research motivation, and aim and objectives. The research methodology involving LC resonance sensor design, establishment of measurement systems and experimental platform, signal processing and analysis. In the end, the layout of the these is listed with 7 chapters.

The next chapter focuses on a detailed literature review regarding mechanism of wheel-rail contact force, WRCFM methods, RFID-based sensors for WFM, ECT sensors for WFM, LC resonance sensing and MRC for WFM, and the development of digitalisation and miniaturization of measurement systems.

Chapter 2. Literature Review

This chapter reviews the mechanism of wheel-rail contact forces (WRCF) and the state-of-the-art progress in wheel-rail contact forces measurement (WRCFM), including techniques such as strain gauges, digital image correlation, and gap sensors. It also examines advancements in WFM using RFID-based sensors, magnetic Barkhausen noise, eddy current testing, LC resonance sensing, wireless power transfer-based sensing, as well as the development of digitalisation and miniaturization of measurement systems. Challenges and problems are then identified based on this review.

2.1 Mechanism of Wheel-rail Contact Forces

Railway transportation has become one of the most popular modes of travel in many countries around the world due to its convenience and comfortability. With the tendency of railway systems towards high speed, high density, heavy load [18], running safety and smoothness of railway vehicles are of paramount significance since they are related to passengers lives and economic development [9]. WRCF, mainly including vertical Q and lateral forces Y [10], as shown in Figure 2.1, are generated during the process of running due to the interaction between the wheel and rail. The vertical force arises from the weight of railway vehicles, which is affected by wheel out-of-round, wheel's load, rail corrugation, and rail joints [18]. The lateral force occurs on account of the friction between the wheel and rail in the horizontal plane. It is influenced by wheel rail creep, hunting motion and curve passing. The ratio of the lateral force to the vertical force (Y/Q) decides the derailment coefficient [19]. In a word, WRCF represent the dynamic behaviour of running vehicles and determine derailment, riding quality, wheel tread wear, and rail conditions. Therefore, there is a need to measure WRCF in real-time to evaluate dynamic performance relative to traveling safety and ride comfort of railway vehicles.

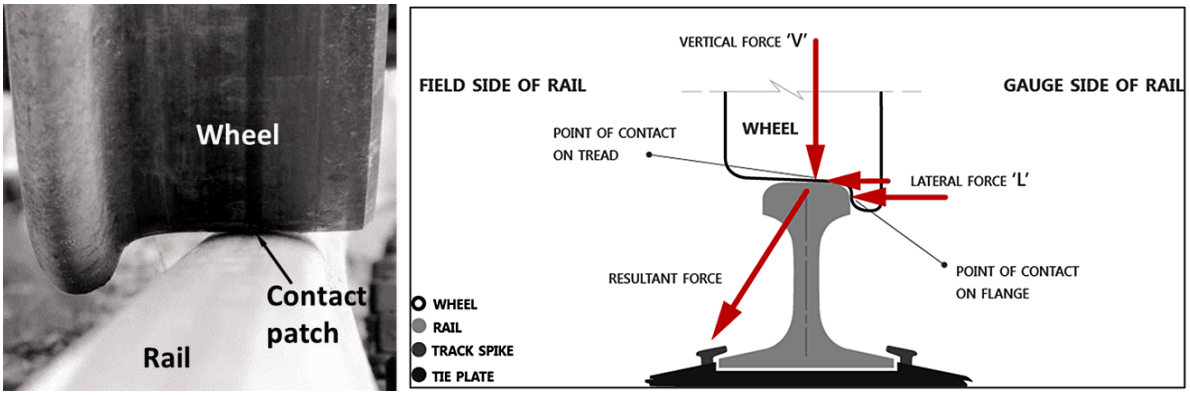

Figure 2.1 The wheel-rail contact of railway vehicles (left) [20] and wheel-rail force distribution (right) [21]

2.2 Review of Wheel-rail Contact Forces Measurement Techniques

The review in this section describes several common methods for WRCFM, which contains strain gauges, gap sensors, and digital image correlation. As the most established method for WRCFM, strain gauges have been paid much attention, ranging from installation positions and placement methods to signal decoupling algorithms. Gap sensors are non-contact devices commonly used for measuring lateral forces by detecting variations in the gap between the wheel and the sensor. Digital image correlation, another non-contact method, relies on monitoring fixed-point strain on the surface of wheel webs. Despite their non-contact nature, these methods are not as popularized as strain gauges.

2.2.1 Strain Gauges

Strain gauges (SGs) have been broadly used in WRCFM due to their high sensitivity to tiny changes in geometric size and low cost [10, 18, 22, 23]. The continuous WRCFM is called instrumented wheelset in which it is a wheelset of the vehicle under tests with some SGs and transducers [10]. SGs are glued onto the wheel web or axle to detect the elastic strain on these components to derive practical WRCF through an appropriate calibration procedure. H Kanehara *et al.* analysed surface strain distribution on wheel disks and determined the installation points of SGs. As shown in Figure 2.2, lateral force was measured by gluing strain gauges on wheel webs while vertical loading was detected by attaching strain gauges inside the holes [24]. Wheatstone bridges in Figure 2.3 are used for strain signal conditioning as it converts tiny resistance variations into measurable voltages, enhancing sensitivity and precise detection while cancelling noise such as temperature drift. In addition to installing SGs on wheel webs, some authors attempted to mount SGs on the axle [25]. Figure 2.4 shows SGs wiring for axle-based methods. The signals are affected by the rotation of the axle, resulting in signals that are amplitude modulated with a purely sinusoidal disturbance in phase with the axle rotation [10].

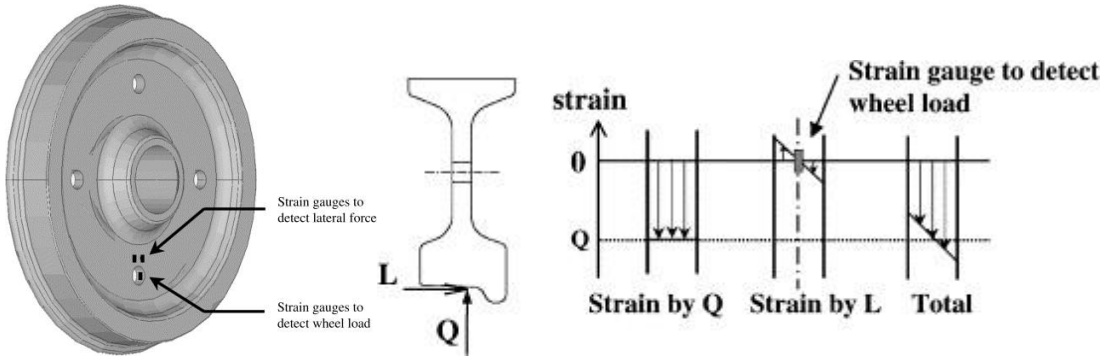

Figure 2.2 Typical location of SGs for WRCFM (left), strains in the web affected by Q and Y forces (right) [24]

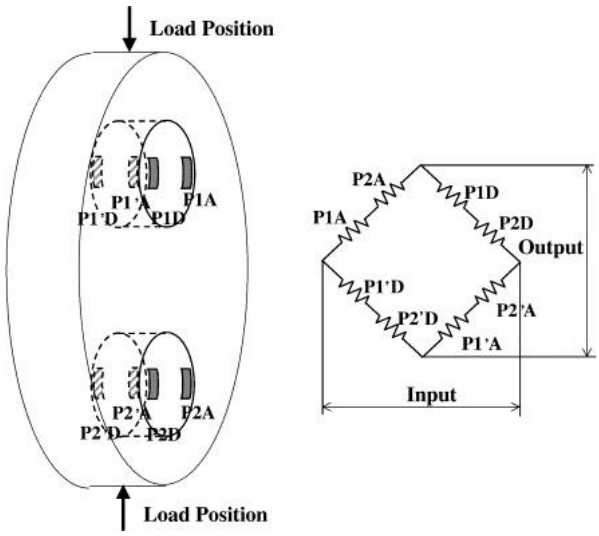

Figure 2.3 Locations of SGs and the bridge for WRCFM [24]

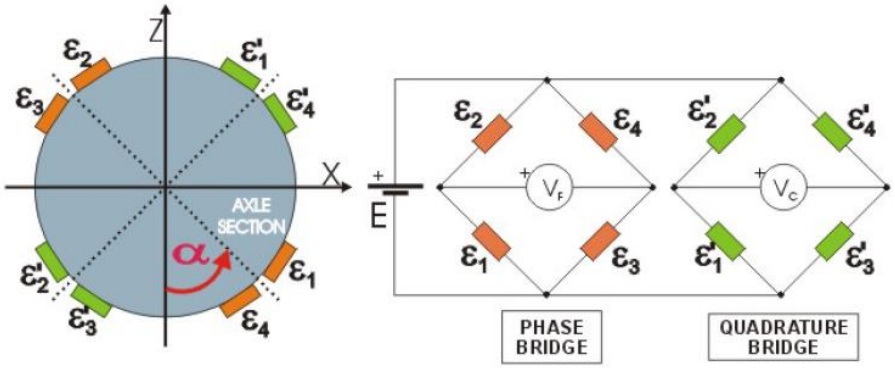

Figure 2.4 SGs wiring for axle-based methods [25]

The installation strategies of SGs play an important role in reduction of WRCFM errors [26]. In Figure 2.5, there are three strategies with different merits and drawbacks. For Figure 2.5(a), multiple SGs are installed at different angular positions. Their sum tends towards the continuous component of strain as the angular position changes [26]. However, this strategy reduces the maximum sensitivity; the output signal always comes with ripples. Figure 2.5(b) shows only a SG is used, which conducts the measurement when the SG passes though the contact point between the wheel and rail. This strategy eliminates the influence of singular position of the wheel but lowers the bandwidth. Figure 2.5(c) presents two SGs with a phase difference of 90º. These two strains are multiplied by two in-phase sinusoidal signals respectively, and the results are summed to obtain a demodulated strain. This strategy also comes with ripple interferences. Cai *et al.* studied the stress and strain distribution on the wheel under vertical and lateral forces to seek optimal positions for SG installation [2]. The criteria were to find an area where the stress or strain was only sensitive to either vertical or lateral forces. Figure 2.6 presents the stress distribution map on the surface of wheel. It indicates that both lateral and vertical forces exhibited minimal coupling interference at certain areas. V. R. Bagheri *et al.* developed a new

arrangement of SGs in the Wheatstone bridge and the wheel web to get elimination of undesired harmonics due to rotation of the wheelset and mean square error (MSE)-based algorithm for selection of optimal ration SG position [12].

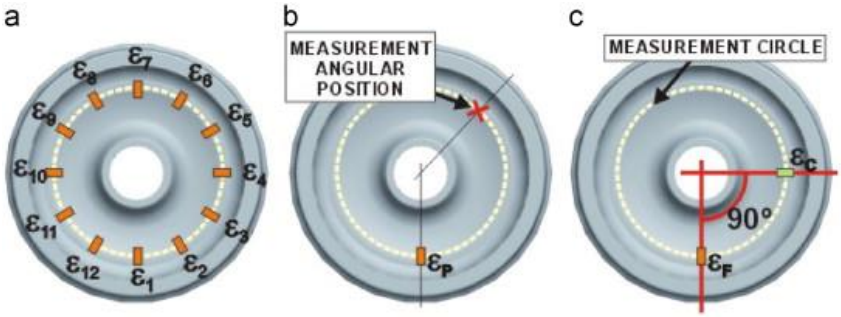

Figure 2.5 Various strategies for the angular positioning of SG [25]

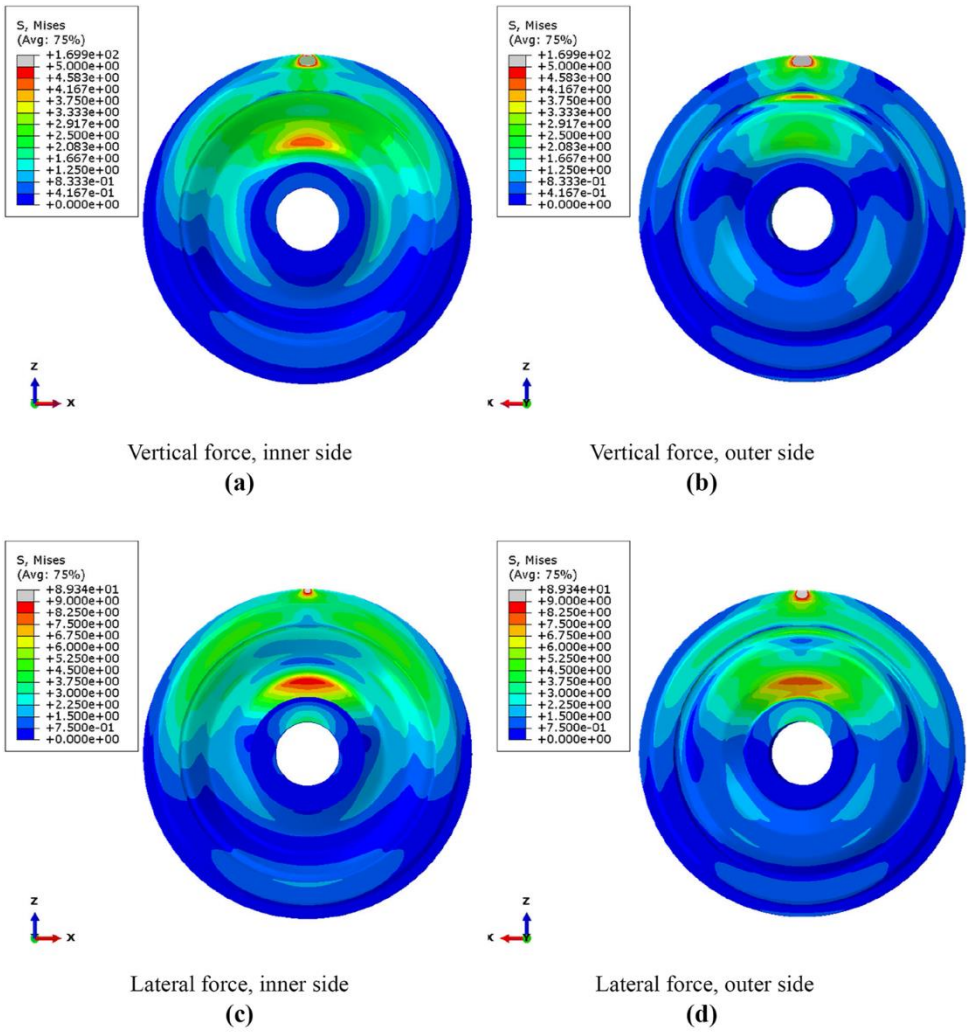

Figure 2.6 Mises stress distribution map on the wheel surface [9]

SGs are mounted on a rotating wheelset while the data acquisition system remains stationary, transmitting data between them poses significant challenges. Therefore, a radio telemetry system or slip ring is necessary to ensure continuous data transmission across the rotating interface, which cannot be achieved through fixed wiring due to the constant motion. SGs are

connected to Wheatstone bridges and then to a radio telemetry system. A telemetry system in Figure 2.7 (top) consists of a rotating antenna, a static antenna, telemetric conditioners with analog outputs, analog to digital converters (ADC), and a computer [15]. The static antenna is fixed on bogie, shown in Figure 2.7 (down) and the rotating antenna is mounted on the axle which follows the rotation of the wheel. The static antenna receives the modulated strain signals from the rotating antenna for demodulation and post-processing.

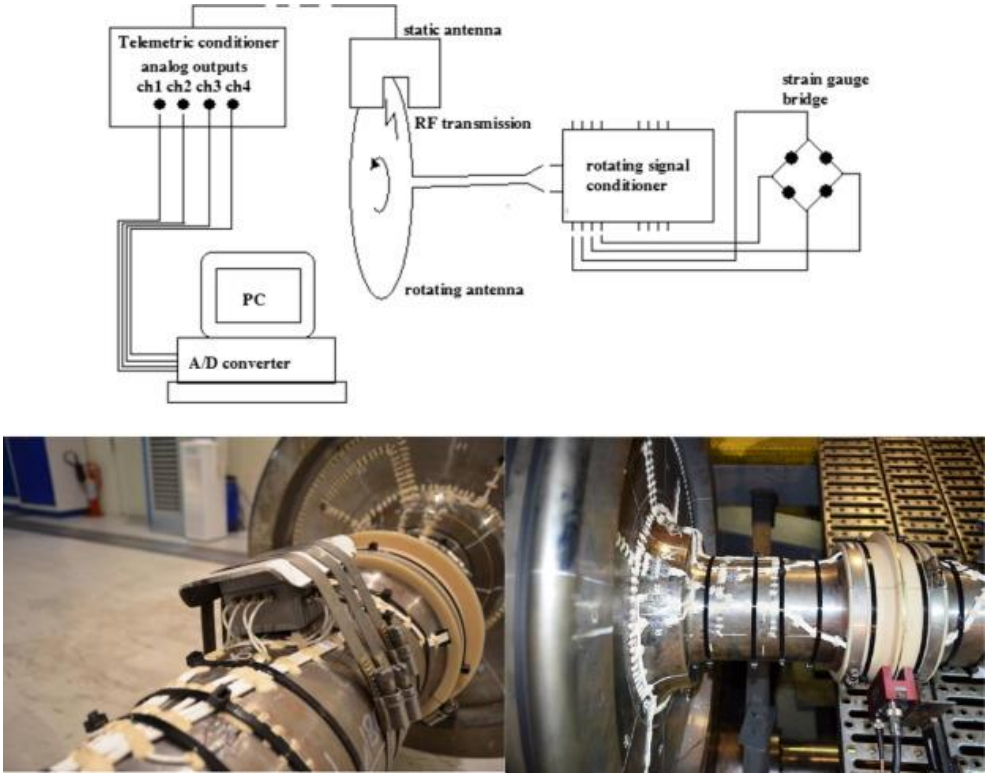

Figure 2.7 The wheelset instrumented with telemetry system (top) under preparation (left) and then on BU300 test rig (right) [15]

SGs on WRCFM have attracted much attention so far due to its advantages of high sensitivity, ease of installation, and low cost. Many scholars have dived this field into a very deep level. However, as a coin has two sides, SGs are a contact measurement approach which requires wiring-connection. It is required that a special processing is implemented for an instrumented wheelset such as drilling holes. The instrumented wheelset lacks sufficient resistance against heat attack by braking [27]. Moreover, signal transmission from a rolling wheelset to the fixed bogie frame is challenging [27]. Telemetry systems have to be used, which are very complicate and delicate electronic devices, and they involve radio frequency signal processing which is susceptible to the environmental and electromagnetic interferences.

2.2.2 Digital Image Correlation

Digital image correlation (DIC) is a non-contact visual method to measure surface deformations, displacements, and strains in materials and structures. The principle of measuring surface strain is implemented by recording the images of the surface before and after deformation [28]. A DIC system comprises a high-resolution camera, light source, computer, and lenses and filters. The recorded and digitized images are stored in computer for further image processing. The images are compared to detect displacements by searching a matched subset from one image to another. The subset consists of multiple pixel points, which has a unique light intensity distribution. It is assumed that this intensity distribution will not change in the progress of deformation. The displacement is determined by searching the area on the image after deformation which has the same light intensity distribution as the image before deformation. Wang *et al.* applied DIC technology on WRCRM based on space fixed points of the wheel web; the DIC set-up for measuring stress is shown in Figure 2.8; two stress concentration points were selected as the fixed points position, corresponding to the lateral and vertical loads in Figure 2.9 respectively [17].

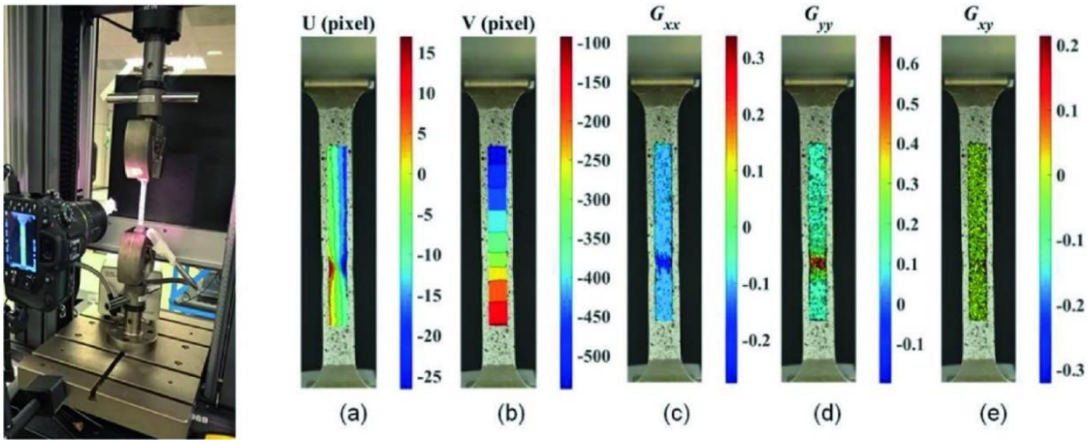

Figure 2.8 Photograph of DIC set-up and results [17]

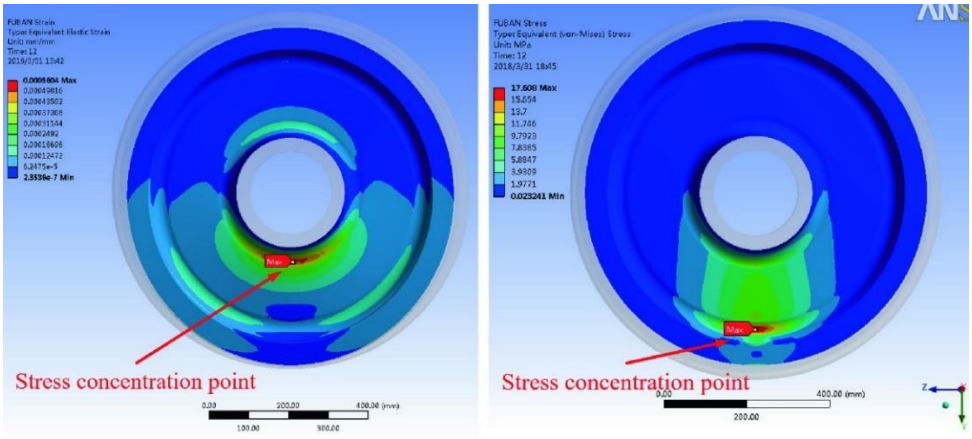

a. Lateral force loaded b. Vertical force loaded

Figure 2.9 Stress concentration distribution for lateral and vertical force loads [17]

It is noted that DIC offers a new insight into WRCFM because of its merits, such as non-contact measurement, full-field data, and high resolution and flexibility. However, it faces challenges from line-of-sight requirement, surface preapration, dependence on spekle patern quality, environmental sensitivity such as vibration and dust, and computation capability of processing large data volumes. Applying this technique to actual WRCFM still has a long way to go.

2.2.3 Gap Sensors

Lateral forces can lead to bending deflection of the wheel [29]. On the basis of this point, researchers have developed new approaches with gap sensors to realize the measurement of lateral forces [27, 29-31]. Gap sensors are non-contact and able to measure tiny displacements or deformation caused by WRCFM, offering benefits of minimal mechanical installation, and real-time monitoring. In Figure 2.10, a non-contact inductive gap sensor is placed close to the outer edge of the wheel web through a sensor base installed on the bearing box to continuously monitor lateral forces [29, 30]. There is another gap sensor close to the boss, which is used for compensation of wheelset movement [29]. P. Urda *et al*. adopted high-precision lasers to measure the lateral wheel-web deflection, as shown in Figure 2.11 [31]. These methods avoid using slip rings or telemetry in signal transmission. However, the limitations of applying gap sensors include indirect force measurement rather than direct force measurement, limited spatial information, and difficulty of calibration.

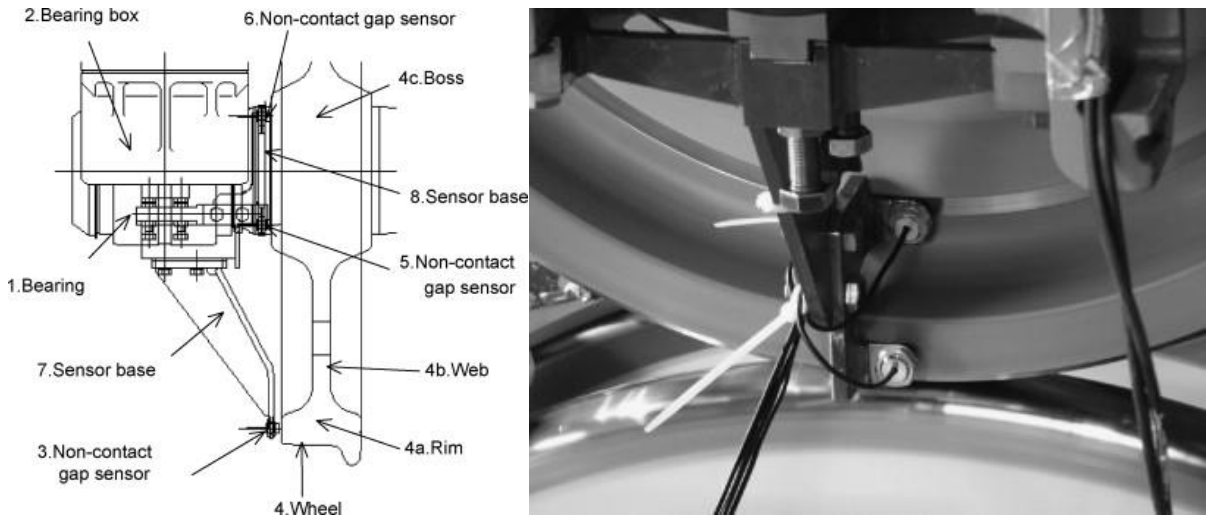

Figure 2.10 Layout of gaps sensors for measuring lateral force [27]

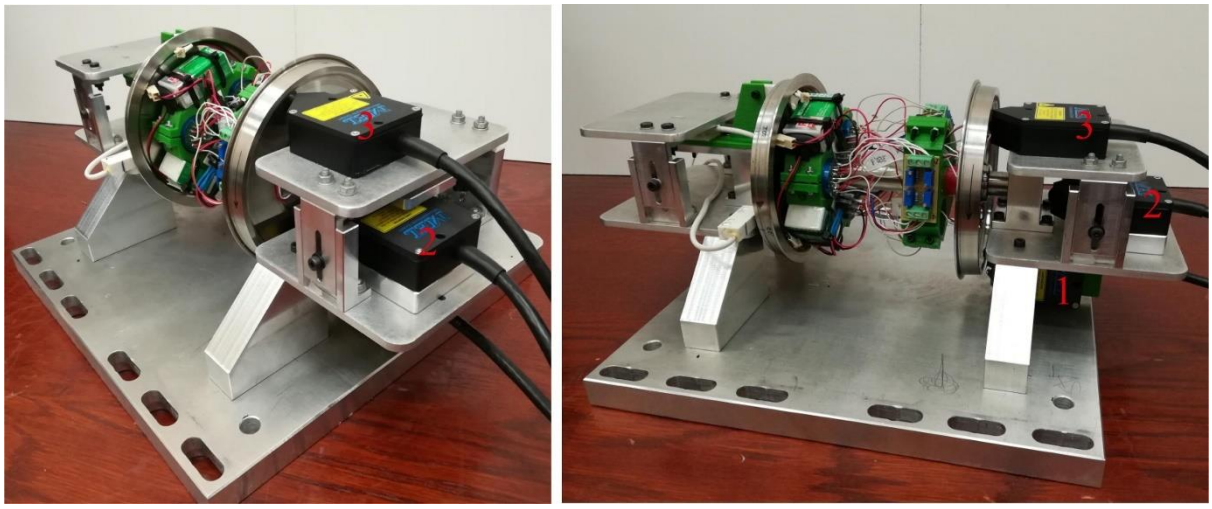

Figure 2.11 Installation of lasers for lateral force measurement [31]

2.3 Review of WFM using Electromagnetic NDT Techniques

Since the aim of this thesis is to develop new wireless measurement approaches for the ultimate goal of WRCFM, the concentration is focused on the development and validation of conceptual ideas. Thus, the problems are simplified from WRCFM to WFM.

Electromagnetic NDT technique offers many potential solutions for WFM, including RFID-based sensors for strain detection, magnetic Barkhausen noise, eddy current testing, LC resonance sensing, and wireless power transfer. These techniques are introduced in terms of the principle, system, and application. Table 2.1 shows a comparison table of these electromagnetic NDT techniques for WFM in terms of principle, measurement parameter, merits, and limitations. Besides, due to the development of measurement systems towards miniaturisation, digitalisation, low cost, and portability, several chip-based systems are reviewed.

Table 2.1 Comparison of electromagnetic NDT techniques for WFM

Method	Principle	Parameter	Merits	Limitations
RFID-tag based sensor	A passive RFID resonator (antenna and tuned circuit) whose mechanical deformation under load shifts its resonance or impedance	Back-scattered signal: resonant frequency shift	Wireless/passive; low cost; compact design; can be embedded into structures	Short read range (cm–m); sensitive to electromagnetic noise; limited sensitivity
Magnetic Barkhausen noise	A ferromagnetic specimen under stress, when magnetized, emits discrete noise bursts (domain-wall jumps). The noise level correlates with stress.	Barkhausen noise amplitude or energy spectral density	Highly sensitive to local stress/strain in ferromagnets; detect microstructural changes	Requires magnetizing coils and sensitive pickup; strongly surface-limited (µm scale); complicated signal processing
Eddy current testing	An AC coil induces eddy currents in nearby conductive material;	Change in coil impedance	Non-contact, high resolution; fast, real-time scanning; good	Penetration limited by skin depth (µm–mm); lift-

	stress-induced changes in conductivity/permeability alter the coil's impedance	(magnitude & phase shift)	surface and near-surface sensitivity	off influence; only works on conductive materials
LC resonance sensing	A passive LC circuit whose capacitance or inductance is mechanically modulated by force, shifting its resonant frequency and amplitude	R_{Peq}, f_{res}	Wireless/passive; high sensitivity to deformation; simple design	Short range, tens of cm; temperature/humidity sensitive
Wireless power transfer-based sensing	Two coupled coils transfer power magnetically; applied force alters a tuning element, which changes reflected impedance	Received power level; shift in transfer-function resonance and impedance amplitude	Simultaneously power and sense; longer range than purely passive tags	Lift-off influence; efficiency sensitive to alignment and distance;

2.3.1 RFID Tag-based Sensor for Stress Detection

Radio frequency identification (RFID) is a wireless technology based on electromagnetic fields and waves, which has been extensively implemented in industrial Internet of Things (IoT) applications for identification, positioning and sensing, such as manufacturing lines, supply chains, warehousing, mobile device navigation, structural health monitoring systems [32-36]. According to operating frequency ranges and energy transfer mechanisms, it can be divided into near-field RFID which operates at low frequencies (kHz-MHz, such as 125-134kHz and 13.56MHz) and relies on electromagnetic coupling through inductive/magnetic fields, limiting their effective range to short distances (~1m), and far-field RFID which utilizes high frequencies (hundreds of MHz-GHz, such as ultra-high frequency (UHF) at 860-960MHz and ultra-wideband (UWB) RFID at 2.45-5.8GHz) and depends on electromagnetic radiation (propagating radio waves), enabling extended communication ranges (tens of meters) suited for large-scale tracking like inventory management or toll collection, albeit with higher power requirements and reduced signal penetration capabilities compared to near-field systems [37].

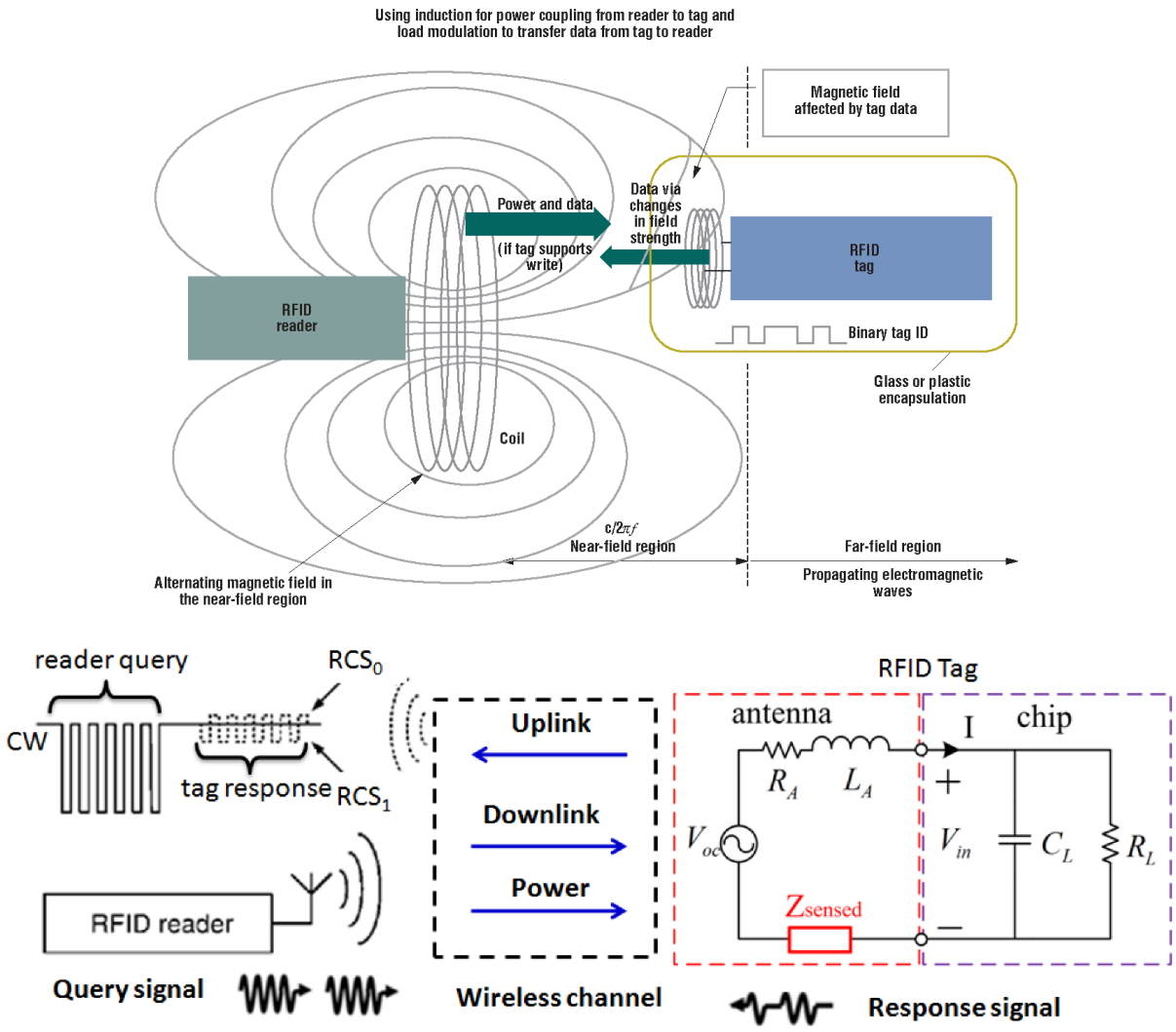

Figure 2.12 Communication mechanism of near-field RFID (upper) [37] and far-field RFID (down) technology [36]

Figure 2.12 illustrates the communication mechanism of near-field (upper) and far-field RFID (down). It consists of an RFID reader and a RFID tag. There are two types of RFID tags. One is active and another passive. Active tags require a power source such as a battery or cable-connected power, which cause the cost, size, and lifetime to be unrealistic in real applications. Passive tags include chip-ed and chipless tags without requirement of power supply as tags are powered by the energy transmitted from the reader. Most of research attention have been put on passive tags with chips. For near-field RFID, a reader passing through an alternating current produces a magnetic field. If a RFID tag is placed to close this magnetic field, an inductive voltage will appear across the tag. This voltage is rectified and regulated to power up the tag chip, which then sends data back to the reader using load modulation via near-field coupling [37]. Another is far-field RFID which utilizes electromagnetic (EM) waves to communicate between a reader and a RFID tag, as shown in Figure 2.12 (down). A RFID tag captures EM waves generated by the reader over the space to power the tag chip, which then transmits the

information stored in the tag back to the reader via backscattering [36]. This backscattering is achieved by that the tag chip alters the reflection coefficient of the tag antenna through varying its internal impedance, resulting in re-radiation of the reader's signal [36].

Even through most of research interests are focused on the RFID tags in applications of tracking, positioning, and identification, recently RFID tag-based sensing have been attracted researchers' attention on strain measurement, and defect and crack detection [34-36, 38-40]. RFID tag-based sensors for strain measurement work by integrating a strain-sensitive element—such as a stretchable antenna or strain gauge—into the RFID tag. When strain is applied, it alters the physical or electrical properties (like impedance or resonance frequency) of the tag. These changes affect the tag's signal response, which can be wirelessly detected and analysed by an RFID reader to determine the amount of strain. Zhang J.*et al* reviewed the application and sensing mechanism of RFID tag antenna based on structural health monitoring [36]. The integration of strain gauges with an RFID tag and an electrical circuit was studied in [41], where the interrogating antenna was used to detect the modulation frequency signal from the RFID tag. This signal varied in accordance with the strain of the target object. Tata U *et al.* studied that a patch antenna as a strain sensing unit was expounded from the point of principle, theory, fabrication, and test [42]. Yi *et al.* simulated and tested a fold-patch antenna against strain changes [43, 44]. Figure 2.13 exhibits the folded patch antenna strain sensor and the experimental set-up at which a RFID reader sends an interrogation signal and receives the backscattering signal from the antenna sensor. The RFID chip was used to modulate the backscattering signal by switching the matched and mismatched impedance to control the amplitude of the backscattering signal, which was beneficial for the differentiation of environmental noise and interrogation signal [43]. Later, they studied the relationship between the strain and the change of dielectric constant of the substrate in the RFID-based sensor due to the shear lag effect, and this relationship was imported into the COMSOL simulation to improve the accuracy [45]. Figure 2.14 shows that strain leads to a shift of original resonant frequency towards the right, as reflected in the S11 curves, with the frequency decreasing as the strain increases.

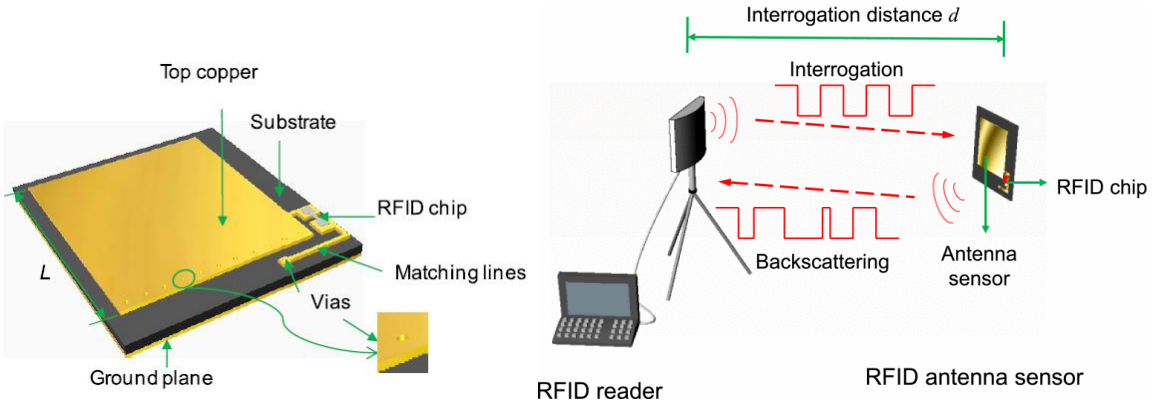

Figure 2.13 Folded patch antenna strain sensor (top left) and experimental set-up (top right) [42, 45]

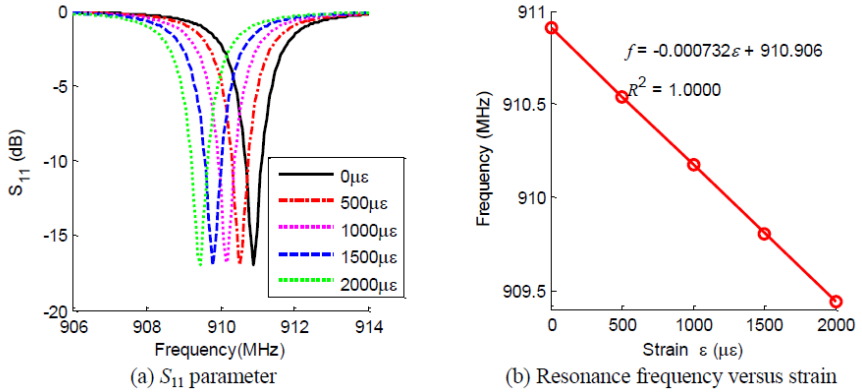

Figure 2.14 Strain simulation results of the antenna sensor [44]

Following the Yi's work, Li D *et al.* presented a rosette-based strain sensor made of the folded patch antennas and slotted patch antennas for measuring an arbitrary strain field [46]. Kuhn *et al.* proposed a wireless strain measurement scenario based on planar inverted-F antenna and a CTC13001 microchip [47]. The change in the tag's resonant frequency as the deformation of the test piece was simulated. The RFID-based strain sensor with the matched impedance exhibited a better linear relationship in terms of strain and the resonance frequency [47]. Figure 2.15 presents a battery-free strain/force tag sensor in which a strain gauge is connected to a RFID tag that harvests energy from the reader to power on the electrical circuits. The RFID tag is comprised of a dipole RF antenna, rectifier, clock, digital processor, memory mapper, and SPI control interface [48].

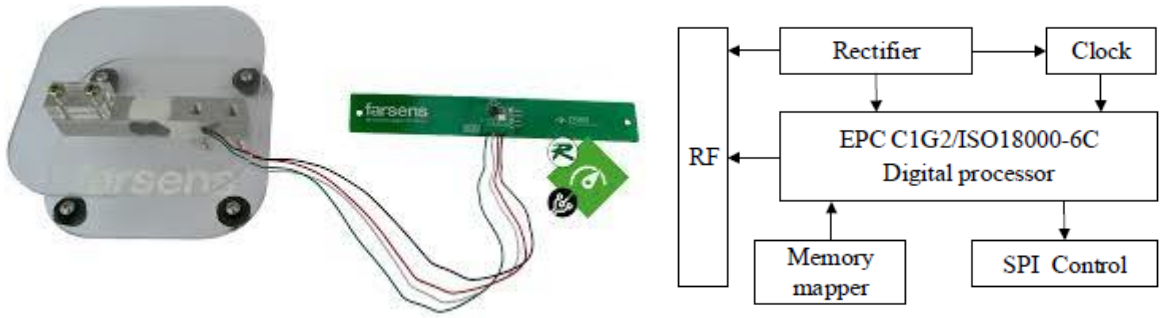

Figure 2.15 Battery-free UHF strain/force sensor tag [35, 48]

Except for the consideration of sensing capability of RFID-based sensors, its fabrication materials such as graphene [49], carbon nanotubes [50] are able to enhance antenna performance such as gain, and radiation pattern. Kim J *et al.* attempted to use silver ink and PDMS to design and fabricate a stretchable RFID strain sensor based on the LC resonator [51]. Pan K *et al.* used graphene ink suitable for screen-printing to design RFID tags at different frequency bandwidths [52]. The fabricated method was non-toxic and environmentally friendly, sustainable, and the read range for the designed UHF RFID tag reached up to 9 m, with high conductivity 7.13e4 S/m. Niu S *et al.* fabricated a stretchable RLC strain sensor tag by using conductive ink and elastomer, as shown in Figure 2.16 [53].

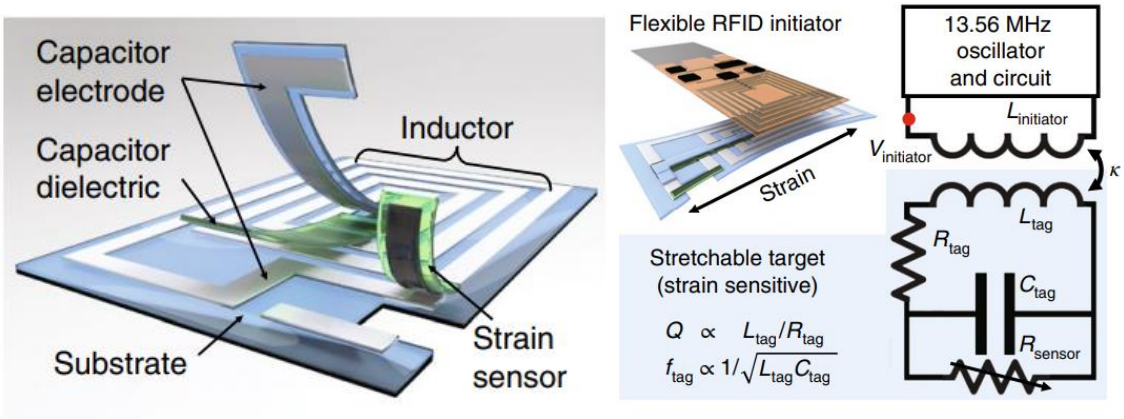

Figure 2.16 Wireless stretchable strain sensor (left) and schematic diagram (right) [53]

2.3.2 Magnetic Barkhausen Noise

Magnetic Barkhausen noise (MBN) is a phenomenon generated by the discontinuous movement of magnetic domain walls in ferromagnetic materials during the magnetization, first discovered by H. Barkhausen in 1919 [54, 55]. It is a micro-magnetic detection method used for characterizing residual stress, hardness, and microstructural properties [56-60]. From microscopic view, ferromagnetic materials are composed of magnetic domains. As shown in Figure 2.17, when there is no external magnetic field, magnetic domains are randomly distributed in each of which the magnetic moments of atoms are aligned in the same direction

due to strong exchange interactions [61]. The random distribution of magnetic domains results from the system which attempts to minimize the total energy. Under magnetization with an alternating magnetic field, the direction of magnetic domains tends to align parallel to the field [61]. The process of magnetization involves the irreversible movement of magnetic domain walls which have to overcome various obstacles such as grain boundaries, dislocations, second phase precipitates, non-magnetic inclusions, and applied or residual stress [55].These obstacles will pin the moving domain wall until the external magnetic field is sufficiently large to overcome it. Once this condition is satisfied, there are abrupt changes in magnetization, which can be seen in Figure 2.17, called Barkhausen jumps. These jumps can be macroscopically observed as a noise-like voltage by placing an inductor coil near the specimen surface [55].

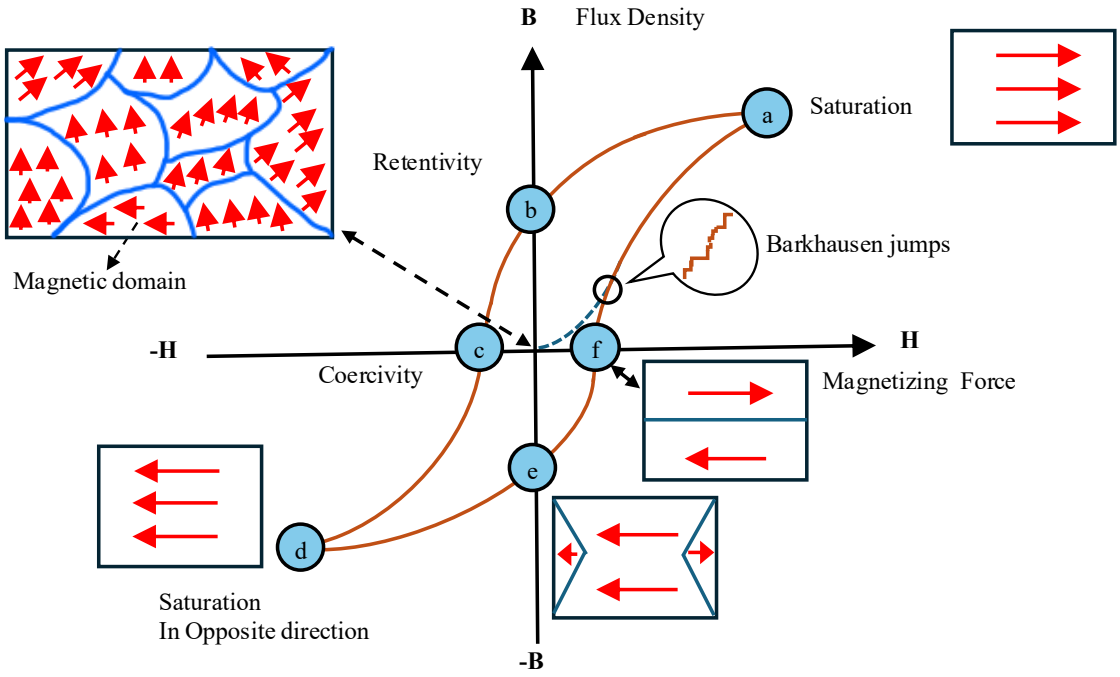

Figure 2.17 Magnetic domain alignment during magnetization

The magnetic flux density (B) and magnetic field strength (H) curve presents the hysteresis loop during magnetization and demagnetization. The value of B increases as H increases, but B tends to stabilize and remain unchanged once H reaches a certain value. This unchanged point is referred to as the saturation point. With a decrease in the value of H, there is a decrease in the value of B. When H decreases to zero, B is not zero and this state is called retentivity. When H continues to decrease along the negative direction, B also decreases. At the point c, it means the ferromagnetic material is completely demagnetized. The corresponding magnetic field strength is called coercivity. At this moment, when H keeps decreasing towards the negative direction, the material reaches the saturation in opposite direction.

The magnetostriction phenomenon is that the dimensional change of a ferromagnetic material under magnetization, which is attributed to the re-orientation of magnetic domains in response to the magnetization, causing internal mechanical stresses [62]. The inverse magnetostriction phenomenon, also known as the Villari effect, is that for positive magnetostriction materials, when a ferrimagnetic material is subjected to an external mechanical stress, the magnetic domains tend to align along with the direction of the tensile stress while perpendicular to the direction of the compressive stress, as seen in Figure 2.18 [61]. The variation of magnetic domains towards the external stress direction leads to a change in magnetic permeability in response to an applied stress [62].

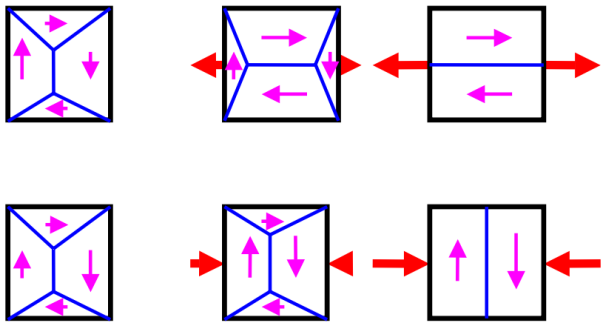

Figure 2.18 Magnetic domain alignment due to tensile and compressive stresses [61]

MBN is highly sensitive to mechanical stress as stress alters the microstructure of the ferromagnetic materials, causing the redistribution of magnetic walls and changing the induced voltage in a pick-up coil. The principle of MBN relies on an AC current-generated magnetic field, which travels through a magnetic yoke to magnetize a ferromagnetic specimen. Due to the process of magnetization, the movements of magnetic domain walls lead to Barkhausen jumps which is then detected by a coil. The detected voltage is a macroscopic symbol of microstructural properties, such as hardness, residual and applied stress. The coil is normally placed near the surface of the material. The excitation to generate MBN signals is a low-frequency signal, such as 0.1 Hz to 20 Hz [61, 63]. However, the MBN signal is a high frequency signal, ranging from 1 kHz to 200 kHz. Thus, a bandpass filter is needed to remove unwanted signals including low-frequency and high-frequency signals. After passing the filter, an amplification module is used to magnify the signal in order to improve signal-to-noise ratio (SNR). Figure 2.19 presents the magnitude of MBN signal increases when the specimen is under tension, but it decreases when the specimen is subject to compression. Based on this, the material's hardness is characterized.

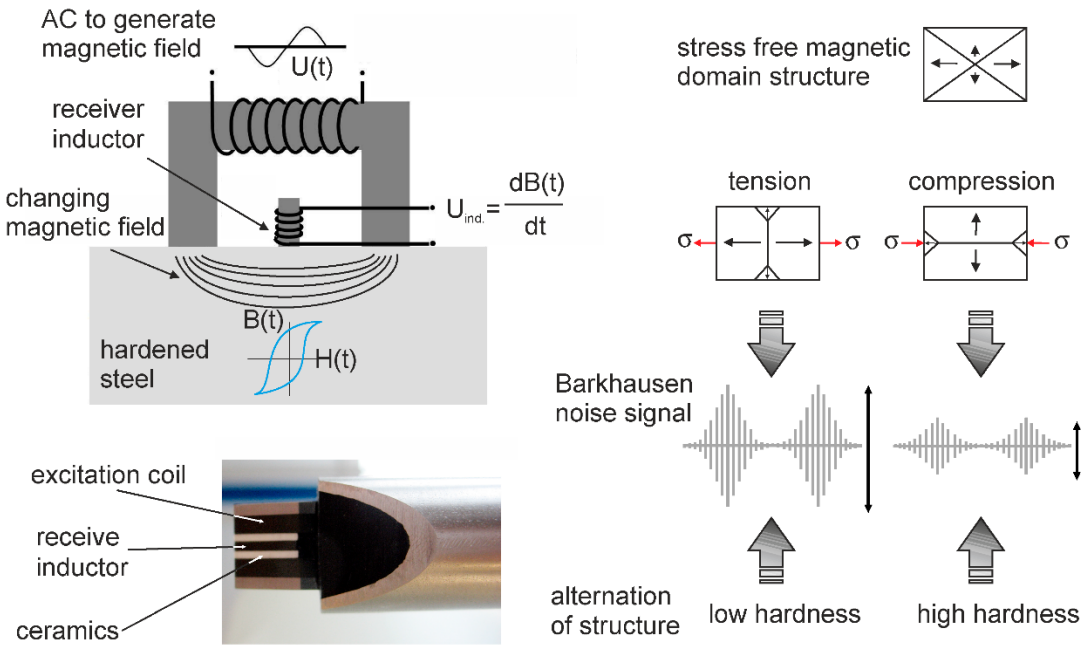

Figure 2.19 The measuring principle for measuring the Barkhausen noise of ferromagnetic materials and typical signals for different materials [64]

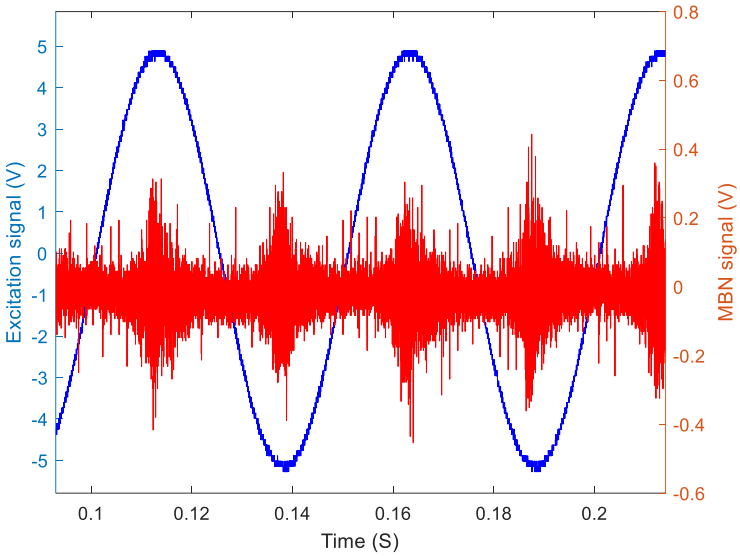

Figure 2.20 Raw signal of MBN excitation and pick-up signals

Figure 2.20 shows the raw signals of MBN's excitation and detection which demonstrate the characteristics of low-frequency excitation and high-frequency detection. Due to the abundant information and stochastic nature in MBN signals, advanced signal processing methods are required. Lots of feature processing algorithms have been investigated, including root mean square (RMS), energy of MBN signal, envelops, time-response histogram of MBN, etc [63, 65, 66]. Liu *et al.* used the peak envelope and RMS value of MBN signals to characterize stress in silicon steel sheets [60], in which the values were averaged after ten cycles. Maciusowicz *et al.* considered the properties of time-frequency (TF) transformations of MBN based on short-time

Fourier transformation (STFT), and extracted the features of TF domain spectrograms to qualify the stress [63], which involved maximum, mean, standard deviation, variance, skewness, Kurtosis, coefficient of variation, spectral entropy, spectral flatness, concentration measure, peak-to-rms, form factor, and so on [67]. The influence of grain and grain boundary distribution under elastic deformation on time-response histograms of MBN was investigated, revealing the variation of the inhomogeneity in magnetic properties under stress and the fact that the grain boundaries were more susceptible to external stresses [66].

MBN provides a medium to characterize ferromagnetic material's microstructure, and it comes with rich time and frequency domain messages. However, due to the complexity of these features, it is difficult to get a stable MBN signals which may affect the subsequent feature selection. Also, MBN requires the probe to have a contact with the specimen, making it difficult to realize non-contact measurement.

2.3.3 Eddy Current Testing

Eddy current testing (ECT) is based on electromagnetic induction theory, which satisfies Maxwell's equations [68]. As it shows in Figure 2. 21, when an excitation coil is driven by an AC current, it will generate magnetic fields around it. These magnetic fields are denoted as primary fields. When bringing a conductor close to the primary fields, the eddy currents occur on the surface of the conductor due to electromagnetic induction. The eddy currents will produce magnetic fields, denoted as secondary fields, which in turn affect the primary fields. Therefore, the total magnetic fields are a superposition of both magnetic fields. The intensity of eddy currents is related to material's conductivity and permeability. If there is a stress, crack, or defect, the distribution of eddy currents will be affected, resulting in a change in the superimposed magnetic fields. By measuring the impedance of the excitation coil or using another pick-up coil to detect the superimposed fields, the material's properties are characterized. Due to non-contact, low-cost, and high-speed properties of ECT, it has become one of the most extensively non-destructive methods for defect inspection and evaluation in aerospace, aircraft, pipeline, and railway industries [69-72].

Figure 2.21 presents an equivalent circuit model for ECT based on Kirchhoff's law, where the excitation coil is regarded as the series combination of an inductor coil L_0 and a resistor R_0, and the specimen is composed of an equivalent inductor L_1 and a resistor R_e. M_{12} is equal to M_{21} where $M_{12}= k\sqrt{L_0 L_1}$; k is the coupling coefficient between the two inductors. V and I_1 are the excitation voltage and current respectively; I_e is the induced current on the specimen. ω is the angular frequency. Therefore, the formula can be established as:

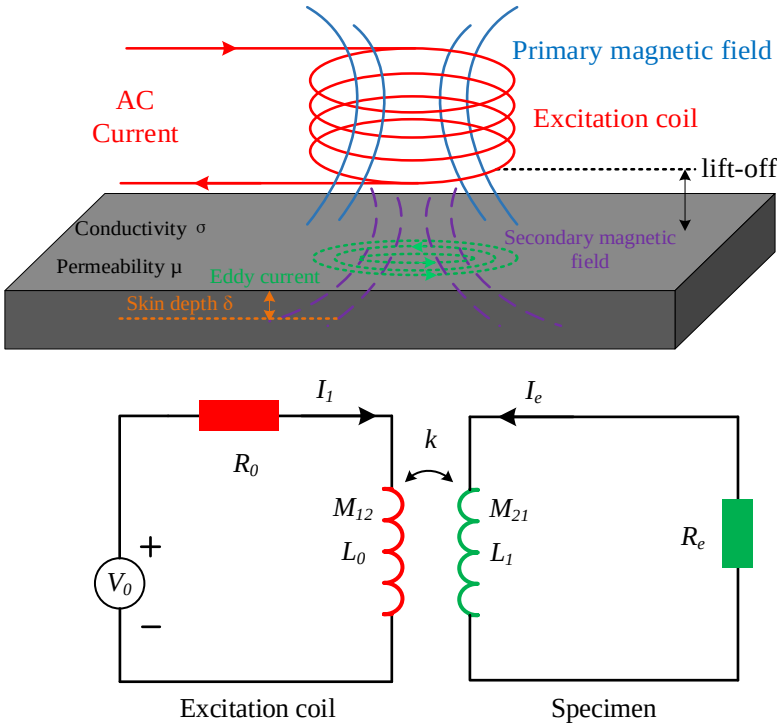

Figure 2.21 Principle of ECT and equivalent circuit model of ECT

$$R_0 I + j\omega L_0 I - j\omega M_{21} I_e = V \tag{2.1}$$

$$I_e(R_e + jwL_1) - j\omega M_{12} I_1 = 0 \tag{2.2}$$

The equivalent impedance $Z_{eq} = V/I_1$ which considers the mutual interaction between the excitation coil and the specimen, is formulated as:

$$Z_{eq} = R_0 + jwL_0 + \frac{k^2 L_0 L_1 \omega^2}{R_e + jwL_1} = R_{eq} + X_{eq} \tag{2.3}$$

$$X_{eq} = j\omega L_0 - j\omega \frac{(\omega k)^2 L_0 L_1 L_1}{R_e^2 + (\omega L_1)^2} \tag{2.4}$$

$$R_{eq} = R_0 + \frac{(\omega k)^2 L_0 L_1 R_e}{R_e^2 + (\omega L_1)^2} \tag{2.5}$$

When the excitation coil is placed in the air, which means there is no interaction with the specimen, the impedance Z_0 is expressed as:

$$Z_0 = R_0 + j\omega L_0 \tag{2.6}$$

The normalised real and imaginary of the impedance Z_{eq} after subtracting Z_0 is derived as [73]:

$$X_{eqn} = \frac{X_{eq}}{j\omega L_0} = 1 - \frac{(\omega k)^2 L_1 L_1}{R_e^2 + (\omega L_1)^2} \tag{2.7}$$

$$R_{eqn} = \frac{R_{eqn} - R_0}{j\omega L_0} = \frac{(k)^2 \omega L_1 R_e}{R_e^2 + (\omega L_1)^2} \tag{2.8}$$

Equation (2.7) and (2.8) represent that the influence of original impedance information of the excitation coil is eliminated, leading to the normalised impedance only related to the testing specimen. Figure 2.22 shows how lift-off and crack affect the normalised impedance plane. The coordinate point of the impedance plane is P_0 (0, 1) when the excitation coil is in the air. Lift-

off is the distance between the excitation coil and the target. As the lift-off decreases, X_{eqn} tends to decrease due to the fact the coupling between the excitation coil and the specimen turns to be stronger. P_1 and P_2 refer to different conductivity σ_1 and σ_2 in which σ_2 is smaller than σ_1, causing two different trajectories in terms of lift-off variations. Obviously, the trajectory with σ_1 is longer than that of σ_2 because eddy current flows increase with respect to P_2, which results in R_{eqn1} larger than R_{eqn2}, and X_{eq1} smaller than X_{eq2} due to stronger eddy currents. When there is a crack on the specimen, it impedes the flow of eddy currents which causes a longer path with reduced eddy current dissipation, and a reduce in the secondary magnetic field, decreasing R_{eqn} and increasing X_{eqn}. The movement from P1 to P2 in Figure 2.22 (left) describes the situation of the excitation coil encountering a crack, corresponding to Figure 2.22 (right).

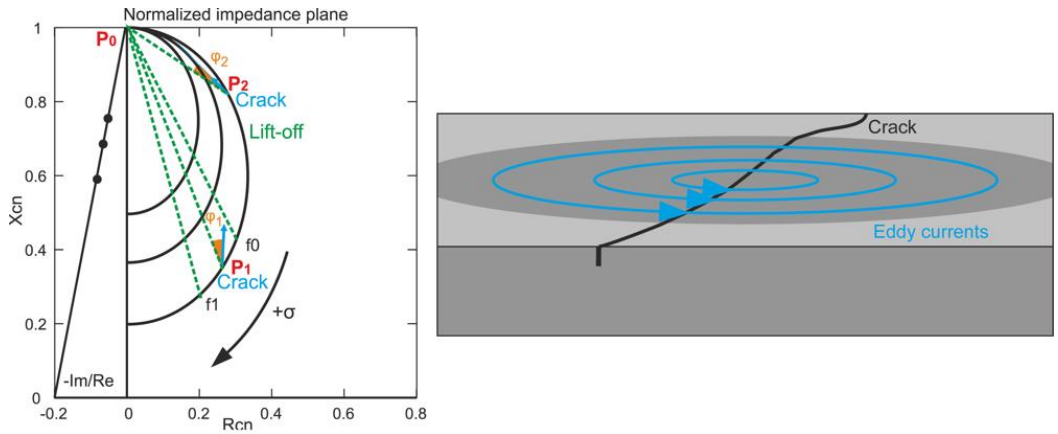

Figure 2.22 Normalised impedance plane: Lift-off curves and crack displacement for two values of conductivity P1 and P2 (left), and altered eddy current when encountering a crack (right) [69]

There is another significant parameter related to ECT, skin-depth δ. It describes how eddy currents penetrate along the depth direction. It is supposed that the eddy current density on the surface is considered to flow only in the x-direction, and it only varies along the z direction. Thus, the surface eddy current density formula can be expressed as [74]:

$$J_x(z,t) = J_{0max} e^{-\frac{z}{\delta}} . \cos\left(\omega t + \alpha_0 - \frac{z}{\delta}\right) \quad (2.9)$$

Where *Jx (z, t)* demonstrates the change of eddy current density against the time and depth *z*. J_{0max} is the value of the eddy current density at z=0; δ is the skin depth; α_0 is the initial phase when t=0 and z=0.

Standard skin depth defines that the amplitude of *Jx (z, t)* at the surface $J_{0max} e^{-\frac{z}{\delta}}$ decays exponentially towards the internal side of the specimen to 1/*e* of the value at the surface. It is expressed as:

$$\delta = \sqrt{\frac{2}{\mu\omega\sigma}} \tag{2.10}$$

In Equation (2.10), μ and σ represent material's permeability and conductivity; ω is an angular frequency. This equation illustrates the skin depth is related to the excitation frequency and material's properties. Figure 2.23 shows the skin-depth curves at two frequencies, 200 Hz for the red line and 10 Hz for the blue line. For low frequencies, the skin depth is deep which means if the ECT probe operates at low frequency, it is able to detect subsurface defects while it detects surface cracks at the surface. Low frequencies can cause a weaker eddy current density at the surface in comparison with high frequencies, which makes the sensitivity of surface defects lower than that of high frequencies.

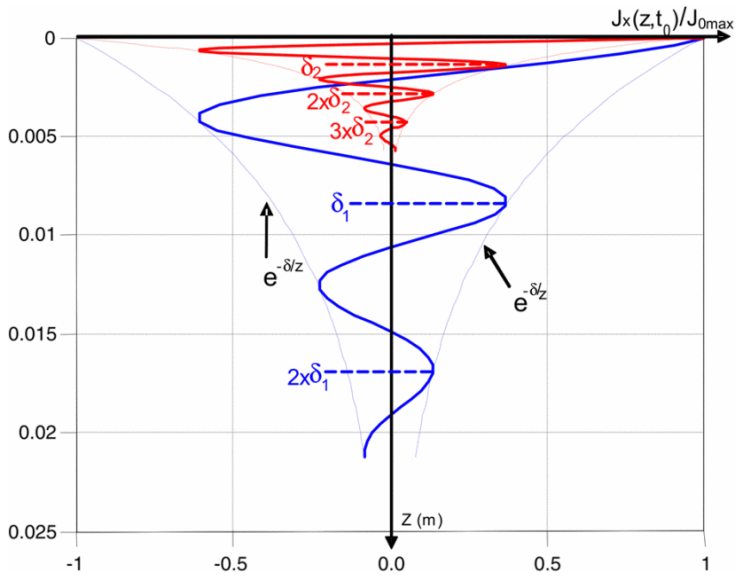

Figure 2.23 Electromagnetic field penetration inside the aluminium for two different frequencies: δ1−200 Hz; δ2−10 kHz [74]

ECT has a variety of coil structures including solenoid coils, pancake coil, and PCB coils, flexible PCB coils [75-78]. Typically, ECT probes can be categorised as absolute, bridge, reflection, and differential probes [79], as illustrated in Figure 2.24. For an absolute probe, it performs both functions of excitation and detection. A balance coil placed within the ECT instrument is used to balance the bridge output. This type of probe requires that both test coil and reference coil have a very close value to reach the balance before carrying out tests. Otherwise, it may exhibit poor performance and even malfunction due to signal saturation. For a bridge probe [80], it is similar to the absolute, but the test coil and the reference coil are placed together so that they have an equal opportunity to experience the change in external environments. The advantage of this type of probe is it is insensitive to lift-off changes. A refection probe consists of a driver coil and a pick-up coil [81]. In this configuration, the driver coil generates eddy currents, and the pick-up coil detects eddy current signals. They do not

share one same excitation source. Therefore, the pick-up coil is not affected by the temperature variation due to long-time operation and heat accumulation in the excitation coil. There are two ways of placement for a reflection probe. One is both excitation and pick-up coils are coaxial [82], and another is they are placed side by side [83] . Regarding a differential probe [84], here, it is composed of a driver coil, and a differential pick-up coil, which offers the advantage of being insensitive to lift-off and noise, and sensitive to surface defects. Absolute and differential probes present different impedance trajectories with absolute display showing a lift-off change first and then a movement caused by a defect or a change in material's properties, and differential display showing an 8-shape trajectory around a convergence point because of the symmetry of differential probes.

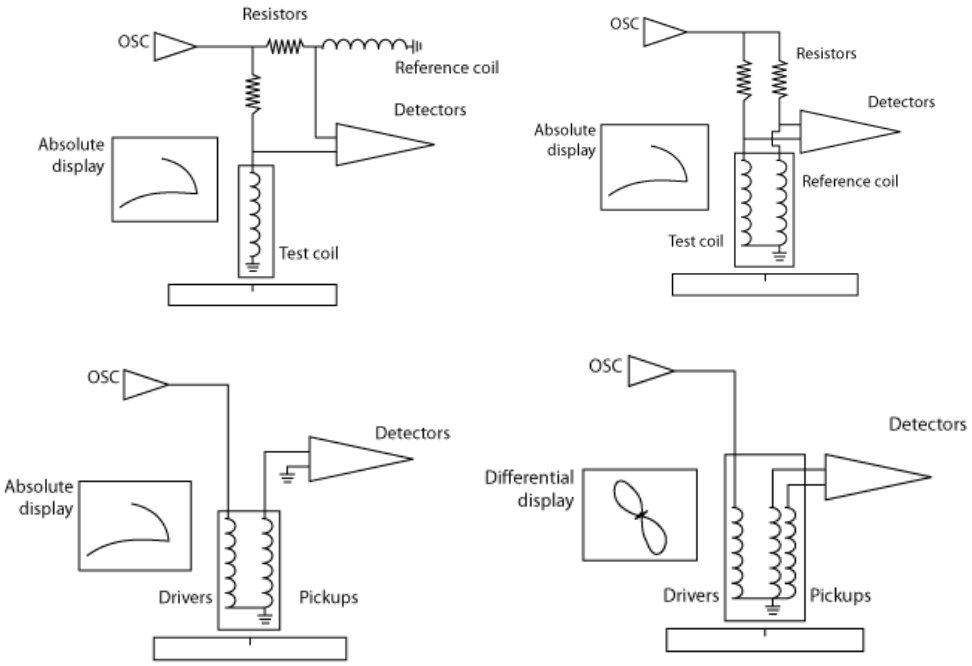

Figure 2.24 Absolute (top left), bridge (top right), reflection (bottom left), and differential types of probes (bottom right) [85]

ECT structures can be varied to improve performance in sensitivity, suppression of lift-off influences and noise, defect detections, which produce special structures such as planar double D-shape coils for surface crack detection (Figure 2.25 left) [84], differential coupling double-layer PCB coil for inspecting surface defects at high lift-offs (Figure 2.25 right) [70], and multi-layer magnetic shielding for deep defects inspection [86]. Two coils with an orthogonal placement and the same current excitation but a 90º phase shift form a new type of structure which can generate rotating eddy currents and be sensitive to arbitrarily oriented defects [87-89]. Figure 2.26 (left) shows one type of orthogonal probe structures. Trung *et al.* proposed an ECT convergence probe with hollows and a copper plate under the excitation coil, and a

unidirectional EC convergence probe with a pair of D-shape cooper cores, as shown in Figure. 2.26 (right), offering self-nulling and self-differential characteristics and enhance signal-to-noise ratio [90]. Ma *et al.* proposed a common-differential ECT probe structure in which two hollow rectangular excitation coils were located on the first and third layer of the PCB board, and a pair of rectangular detection coils were located on the second and third layer of the board, also in the middle area if the hollow excitation coils; the output from the bridge circuit of two excitation coils served as lift-off estimation, and the detection coils served as the defect detection [91]. Xiao *et al.* designed an external pulsed remote field eddy current (RFEC) probe for detecting inner and outer defects along a pipe; the probe consisted of a bobbin receiving coil, and two rectangular excitation coils with shielding cages which realized double through-wall Poynting vector transmission phenomenon [92].

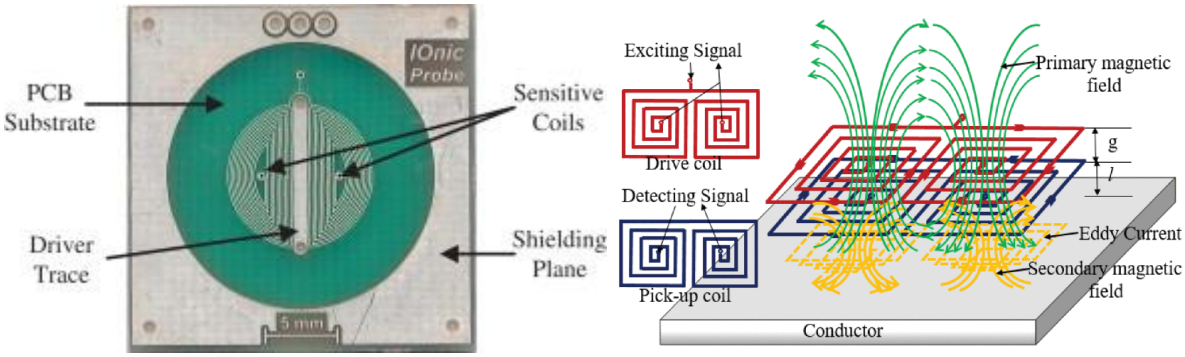

Figure 2.25 Planar double D-shape coils (left) [84], and differential coupling double-layer PCB coil (right) [70]

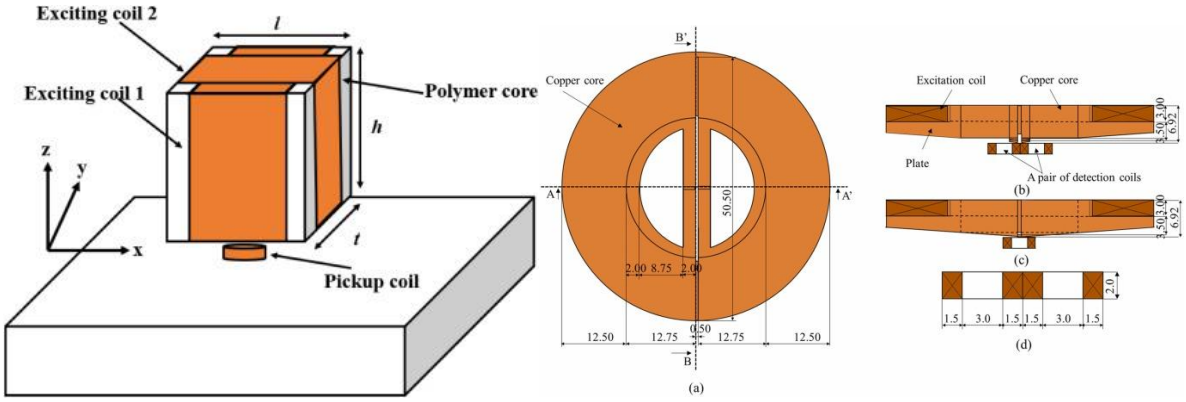

Figure 2.26 Rotating ECT probe with orthogonal coils (left) [93], and structures of ECT convergence probe with hollows and a copper plate under the excitation coil (right) [90]

Most of ECT probes take a single frequency excitation with a frequency ranging from a few hundred Hz up to a few MHz, which limits the inspection information since penetration depth is fixed [94]. There is only a magnitude and phase in frequency domain for a single frequency probe. Also, constant operations of a probe with single frequency excitation cause an increase in temperature and energy loss [95]. In order to obtain more information about targeting

materials, multi-frequency excitation with either simultaneous or sequential operation is investigated [94, 96, 97], providing abundant impedance information regarding lift-off, depth, spectrum components, and resolution. Pulsed eddy current testing (PECT) is an emerging excitation method which applies a pulse or rectangular signal to drive the probe, and another detection coil or magnetic sensor is harnessed to receive the PECT signal [94, 98]. Due to the jump of an excitation pulse at rising and falling edges, transient eddy currents are induced. Compared with traditional ECT methods, PECT owns much richer frequency contents, which means more specimen information such as defect size, depth, and location can be detected. In addition to richer frequency components, the pulse excitation reduces energy loss in excitation coils due to the fast switch between high and low voltage levels. PECT has been employed into metal thickness measurement under insulation and coating at a very high lift-off, and subsurface defect detection [99, 100]. The pick-up signal is a transient signal, so features including time to peak, zero-crossing time, peak points, arrival time of descending point are extracted to characterize defects [100]. A principal component analysis (PCA) was first explored to reduce the number of the PEC data dimensions and extract features that contained most relevant information, which allowed effective classification of defects [101]. Except for single frequency, multifrequency, and pulse excitation, some authors have conducted research on excitation with chirp frequency, sinusoidal modulation, and pulse modulation (shown in Figure 2.27) for improvement in signal-to-noise ratio, resolution, and defect imaging [102, 103].

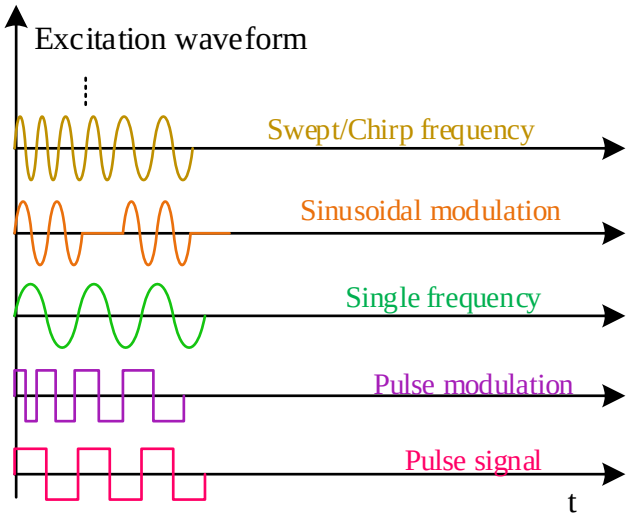

Figure 2.27 ECT Excitation signals

ECT have also been used for evaluation of material properties (conductivity, and permeability) and stress measurement [75, 104-107]. Wang *et al.* proposed a non-contact measurement of electrical conductivity using ECT; the logarithm of phase change was found linear to the electrical conductivity [108]. Ma *et al.* investigated a conductivity measurement method based

on the peak-frequency feature of imaginary components in inductance change via a sweep-frequency ECT sensor, which provided an analytical analysis to avoid lift-off effects by the spatial-frequency calibrations with a known conductivity [75]. Yin *et al.* found a permeability invariance phenomenon with a controlled lift-off, which was employed for reducing impact of permeability in electrical conductivity measurement of ferromagnetic materials [109]. Later, a similar invariance phenomenon was found in conductivity at a certain lift-off and it was applied for permeability measurement for ferrite metallic plates [110]. Adewale *et al.* investigated the decoupling of permeability and conductivity in PECT using normalisation in order to reduce inhomogeneity of material testing, which also revealed that conductivity effects are prominent in the rising edge of the transient response that corresponds to high-frequency components while permeability effects are dominant in the stable phase that corresponds to low-frequency components [111]. It has been proven that stress can be effectively evaluated through ECT [112, 113]. The stress on the specimen causes changes in electromagnetic properties such as electrical conductivity and permeability due to piezo-resistivity and inverse magneto-strictive effect, and results in changes to the ECT signals [114, 115]. Bai *et al.* applied pulsed eddy current thermography to improve the sensitivity and spatial resolution for the evaluation of the anisotropic dependency of electrical conductivity of steel subjected to tensile stress, but the cost of the infrared camera is prohibitive, and the experimental set-up is complex [115]. Morozov *et al.* [113] studied the relationship between the elastic-plastic state of aluminium alloys and their eddy current response. The real component of the response was found to be sensitive to elastic stress while the imaginary component was sensitive to plastic stress. Li *et al.* evaluated the stress distribution along a ferromagnetic specimen under tension based on ECT and a backpropagation (BP) neural network within the elastic range [116]. Ricken *et al.* designed a U-shaped NiZn-ferrite yoke with two coils placed on the poles in series connection for stress measurement in steel strand wires; the serial circuit of six ECT sensors were placed onto the steel wire with a solid system housing to maintain a constant air gap between ferrite surface and steel wires; their research disclosed the dependency of ECT inductance variations under applied stress and material dependent magnetostriction coefficients, and the remanence after a few definite load curves was set to a stable point in which reproducibility error of ECT inductance deviation tended to be zero [106]. Schoenekess *et al.* used two annular magnets to stabilise the operation point of magnetisation state to dimmish the measurement error on dynamic stress measurement of steel strand wires [117]. Liu *et al.* improved sensor sensitivity and linearity of ECT sensors for force and stress measurement by miniaturing the U-core and E-core sensor structures, which also reduced hysteresis during loading and unloading [118]. Zhou *et al.* proposed a U-shaped pulsed electromagnetic sensor for tensile stress assessment in the

ferromagnetic materials in which the peak values was extracted from differential signal to represent the tensile stress [119]. Bassam *et al.* developed frequency-dependent apparent eddy current conductivity (AECC) technique based on piezoresistivity effects for residual stress profiling in surface-treated engine alloys [120]. Ji *et al.* designed a real-time strain monitoring system for steel structures based on eddy current effects where the eddy current sensor was integrated with an excitation, detection, and wireless transmission module; the strain data were transmitted to the cloud platform using MQTT protocol [121].

2.3.4 LC Resonance Sensing

ECT technology has been extensively exploited in material's characterization and evaluation, offering advantages of no contact, low cost, and fast measurement. However, it is restricted by lift-off, sensitivity, and power consumption. The impedance curve of an ECT coil shows a phenomenon that impedance increases with frequency and reaches the maximum at its resonant frequency and then decreases. The frequency-dependent impedance characteristics demonstrate that the transition of an ECT coil from inductive to capacitive reactance due to the existence of parasitic capacitance led by winding of the wire, the space between turns, coaxial cable [122]. In this case, an ECT coil can be modelled as a parallel connection between a capacitor and an inductor. As the frequency rises and reaches the resonant frequency, the inductive reactance and capacitive reactance cancel each other out, causing the ECT coil to resonate and the impedance reaches the maximum. Research has shown that an ECT coil working near electrical resonance (NER) can significantly enhance signal-to-noise ratio (SNR) for sub-millimetre defect detection due to the fact that impedance varies sharply close the resonant frequency [123, 124]. Figure 2.28 presents near electrical resonance SNR plot of signal magnitude (left-axis) for three discontinuities of varying depth in relation to electrical resonance on Ti6-4 (right-axis), highlighting the enhancement in SNR of operation close electrical resonance [124]. Xiu *et al.* proposed a single-coil structure based on electrical resonance to improve sensor sensitivity for tension measurement of the ferromagnetic material; both the impedance magnitude peak and phase at the self-resonant frequency of the coil were observed to have a linear relationship with the external tension [125].

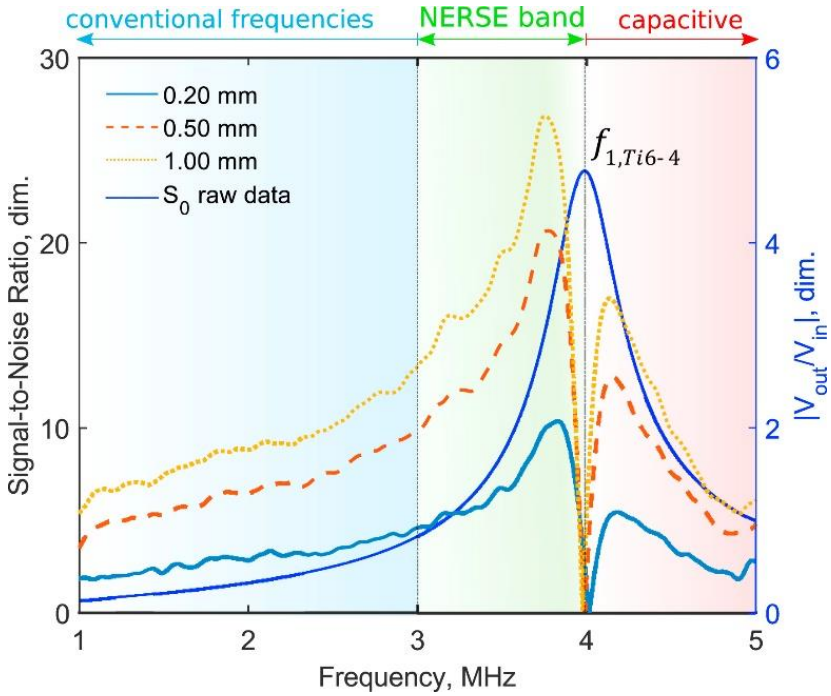

Figure 2.28 Near Electrical Resonance Signal Enhancement (NERSE) signal-to-noise ratio (SNR) plot of signal magnitude (left-axis) for three discontinuities of varying depth in relation to electrical resonance on Ti6-4 (right-axis) [124]

In addition to operating an ECT coil near electrical resonance frequency for detect inspection, a capacitor can be added into an inductor coil to form an inductor-capacitor (LC) resonator, acting either as an inductive or capacitive sensing, depending on the sensing unit. LC sensors have been widely investigated in wireless measurement, such as temperature, humidity, pressure, strain, gas, biomedical parameters, and speed due to the advantages of passive operation with no requirement of batteries, remote readout capability, long-term stability, low cost, easy design of sensing structures with minimal components and small size, flexible fabrication, and customizable resonance, high sensitivity to target parameters [126-129]. Most of research have been concentrated on using the capacitor as the sensing unit, and the inductor as the communication unit. As shown in Figure 2.29 (a), an LC sensor system consists of a readout coil and an LC sensor, where changes of capacitance in response of parameters of interest result in shifts its resonant frequency through monitoring the impedance magnitude and phase spectrum of the readout coil. The interaction between the readout coil and the LC sensor is finished by near-field magnetic coupling. The equivalent circuit of the sensor system is very similar to an ECT equivalent circuit, consisting of an inductor coil L_0 in the readout coil side, and a series connection of an inductor coil L_s, a sensing capacitor C_s, and a resistor R_s.

The equivalent input impedance at the terminal side of the readout coil is expressed in [126]:

$$Z_{in} = \frac{U_0}{i_0} = j\omega L_0 + Z_R = j\omega L_0 + \frac{\omega^2 M^2}{R_s + j\omega L_s + 1/j\omega C_s} \tag{2.11}$$

Where Z_R is the reflected impedance, and M is the mutual inductance.

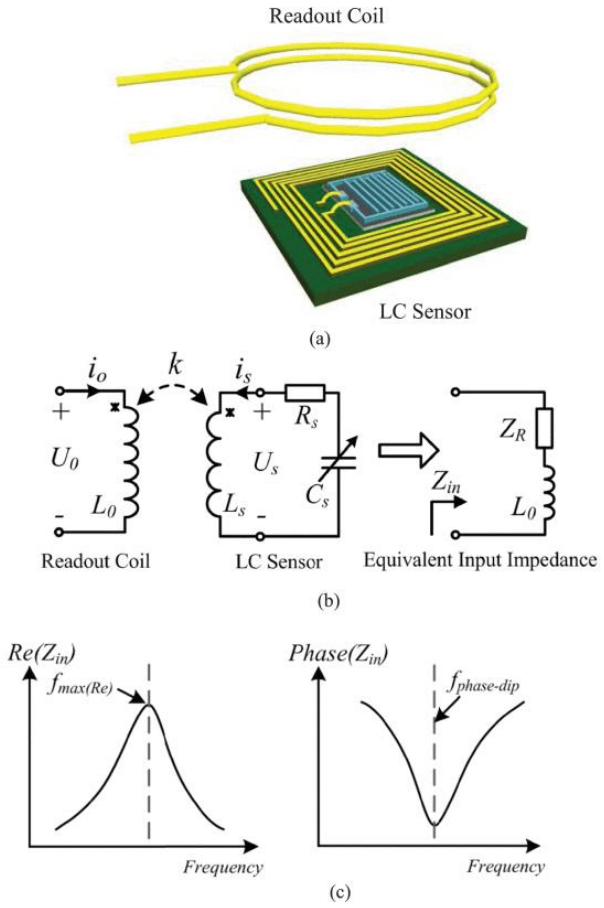

Figure 2.29 (a) Schematic representation of an LC sensor system. (b) Equivalent circuit of an LC sensor system. (c) Characteristic curve of Re (Zin) and Phase (Zin) [126]

The resonant frequency f_s and quality factor Q of the LC sensor are written as:

$$f_s = \frac{1}{2\pi\sqrt{L_s C_s}} \tag{2.12}$$

$$Q = \frac{1}{R_s}\sqrt{\frac{L_s}{C_s}} \tag{2.13}$$

The real and imaginary parts of the equivalent input impedance Z_{in} after combining equation (2.12) and (2.13) are derived as [126]:

$$Re(Z_{in}) = 2\pi f L_0 k^2 Q \frac{\frac{f}{f_s}}{1+Q^2\left(\frac{f}{f_s}-\frac{f_s}{f}\right)^2} \tag{2.14}$$

$$Im(Z_{in}) = 2\pi f L_0 [1 + k^2 Q^2 \frac{1-\left(\frac{f}{f_s}\right)^2}{1+Q^2\left(\frac{f}{f_s}-\frac{f_s}{f}\right)^2}] \tag{2.15}$$

Where k is the coupling coefficient between the readout coil and the LC sensor. By solving the derivative of equation (2.14) and making it equal to zero, the resonant frequency corresponding to maximum of $Re(Z_{in})$ is obtained as:

$$f_{max(Re)} = \sqrt{\frac{2Q^2}{2Q^2-1}} \times f_s \approx (1 + \frac{1}{4Q^2}) f_s \tag{2.16}$$

Equation (2.16) demonstrates that $f_{max(Re)}$ is only relevant to Q and f_s, and independent of k. Measuring the frequency for maximum real part of $Re(Z_{in})$ is only related to the LC sensor, which reduces the influence of the distance between the readout coil and the sensor. Figure 2.29 shows the maximum of $Re(Z_{in})$ at the resonant frequency f_s.

The phase of the input impedance is expressed as:

$$phase(Z_{in}) = arctan \frac{Im(Z_{in})}{Re(Z_{in})} \tag{2.17}$$

Similarly, by making the derivate of *phase(Zin)* equal to zero, the frequency respective to the minimum of the phase is obtained as:

$$f_{phase-min} \approx (1 + \frac{1}{4}k^2 + \frac{1}{8Q^2}) f_s \tag{2.18}$$

Obviously, this frequency is not only related to f_s and Q, but also related to k. In order to obtain information only related to the LC sensor, the measurement strategy should be taken such as fixing the distance between the readout coil and the sensor or setting a minimum coupling so that the influence of k can be ignored.

A vector network analyser (VNA) or impedance analyser is normally used for measurement of these parameters via sweeping the frequency through the readout coil while monitoring the maximum of real (Z_{in}) and minimum of the phase [130-133]. Advances in micromechanical systems (MEMS) and novel materials have enabled wireless LC sensors to achieve smaller footprints, higher sensitivity, and longer transmission distances[134-136]. Harpster *et al.* designed a single-chip integrated humidity sensor which was able to operate wirelessly through inductive coupling with a remote antenna; the sensor performance parameters including resolution, sensitivity, detection range, hysteresis, and drift were investigated [130]. Lv *et al.* demonstrated an LC wireless passive humidity sensor based on MWCNTs (multiwalled carbon nanotubes) and WS_2 nanocomposites [133]. Xu *et al.* applied MWCNT and polydimethylsiloxane (PDME) to develop a radio frequency resonator-based flexible wireless pressure sensor with a bilayer pyramid dielectric structure [137]. Rodriguez *et al.* presented a wireless resonant LC temperature sensor with the capacitive sensing element which was made by Lead-Lanthanum-Zironate-Titanate ceramic, operating at a rotating component and a harsh environment where temperature was over 200 °C [128]. Tan *et al.* applied screen-printing technique, low-temperature co-fired ceramic (LTCC), and imidization process to design an LC wireless passive temperature-pressure-humidity (TPH) sensor in harsh environments, with ranges of 25-200 °C, 70-220 kPa, and 24-90% RH; Figure 2.30 (a) presents the structure of the

designed TPH sensor in which a readout antenna was utilised to interrogate the TPH sensor, and the interrogation signal S11 in Figure 2.30 (b) shows three different resonance frequencies; The frequency difference between each sensor's response was large enough to reduce mutual coupling; Figure 2.30 (c) and (d) illustrate the spatial configurations of layers [138]. Later, they applied high-temperature co-fired ceramic to develop an LC temperature-pressure sensor operating at an extreme 1100 °C environment with a sensitivity of 92.98 kHz/kPa in a range of 70-120 kPa [139]. Wang *et al.* designed a dual-parameter sensor with a strain-sensitive interdigital capacitor, and a temperature-sensitive plate capacitor; the temperature sensor was connected to the inner part of the inductor coil while the other was connected to the outer part of the coil, forming two LC loops using a single inductor coil; the sensors were analysed by HFSS and fabricated on a polyimide film using electroplating technology [132]. Deng *et al.* presented a symmetric LC topological circuit configuration for both pressure and humidity measurement, in which the symmetric structure separated the resonant frequencies of two LC resonators; the change in the sensing capacitor of one LC resonator only affected its own resonant frequency while remaining independent of the other resonant frequency, and vice versa; this new configuration provided multiple-parameter monitoring simultaneously [131]. Dong *et al.* utilised a relay switch to actuate on and off states of the connection in a multifunctional LC sensor system [140]. Li *et al.* proposed a wireless passive flexible strain sensor based on aluminium nitride (AIN) film where the AIN film was deposited in an interdigital capacitor to enhance the sensing capability; the sensor could measure a strain in the range of 0-3000 με with a resolution of 20 με [127]. Chen *et al.* proposed an implant-based wireless microsensor for continuous intraocular pressure monitoring where the sensor consisted of a pressure-sensitive parallel-plate variable capacitor embedded in a deformable diaphragm chamber, and a spiral coil on a flexible and foldable substrate [136].

In addition to using new materials to the design and fabrication of LC sensors, there are many researchers focusing on readout distance enhancement and portable telemetry systems. Tan *et al.* proposed a dual-inductor resonator (DIR)-based signal readout for LC pressure sensors in rotating environment; the LC pressure sensor was installed on an electric fan and one inductor was interrogated with it; this inductor was connected to another inductor to constitute a dual inductor, and then interacted with the readout antenna to transmit the signal from the sensor, as show in Figure 2.31 [141]. Dong *et al.* applied a cyclic scanning repeater to enhance the readout distance of LC sensors; the repeater was composed of an LC resonator and a varactor which changed its capacitance based on a periodic voltage signal; when the scanning frequency of the repeater matched the resonant frequency of the LC sensor, the strongly magnetic resonance

coupling happened, greatly extending the readout distance by 3 times [134]. Zhang *et al.* developed a portable telemetry unit for measuring the resonant frequency of LC sensors, which was based on a standing wave ratio (SWR) bridge [135].

However, When LC resonance sensors are placed near metallic objects, eddy currents are induced. These currents negatively impact sensing performance by altering the sensing distance, quality factor, resonant frequency, and equivalent parallel resistance.

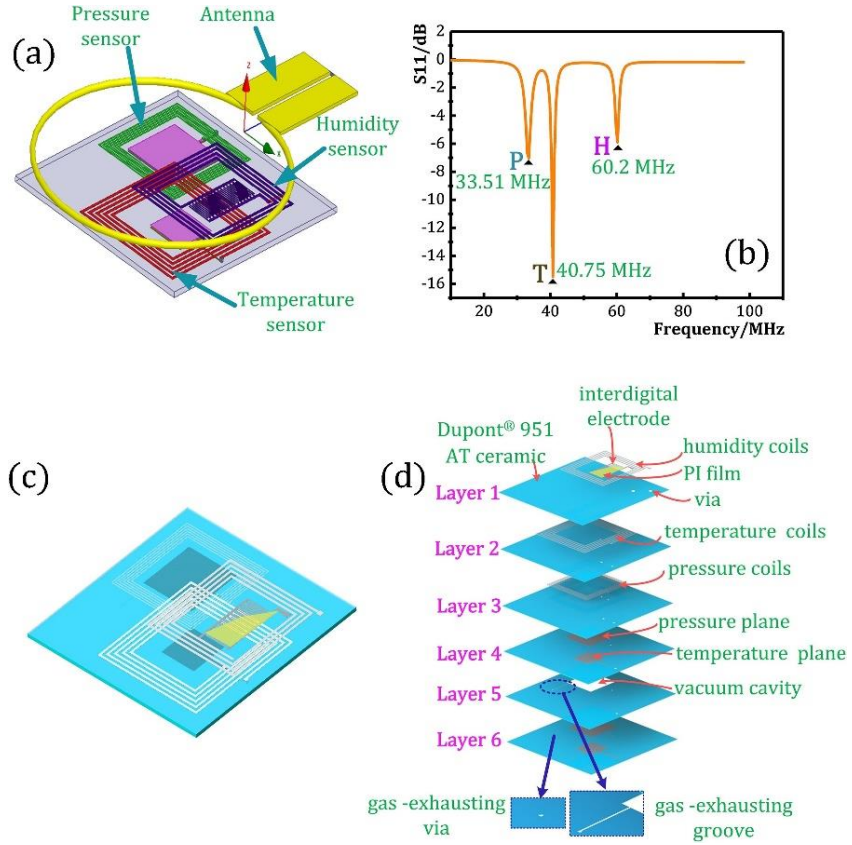

Figure 2.30 (a) The model of the designed temperature-pressure-humidity (TPH) sensor (b) S11 versus frequency against three resonant frequencies for TPH (c) Ichnographical configuration (d) Layer configuration of the TPH sensor [138]

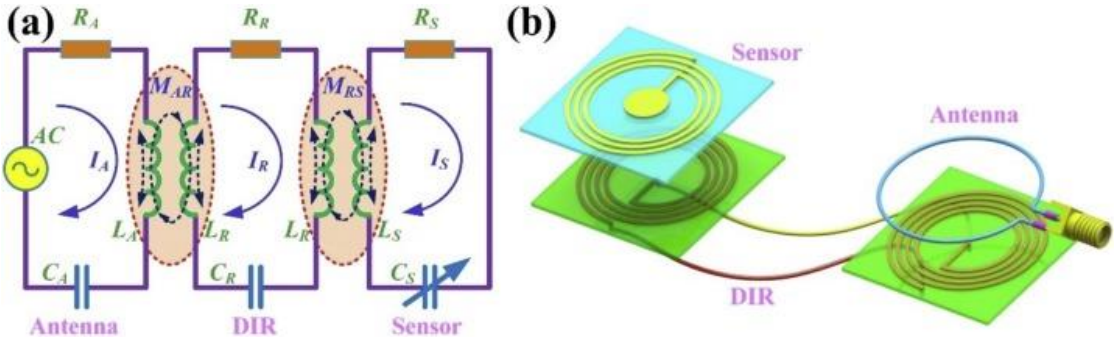

Figure 2.31 (a) Equivalent circuit of a sensor, dual-inductor resonator, and antenna (b) Transmission model of the dual-inductor resonator-based readout system [141]

2.3.5 Wireless Power Transfer-based Sensing

The concept of wireless power transfer (WPT) was firstly proposed by Nicole Tesla, later, who verified this concept through powering a small lamp by current induced in a three-wound coil [142]. WPT has gained widespread attention in energy acquisition, offering cordless connection between the sources and devices, and reducing the need that relies on battery; it has been applied in portable electronic devices, such as mobile phone, laptop, earphone, and implantable medical devices, electric vehicles, and mobile robots [143]. WPT is divided into two categories, far-field and near field. Far field WPT includes laser power transfer, microwave power transfer, and solar power satellite [144]. Although far-field WPT can realize a long-distance transmission, it has the issue of energy loss. Near-field WPT contains capacitive power transfer, inductive power transfer and magnetic resonant coupling (MRC) [145]. MRC-WPT has been paid much attention since a researcher MIT proved that WPT via strongly coupled magnetic resonance is able to realize power transfer over distances up to 8 times the radius of the coils and higher power efficiency transfer [142, 146]. An MRC-WPT system is typically composed of two resonant coils, named Rx and Tx, where each resonator includes a coil and a capacitor. The magnetic coupling reaches the maximum when the two resonators are tuned to the same resonant frequency. There are four types of MRC-WPT structures according to the connection approach of a coil and a capacitor, denoting serial-serial (SS), serial-parallel (SP), parallel-serial (PS), parallel-parallel (PP) [147], as shown in Figure 2.32.

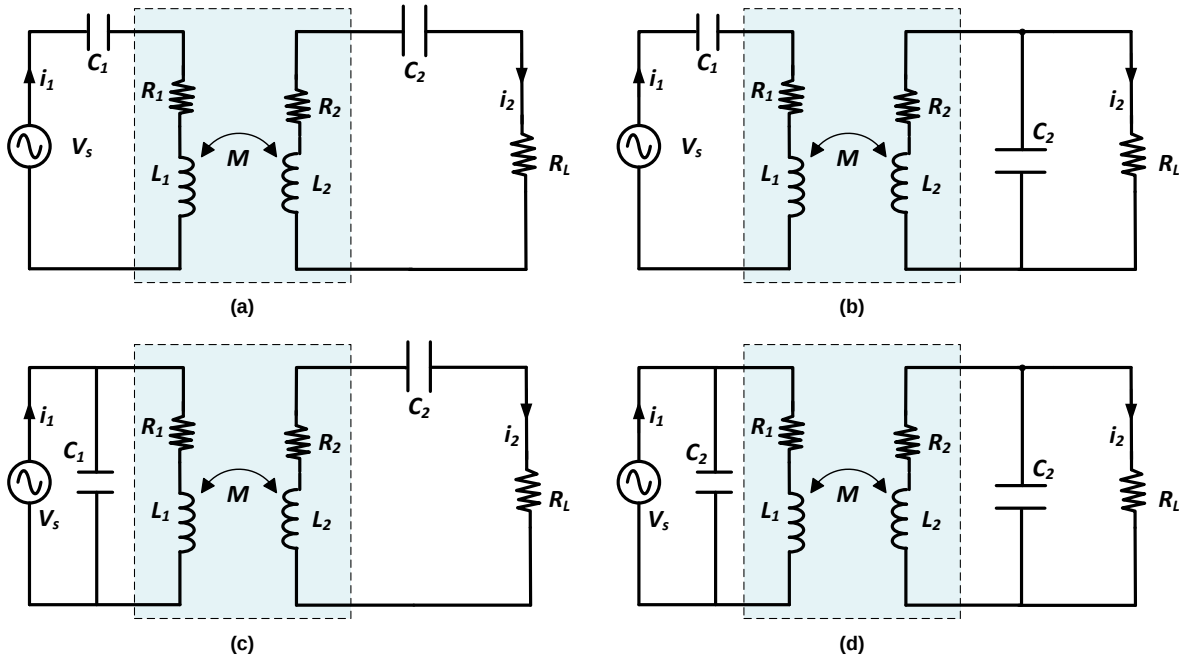

Figure 2.32 Four topologies of MRC-WPT: (a) SS topology (b) SP (c) PS (d) PP

Each of them provides unique benefits. SS provides load-independent constant current which is ideal for EV charging. SP delivers stable voltage which is suitable for medical devices. PP is

excellent in high-power applications with soft switching. PS is well adaptable to dynamic loads such as loads. However, the selection of them depends on whether the priority is current/voltage regulation, power transfer efficiency, or load flexibility [148]. Research in WPT has mainly concentrated on enhancement of transmission efficiency, WPT to multiple receivers, energy maximization during coil misalignment, transmission distance, impedance matching, metamaterial-based power transfer efficiency, omnidirectional charging [145, 149, 150]. Both coupled-mode theory (CMT) and reflected load theory (RLT) are used to theoretically analyse power transmission model of WPT [145].

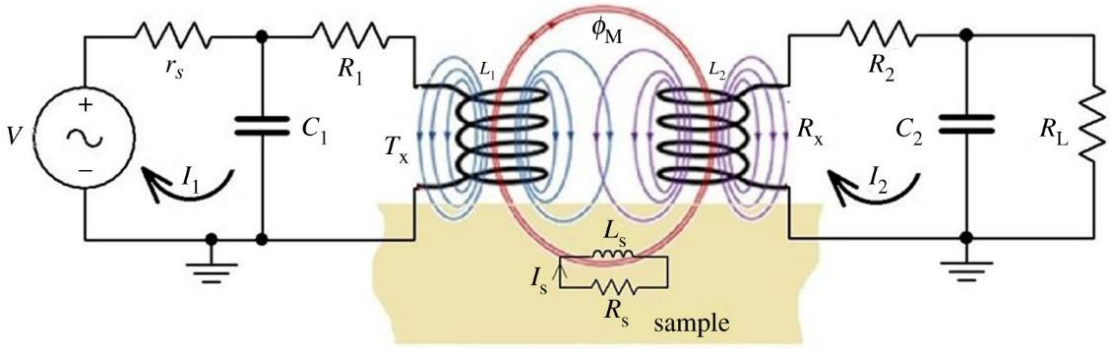

Figure 2.33 Equivalent circuit of WPT-based ECT for defect detection [151]

The previous description of WPT is primarily stressed on energy transfer as this is the origin of WPT. In addition to applying WPT-related structures on energy collection and power transfer, they can also be utilized for sensing information, such as structural health monitoring in pipelines, bridges, railway rails, buildings, aircrafts to monitor crack, defect, strain, and stress. [151-153]. Daura *et al.* utilised the splitting frequency phenomenon of WPT where it produces two resonant frequencies and magnitudes for crack detection and characterization in Aluminium material; principal component analysis (PCA) was adopted to investigate the relationship between crack size and feature information [154]. Afterward, the author performed WPT-based ECT test via flexible printed coil array on a curved pipeline; Figure 2.33 presents the equivalent circuit model of WPT-based ECT, which employs the interaction between Tx (parallel), Rx (parallel), and the sample [151]. A modified parallel/series-parallel/series (PS-PS) WPT-based ECT topology was designed for investigation of multiple features on inclined angular rolling contact fatigue (RCF) cracks [155]. Zhang *et al.* investigated the magnetic resonance coupling based wireless triboelectric nanogenerator (MRC-TENG) and self-powered wireless sensors; in Figure 2.34, the Polyvinylidene fluoride (PVDF)-based capacitive pressure sensor was integrated in the resonant circuit of TENG, varying its capacitance value with applied pressure and in turn shifting the resonant frequency; the TENG provided energy to produce the resonant signal containing the sensing information and transmitted it to the receiver wirelessly [156].

Yang *et al.* developed an integrated wireless theranostic contact lens based on capacitive sensing and WPT for in-situ intraocular pressure monitoring and on-demand drug delivery [157]. Lin *et al.* demonstrated a battery-free body sensor network using near-field-enabled clothing to establish wireless power and data transmission for continuous strain and temperature monitoring; the clothing comprised of a network with a single hub and multiple terminals in which the hub coil collected energy from the reader and then provided it to the terminals [158]. Ertsgaard *et al.* proposed a method capable of realizing wireless dielectrophoretic trapping and remote impedance sensing through resonant WPT where the change in load impedance varied the reflected impedance in the primary coil; a critical coupling was found that power transfer efficiency reached the maximum, as shown in Figure 2.35 and 2.36 [152].

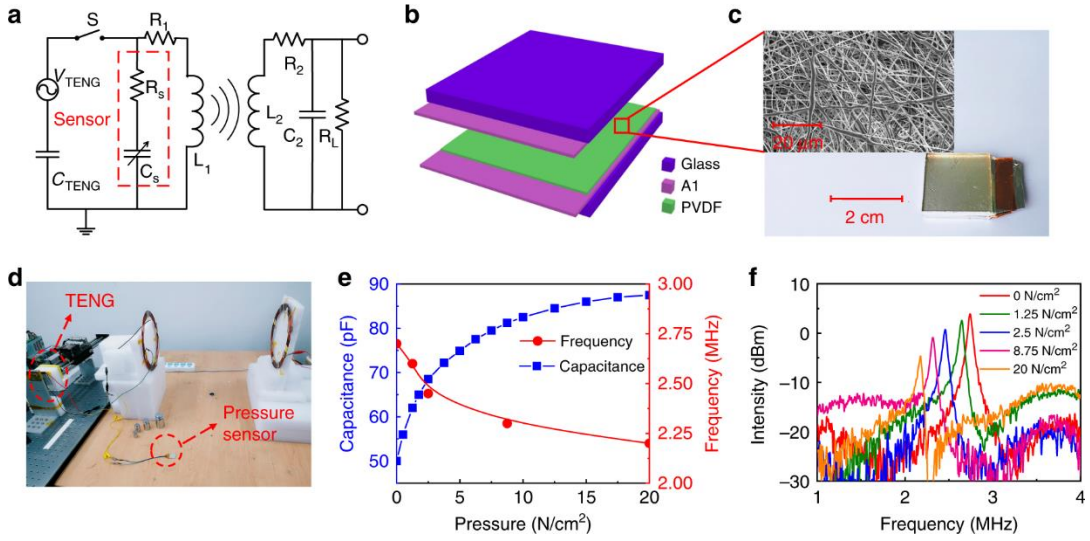

Figure 2.34 MR-TENG-based wireless chipless sensors. (a) The configuration of a capacitive pressure sensor integrated in the TENG resonant circuit; (b) and (c) the structure and photo of PVDF nanofiber membrane-based capacitive pressure sensor; (d) the photo of the wireless sensing system; (e) the capacitance variation with different pressures applied to the sensor (f) Spectrum of received signal from the sensor as a function of applied pressure [156]

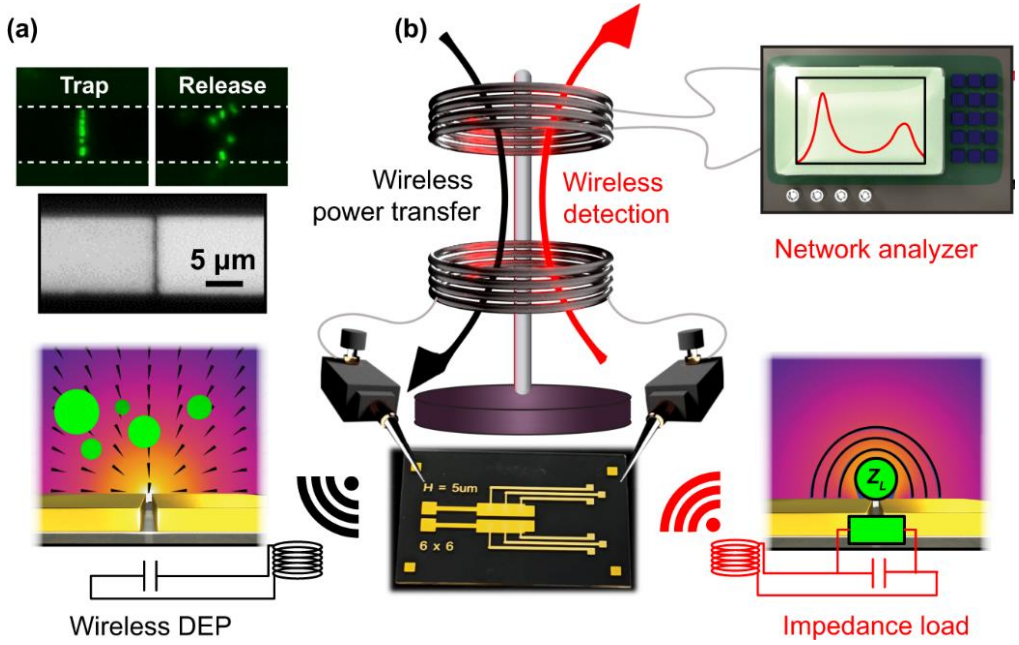

Figure 2.35 Experiment concept: dielectrophoretic trapping and remote impedance sensing via resonant wireless power transfer (a) A microscope image of a single coplanar nanogap used for trap and release experiments; (b) A concept diagram of the experimental setup w with a primary and secondary coil inductively coupling RF power to a nanogap capacitor [152]

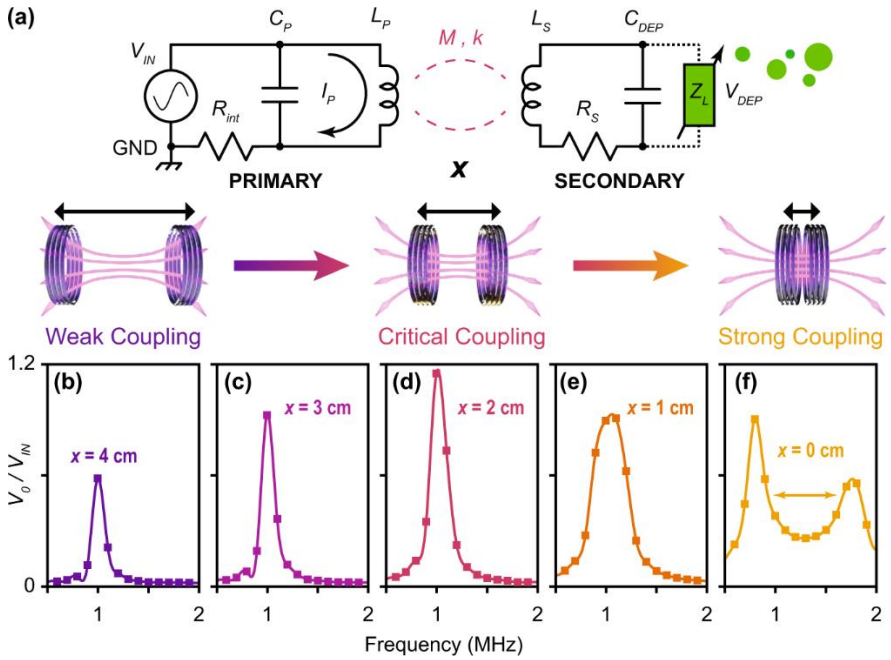

Figure 2.36 Circuit architecture and optimal coupling regime for impedance sensing [152]

2.3.6 Digitalisation and Miniaturization of Measurement Systems

The conventional measurement systems involve lots of discrete components, such as signal generator, power amplifier, signal conditioning circuits, and data acquisition systems for MBN and ECT system, VNA or impedance analyser for LC sensors. Their combinations lead to a large dimension, heavy weight, high power consumption, and expensive cost. Nowadays, the

development of measurement systems has been moving toward the direction of miniaturisation, portability, low consumption, digitalisation, and low cost [159-164]. Highly integrated impedance measurement converters are beneficial to reduce the size and cost of the system, minimize the noise interference, lower the power consumption, and improve the measurement precision and repeatability. AD5933 is a high-precision impedance measurement converter which combines an on-board frequency generator, with a 12 bit, 1MSPS analog-to-digital converter (ADC) [159]. As Figure 2.37 displays, the oscillator generates signal to drive the external complex impedance, and the response signal is sampled to the on-board ADC and a discrete Fourier transform, returning a real part and imaginary part of the measured complex impedance. It means that the complicated impedance measurement is realized by this highly integrated AD5933, which is easy to be read by only a microcontroller with I^2C interface, making it applicable to portable, low-cost measurement, such as non-destructive testing, structural health monitoring, and material property analysis [160, 165]. An ECT measurement system based on AD5933 was proposed in [160], where the impedance of a coil was captured to detect the defect around the weld area. Koerner *et al.* demonstrated a miniaturised and embedded electrical impedance analyser using AD5933 for identifying mechanical parameters of mass, spring constant, and damping coefficient from the impedance of a voice coil motor [166]. Another application is that AD5933 was used for electrical impedance tomography for bioimpedance measurement [167]. Li *et al.* combined AD5933 and piezoelectric transducers with a wireless communication system to propose a electrochemical impedance-based SHM method for aircraft wing health monitoring [168]. Liang *et al.* developed a wireless multichannel impedance system based on AD5933 which features wireless data transmission, multichannel acquisition, and remote data post-processing; the developed system was verified by a bolt loosening on the flange connection of a pipeline specimen for the damage localisation and severity quantification [169].

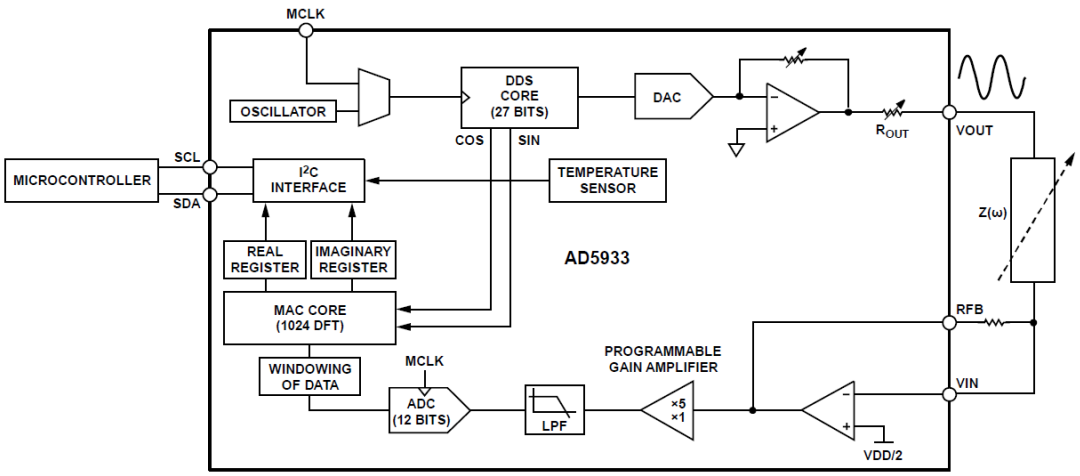

Figure 2.37 Block diagram of AD5933 for impedance measurement [159]

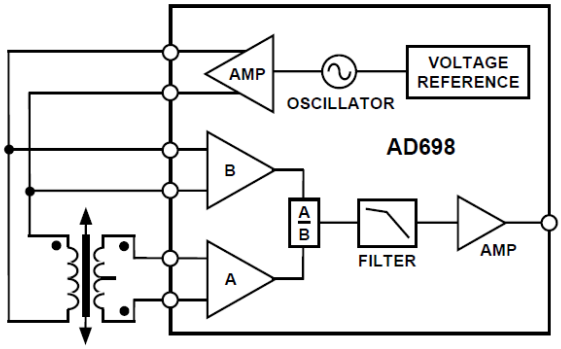

Figure 2.38 Block diagram of AD698 for LVDT signal conditioner [162]

AD698 is a linear variable differential transformer (LVDT) signal conditioning subsystem which integrates signal generator, power amplifier with signal demodulator, transforming the ratio of the input detection signal voltage to the drive voltage into an output voltage proportional to it [162]. This chip can be configured to work with a frequency range from 20 Hz to 20 kHz and amplitude from 2V and 24V rms by only changing the external capacitor, widely used for displacement sensing and ECT defect detection [170, 171]. Figure 2.38 presents a diagram of AD698 configured as a series-opposed connected LVDT transducer, where the primary winding is energized by the sine wave from the oscillator, and the two secondary windings are connected in the series opposed configuration, offering the differential output. Li *et al.* used AD698-based signal conditioning for radial and axial integrated inductive displacement sensor on magnetic bearing system [172]. Li *et al.* proposed a differential transformer ECT probe based on AD698 LVDT signal conditioning for rolling contact fatigue cracks with different orientations; the probe consisted of four-square excitation coils that generated unidirectional eddy currents, and two 8-shape detection coils capable of sensing cracks in different directions and being insensitive to the lift-off [171].

LDC1612/4 is a multi-channel 28-bit inductance to digital converter (LDC) that measures the inductance by measuring the resonant frequency (f_s) of an LC resonator with a known capacitance, providing high resolution, fast response, simplified circuit design, digital outputs and low power consumption [163]. Figure 2.39 is the diagram of LDC1614 which has 4 resonant circuit drivers, a measurement core, an I^2C interface, and an external 40 MHz oscillator. The chip integrates resonant circuit drivers with frequency meters in a small package WQFN-16 which supports a wide sensor frequency range of 1 kHz to 10 MHz, and an equivalent parallel resistance larger than 0.6 kΩ. LDC1612/4 outputs digital values proportional to the resonant frequency via I^2C interface, which can be simply programmed by a microcontroller with I^2C function. In addition, due to the fact that an LC resonator works at its resonant frequency, the equivalent parallel resistance (R_p) reaches the maximum. Thus, the power

required to resonate is minimum. LDC1612/4 has been broadly used in high-precision displacement sensors, buttons in home electronics, tactile sensors, and metal detection [173-176].

Since LDC1612/4 merely provides the function of frequency measurement, the measurement of the equivalent parallel resistance of an LC resonator is not supported, and the maximum sample rate is 4.08 kSPS due to I^2C interface, limiting its application fields. However, LDC1001 and LDC1101 make up this limitation, offering both measurement functions of f_s and R_p with a maximum sample rate of 180 kSPS through SPI interface [177, 178]. LDC1001 provides a 16-bit resolution for R_p and a 24-bit resolution for f_s, enabling an LC resonator to operate with an f_s range of 5 kHz to 5 MHZ, and an R_p range of 0.798 kΩ to 3.93 MΩ. The power supply for this chip contains anlog power supply with 4.75 V to 5.25 V, and digital power supply with 1.8 V to 5.25 V. LDC1101 has the similar parameters in the resolution but only one power supply with a range of 1.8 V to 3,3 V, smaller than that of LDC1001, as shown in Figure 2.40. It can drive an LC sensor with a f_s of 500 kHz to 10 MHz and a R_p of 1.25 kΩ to 90 kΩ. LDC1001 and LDC1101 have been used for defect detection and magnetic induction tomography due to its multiple parameters and digital outputs [179-181]. Tian *et al.* applied LDC-based multi-parameter ECT for crack characterization on aluminium and steel specimens; the f_s and R_p characteristic curves presented the influence of lift-off and crack size [179]. Liang *et al.* investigated the correlation between the crack width and the half-peak width using the LDC1101-based ECT system [180]. Feldkamp *et al.* demonstrated the application of LDC1101 to measuring coil loss in single-coil magnetic induction tomography [181].

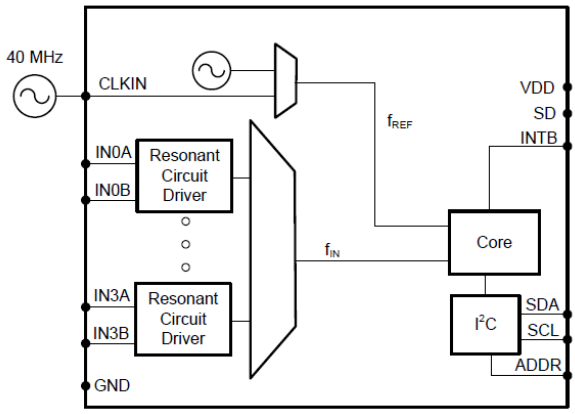

Figure 2.39 Block diagram of LDC1614 for inductive sensing [163]

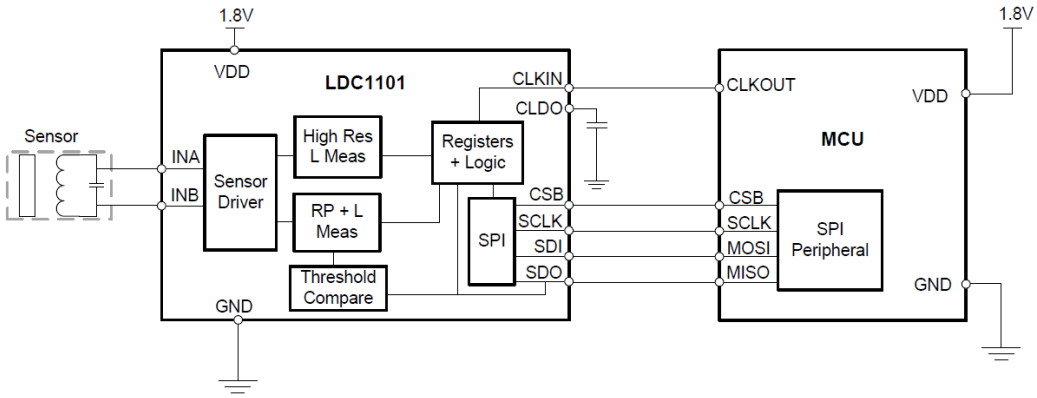

Figure 2.40 Block diagram of LDC1101 for inductive sensing [178]

2.4 Challenges and Problems

In the mentioned approaches for WRCFM, SGs have been attracted much attention and successfully applied on practical railway vehicles. However, there are several drawbacks for this method. Firstly, SGs are required wiring-connection, which can cause entanglement of lots of wires, leading to the difficulty of identifying the failed one to replace it. Secondly, the installation of SGs needs to drill holes on the web. Although this way measures the vertical force, to some extent it destroys the integrity of wheel structures. Thirdly, the tricky thing is to transmit strain signals from a rolling wheelset to a static bogie frame. This increases the complexity and cost of the system. DIC technique provides a new insight for WRCFM, but it requires complex image processing and signal acquisition systems. It is difficult to implement this method in practical wheels due to the extra surface preparation, lighting, and high-speed motion. While gaps sensors are feasible for measuring the lateral force by indirectly detecting the displacement or deformation caused by mechanical loading, they still face challenges in providing accurate and direct force measurements in wheel-rail systems.

The research progress using electromagnetic NDT techniques for WFM brings new insights into WRCFM. UHF RFID tag-based sensors are excellent in remote sensing. However, it requires a bulky reader which brings challenges in practical installation, environmental interferences, feature extraction of backscattering signal, and data sampling rate. MBN is capable of detecting microscopic structure of ferromagnetic materials and characterizing their residual stress, but this method requires the probe to maintain direct contact with the specimen that means a zero lift-off. Additionally, the MBN signal is a high-frequency, noise-like signal, making it challenging to extract its features and perform quantitative analysis. ECT is simple and fast testing method which demonstrates its effectiveness in stress measurement. However, it has limitations in sensitivity and lift-off, especially when detecting small changes in material's electromagnetic properties. Consequently, ECT for force measurement often requires a zero

lift-off to ensure accuracy. The occurrence of LC resonance sensing addresses the drawbacks of ECT by utilizing a sharp impedance change near the resonant frequency, which significantly enhances both sensitivity and lift-off. By means of MRC in WPT, lift-off can be extended due to the resonance between two LC resonators. However, most measurement systems reply on VNA or impedance analysers to implement the measurement of the resonant frequency and impedance amplitude through frequency sweeping, which significant slows down the data sampling rate, particularly in rotating platforms.

The combination of LC resonance sensing and LDC-based measurement systems effectively enhances sensitivity and operational lift-off while reducing system complexity. This is achieved by leveraging the resonance characteristics and LDC-based systems which enables fast and simplified measurements. There remain several potential challenges, including the design of LC resonance sensors, the development of LDC-based measurement systems, the separation of force at varying lift-offs, the enhancement of lift-off and sensitivity, and signal readout and feature analysis on a rotating testing platform.

2.5 Chapter Summary

This chapter covers a range of literature review, from the background of wheel-rail contact forces, common methods for WRCFM to electromagnetic NDT-based techniques for WFM. Wheel-rail contact forces are caused by the interaction between the wheel and the rail during the running operation, which decide the running safety stability of the railway system. Strain gauge-based WRCFM is the most common method due to its high-sensitivity, and low-cost, but it has a strict requirement for the installation, signal transmission and processing. Many researchers have been seeking for non-contact or wireless solution for WRCFM. Digital image correlation and gap sensors exhibit the efforts in this direction. However, considering the cost, feasibility, and system complexity, these methods are not good enough. Electromagnetic NDT-based techniques may provide new insights into WRCFM, especially for WFM. Therefore, the problems of WRCFM are transformed into WFM, which is the simplification of complex wheel-rail force mechanism, offering potential alternative solutions for the present techniques. RFID-based sensor for stress measurement, MBN, ECT, LC resonance sensing, WPT-based sensing are subsequently reviewed regarding the principle, system, and state-of-the art progress in WFM. In addition, the development of measurement systems is towards miniaturisation, integration, low cost, and portability, chip-based systems including impedance converter AD5933, linear variable differential transformer (LVDT) AD698, and inductance-to-digital converters LDC1614/LDC1101 are introduced. These chips do not need complicated external

components, and they can be easily integrated with a microcontroller to establish a complete and accurate measurement system.

LC resonance sensing is selected as the research topic for this thesis thanks to its advantages in wireless measurement, high sensitivity led by impedance characteristics at resonant frequency, and simple measurement system. LC resonance sensing can provide promising solutions for WFM and WRCFM. The work focus on the feasibility of applying LC resonance sensing for WFM by LDC-based measurement systems, separation of lift-off and force, and enhancement of sensitivity and lift-off through semiconductor strain gauge, magnetic resonance coupling, and LDC-based system. The next chapter will present the investigation of using LC resonance sensing for wireless force measurement.

Chapter 3. Investigation of Using LC Resonance Sensors for Wireless Force Measurement

This chapter conducts the investigation of applying LC resonant sensors for wireless force measurement (WFM). A brief introduction of the relevant research progress in WFM was described. The measurement principle of LC resonance sensing for WFM was presented. Afterwards, the LC resonance sensor and the LDC1614-based resonant frequency measurement system was designed and developed. Experimental study including repeatability tests, comparison of strain gauges and LC resonance sensor, lift-off influence, and aspect ratio of inductance coils were performed to verify the application of LC resonance sensors in WFM.

3.1 Introduction

Although the ECT-based methods can evaluate the stress, they used the discrete driver and detection modules and the sensitivity and signal noise to ratio (SNR) is low. Operating the ECT probe at frequencies close to its electrical resonance can enhance the sensitivity and SNR through measuring the shifting of electrical resonant frequency as the impedance at this frequency can reach the maximum [182]. However, the resonance frequency is dependent on the capacitance of the coaxial cable and adjacent coil turns, especially at high frequencies. It is susceptible to external factors such as the distortion of cables and parasitic capacitance due to temperature change. The tune of resonant frequency is tough as the cable length is fixed. Like ECT performing at the electrical resonance, inductor-capacitor (LC) wireless passive sensors are also based on the measurement in the shift of the resonant frequency. They have been successfully utilized on strain measurement [126, 183]. An LC sensor consists of an inductor coil and a sensing capacitance where the capacitance changes in response to parameters of interest, with a shift in its resonant frequency [126]. An additional readout coil connected to a vector network analyser (VNA) can be used to interrogate LC sensors and detect the frequency shift by monitoring the impedance change and return loss of the readout coil. Most research on LC sensors concentrates on the design of sensing capacitors using advanced materials such as polymer, graphene, multiwalled carbon nanotubes (MWCNs), nanocomposite, and polydimethylsiloxane (PDMS) [127, 132, 133, 184]. The induction coil in those studies only plays a role of signal transmission rather than sensing. The presence of metals has a significant influence on the performance of LC sensors as they can shield electromagnetic waves and affect the signal readout [185]. During wireless interrogation via a readout coil using an impedance analyser or VNA, nearby metals induce eddy currents. These currents generate opposing magnetic fields that counteract the magnetic fields in LC sensors, resulting in detuning of the

resonant frequency, attenuation of the sensor's amplitude, and reduction in the maximum readout distance. This limits LC sensors for further application on metallic objects. Although the approaches above have shown significant progress for strain measurement, they require a sweeping frequency to measure the resonant frequency that is time-consuming, and the measurement platform is bulky and costly.

There is limited research using LC inductive sensing to measure the stress on ferromagnetic materials. For example, Chen *et al.* proposed a stress measurement method for steel strands based on the inductance variation in LC resonance[186, 187]. The steel strands were regarded as the inductance component and changed the resonant frequency in response to stress. A set of discrete measurement systems including a resonance circuit, and a frequency meter were used in his research. As a result of the development of both the frequency output sensor and inductance to digital converters (LDCs, Texas Instruments, USA) [163] ,the resonant driver and frequency measurement of LC sensors can be achieved in an integrated module. LDCs-based measurements do not need any external instrument such as a signal generator, power amplifier, data acquisition device, VNA or oscilloscope, which have previously been applied for the research of displacement sensors, inductive tactile and soft angle sensing, angular displacement, defect detection, and human-robot interaction [173, 175, 188-190]. In contrast to a VNA, LDCs are miniaturized, portable, and cost-effective.

This chapter describes for the first time the use of LC resonance sensing based on material's electromagnetic properties and LDCs for force measurement of ferromagnetic materials. The work provides a preliminary study on the application of non-contact measurements for wheel-rail forces. The induction coil was used for sensing the change in electromagnetic properties in response to the loading force and with an adjusted capacitance to change the resonant frequency. within comparison to traditional ECT methods and LC sensors interrogated by an extra readout coil, this new system had advantages of low cost, miniaturization, high resolution, fast response, and excellent sensitivity. The LC resonance sensor was initially designed to connect to an LDCs module to measure the force applied on a ferromagnetic specimen during uniaxial tensile tests. Repeated tests were carried out and the results are compared to those with strain gauges. In addition, lift-off influence and different structures of the coils were compared for sensitivity.

3.2 Principle of Force Measurement using LC Resonance Sensing

LC resonance sensing can be used to measure wheel-rail contact forces by detecting changes in the electromagnetic properties (permeability and conductivity), as shown in Figure 3.1. The change can be wirelessly sensed by an LC resonance sensor through electromagnetic induction.

The resonant driver module outputs AC currents to make the LC sensor resonate, inducing a time-varying magnetic field around the inductance coil. When a test specimen under force is brought into the vicinity of the LC resonance sensor, the alternative magnetic fields will induce eddy currents on the surface of the specimen, which are a function of the electromagnetic properties and loading forces. The eddy currents then generate magnetic fields opposed to the original fields produced by the inductance coil, thus changing the inductance of the LC resonance sensor and the corresponding resonant frequency. The frequency counter is used to measure the frequency representing the force loading on the specimen. LDCs integrate both the resonant driver circuit and frequency measurement of LC resonance sensors.

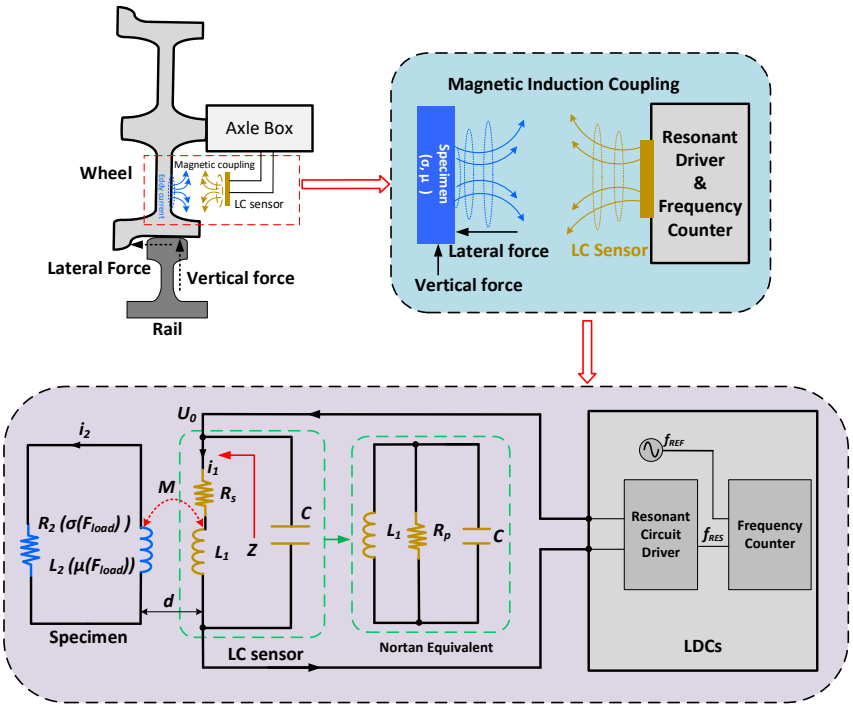

Figure 3.1 Principle of LC resonance sensing for wheel-rail forces and the equivalent circuit

Since the electromagnetic properties of the wheel are dependent on its electrical conductivity and permeability, this system can be applied to an equivalent specimen with similar attributes, as shown in Figure 3.1. The specimen can be represented by a series resistance R_2 inversely proportional to the electrical conductivity σ, and an inductance L_2 relative to the permeability μ. When applying a force on a specimen, both σ and μ change, which in turn causes changes in R_2 and L_2. The LC sensor can be regarded as an LC tank consisting of an inductance coil L_1 and a capacitor C. R_s represents the series resistance of the coil. According to the Norton's theorem, the series R_s, can be transformed into the parallel resistance, R_p (R_p=L_1/($R_s$$C$)). The value of R_p decides the drive current. The larger R_p, the lower the drive current. M is the mutual coupling between the inductance coil L_1 and the equivalent inductance L_2 of the specimen. It is described as follows:

$$M = k\sqrt{L_1 L_2}(0 < k < 1) \tag{3.1}$$

where k is the coupling coefficient of L_1 and L_2. It is dependent on the lift-off d (the distance between the LC sensor and the specimen).

According to Kirchhoff's voltage law (KVL), the equivalent circuit model between the inductance coil of the LC sensor and the specimen can be presented as:

$$\begin{bmatrix} R_s + j\omega L_1 & -j\omega M \\ -j\omega M & R_2 + j\omega L_2 \end{bmatrix} \begin{bmatrix} i_1 \\ i_2 \end{bmatrix} = \begin{bmatrix} U_0 \\ 0 \end{bmatrix} \tag{3.2}$$

where U_0 is the driver voltage provided by the LDC device; i_1 is the current through the inductance and i_2 is the induced current on the specimen; ω is the resonant angular frequency.

Through solving Equation (3.2), the impedance Z of the inductance coil under the interaction with the specimen due to eddy currents is described as [39]

$$\begin{aligned} Z = \frac{U_0}{i_1} &= R_s + \frac{\omega^2 M^2}{R_2^2 + \omega^2 L_2^2} R_2 + jw\left(L_1 - \frac{\omega^2 M^2}{R_2^2 + \omega^2 L_2^2} L_2\right) \\ &= R_{\mathrm{eq}} + j\omega L_{\mathrm{eq}} \end{aligned} \tag{3.3}$$

where R_{eq} and L_{eq} represent the equivalent series resistance and inductance, respectively. They are extracted in Equation (3.4) and (3.5). It can be seen that both R_{eq} and L_{eq} are functions of σ and μ dependent on the loading force.

$$R_{eq} = R_s + \frac{\omega^2 M^2}{R_2^2 + \omega^2 L_2^2} R_2 = R_s + \frac{\omega^2 k^2 L_1 L_2 (\mu(F_{load}))}{R_2(\sigma(F_{load})) + \frac{\omega^2 L_2^2 (\mu(F_{load}))}{R_2(\sigma(F_{load}))}} \tag{3.4}$$

$$L_{eq} = L_1 - \frac{\omega^2 M^2}{R_2^2 + \omega^2 L_2^2} L_2 = L_1\left(1 - \frac{k^2}{1 + \frac{R_2^2(\sigma(F_{load}))}{\omega^2 L_2^2(\mu(F_{load}))}}\right) \tag{3.5}$$

The parallel equivalent resistance R_{Peq} after considering the interaction is written as:

$$R_{Peq} = \frac{L_{eq}}{R_{eq} C} \tag{3.6}$$

Research outcomes in [104, 105, 111, 119] suggested that the change in permeability primarily affects the coil's inductance at low frequencies but have little influence at high frequencies. As magnetization dominates at low frequencies, and eddy currents dominate at high frequencies [111]. It means the change in permeability due to loading at high frequencies can be ignored, and only conductivity σ is left as a factor. When a force F_{load} is applied to a specimen, it is assumed to be positively correlated to the change in conductivity. Since conductivity is inversely proportional to resistance, R_2 is inversely proportional to F_{load}. Assuming the lift-off is fixed, Equation (3.5) can be further simplified as

$$L_{eq} = a\left(1 - \frac{b}{1 + c\frac{1}{(F_{load})^2}}\right) = a\left(1 - \frac{b(F_{load})^2}{(F_{load})^2 + c}\right) \tag{3.7}$$

where a, b, and c are coefficients related to the inductance at zero force loading, the coupling efficient, and $\omega^2 L_2^2$ respectively. It can be deduced from Equation (3.7) that as the load F_{load} increases, L_{eq} decreases and vice versa.

The resonant frequency f_{res} of the LC resonance sensor, determined by L_{eq} and C, is derived as Equation (3.8). Through LDC's frequency counter, the resonant frequency can be measured and thus the inductance is determined.

$$f_{res} = \frac{1}{2\pi\sqrt{L_{eq} \cdot C}} \tag{3.8}$$

3.3 Design of LC Resonance Sensor

When designing an inductance coil for an LC resonance sensor, inductance, frequency of operation, coil geometry including shape, layers, and turns, substrate materials, trace width, and trace spacing. An LC resonance sensor based on electromagnetic induction was designed and fabricated on a PCB board. Table 3.1 shows the parameters of the LC resonance sensor. This sensor can be used to measure wheel-rail contact forces by detecting changes in the electromagnetic properties of the wheels. As shown in Figure 3.2, the sensor was composed of a parallel capacitor and a dual-layer rectangular PCB inductance coil. A rectangular coil was found to be more sensitive to the directional force [112, 113]. The inductance coil was 29.0 mm long, 19.0 mm wide, and 1.6mm thick. It was around 36 μH in the air with a quality factor of 20. Moreover, the rotation of the coils in the top and bottom layers were opposed to enhance the magnetic fields and increase the overall inductance. For the capacitance, a COG/NPO-grade 0603 capacitor with 330 pF was selected since it had the advantages of the highest ceramic dielectric, minimal aging shift, excellent temperature stability, and low ESR (equivalent series resistance). The inductance and capacitance in air led to an initial resonant frequency of 1.460 MHz.

Table 3.1 Parameters of the LC resonance sensor

Parameter	Value
Length	29.0 mm
Width	19.0 mm
Thickness	1.6 mm
Turns per layer	23.0
Layers	2.0
Trace width	6.0 mil
Spacing between traces	9.0 mil

Cp	330.0 pF

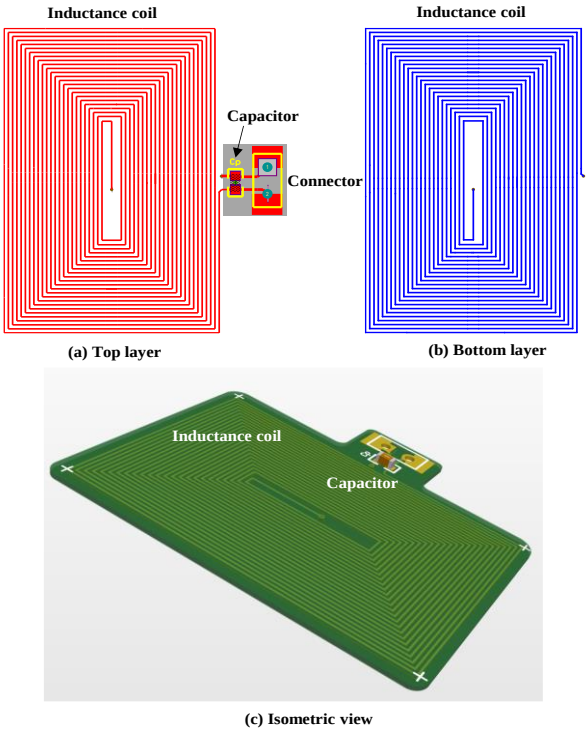

Figure 3.2 The designed LC resonance sensor with (a) Top layer, (b) Bottom layer, and (c) Isometric view

3.4 LDC1614-based Resonant Frequency Measurement System

To drive the LC resonance sensor, an LDC1614-based resonant frequency measurement system was developed, as shown in Figure 3.3. It was composed of interfaces to LC resonance sensors, an LDC1614, I^2C interfaces to the microcontroller, and a MSP430 microcontroller. LDC1614 was a 28-bit inductance to digital converter (LDCs) chip with 4 channels for inductive sensing solutions. It integrated a driver circuit with a frequency counter for LC resonance sensor excitation, frequency measurement, and I^2C communication. The LDC1614 drove the sensor with AC currents to interact with the specimen, and the sensor resonated at its resonant frequency. It supported a wide range of LC resonance sensor frequency, from 1 kHz to 10 MHz. Figure 3.4 shows the frequency measurement principle by using a crystal, counter, Schmitt triggers, and gates. An input signal is connected by a frequency divider and then goes through a Schmitt trigger which converts the input signal to trigger pulses. Similarly, a crystal signal is connected to a frequency divider and a Schmitt trigger as the reference to provide gate-on time to count the number of trigger pulses from the input signal passing through the gate, and the frequency is measured. Table 3.2 presents the registers of LDC1614 which determine whether the LC resonance sensor can work properly. RCOUNT0 determines the conversion time. A longer conversion time provides a higher resolution measurement. SETTLECOUNT0 sets the

settling time to allow the LC resonance sensor to stabilize before the initiation of a conversion. DRIVE_CURRENT0 configures the drive current for the LC resonance sensor. The proposed LDC1614 system has the advantages of being compact, low-cost, portable, and not requiring analogue digital converters (ADCs). The MSP430 was responsible for controlling register configurations, processing, and transmitting the conversion results via I^2C and USB interfaces.

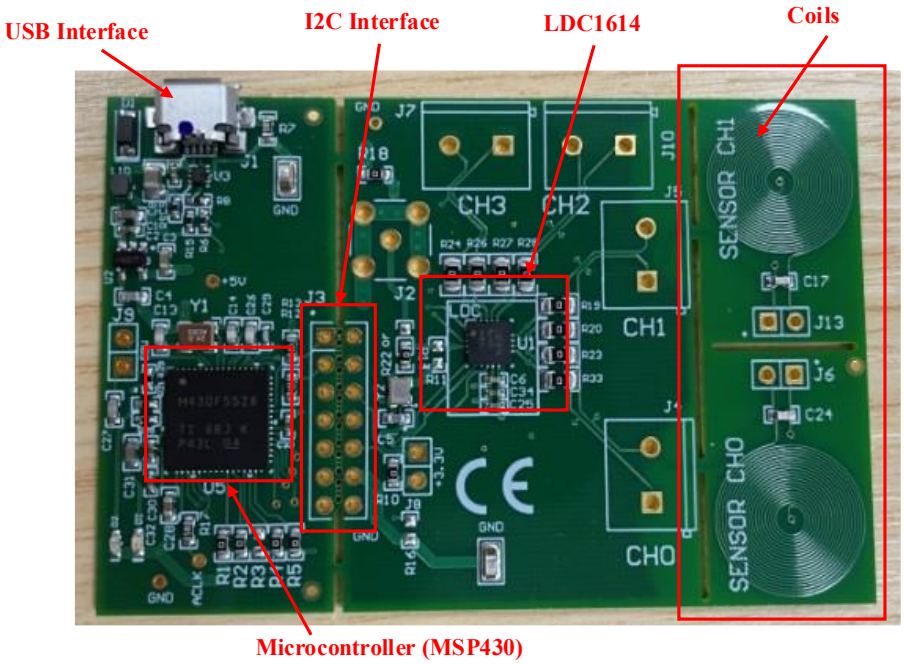

Figure 3.3 LDC1614 experimental measurement board

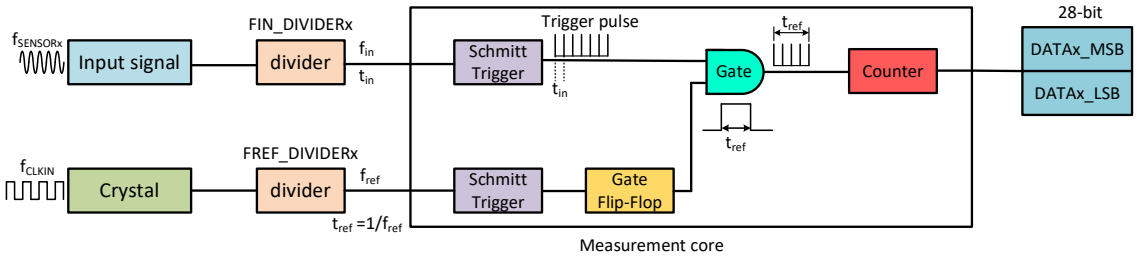

Figure 3.4 Frequency measurement diagram based on LDC

Table 3.2 Registration description

Address	Name	Description
0x00	DATA0_MSB	Channel 0 MSB conversion result (counter value)
0x01	DATA0_LSB	Channel 0 LSB conversion result
0x08	RCOUNT0	Reference count conversion interval time
0x10	SETTLECOUNT0	Channel 0 conversion settling
0x14	CLOCK_DIVIDERS0	Reference and sensor divider setting
0x1E	DRIVE_CURRENT0	Sensor current drive configuration

3.5 Experimental Study and Results

To investigate the feasibility of the proposed LC resonance sensor based on LDCs for force measurement of ferromagnetic materials, experimental studies including definition of experiment set-up, reliability and repeatability tests, comparison with strain gauges, lift-off influence, and aspect ratio of the inductance coil for the sensitivity of the LC sensors were undertaken.

3.5.1 Experimental Set-up

Figure 3.5 depicts the experiment set-up implemented using the LDC1614-based measurement system and the SHIMADZU Autograph AGS-100kNX tensile testing machine. A dog-bone specimen made of carbon steel C50, with dimensions of 250.0 mm in length, 30.0 mm in width, and 3.0 mm in thickness, was used for the force loading test. The width of the specimen was relatively larger than that of the inductance coil which could reduce edge effects [69]. C50 has the similar material properties to those of rail wheels. The mechanical properties of C50 are provided in Table 3.3. The LC resonance sensor was driven and measured using the LDC1614-based measurement system, which consisted of an LDC1614 chip and an MSP430 chip. In the study, only channel 0 was used as it can provide a high current sensor drive for a current greater than 1.5 mA and the minimum requirement of R_{peq} is 250 Ω [163].

During the tensile test the specimen was clamped using wedge grips and loaded by the testing machine. Both the upper and lower wedge grips were well aligned with each other and maintained their alignment during the test. The width of the grip section of the specimen was equal to the width of the wedge grip face, ensuring that the specimen under tensile load only underwent changes along the loading direction and did not cause misalignment with the sensor. The load cell monitored the loading force and raw data was logged. The LC resonance sensor, connected to LDC1614, was kept at a predetermined lift-off from the specimen. PC GUI software was used to configure LDC1614 registers and receive the conversion data from the LDC1614-based measurement board via USB. To prevent electromagnetic interference, a pair of shielding cables were used to connect the LC sensor to LDC1614 channel 0. As the specimen was loaded, the LDC1614 collected data. In addition, a commercial strain gauge indicator was used as the reference measuring the force loading on the specimen. The strain gauge was 350 Ω and had a measurement range of ±31000 με with 1με resolution.

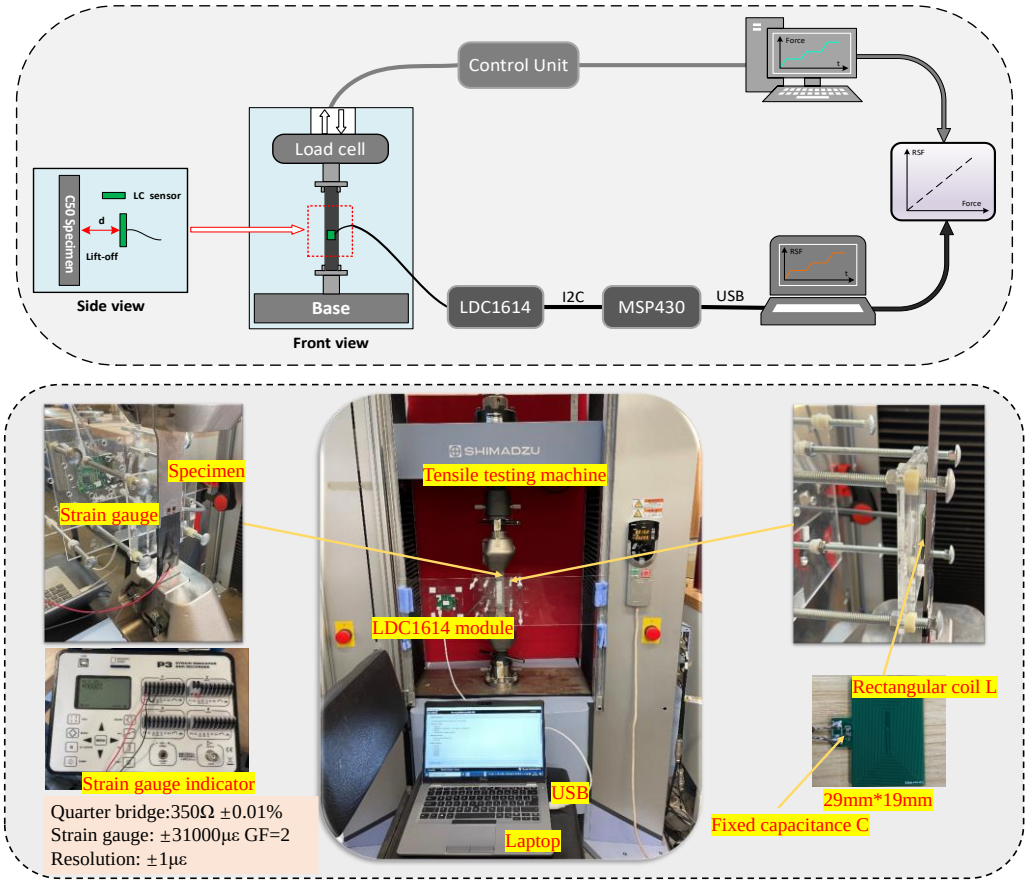

Figure 3.5 Experiment set-up diagram and practical photograph

Table 3.3 Mechanical properties of carbon steel C50 (250 mm x 30 mm x 3 mm)

Property	Value
Yield strength (MPa)	330.00
Young's modulus (GPa)	190.00
Ultimate strength (MPa)	660.00
Poisson's ratio	0.29
Elongation at break	14.00%

3.5.2 Repeatability Tests

To improve test stability and repeatability and eliminate compressive forces on specimens due to testing grips, a 4 kN pre-load was adopted [186]. The test proceeded from 4 kN to 26 kN, with steps of 1.5 kN. The crosshead speed of the testing machine was set to 0.5 mm/min. When the testing machine applied the force on the prepared specimen, the LDC1614-based measurement system started working. SETTLECOUNT0 and RECOUNT0 were set to 400 and 6500 respectively. The high current sensor drive mode was enabled and the value for DRIVE_CURRENT0 was 24 at a lift-off of 0.5 mm. Each time the loading force was increased by 1.5 kN, the testing machine held for 30 seconds for signal alignment and processing. To

obtain the repeated results, the interval between each test was set for 30 minutes. Although the thickness and width of the specimen may change under force, their influence on the the output of the LC sensor can be neglected due to the capability of LDC1614. Figure 3.6 (a) shows the applied loading force from the testing machine for three repeats, with each loading force applied for a period of time. Figure 3.6 (b) shows the corresponding response outputs from the LC resonance sensor at each loading force applied. It can be observed that the output frequency of the LC resonance sensor varied with the loading force, and exhibited good repeatability. However, there are several spikes in several regions that appear to be abnormal comapred with the values around them. These spikes could be attributed to noise and environmental interference, and can be considered as outliers that can be removed by signal processing. Figure 3.7 represents the flowchart of the data processing steps used to establish the relationship between the loading force and the resonant frequency. During each hold stage, the loading force and the corresponding frequency were extracted by segmenting and aligning the data. Outliers were removed from the data first, and then the mean of the force and the frequency during the hold stage were calculated. Finally, the relationship between the force and the frequency was established.

Repeatability tests validated the reliability of an LC resonance sensor for force measurement by demonstrating its ability to produce consistent output signals, typically shifts in resonant frequency, under repeated applications of the same force. These tests confirmed the sensor's precision and stability by assessing whether the force-to-frequency response remained unchanged over multiple trials, thereby indicating minimal influence from noise, hysteresis, or material fatigue. Reliable repeatability ensured that the sensor could be trusted to deliver consistent measurements over time, which was essential for applications requiring accurate and repeatable force monitoring.

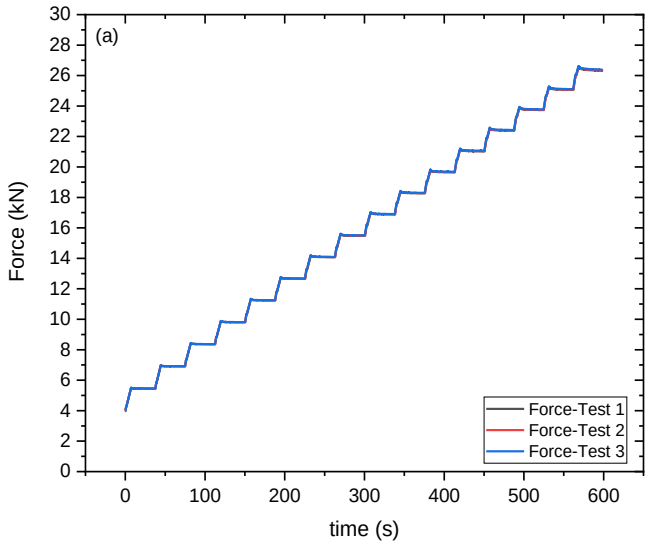

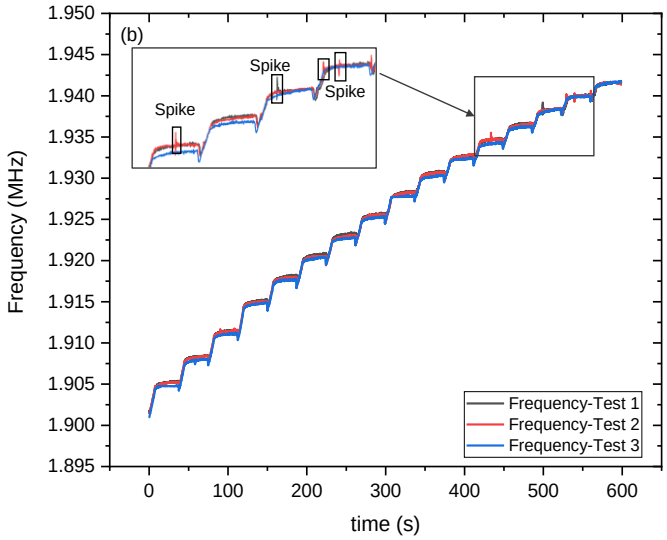

Figure 3.6 (a) Force loading versus time and (b) The frequency output of the LC resonance sensor

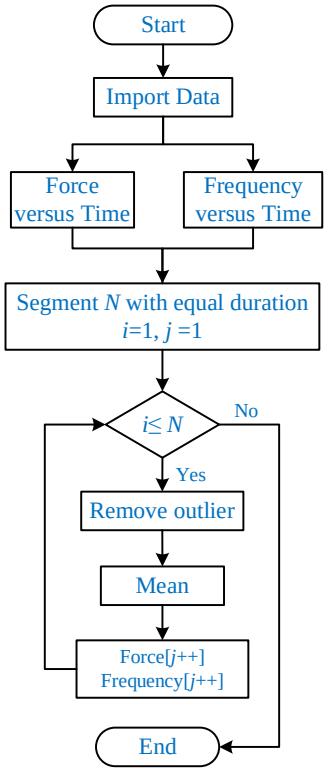

Figure 3.7 Flowchart of data processing

3.5.3 Comparison of Strain Gauge and LC sensor Measurements

Figure 3.8 shows the curves of strain and the resonant frequency versus loading force with error bars for three tests. As shown in Figure 3.8 (a), the strain gauge sensitivity was 52 με/kN from the fitting curve. The strain was proportional to the force. The response of the strain gauge proved the specimen experiencing from the force and the strain increases as the load increase. Figure 3.8 (b) was the resonant frequency of the LC resonance sensor versus force with error

bars for three tests. By combining the measured data with Equotion (3.7) and (3.8), the coefficients *a*, *b*, and *c* can be determined. The values of *a*, *b*, and *c* were 21.262, 0.062, and 327.749, respectively. The fitting curve was presented in Figure 3.8 (b). The relationship between the resonant frequency and the force, was that as the specimen's loading force increases, the resonant frequency also increases. This can be explained by the fact that the loading force increased the conductivity, which in turn increased the intensity of eddy currents, thereby decreasing the inductance and increasing the frequency. This findings was in agreement with the assumption in Equation (3.7). The results presented in Figure 3.8 (b) demonstrated that the force loading on a ferromagnetic material can be wirelessly measured by measuring the variation of electromagnetic properties. Compared with the standard deviation of strain versus force, the proposed LC resonance sensor had a lower standard deviation, indicating its potential for accurate and relible force measurement.

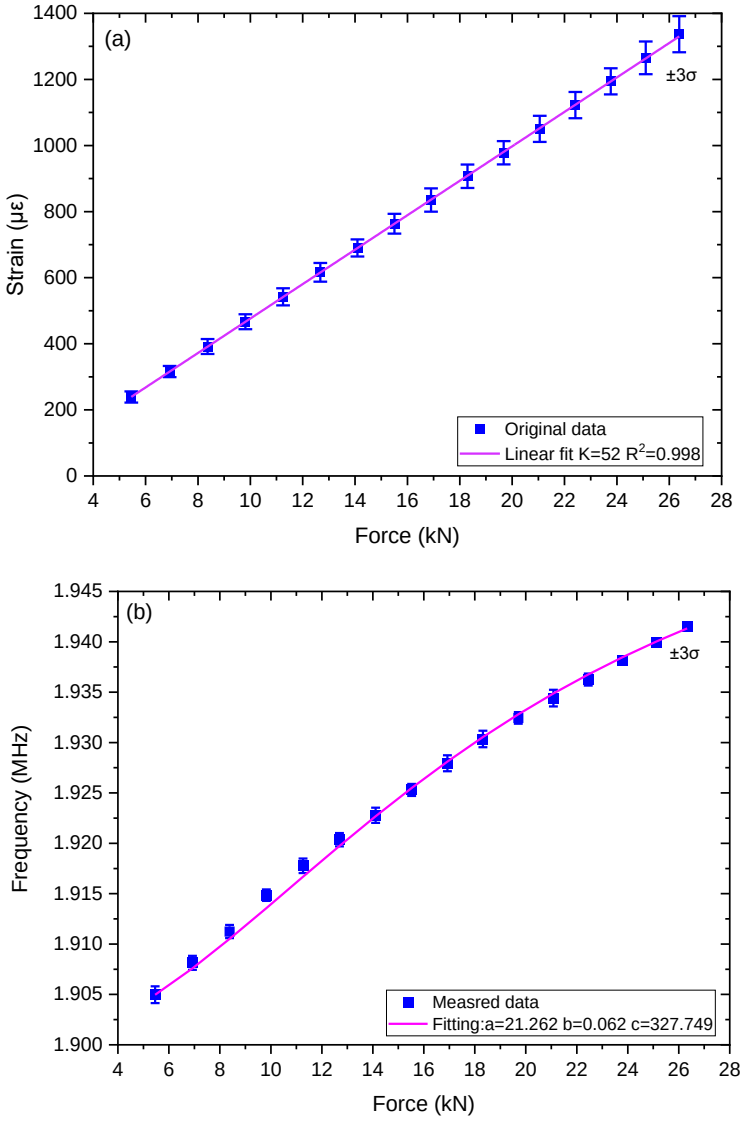

Figure 3.8 (a) Strain-loading force curve with error bars (b) Resonant frequency of LC resonance sensor versus force with error bars at lift-off of 0.5mm

3.5.4 Lift-off Influence

To study the effect of lift-off for the measurement sensitivity, the tests were performed with lift-offs of 0.5 mm, 1.0 mm, 2.0 mm, and 3.0 mm. Figure 3.9 presents the comparison of the resonant frequency difference versus force at different lift-offs, with dash-dot lines representing the fitting curves. The frequency difference was obtained by subtracting the first measured frequency from the measured frequencies for each test, resulting in all the curves starting from the same point for ease of comparison in different situations. In order to make the comparison easier, linear fitting was used, and the slope K represented the sensitivity of frequency against force. The lift-off of 0.5 mm showed the highest sensitivity with 1640 Hz/kN, whereas the sensitivity decreased to 180 Hz/kN when the lift-off was 3.0 mm. A lower lift-off resulted in higher sensitivity because it increased the intensity of electromagnetic induction between the LC resonance sensor and the specimen.

In real applications, maintaining a constant lift-off is challenging because of the dynamic motion, and surface variability. However, the change caused by lift-offs can be compensated using an extra sensor to measure the lift-off to current the primary sensor output.

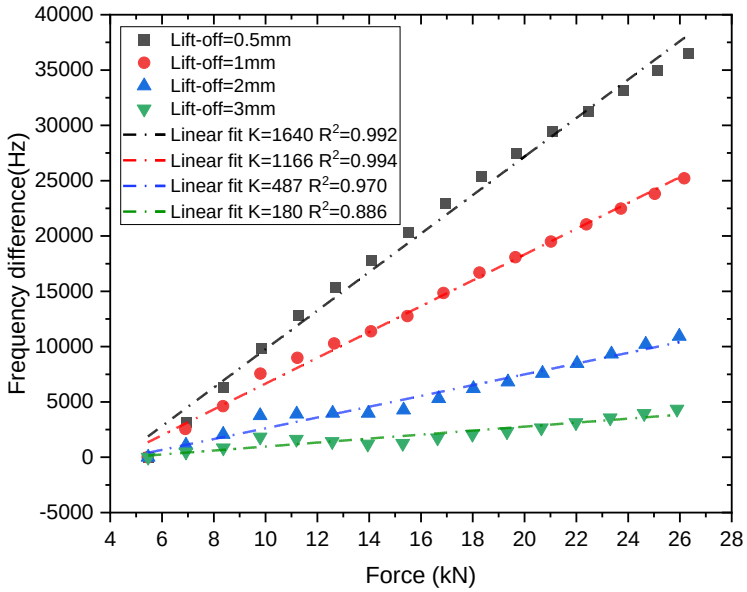

Figure 3.9 Frequency versus loading force under different lift-offs

3.5.5 Aspect Ratio Study of Inductance Coil

The inductance coil at different aspect ratios of LC resonance sensors was studied to compare the sensitivity for force measurement. In addition to the previously used rectangular coil with an aspect ratio (W/L) of 1.0:1.5, two further coils with the ratio of 1:1 and 1.0:2.0 were prepared. These are shown in Figure 3.10; they had the same width with 19 mm and the same turns. Considering the minimal drive requirement of LDC1614 for the three inductance coils, a

capacitor with 220 pF was selected as it provided a relatively large R_p value at this level and the LC resonance sensor can resonate normally. The tests maintained the same specimen, force configuration, and lift-off configuration. Two lift-off tests were performed to verify the consistency of the test. Figure 3.11 (a) and (b) illustrate the relationship between the frequency difference and force regarding the three types of LC resonance sensors at lift-offs of 1mm and 0.5mm. The frequency difference was obtained by subtracting the first measured frequency from the measured frequencies for each test. Table 3.3 displays the sensitivity comparison in the region I and II of Figure 3.11 for the compared coil structures. Based on the derived relationship between the inductance and the loading force in Equation (3.7) and (3.8), when the force F_{load} was much larger than c, L_{eq} was tending to a constant, and the resonant frequency was approaching a constant. It meant when the force continued to increase, it did not contribute to the output of the LC resonance sensor. Thus, to compare their sensitivity through linear fitting, the relationship of c and loading force $(F_{load})^2$ can be used to divide the signal into region I and II. The region I shows the condition that c is larger $(F_{load})^2$ and region II shows c is gradually smaller than $(F_{load})^2$ and eventually was ignored when F_{load} kept increasing.

In terms of the region I, before 15.5 kN, the square coil had a higher sensitivity with 3809 Hz/kN at 1.0 mm lift-off and 4694 Hz/kN at 0.5 mm lift-off, compared with the rectangular coil and the long rectangular coil. The latter two had similar sensitivity in this range. However, in region II, after 15.5 kN, the long rectangular coil demonstrated the highest sensitivity with 966 Hz/kN at 1.0 mm lift-off and 1875 Hz/kN at 0.5 mm lift-off while the square coil had the smallest sensitivity with 446 Hz/kN at 1.0 mm lift-off and 850 Hz/kN at 0.5 mm lift-off. In region I, the force's weight was smaller than the coefficient c, so an increase in force could result in a relatively large change in the output. However, as the force continued to increase in region II, the weight of force gradually became larger than c, leading to a slower rate of change in the output. Overall, the long rectangular coil was preferred in the elastic range, it had a consistent sensitivity and a large response range. It can conclude that the aspect ratio of the inductance coil influenced the directional sensitivity of the LC resonance by shaping the magnetic field distribution. As the applied force was unidirectional, a smaller aspect ratio corresponded to a longer inductance coil, resulting in a longer eddy current parallel to the loading direction of the specimen, which exhibited a wider response range from the experimental results.

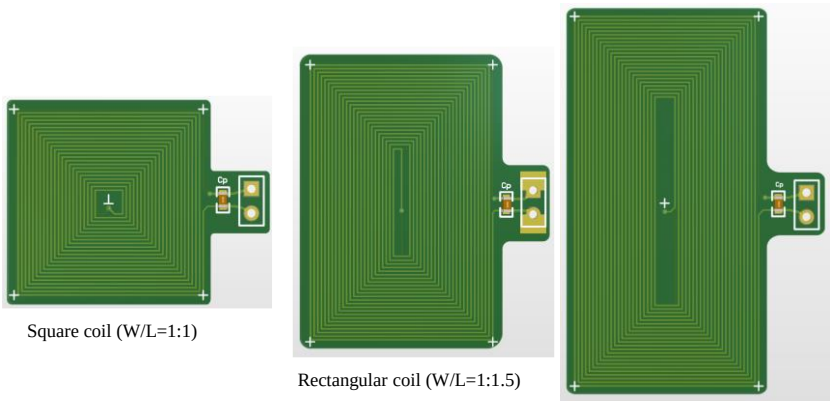

Figure 3.10 Three coil structures with the same width and different length

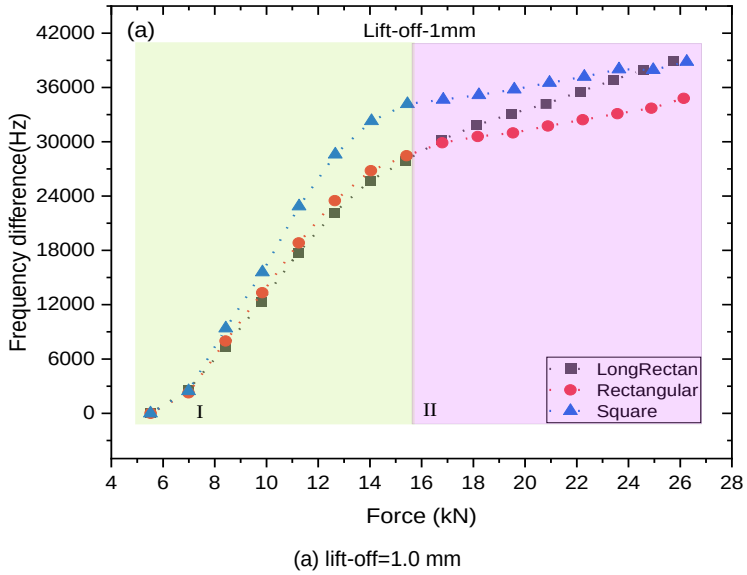

(a) lift-off=1.0 mm

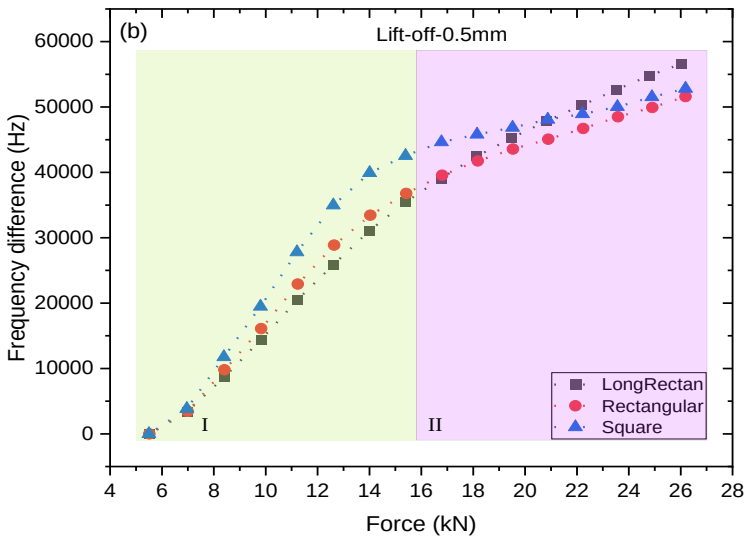

(b) lift-off=0.5 mm

Figure 3.11 Frequency versus force of three coil structures at: (a) lift-off=1.0 mm. (b) 0.5 mm

Table 3.4 Sensitivity comparison for the three coil structures at different lift-off

Lift-off	1.0 mm		0.5 mm	
Region	I	II	I	II
Square coil (Hz/kN)	3809	446	4694	850
Rectangular coil (Hz/kN)	3153	506	3974	1255
Long rectangular coil(Hz/kN)	3049	966	3755	1875

3.5.6 Discussion

The proposed LC resonance sensor based on LDCs proves that the force loading on a ferromagnetic specimen can be measured wirelessly via the measurement of a specimen's electromagnetic properties due to the eddy current effects. It demonstrates the possibility to replace the current use of strain gauges for measuring wheel-rail contact forces. In addition, it can be used to monitor the stress status of test materials in other situations.

The loading force not only changes the electromagnetic properties of the specimen but also causes dimensional changes. Specifically, when a force is applied along the longitudinal direction, both the thickness and width of the specimen change. However, these changes have a weak effect for the output of the LC resonance sensor compared to the changes in specimen's properties. This can be verified by the fact that the resonant frequency of the LC resonance sensor increases as the force increases. As the force increases, the specimen tends to become thin and narrow in the transverse and lateral directions. This should increase the lift-off and therefore increases the inductance of the LC sensor, causing the resonant frequency to decrease. However, this is contrary to the experiment results. Additionally, the variation in the lateral and transverse dimensions is on the order of tens of nanometres, which is out of the measurement range of the system. As a result, lift-off due to transverse and longitudinal deformation of the specimen is neglected. The current LC resonance sensor can only respond to the force when the lift-off is below 1.0 mm, making it difficult to carry out wheel-rail force measurement in real-word situations. Future investigation is necessary to develop an LC resonance sensor capable of working at a high lift-off while maining a high sensitivity. The LC resonance sensor has limited measurememnt range and sensitivity dependent on the intrinsic characteristics of LC resonance sensor according to Equation (3.7), such as the initial inductance, coupling efficient, and electroelastic coefficient (stress coefficient of the electrical conductivity). The design of the LC resonance sensor should take these factors into account.

Furthermore, lift-off significantly influences the useful measurement information. The separation and compensation of lift-off variations and force information is crucial. In this study,

only the resonant frequency is measured and the equivalent parallel resistance R_{peq} is not being used. Measuring R_{peq} in the future could assist the seperation of lift-off effects. Additionally, the aspect ratio of the LC resonance sensor influences sensitivity, which is affected by the direction of loading forces. Practical wheel-rail contact forces have different directions, so the design of LC resonance sensors should be directional and provide decoupling of the measured forces.

3.6 Chapter Summary

In this paper, an LC resonance sensing system for non-contact force measurement was presented, based on the material's electromagnetic properties due to eddy current effects. Through uniaxial tensile tests on the specimen, it demonstrated the feasibility of non-contact force measurement using the LC resonance sensor. The resonant frequency of the LC sensor had a monotonic relationship with the force. The lift-off and the aspect ratio of coils were also studied. It was found that the change of lift-off has a clear effect on the sensitivity of the LC sensor. Specifically, a lower lift-off, such as 0.5 mm, had a higher sensitivity with 1640 Hz/kN due to the enhanced eddy current density. Additionally, the study concluded that the long rectangular coil structure (W/L=1:2) was better than the other two for directional force measurement. Overall, these findings provide the design rules and working performance of LC sensors used for force measurement.

This chapter demonstrated that the rectangular LC resonance sensor successfully achieved WFM by measuring the resonant frequency using the LDC1614-based system to represent the applied force. However, similar to ECT, this approach is also influenced by lift-off which can result in misinterpretation between lift-off and force. Additionally, the LDC1614 can only measure the resonant frequency, omitting the equivalent parallel resistance. The next chapter will focus on the measurement and separation of lift-off and force using an orthogonal LC resonance sensor, LDC1101-based multi-parameter measurement system, and isoparametric coordinate transformation algorithm.

Chapter 4. Measurement and Separation of Forces and Lift-Offs Using LDC-Based Orthogonal LC Resonance Sensors and Multiple Parameters

This chapter addresses the separation issue of lift-off and force based on the orthogonal LC resonance sensors, the developed LDC1101-based multi-parameter measurement system, and an 8-node isoparameteric quadrilateral transformation algorithm. The state-of-the-art progress in the measurement and separation of ECT-based technology was introduced. The principle of LDC-based orthogonal LC resonance sensing principle and separation of force and lift-off were then described. Finally, Experimental set-up regarding force tests at different lift-offs was conducted and the separation using the 8-node isoparametric coordinate transformation was implemented.

4.1 Introduction

The previous work demonstrated that the force can be wirelessly measured by assessing the electromagnetic properties of the testing sample using LC resonance sensors, which rely on the measurement of resonant frequency [191]. LC resonance sensors are affected by lift-offs as they depend on electromagnetic induction. Lift-off is the distance between the sensor and the test object. Vibration or unevenness of a surface in real environments causes a change in lift-off, which in turn influences the measurement information. The lift-off effects pose a challenge on identification of the measured parameter. Many researchers have been involved in reduction, elimination, compensation, and separation of these effects in the past few decades [80, 110, 192-200].

Lift-off invariance (LOI) describes the frequency or time-based signal outputs for eddy current testing intersecting at a point where signal features such as intersection time or amplitude are independent of lift-off variations. LOI has been employed for conductivity, permeability, and thickness measurement [110, 194, 195]. Nevertheless, determining LOI points is subjective, as LOI may not occur at a specific point but rather within a range. The extraction of LOI features is also difficult as it requires multiple lift-off tests to attain the intersection information, thereby making it hard to achieve industrial applications. Applying LOI to LC resonance sensors is not feasible because these sensors measure the resonant frequency or the equivalent impedance of the resonance signal, rather than time-sequence or frequency sweeping signals [191, 199]. In addition to LOI research, analytical solutions, and mathematical normalisation processing are studied to minimize lift-off effects. To eliminate lift-off in conductivity measurement, Dziczkowski proposed an algorithm based on solving two parameters by measuring the change of coil resistance and inductance; one parameter was the ratio of the distance between the coil

and the normalised half-space, while the other depended on conductivity and the angular frequency of the coil current [193]. Fan *et. al.* developed a model-based inversion method for lift-off reduction in characterization of conductivity and thickness of a nonmagnetic plate [198]. A normalisation method by means of two reference signals to reduce lift-off issue was demonstrated [197]. Ma *et.al.* proposed a dual signal conditioning system consisting of a bridge and transformer to realize multiple parameters measurement for lift-off reduction and separation [80]. These methods applied complex mathematical solutions and post-processing algorithms to deal with lift-off issues, leading to a complicated usage condition. At high-frequency apparent eddy current conductivity (AECC) spectroscopy, a four-point linear system calibration was performed on two reference calibration blocks with high and low conductivity respectively, at two different lift-offs [120, 200]. The measured conductivity was estimated through simple linear interpolation in the established calibration impedance curves. Later, after taking lift-off non-linearity into account, a six-point semi-quadratic system calibration was developed which further decreased measurement sensitivity to lift-off [201]. This calibration method was based on coordinate transformation of isoparametric quadrilateral elements [202]. By combining the measurement values at calibration points with appropriate shape functions, the measurement coordinate was transformed into the calibration coordinate in which conductivity and lift-off were separated [199, 203]. However, while significant progress has been made in addressing lift-off problems, most efforts mainly focused on thickness or conductivity measurement on non-magnetic specimens. There is almost no research on lift-off variations of ferromagnetic materials under stress since most electromagnetic methods need a close contact between the probe and the test pieces [114, 204]. LC resonant sensing operated in steep impedance variations, significantly enhancing detection sensitivity and detection range [179, 205]. To extend the previous research and take into lift-off separation into consideration, an LDC-based orthogonal LC resonance sensor in this chapter, combined with an 8-node quadrilateral interpolation method, was proposed to achieve the measurement and separation of forces and lift-offs in the ferromagnetic sample.

4.2 Principle of the LDC-Based Orthogonal LC Resonance Sensor for Force Measurement

An LC resonance sensor consists of an inductor coil and a parallel capacitor that together determine the resonant frequency (*Frequency*) and equivalent parallel resistance (R_p). The principle of using an LC resonance sensor to measure the force is based on the changes in the electromagnetic properties (conductivity σ, and permeability μ) of the specimen. When a specimen is subject to the force, its electromagnetic properties change due to inverse magneto-

strictive effects [114] and piezoresistive effects [113]. An LC resonance sensor excited by an alternating current resonates at the resonant frequency and generates primary magnetic fields, which interact with the specimen and induce eddy currents on its surface. The eddy currents are a function of the lift-off and the electromagnetic properties [69]. These eddy currents generate its own magnetic fields (secondary magnetic fields) that oppose the original fields. Due to mutual coupling of these magnetic fields, the equivalent inductance L_s and resistance R_s of the inductor coil varies, leading to changes in the resonant frequency and R_p of an LC resonance sensor. By measuring them, it is possible to characterize the force applied to the specimen as well as assess lift-off. Figure 4.1 shows the schematic diagram of the proposed LDC1101-based orthogonal LC resonance sensing for force measurement. There are two LC resonance sensors positioned in a parallel and perpendicular direction to the specimen respectively, forming an orthogonal LC resonance sensor. They provide multiple measurement parameters about the force and lift-off in different directions which contribute to the separation of force and lift-off. To minimize mutual interferences, these two sensors work in sequence controlled by an ESP32S3 microcontroller (Espressif Systems). As one is selected to work, the other one is grounded. LDC1101 injects energy into the activated sensor to make it resonate [178]. When the specimen under loading is near the LC resonance sensors, its varying electromagnetic properties are monitored by measuring the resonant frequency and R_p of the LC resonance sensors. The proposed LDC1101-based system measures the resonant frequency and monitors the energy injected into the sensor to obtain R_{pi}. Forces and lift-offs are then obtained from the measured resonant frequency and R_{pi}.

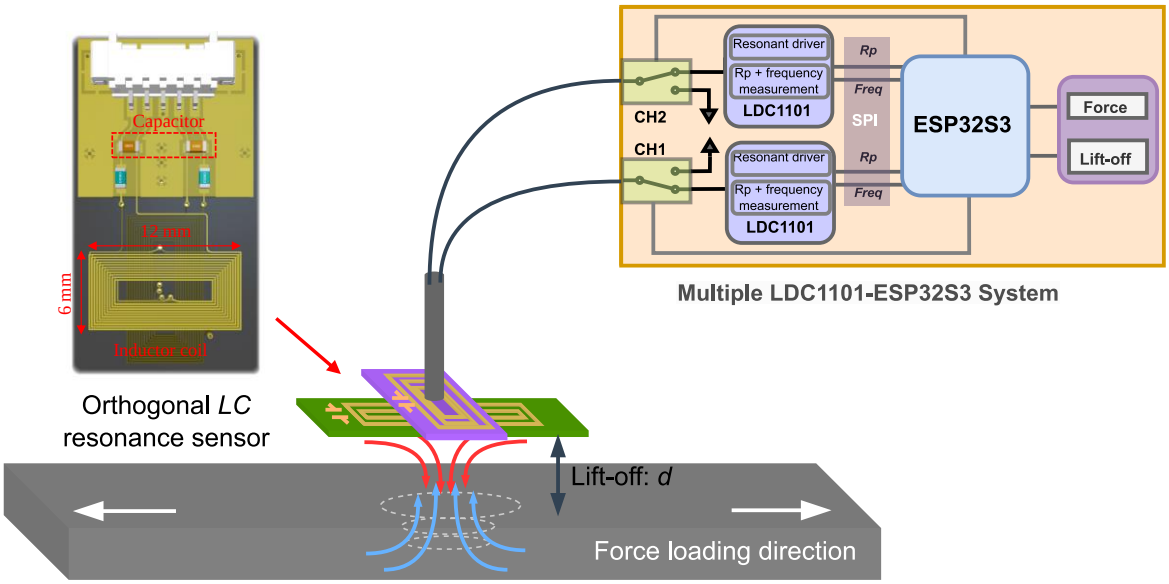

Figure 4.1 Schematic diagram of LDC1101-based orthogonal LC resonance sensing for force measurement

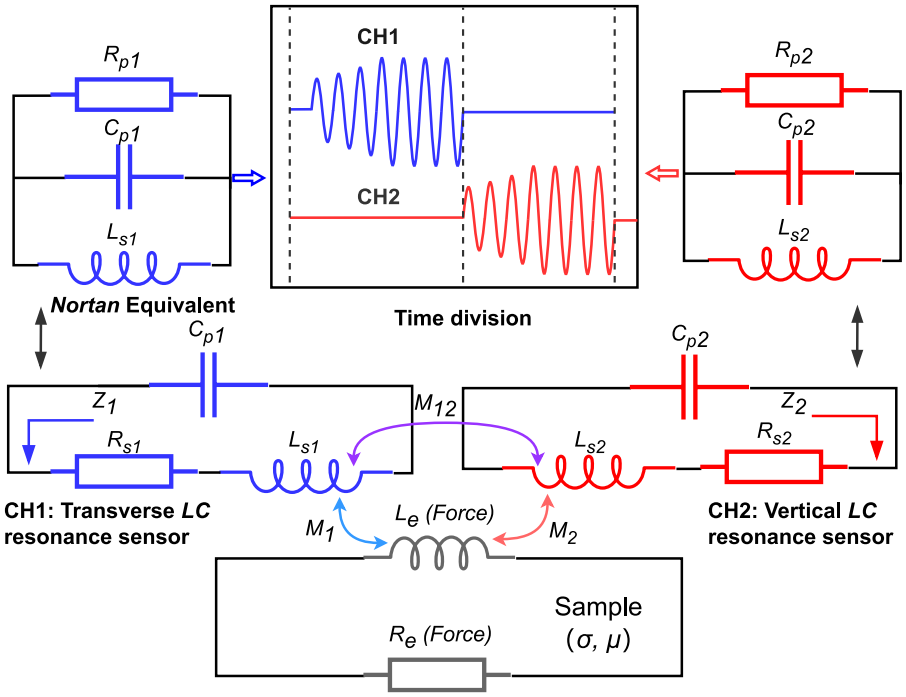

Figure 4.2 Equivalent circuits of LC sensors and the sample

Figure 4.2 presents the equivalent transformer model of two LC resonance sensors and the sample. Since only one sensor is active at a time while the other one (the inactive one) is grounded, this process is reflected in the time division signals. Grounding the inactive one creates an incomplete closed loop, which helps eliminate the eddy current effects and minimize the coupling effects. Thus, the mutual coupling M_{12} between the transverse and vertical LC resonance sensors is ignored. As shown in Figure 4.2, the impedance of each inductor coil does not take M_{12} into consideration. Equation (3.3) shows the impedance Z_i of each inductor coil, where i denotes the sensor number; R_{si} is the equivalent series resistance of the coil and ω is the resonant angular frequency; Equation (3.1) represents the mutual coupling of the inductor coil and the sample, dependent on the coupling coefficient k_i that is affected by the lift-off d; R_e and L_e are the resistance and inductance of the induced eddy current loop, respectively [69]. L_{si} is the equivalent series inductance of the coil. In Equations (3.4) and (3.5), R_{eqi} and L_{eqi} represent the equivalent series resistance and inductance of the inductor coil, respectively, in response to the sample's conductivity and permeability. Since the resonant frequency of the sensor is in the MHz range, permeability variations due to loading are disregarded as eddy currents dominate at high frequencies [119, 206], thereby only considering conductivity σ. According to Norton's theorem, LC resonance sensors are transformed into an RLC parallel model, where R_{pi} describes the equivalent parallel resistance, and it is presented by Equation (3.6). Equation (3.7) demonstrates the resonant frequency (*Frequencyi*) of an LC sensor in which C_{pi} is the parallel capacitor.

4.3 Separation of Force and Lift-off by Isoparametric Quadrilateral Transformation

The LDC1101 measurement system provides four parameter outputs, R_{p1}, the resonant frequency 1 (*Frequency1*), R_{p2}, the resonant frequency 2 (*Frequency2*), representing the responses of the LC resonance sensors to loading forces in transverse and vertical directions. Properly arranging them helps to extract force and lift-off parameters. The four-point and six-point calibration methods have been demonstrated in effectively removing lift-off effects in conductivity measurement through linear and semi-quadratic interpolation [199, 200]. These methods originate from isoparametric quadrilateral elements, which have been widely used in finite element analysis (FEA) to simplify the model and reduce the calculation complexity [202]. The isoparametric quadrilateral elements used in our study are established by measuring the outputs of the sensors while varying the lift-off and force, respectively. The specimen under the force (within the elastic region) changes the lift-off, but this kind of variation is ignored since it is too small (nanometre scale), unable to be measured by the LDC1101 measurement system. Also, the direction of the force loading and lift-off variation is perpendicular in space. The force loading is along the longitudinal direction of the specimen while the lift-off variation is along the transverse direction. Therefore, it is assumed that lift-off and force have independent effects on the sensor characteristic curves and maintain a monotonic relationship with the sensor outputs. At a certain lift-off, regardless of how much force is applied and causes the change in electromagnetic properties, the lift-off remains constant. Similarly, at a certain applied loading force, regardless of how the lift-off varies, the force remains constant. Based on these two conditions, an 8-node quadrilateral interpolation method is proposed to separate force and lift-off, as shown in Figure 4.3.

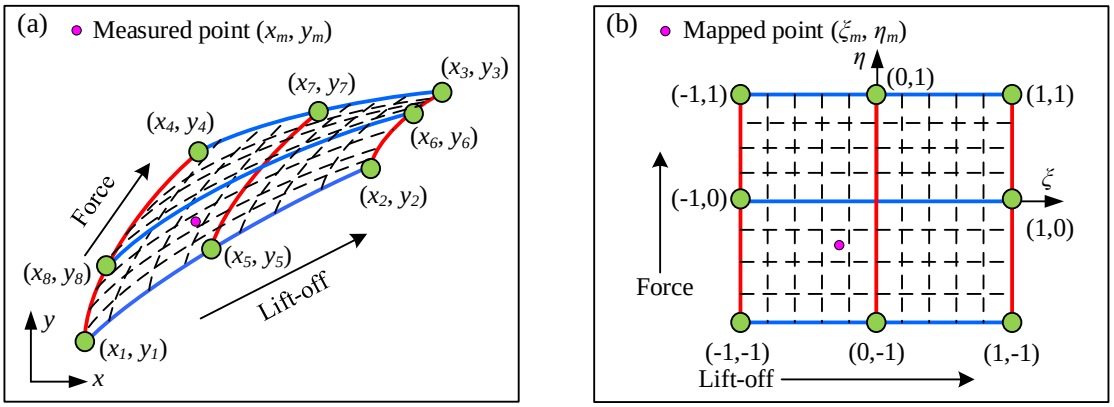

Figure 4.3 (a) Measurement Cartesian x-y coordinate (b) Mapped ξ-η coordinate

Figure 4.3 (a) shows the measurement Cartesian *x-y* coordinate, which is constituted by any arrangement of R_{p1}, *Frequency1*, R_{p2}, *Frequency2*. Figure 4.3 (b) is the transformed *ξ-η* coordinate. There are 8 selection calibration points that cover the measurement range of force

sand lift-offs. Therefore, a mapping relationship is established, (x_1, y_1) to (-1, -1), (x_2, y_2) to (1, -1), (x_3, y_3) to (1, 1), (x_4, y_4) to (-1, 1), (x_5, y_5) to (0, -1), (x_6, y_6) to (1, 0), (x_7, y_7) to (0, 1), (x_8, y_8) to (-1, 0). Any measured point (x_m, y_m) falling into the measurement Cartesian coordinate is transformed into the mapped point (ξ_m, η_m) in the mapped coordinate by selecting proper shape functions [199, 201]. Here, the selected 8-node shape functions N_i (i=1, 2, …,8) are described as follows:

$$N_1 = \frac{-1}{4}(1-\xi)(1-\eta)(1+\eta+\zeta) \tag{4.1}$$

$$N_2 = \frac{-1}{4}(1+\xi)(1-\eta)(1+\eta-\zeta) \tag{4.2}$$

$$N_3 = \frac{-1}{4}(1+\xi)(1+\eta)(1-\eta-\zeta) \tag{4.3}$$

$$N_4 = \frac{-1}{4}(1-\xi)(1+\eta)(1-\eta+\zeta) \tag{4.4}$$

$$N_5 = \frac{1}{2}(1-\xi^2)(1-\eta) \tag{4.5}$$

$$N_6 = \frac{1}{2}(1+\xi)(1-\eta^2) \tag{4.6}$$

$$N_7 = \frac{1}{2}(1-\xi^2)(1+\eta) \tag{4.7}$$

$$N_8 = \frac{1}{2}(1-\xi)(1-\eta^2) \tag{4.8}$$

The mapped point can be obtained by solving the following equations:

$$\sum_{i=1}^{8} x_i \cdot N_i = x_m \tag{4.9}$$

$$\sum_{i=1}^{8} y_i \cdot N_i = y_m \tag{4.10}$$

The solved ξ_m and η_m represent the force and lift-off respectively. It is observed from Figure 4.3 (b) that the force remains constant as the lift-off distance changes, and similarly, the lift-off distance remains constant as the force changes.

4.4 Development of Multi-parameter Measurement System and MATLAB-based GUI

A multi-parameter measurement system based on ESP32S3, LDC1101, and multiplexer TMUX1134 was developed. Figure 4.4 shows the block diagram where TMUX1134 is connected to ESP32S3 to control which LC sensor to work while grounding the other one. As two LDC1101s share the same SPI wires, only one chip is selected every time. Data collected from LC resonance sensors are sent to MATLAB GUI via USB for data visualisation and storage. There is a schematic diagram in Figure 4.5 which presents the actual design for wiring LDC1101, TMUX1134, and interfaces of ESP32S3. A 16 MHz oscillator (632L3I016M00000) is employed for providing the reference frequency for LDC1101, which requires a consistent impedance 50 Ohm in its pin routing. All the power supplies are decoupled by two bypass capacitors to reduce EMI interference and regulate the circuit. Because there is a ready-made

module for ESP32S3, only SPI interfaces and power wires are needed to connect LDC1101, TMUX1134, and ESP32S3.

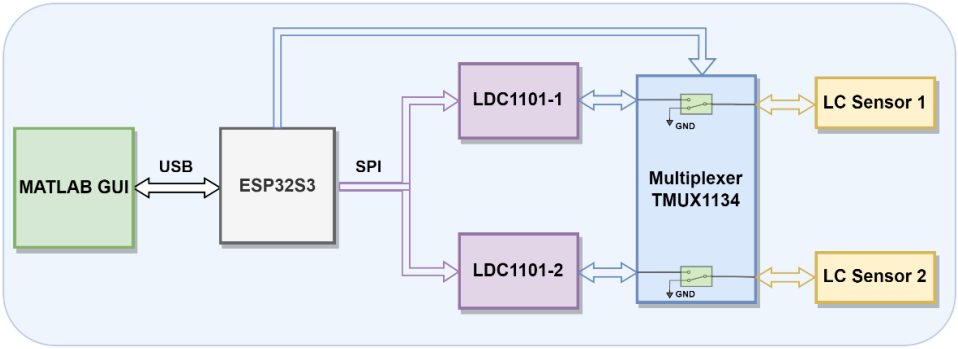

Figure 4.4 Block diagram of multi-parameter measurement system based on ESP32S3 and LDC1101

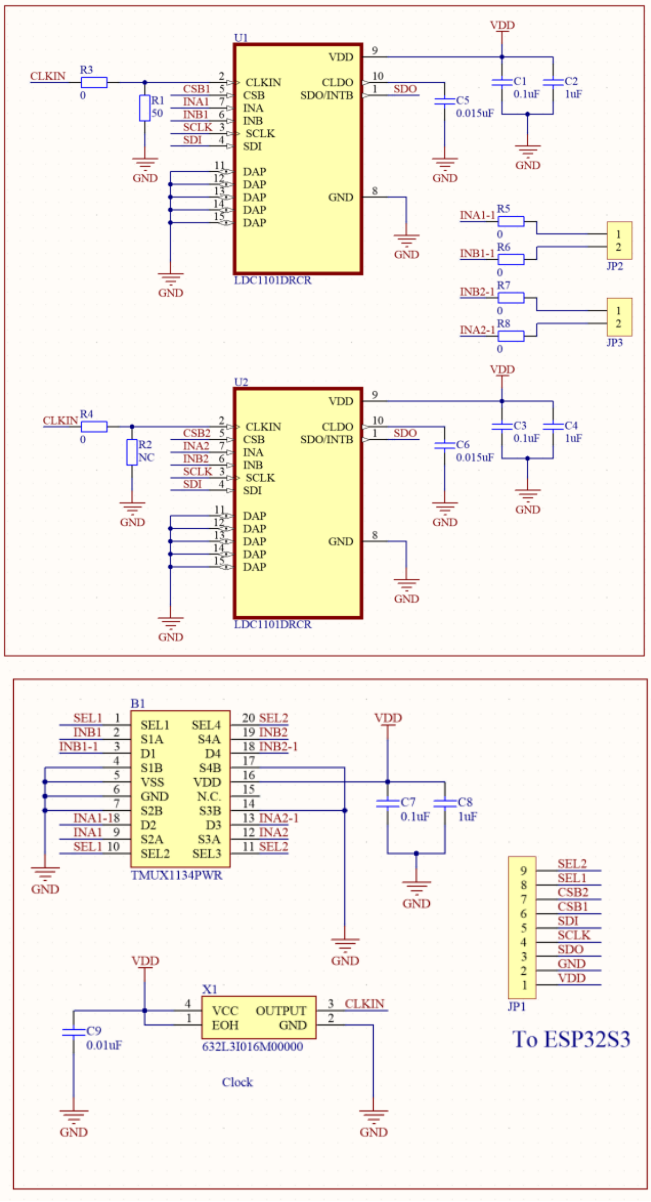

Figure 4.5 Schematic of LDC1101-ESP32s3 based measurement system

Figure 4.6 is the flowchart of configuring the registers of LDC1101 and reading value from it. There are several significant registers in LDC1101 which have to be set appropriately, such as RP_SET (0x01), TC1 (0x02), TC2 (0x03), DIG_CONFIG (0x04). RP_SET configures the maximum and minimum range of *Rp* from 0.75 kΩ to 96 kΩ. Additionally, *Rp* measurements require configure TC1 and TC2 to set internal time constants. TC1 is dependent on the minimum sensor frequency in the system; typically, this occurs when there is no target interacting with the LC resonance sensor. TC2 is determined by the parallel capacitor of LC resonance sensor and minimum *Rp*. In register DIG_CONF, the sensor minimum frequency should be set that is based on the lowest possible sensor range when the target has minimum interaction with the sensor; the response time setting is also important which determines the conversion time. The conversion time is equal to the response time divided by 3 times sensor frequency. The response time set starts from 192, 384, 768, 1536, 3072, and 6144. A larger response time have a slower sample rate but a higher resolution conversion. It should be a trade-off between sensor resolution and conversion time for different applications.

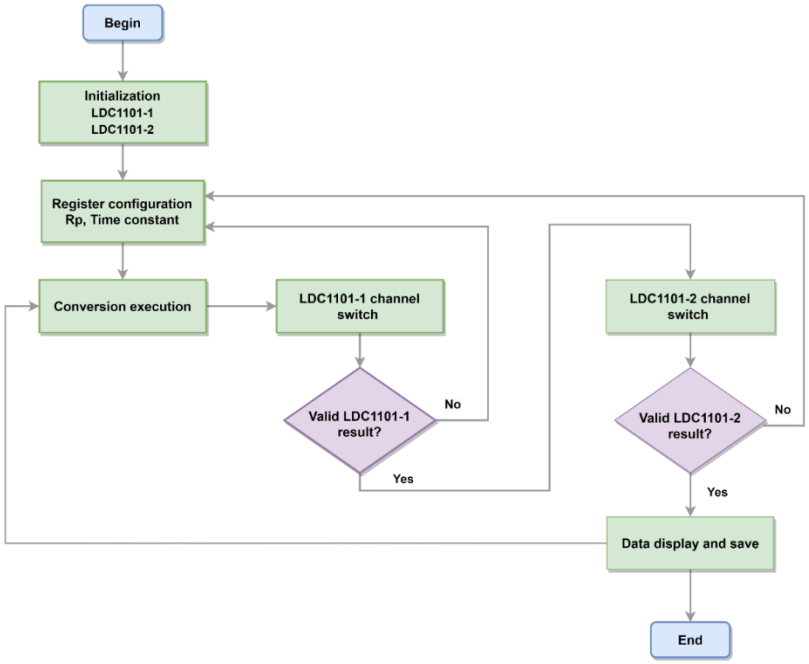

Figure 4.6 Flowchart of driving and reading LDC1101 via ESP32S3

The MATLAB-based GUI was designed in MATLAB R2023a based on MATLAB App designer. The sensor data after collecting from ESP32S3 are transmitted to the GUI through USB communication. In the programming of ESP32S3, the four parameter outputs, R_{p1}, *Frequency1,* R_{p2}, *Frequency2*, are printed by serial communication, respectively. The GUI read the serial port according to the preset baud rate, COM port. The incoming data is a string structure which contains a four-parameter label and numeric values. An expression is used to sperate them and save in different pre-defined array accordingly. Meanwhile, these separated

data are plotted in real-time. The GUI also features the function of measuring temperature and humidity for further research, offering more useful data support.

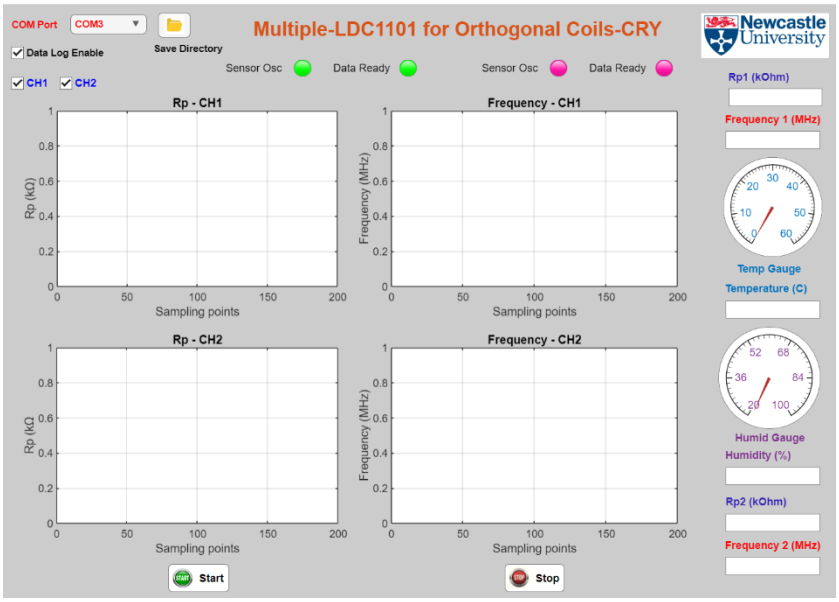

Figure 4.7 MATLAB-based GUI for data collection and display

4.5 Experimental Set-up and Results

The proposed LDC-based orthogonal LC resonance sensing system was performed via an experimental set-up to verify force and lift-off measurement. As shown in Figure 4.8, the system comprised a universal test machine Instron 3369, a C50 ferromagnetic specimen (250 mm in length, 30 mm in width, and 3 mm in thickness) whose mechanical properties are presented in Table 3.3, an orthogonal LC resonance sensor, a LDC1101-ESP32S3 based multi-parameter measurement system, and a MATLAB-based GUI. The orthogonal LC resonance sensor consisted of two identical inductor coils with the same number of turns and layers, but placed in perpendicular directions, along with identical parallel capacitors. The two coils were fabricated using printed circuit board (PCB) technology, on an 8-layer PCB board, with the first four layers on the top being for the vertical inductor coil, parallel to the loading direction, and the last four layers on the bottom for the transverse inductor coil, perpendicular to the loading direction. The size of the inductor coil was 12 mm in length and 6 mm in width since directional coils are more sensitive to forces in a particular loading direction [113]. The inductance of each inductor coil was 17 μH at 2 MHz. Two 330 pF capacitors on the top layer were connected to two inductor coils in parallel to form LC resonance sensors, generating a resonant frequency of 2.1249 MHz. Commencing, the ESP32S3 selected one of the LC resonance sensors and grounded the other by controlling the channels of the multiplexer. LDC1101 then drove the selected LC resonance sensor and measured the resonant frequency and R_p when the specimen

was loaded. After the first one was completed, switched to the next one, and then repeated in sequence. The measured data were sent to the MATLAB-based GUI by a USB cable.

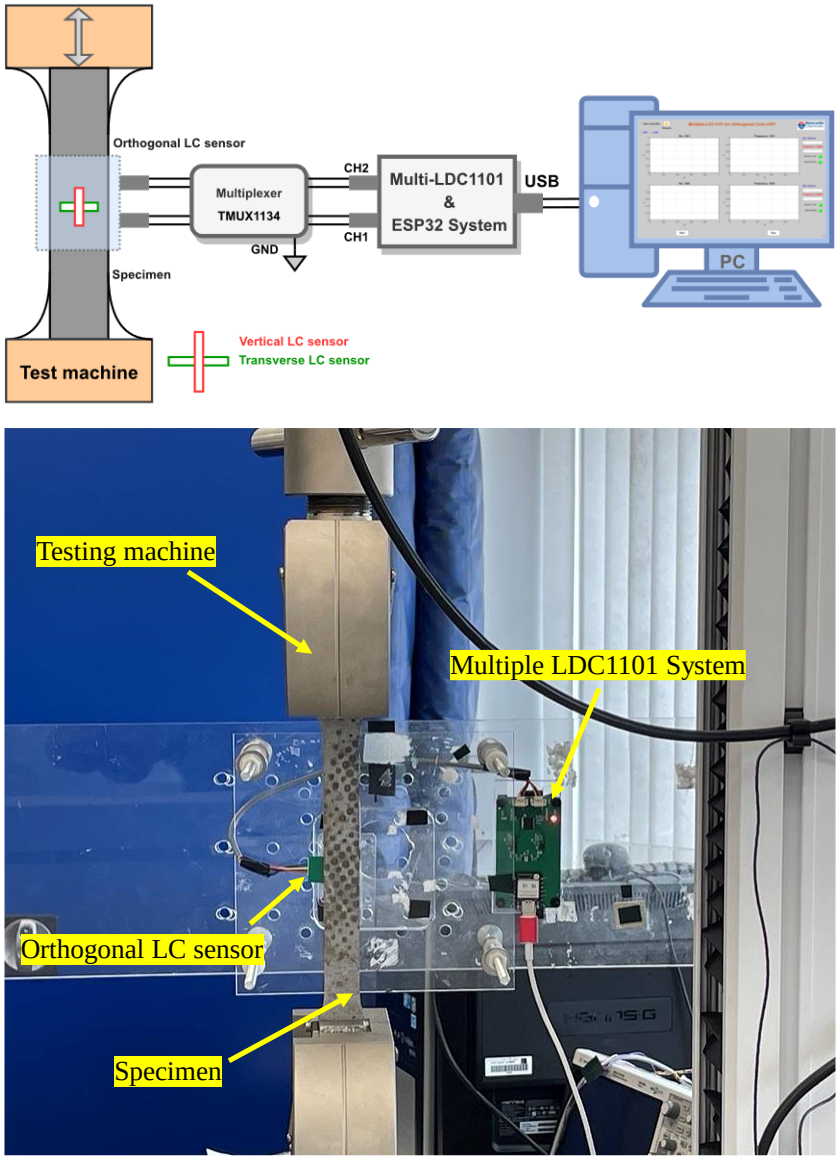

Figure 4.8 System measurement diagram and photograph of experimental set-up

4.5.1 Force Tests at Different Lift-offs

The specimen was loaded by the tensile testing machine from 2 kN to 14 kN. There was a 2 kN pre-load eliminating the influence of compressive force in the grips [186]. The orthogonal LC resonance sensor was fixed at lift-offs of 1.0 mm, 1.3 mm, 1.5 mm, 1.9 mm, and 2.0 mm. After the lift-off was set the specimen was loaded and the orthogonal LC resonance sensor begun to work. There were 5 tests in total at the different lift offs. There were four measurement outputs, R_{p1}, *Frequecny1*, R_{p2}, *Frequency2*, from two LC resonance sensors containing information of forces and lift-offs from the vertical and transverse directions. Responses were shown in Figure 4.9. It was observed that R_{p1} and R_{p2} monotonically decreased as the force increased whereas *Frequency1* and *Frequency2* exhibited a reverse trend, which can be explained by the increased

conductivity. According to Equation (3.4)-(3.6), the increased conductivity induced a stronger eddy current and increased the eddy current loss R_{eqi} [119], leading to a reduction of R_{pi}. The stronger eddy current generated a stronger secondary field which weakened the primary field and further reduced the L_{eqi}. This, in turn, increased the resonant frequency. As lift-off varied from a low value to a high value, the four outputs reduced their corresponding sensitivity. This was due to the fact that the attenuated eddy current decreased the secondary magnetic field to interact with the primary field. Compared with R_{p1}, *Frequency1* showed a better response range after the force exceeded 8 kN while the former became unchanged. In terms of R_{p2} and *Frequency2*, their variation curves appeared similar to the previous ones, but the sensing direction was vertical to the loading direction. It was challenging to separate forces and lift-offs when using only one parameter. The combination of multiple parameters was necessary to improve their separation.

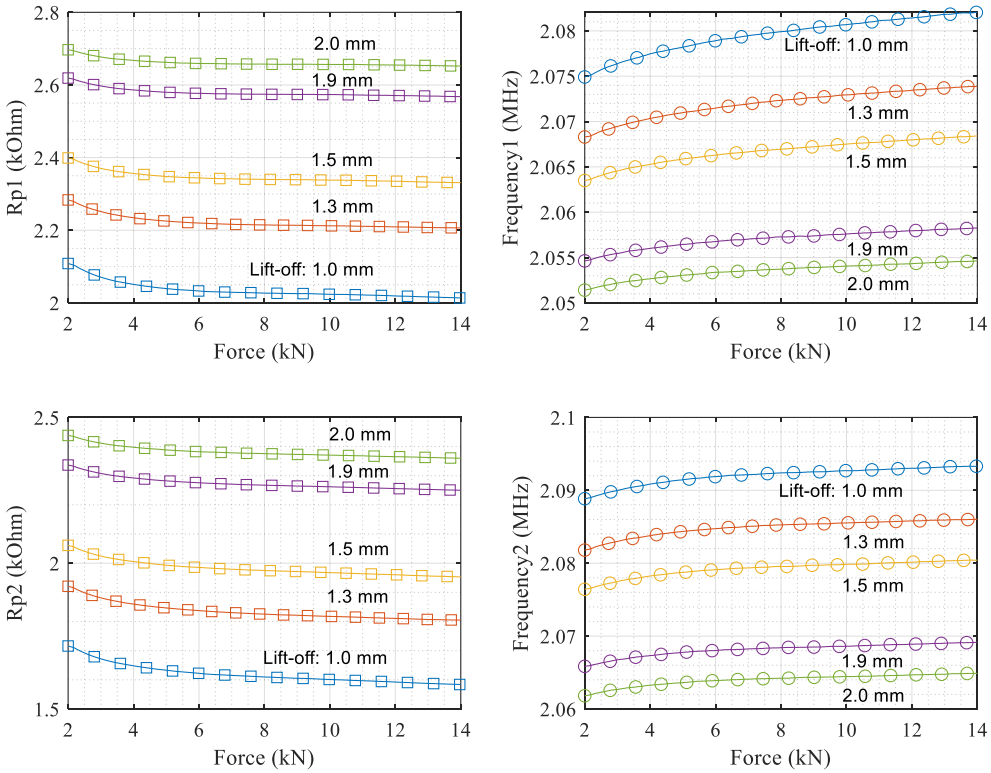

Figure 4.9 R_{p1}, *Frequecny1*, R_{p2}, *Frequency2* versus forces at different lift-offs

4.5.2 Characteristic Planes of Rp and Frequency

Like traditional eddy current testing where impedance planes were used for analysis of defects, conductivity, and lift-off, *Frequency*-R_p curves were established to characterize material, lift-off, and cracks [204]. Figure 4.10 show *Frequency*-R_p planes of the vertical LC resonance sensor and the transverse LC resonance sensor for force tests at different lift-offs respectively. In contrast with a single parameter against force, *Frequency*-R_p planes provided apparent messages about force and lift-off variations. It was seen that the change in forces caused the

Frequency-R_p curve to shift towards the top left while the lift-off caused that curve to shift towards the bottom right. They had reverse effects on the shift of *Frequency-R_p* curves. One noteworthy point was the *Frequency-R_p* curves for the vertical and transverse LC resonance sensors exhibited distinguishable characteristics. The former varied in a quadratic function and the latter varied in a linear function. The difference between them was attributed to the sensing direction. The vertical direction was parallel to the loading direction, which was more sensitive to the force change, thereby making the *Frequency-R_p* curves more distinct than the transverse one. Although the transverse LC resonance sensor can measure the change in forces and lift-offs, from the *Frequency-R_p* curves, there were overlaps at certain points which resulted in recognition difficulty for their respective effects. The transverse LC resonance sensor can perform compensation measurements to help the vertical LC resonance sensor to separate the force and lift-off. Therefore, a new combination pattern called *R_{p1}-R_{p2}*, *Frequency2-Frequency1* was proposed, as shown in Figure 4.11. Force and lift-off variations led to a pronounced difference for *R_{p1}-R_{p2}* and *Frequency2-Frequency1* curves. By plotting the curves of *Frequency1-R_{p1}, Frequency2-R_{p2}, R_{p2}-R_{p1}, and Frequency2-Frequency1* with the same force at different lift-offs, as shown in Figure 4.12 and Figure 4.13, they reflected the response of the LC resonance sensors at the same loading but different lift-offs. To apply the separation method, it is required that the sensor outputs caused by forces and lift-offs are independent, implying that there are no intersection points between forces and lift-offs. However, Figure 4.12 (a) presents an intersection between 2 kN and 3.3 kN which could potentially result in no solution for the applied separation method. Figure 4.12 (b) shows multiple intersection points as the transverse LC resonance sensor was unable to distinguish forces and lift-offs due to the sensing direction. Fortunately, in Figure 4.13, *R_{p2}-R_{p1}*, and *Frequency2-Frequency1* planes show promising characteristics as each applied force at different lift-offs resulted in an independent output and there were no intersecting points. These characteristics were derived from the similarity between two LC resonance sensors as they had the same geometrical structure and dimensions. The dimensions of two LC resonance sensors were smaller than the size of the specimen, which minimized the edge effects due to eddy currents [69]. This meant both LC resonance sensors were simultaneously sensitive to the changes in lift-offs, causing their combined pattern to be nearly linear, as shown in Figure 4.13. Additionally, the difference in their sensing directions for forces resulted in one sensor being sensitive to force while the other was not. These importantly showed that the application of the separation method was achievable.

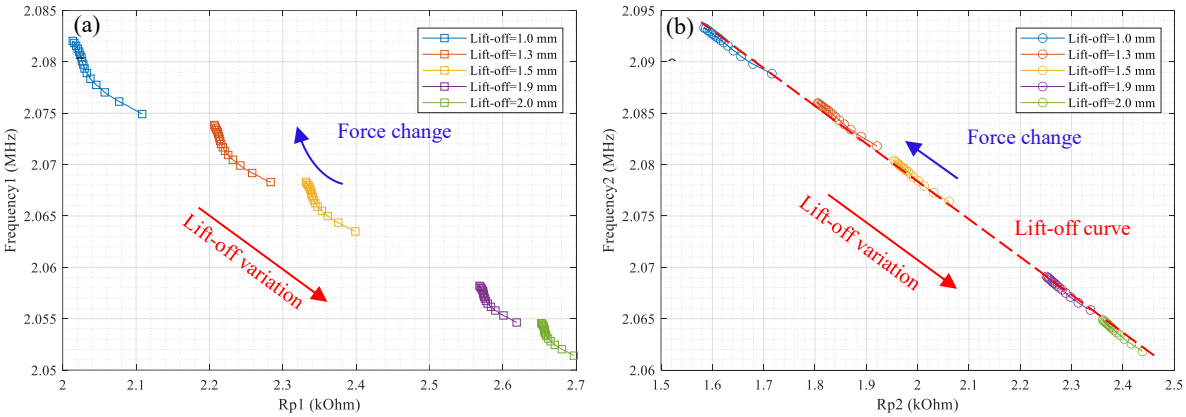

Figure 4.10 Force tests at different lift-offs (a) *Frequecny1*- R_{p1} plane of the vertical LC resonance sensor (parallel to the specimen), (b) *Frequecny2*- R_{p2} plane of the transverse LC resonance sensor (perpendicular to the specimen)

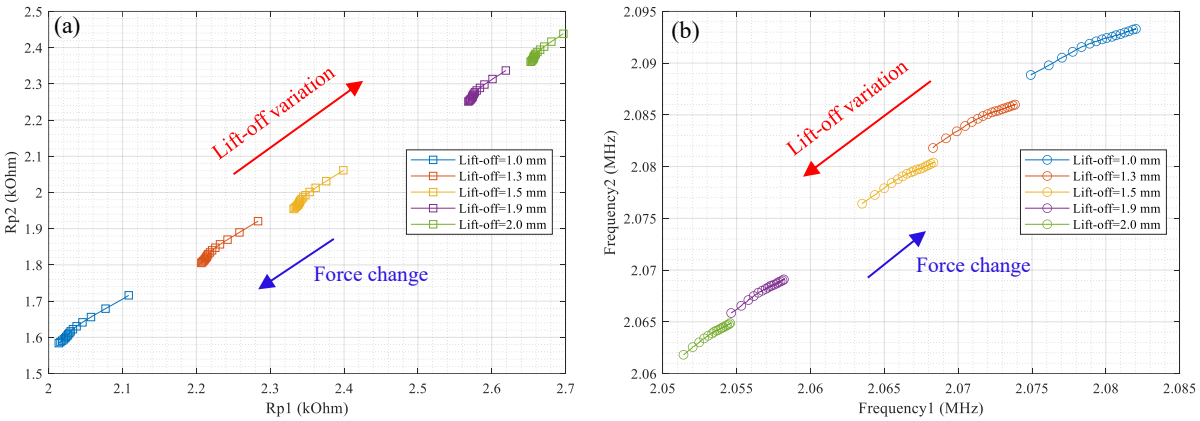

Figure 4.11 Force tests at different lift-offs (a) R_{p2}-R_{p1} plane (b) *Frequecny2-Frequecny1* plane

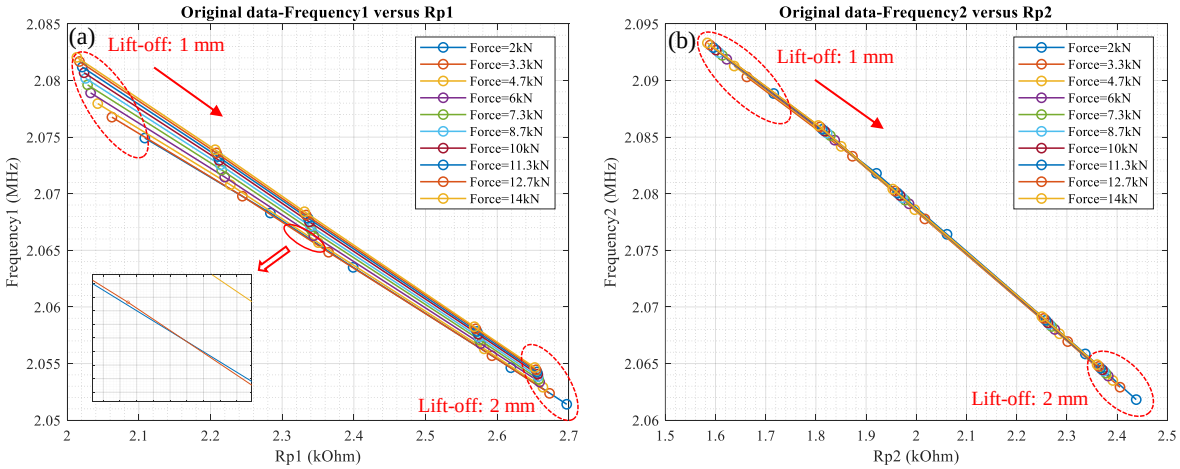

Figure 4.12 Plotting same force at different lift-offs (a) *Frequency1*-R_{p1} plane (b) *Frequecny2-Frequecny1* plane

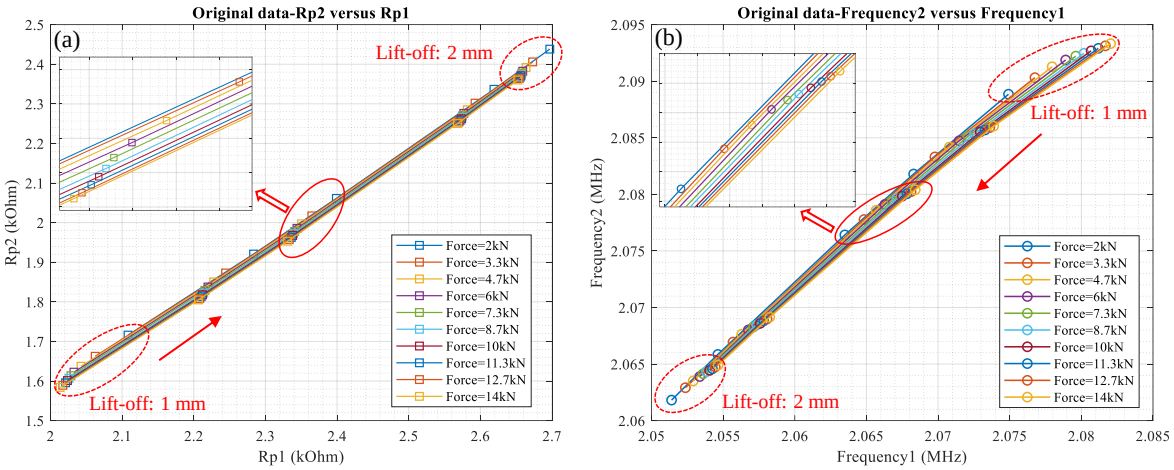

Figure 4.13 Plotting same force at different lift-offs (a) R_{p2}-R_{p1} plane (b) *Frequecny2-Frequecny1* plane

4.5.3 Separation of Forces and Lift-offs

R_{p2}-R_{p1}, and *Frequency2-Frequency1* planes were appropriate options for the separation of forces and lift-offs as they met the conditions of the separation method. Specifically, R_{p2}-R_{p1} in Figure 4.13 (a) had no intersection points, and the increase of forces shifted R_{p2}-R_{p1} curves towards bottom left while lift-off shifted the curves towards top right. *Frequency2-Frequency1* in Figure 4.13 (b) presents a reverse phenomenon. For a single applied force, the R_{p2}-R_{p1} curve or *Frequency2-Frequency1* curve appeared a straight line at different lift-offs, which meant the lift-off change was linear. For a certain lift-off, the R_{p2}-R_{p1} curve or *Frequency2-Frequency1* curve seemed to be quadratic. The fitting relationship between η_m and force was quadratic, and the relationship between ξ_m and lift-off was linear. Therefore, according to Figure 4.3, the data of R_{p2}, R_{p1}, *Frequency2*, and *Frequency1* were extracted as the calibration points at forces of 2 kN, 6 kN, and 14 kN and lift-offs of 1.0 mm, 1.5 mm, and 2.0 mm because these ranges covered the overall measurement range. Based on the calibration data, the remaining data were used in Equations (4.9) - (4.10) to solve ξ_m *and* η_m. Finally, the measurement points were mapped onto the transformed coordinate, and forces and lift-offs were calculated using Equations (4.11) - (4.12). Figures 4.14 and 4.15 show the transformed η and ξ for R_{p2}-R_{p1} and *Frequency2-Frequency1* in Figure 4.13, along with the forces and lift-offs accordingly. It can be observed that lift-offs and forces were effectively separated. The transformation of R_{p2}-R_{p1} for forces had a smaller error with the maximum relative error (RE) of 18.90% compared with that of *Frequency2-Frequency1* with the maximum relative error (RE) of 22.61%. These measurement errors can arise from the nonlinearity due to lift-off variations, and the material's inhomogeneity resulting from mechanical and heat treatment during fabrication [111], and the change in the specimen's permeability under force. Although this was neglected in our study because of high

frequencies, it still contributed to the sensor outputs, resulting in the errors. The transformation of lift-offs demonstrated tiny errors for both R_{p2}-R_{p1} with the maximum RE of 1.17% and *Frequecny2-Frequency1* with the maximum RE of 1.66%. The transformation results are presented in Tables 4.1 to 4.4. These results indicated that the proposed orthogonal LC resonance system combined with the separation method was effective for the measurement and separation of forces and lift-offs.

$$Force_measured = 2\eta_m^2 + 6\eta_m + 6 \tag{4.11}$$

$$Lift-off\_measured = 0.5(\xi_m - 1) + 2 \tag{4.12}$$

This study focused on the elastic region of the material and the measurement results were valid only within this region as the change in material properties within this region are reversible. The research outcomes using the separation approach are applicable within a lift-off range of 1 mm to 2 mm and a force range between 2 kN and 14 kN. Any measured lift-off and force outside of this range necessitates a new calibration which means the measurement range for both parameters should be known before testing. Calibration can be challenging in the practical application since it is unrealistic to control the loading force to meet the calibration conditions on the test objects. Considering that LC resonance sensors measure the material's electromagnetic properties, one potential approach is the manual fabrication of calibration blocks that represent approximate performance at the minimum and maximum ranges. The applied loading in the test is uniaxial that simplifies the modelling of practical wheel-rail contact forces. Force loading in multi-directions will be performed to further approach the complexity of the real system. The characteristics of the new combination ways are derived from the similarity between two LC resonance sensors, but they differ in their sensing direction to forces. This similarity means both sensors are sensitive to lift-offs, but the difference in sensing direction results in one being sensitive to force while the other is not. This distinction facilitates the application of the separation method. The current test involves applying forces that are parallel to the vertical LC resonance sensor, and the transverse is used as the auxiliary measurement. Similarly, if the force is applied along the transverse direction, the vertical LC resonance sensor is then used as the auxiliary measurement. The sensitivity and measurement range of LC resonance sensors are constrained by Equations (3.4) and (3.5) according to their mutual coupling correlations. Both R_{eqi} and L_{eqi} tend to stabilize at a certain value, despite continued increases in the applied force. Addressing this limitation can begin with the design of the LC resonance sensor and utilize special materials, such as metamaterials, to enhance the induced eddy currents and magnetic fields in the area of interest [207].

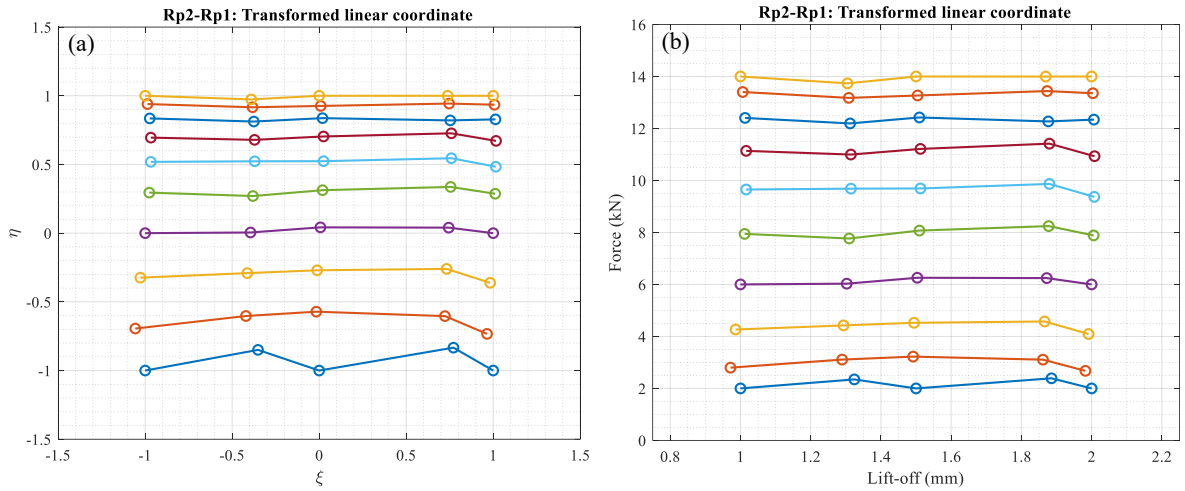

Figure 4.14 Separation results of R_{p2}-R_{p1} plane: (a) ξ and η, (b) Force and lift-off

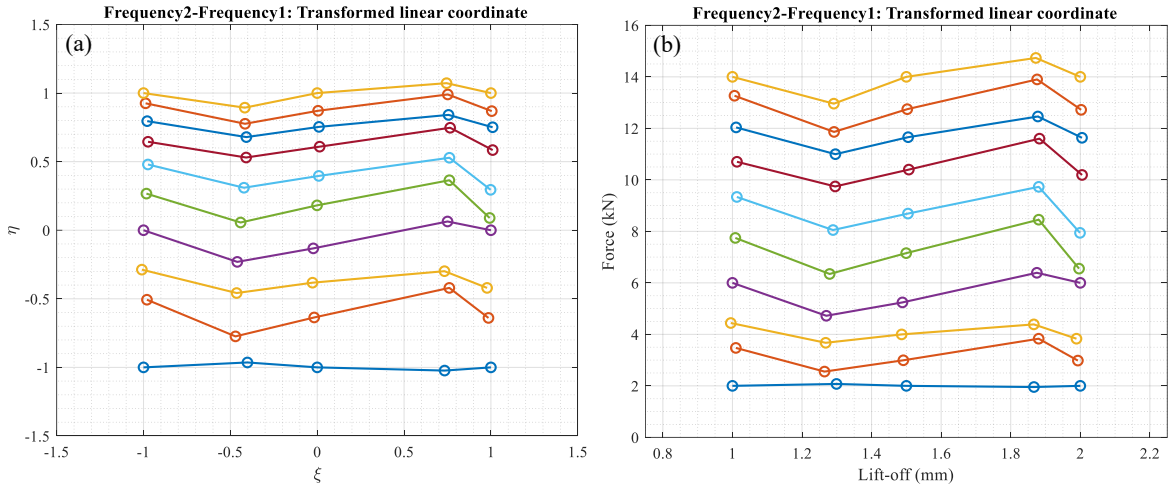

Figure 4.15 Separation results of Frequency2-Frequency1 (a) ξ and η, (b) Force and lift-off

Table 4.1 R_{p2}-R_{p1} force transformation results

	Lift-off = 1.0 mm		**Lift-off = 1.3 mm**		**Lift-off = 1.5 mm**		**Lift-off = 1.9 mm**		**Lift-off = 2.0 mm**	
A_Force * (kN)	M_Force (kN)	RE (%)	M_Force (kN)	RE (%)	M_Force (kN)	RE (%)	M_Force (kN)	RE (%)	M_Force (kN)	RE (%)
2.0000	2.0000	0.0000	2.3460	17.3003	2.0000	0.0000	2.3885	19.4263	2.0000	0.0000
3.3000	2.7987	15.1915	3.1089	5.7906	3.2239	2.3051	3.1065	5.8643	2.6763	18.8999
4.7000	4.2654	9.2467	4.4242	5.8677	4.5240	3.7451	4.5750	2.6592	4.0931	12.9137
6.0000	6.0000	0.0000	6.0294	0.4892	6.2568	4.2807	6.2443	4.0724	6.0000	0.0000
7.3000	7.9444	8.8273	7.7673	6.4020	8.0730	10.5893	8.2448	12.9426	7.8852	8.0168
8.7000	9.6520	10.9423	9.6849	11.3209	9.6925	11.4083	9.8671	13.4149	9.3688	7.6869
10.0000	11.1387	11.3866	10.9969	9.9687	11.2133	12.1333	11.4166	14.1660	10.9332	9.3325
11.3000	12.4059	9.7867	12.1941	7.9127	12.4237	9.9445	12.2716	8.5985	12.3410	9.2124
12.7000	13.4031	5.5364	13.1774	3.7587	13.2695	4.4839	13.4395	5.8227	13.3564	5.1682
14.0000	14.0000	0.0000	13.7357	1.8878	14.0000	0.0000	13.9982	0.0130	14.0000	0.0000

*A_Force represents: actual force; M_Force: measured force; RE: relative error; The bold parts are calibration points.

Table 4.2 R_{p2}-R_{p1} lift-off transformation results

	Lift-off = 1.0 mm		**Lift-off = 1.3 mm**		**Lift-off = 1.5 mm**		**Lift-off = 1.9 mm**		**Lift-off = 2.0 mm**	
A_Force * (kN)	mLift_off _(mm)	RE (%)	mLift_off _(mm)	RE (%)	mLift_off _(mm)	RE (%)	mLift_off _(mm)	RE (%)	mLift_off _(mm)	RE (%)
2.0000	1.0000	0.0000	1.3242	1.2099	1.5000	0.0000	1.8859	0.7074	2.0000	0.0000
3.3000	0.9715	0.8622	1.2894	0.3197	1.4918	0.2499	1.8614	1.1692	1.9824	0.5348
4.7000	0.9861	0.2952	1.2934	0.1401	1.4943	0.1217	1.8662	0.7192	1.9913	0.1846
6.0000	1.0000	0.0000	1.3026	0.0440	1.5036	0.0598	1.8723	0.4624	2.0000	0.0000
7.3000	1.0118	0.1615	1.3097	0.1327	1.5097	0.1329	1.8778	0.3044	2.0058	0.0799
8.7000	1.0161	0.1855	1.3147	0.1684	1.5126	0.1449	1.8798	0.2317	2.0077	0.0879
10.0000	1.0163	0.1627	1.3144	0.1442	1.5125	0.1247	1.8799	0.2008	2.0083	0.0830
11.3000	1.0131	0.1161	1.3122	0.1083	1.5095	0.0844	1.8766	0.2066	2.0065	0.0578
12.7000	1.0065	0.0511	1.3084	0.0662	1.5045	0.0355	1.8734	0.2094	2.0037	0.0288
14.0000	1.0000	0.0000	1.3048	0.0346	1.5000	0.0000	1.8694	0.2189	2.0000	0.0000

*mLift-off represents measured lift-off.

Table 4.3 *Freqency2-Frequency1* force transformation results

	Lift-off = 1.0 mm		**Lift-off = 1.3 mm**		**Lift-off = 1.5 mm**		**Lift-off = 1.9 mm**		**Lift-off = 2.0 mm**	
A_Force * (kN)	M_Force (kN)	RE (%)	M_Force (kN)	RE (%)	M_Force (kN)	RE (%)	M_Force (kN)	RE (%)	M_Force (kN)	RE (%)
2.0000	2.0000	0.0000	2.0742	3.7120	2.0000	0.0000	1.9545	2.2754	2.0000	0.0000
3.3000	3.4731	5.2442	2.5540	22.6067	2.9928	9.3099	3.8308	16.0836	2.9810	9.6658
4.7000	4.4405	5.5209	3.6720	21.8733	3.9973	14.9506	4.3866	6.6688	3.8308	18.4942
6.0000	6.0000	0.0000	4.7215	21.3077	5.2406	12.6568	6.3906	6.5101	6.0000	0.0000
7.3000	7.7440	6.0819	6.3449	13.0842	7.1532	2.0112	8.4519	15.7797	6.5523	10.2431
8.7000	9.3353	7.3025	8.0503	7.4677	8.6898	0.1168	9.7281	11.8173	7.9414	8.7194
10.0000	10.7015	7.0147	9.7431	2.5686	10.3979	3.9792	11.5991	15.9914	10.1899	1.8989
11.3000	12.0365	6.5176	10.9961	2.6895	11.6565	3.1551	12.4601	10.2666	11.6326	2.9431
12.7000	13.2656	4.4538	11.8614	6.6032	12.7440	0.3462	13.8995	9.4447	12.7191	0.1505
14.0000	14.0000	0.0000	12.9584	7.4397	14.0000	0.0000	14.7335	5.2395	14.0000	0.0000

Table 4.4 *Frequency2-Frequency1* lift-off transformation results

	Lift-off = 1.0 mm		**Lift-off = 1.3 mm**		**Lift-off = 1.5 mm**		**Lift-off = 1.9 mm**		**Lift-off = 2.0 mm**	
A_Force * (kN)	mLift_off _(mm)	RE (%)	mLift_off _(mm)	RE (%)	mLift_off _(mm)	RE (%)	mLift_off _(mm)	RE (%)	mLift_off _(mm)	RE (%)
2.0000	1.0000	0.0000	1.2991	0.0435	1.5000	0.0000	1.8668	1.6623	2.0000	0.0000
3.3000	1.0098	0.2975	1.2647	1.0696	1.4913	0.2632	1.8804	0.5949	1.9931	0.2099
4.7000	0.9952	0.1018	1.2680	0.6799	1.4865	0.2880	1.8664	0.7146	1.9890	0.2336
6.0000	1.0000	0.0000	1.2699	0.5021	1.4888	0.1875	1.8752	0.4138	2.0000	0.0000
7.3000	1.0084	0.1146	1.2795	0.2815	1.4995	0.0069	1.8805	0.2673	1.9965	0.0486
8.7000	1.0127	0.1457	1.2891	0.1249	1.5046	0.0523	1.8806	0.2230	1.9992	0.0096
10.0000	1.0130	0.1303	1.2954	0.0461	1.5070	0.0702	1.8827	0.1730	2.0051	0.0511
11.3000	1.0106	0.0936	1.2960	0.0355	1.5051	0.0451	1.8780	0.1943	2.0049	0.0437
12.7000	1.0059	0.0466	1.2922	0.0616	1.5026	0.0202	1.8759	0.1900	2.0025	0.0198
14.0000	1.0000	0.0000	1.2915	0.0609	1.5000	0.0000	1.8723	0.1977	2.0000	0.0000

4.6 Chapter Summary

In this chapter, an LDC-based orthogonal LC resonance sensing system combined with an 8-node quadrilateral interpolation method was proposed to achieve the measurement and separation of forces and lift-offs in the ferromagnetic sample. The force tests at different lift-offs were carried out using the tensile testing machine and the LDC-based orthogonal LC resonance sensor. The following conclusions are drawn from this study:

1) The proposed LDC-based measurement system integrates two LDC1101s and a multiplexer into a single measurement board. The orthogonal LC resonance sensor is fabricated on an 8-layer PCB board, consisting of two LC resonance sensors positioned in perpendicular directions. The system employs time division and grounding processing to allow two LC resonance sensors to work sequentially with minimum interference. This approach not only reduces the sensor size but also enables the measurement of multiple parameters in different directions. The system offers advantages such as low cost, capability of measuring multiple parameters, low power consumption, and fast response.
2) Unlike traditional impedance planes and *Frequency*-R_p planes, a new combination pattern named R_{p2}-R_{p1}, *Frequency2-Frequency1* planes, which incorporates force and lift-off information in both the vertical and transverse directions, is utilized for separation of forces and lift-offs.

3) The experimental results indicate that forces and lift-offs are measured effectively. Through the 8-node isoparametric coordinate transformation, the loading force and lift-off are separated respectively, with the maximum relative error of 22.61% for forces and 1.66% for lift-offs.

The ESP32S3 also provides an IoT interface to enable measurement data to transmit to the cloud platform and visualize the real-time data, as one part of structural health monitoring on future wheel-rail forces in high-speed railways.

This chapter addressed the separation of the force and lift-off, but the lift-off was limited to under 2 mm, which may pose a challenge in practical installation by increasing the risk of contact between the sensor and the testing objects, potentially causing damage to the sensor. The next chapter will investigate the enhancement in lift-off and force measurement sensitivity using semiconductor strain gauge, magnetic resonance coupling, and the developed LDC1101-based measurement system.

Chapter 5. MRC-LDC Based Impedance Sensing with Semiconductor Strain Gauges for Force Measurement at High Lift-offs

This chapter introduces a novel approach to wireless force measurement (WFM) based on impedance sensing through magnetic resonant coupling (MRC), coupled with a semiconductor strain gauge (SSG), and measured by a developed inductance to digital converter (LDC)-based system. Section 5.2 describes the methodology of applying MRC-WPT coupled with an SSG for force measurement. Section 5.3 presents simulations using LT-Spice to investigate the influence of SSG at various coupling coefficients using parallel-parallel (PP) and series-parallel (SP) MRC topologies. In section 5.4, experimental studies are conducted compare the traditional SG and SSG and PP and SP topologies at various lift-offs and SSGs. Additionally, the response and sensitivity of the two topologies were analysed regarding different lift-offs and SSGs. The results are then discussed. The final section concludes the work and outlines future work.

5.1 Introduction

Many scholars have made significant advancements in WFM. Table 5.1 lists the existing WFM methods, especially for applications on metal components. Radio frequency identification (RFID)-based methods have been broadly applied in WFM based on their excellent capability in power and data transfer [35, 45, 47, 48]. A force sensor was integrated with an RFID tag, signal conditioning circuits, and a microcontroller for WFM [35]. The RFID tag harvested energy from an RFID reader to activate the sensor system. Then sensor data was processed by the microcontroller and transmitted wirelessly by the RFID tag's antenna. Since these methods operate at ultra-high frequency (UHF), signal transmission is based on far-field electromagnetic radiation, allowing communication over long distances, up to several meters. However, RFID readers are usually large, limiting their use in confined spaces. Also, RFID tags operate at high frequencies, and they are more susceptible to electromagnetic interference (EMI) and environmental factors such as temperature and humidity [34]. Apart from far-field RFID-based WFM, substantial research focuses on near-field inductive sensing for WFM [126, 208]. Li *et al.* designed a wireless passive flexible inductor-capacitor (LC) strain sensor using aluminium nitride film for rolling bearings where a readout coil connected to a vector network analyser (VNA) was employed to measure the resonant frequency of this LC sensor in response to strain, offering the advantages of small size and high resolution [127]. A battery-less and wireless strain sensor made with stretchable silicone rubber and a serpentine coil was presented in [209], which monitored the shift in resonant frequency caused by stomach mobility. Although these

methods offer new insights into WFM, the signal readout approach requires an expensive and bulky VNA, which hinders the achievement of low cost and portability. Besides, the measurement time is also prolonged due to the need for frequency sweeping to obtain the resonant frequency [210].

Table 5.1 Comparison of WFM methods, especially for metal applications

Literature	Method	Parameter	Merit	Limitation
Wu *et al.* [18]	SG, Wheatstone bridge, slip ring	Resistance	Direct measurement	Wired connection, complicated signal transmission system
Li *et al.* [127] Lee *et al.* [209]	Stretchable LC strain sensor + Readout coil + VNA	f_{res}	Wireless/passive	Unable to apply on metal, expensive measurement device, frequency sweeping
Cui *et al.* [35] Cheng *et al.* [48]	SG + MCU + RFID Antenna + Reader	Resistance	Wireless/accurate Long distance (up to 5 m) Power supply requirement	Complicated circuit, and bulky reader, frequency sweeping
Yi *et al.* [45] Kuhn *et al.* [47]	RFID-based strain antenna+ RFID reader	f_{res}	Wireless Long distance, tens of cm	Susceptible to EMI and bulky system
Wang *et al.* [17]	Digital image correlation technology	Strain at space fixed points	Non-contact	Expensive device, complicated image processing
Yang *et al.* [191, 211]	LC resonance sensor + LDC (eddy current effects)	R_{Peq}, f_{res}	Non-contact, able to measure material's properties	Low lift-off (<2mm), low sensitivity
This work	SSG (deformation) + MRC + LDC	R_{Peq}, f_{res}	Wireless/low cost/portable/fast measurement/miniaturization/suitable for metal objects/high lift-off (up to 40 mm)	Lift-off interference and misalignment (coupling coefficient)

Considering cost, portability and measurement time, a miniaturized, low-cost, and portable measurement system is needed. The previous research demonstrated the feasibility of utilizing LC resonance sensors with an LDC-based measurement system to realize non-contact force measurement [191]. This was accomplished by sensing variations in the electromagnetic properties of the specimen under applied forces. The LDC-based system integrated both the resonant driver and the frequency measurement unit into a single chip with the size of 3.8 mm * 3.8 mm * 0.8 mm [163]. It only requires a small microcontroller and several passive components to compose a complete system, providing advantages such as miniaturization, portability, and low power consumption in comparison to those systems composed of discrete components, such as a signal generator, oscilloscope, power amplifier, and signal conditioning circuits. The measurement and separation of forces and lift-offs (the distance between the sensor

and the test object), were also investigated by the proposed orthogonal LC resonance sensor and 8-node isoparametric coordinate transformation, effectively achieving the separation of forces and lift-offs within 14 kN and 2 mm [211]. However, as they relied on electromagnetic induction, their effective lift-offs were restricted to less than 2 mm. This limitation could lead to sensors contacting the measured objects in real-world applications due to vibration or irregular movement, potentially damaging sensors. Therefore, it is necessary to find a way to extend lift-offs. The utilization of wireless power transfer (WPT) concepts can offer a potential solution [143, 144, 212].

The medium-range magnetic resonant coupling WPT (MRC-WPT) [212] consists of a transmitter coil, a receiver coil, and a capacitive compensation network, which has garnered significant attention due to its high transfer efficiency and greater transmission distance compared to other WPT methods. An MRC-WPT system comprises two LC tanks—one for the transmitter (Tx) and another for the receiver (Rx). Most research scholars concentrate on topics related to energy transmission efficiency [213], distance enhancement [149], coil misalignment [214], cross-coupling [215], frequency splitting [216] and smart multi-receiver system [217]. However, there is limited research investigating WPT-based sensing.

In terms of sensing or signal transmission, MRC-WPT can achieve extended measurement distances when not used for energy transfer. This chapter demonstrates a novel impedance sensing approach using SSG, MRC-WPT, and a developed LDC-based measurement system to achieve WFM and extend the lift-off. The proposed approach employs two LC tanks (Rx and Tx) integrated with the SSG and LDC-based system. The SSG is connected to Rx and responds to changes in force, resulting in a change in the impedance of Rx. Through MRC, this change in Rx's impedance is reflected in the impedance of Tx. The use of SSG is a crucial factor due to its high gauge factor compared to metal foil strain gauges, resulting in a relatively significant change in impedance and enhanced sensitivity. The LDC-based system measures the real part (equivalent parallel impedance R_{Peq}) and imaginary part (resonant frequency f_{res}) of Tx's impedance. This approach fully employs the extended distance capability of MRC-WPT, the high gauge factor of the SSG, and the low cost and fast response of the developed LDC-based measurement system, achieving significantly longer lift-off measurements compared to the previous work [191, 211]. The achievements of this chapter can be summarized as:

1) The high sensitivity of the SSG, transmission characteristics of MRC, and an integrated LDC-based system were utilized to achieve WFM ranging from 2 kN to 14 kN, with a maximum lift-off up to 40 mm. This approach surpasses the limitations of using only an

LC resonance sensor for force measurement, which has a maximum lift-off of 2 mm. Both the simulation and experimental results showed good agreement.

2) The use of traditional SG and SSG for WFM were compared. The latter exhibited a higher response than the former, approximately 32 times greater for R_{Peq} and 59 times greater for f_{res}.

3) The sensitivity of PP and SP topologies at different lift-offs and SSG values R_{str} was analysed, highlighting that optimal sensitivity is not only related to lift-offs and topologies but also to SSG values. Overall, the SP topology has a more comprehensive working range than the PP topology.

5.2 Methodology

This section presents the principle of MRC-WPT-based impedance sensing for force measurement. Formulas related to the PP and SP topologies of MRC-WPT models are derived.

5.2.1 Principle of MRC-WPT-based Impedance Sensing

As shown in Figure 5.1 (a), MRC-WPT-based impedance sensing utilizes the resistance change in an SSG caused by force, which affects the impedance of Rx. This change is then reflected to the Tx side via magnetic coupling. The Tx is connected to an LDC-based system to measure the equivalent parallel resistance R_{Peq} and resonant frequency f_{res} that are related to the Tx's impedance. As the LDC-based system requires the LC tank to be parallel, the Tx side is configured for a parallel connection. Figure 5.1 (b) and (c) show the equivalent circuit models of PP and SP topologies connected to the SSG R_{str}. The only difference is on the Rx side, where the PP topology features a parallel connection between R_{str}, the capacitor C_t, and the equivalent circuit of an inductor coil that includes a series resistance R_t and series inductance L_t. In contrast, in the SP topology, all the components are connected in series. Figure 5.1 (d) illustrates how the reflected impedance Z_r couples from the PP/SP topology to the Tx side [147], and the LDC-based measurement system is shown in Figure 5.1 (e).

In addition, the presence of metallic materials can cause the coils on the Tx and Rx sides to induce eddy currents in the specimen, which may affect the signal sensing and transmission [185]. It is imperative to minimize the influence of eddy currents. Electromagnetic interference shielding (EMI) structures can suppress these eddy currents by isolating the Tx/Rx coil from metal objects and focusing the magnetic fields between the Tx and Rx coils [218]. This work differs from the previous research, which heavily relied on eddy currents in the specimen to characterize the electromagnetic properties (electrical conductivity σ and permeability μ) in

response to forces [211]. However, the intensity of eddy currents is strongly related to the lift-off. An increase in the lift-off results in an exponential decrease in the intensity, causing to a low sensitivity in testing [219]. To address this challenge, we employ an SSG as a force sensor and transform its variation into the impedance change via MRC-WPT. This approach enables wireless sensing and long-distance transmission for force measurement.

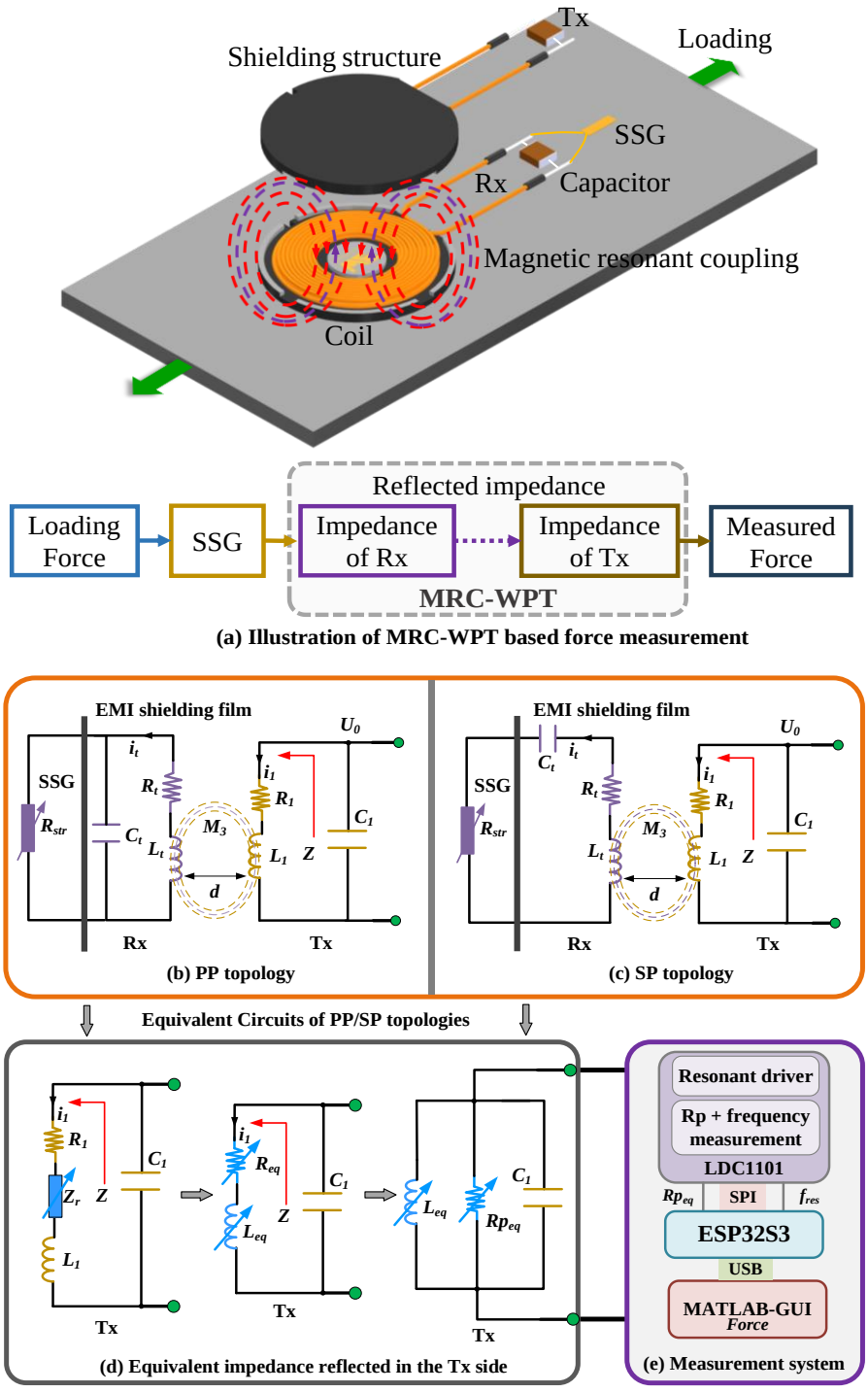

Figure 5.1 (a) Illustration of MRC-WPT-based impedance sensing for force measurement (b) PP topology (c) SP topology (d) Equivalent impedance reflected in the Tx side (e) The LDC-based measurement system

5.2.2 Formula Derivation of PP/SP Topology

Based on Kirchhoff's circuit laws, the circuits in Figure 5.1 can be further derived and simplified. The impedance of Rx (Z_{Rx}) in terms of the PP topology, is derived as follows:

$$\mathrm{Z}_{Rx} = \frac{1}{j\omega C_t} // R_{str} + (R_t + j\omega L_t) = \frac{R_{str}}{1 + j\omega C_t R_{str}} + R_t + j\omega L_t \tag{5.1}$$

For the SP topology, Z_{Rx} is given as:

$$\mathrm{Z}_{Rx} = \frac{1}{j\omega C_t} + R_{str} + (R_t + j\omega L_t) \tag{5.2}$$

The reflected impedance Z_r is expressed as [147]:

$$\mathrm{Z}_r = \frac{\omega^2 M^2}{\mathrm{Z}_{Rx}} \tag{5.3}$$

Where ω is the angular frequency and M is the mutual inductance between the Tx coil and Rx coil, k is the coupling coefficient dependent on the lift-off (the distance between two coils) and M is described as:

$$M = k\sqrt{L_t L_1}\ (0 < k < 1) \tag{5.4}$$

The impedance of Tx (Z_{Tx}) after combing Z_r together is written as:

$$\mathrm{Z}_{Tx} = \frac{1}{j\omega C_1} // (R_1 + j\omega L_1 + \mathrm{Z}_r) = \frac{1}{j\omega C_1} // Z \tag{5.5}$$

Where Z is the equivalent impedance from the Tx coil's point view, it is equal to:

$$Z = R_1 + j\omega L_1 + \mathrm{Z}_r = R_1 + j\omega L_1 + \frac{\omega^2 M^2}{\mathrm{Z}_{Rx}} \tag{5.6}$$

For the PP topology, Z is derived as (5.7):

$$\begin{aligned} Z = {} & R_1 + j\omega L_1 \\ & + \frac{\omega^2 M^2}{\left(R_t + R_{str}(1 - \omega^2 L_t C_t)\right)^2 + \omega^2 (L_t + C_t R_{str} R_t)} \Big(R_{str} + R_t \\ & + \omega^2 {C_t}^2 R_t {R_{str}}^2 + j\omega \left({R_{str}}^2 C_t (1 - \omega^2 L_t C_t) - L_t \right) \Big) \\ = {} & R_1 + \frac{\omega^2 k^2 L_1 L_t}{\left(R_t + R_{str}(1 - \omega^2 L_t C_t)\right)^2 + \omega^2 (L_t + C_t R_{str} R_t)} \left(R_{str} + R_t + \omega^2 {C_t}^2 R_t {R_{str}}^2 \right) \\ & + j\omega \left(L_1 + \frac{\omega^2 k^2 L_1 L_t \left({R_{str}}^2 C_t (1 - \omega^2 L_t C_t) - L_t \right)}{\left(R_t + R_{str}(1 - \omega^2 L_t C_t)\right)^2 + \omega^2 (L_t + C_t R_{str} R_t)} \right) \\ = {} & R_{eq} + j\omega L_{eq} \end{aligned} \tag{5.7}$$

Similarly, Z in the SP topology is derived as (5.8):

$$Z = R_1 + j\omega L_1 + \frac{\omega^2 M^2}{R_{str} + R_t + j\left(\omega L_t - \frac{1}{\omega C_t}\right)}$$

$$= R_1 + \frac{\omega^2 k^2 L_1 L_t (R_{str}+R_t)}{(R_{str}+R_t)^2 + \left(\omega L_t - \frac{1}{\omega C_t}\right)^2} + j\omega\left(L_1 - \frac{\omega^2 k^2 L_1 L_t (L_t - \frac{1}{\omega^2 C_t})}{(R_{str}+R_t)^2 + \left(\omega L_t - \frac{1}{\omega C_t}\right)^2}\right) \quad (5.8)$$

$$= R_{eq} + j\omega L_{eq}$$

Thus, the equivalent parallel resistance R_{Peq} of the Tx is:

$$R_{Peq} = \frac{L_{eq}}{R_{eq} C_1} \quad (5.9)$$

The resonant frequency f_{res} is expressed as:

$$f_{res} = \frac{1}{2\pi\sqrt{L_{eq} C_1}} \quad (5.10)$$

Equations (5.1) - (5.10) illustrate how the resistance of an SSG, R_{str}, affects the impedance of Rx (Z_{Rx}), the reflected impedance Z_r and subsequently the impedance of Tx (Z_{Tx}). The LDC-based system then measures the real and imaginary parts of Z_{Tx}, represented by R_{Peq} and f_{res}, which are then measured by the LDC-based system.

5.3 Simulation

In this section, circuit modelling was conducted using LT-Spice to investigate the MRC-WPT coupling coefficients for PP/SP topologies with and without an SSG, the phenomenon of frequency splitting, and the influence of an SSG on the impedance of Tx.

5.3.1 PP/SP without SSG: Coupling Coefficient and Frequency Splitting

To investigate the influence of an SSG on MRC-WPT circuit models, a model without an SSG was constructed, consisting of only two LC tanks: one representing Rx on the left side and the other for Tx on the right side. Rx consisted of a 470 pF capacitor (C_t), a 10 µH inductor (L_t), and a series resistor R_t of 0.5 Ω, as shown in Figure 5.2 (a). Tx had the same components as Rx. Each LC tank corresponded to a resonant frequency of 2.3215 MHz. An AC analysis was employed to simulate the impedance-frequency characteristics. The coupling coefficient k was varied from 0 to 0.1 with a step of 0.025, representing changes in the lift-off, while the frequency was swept from 2.15 MHz to 2.5 MHz in 100 Hz increments.

Figure 5.2 (b) illustrates the impedance-frequency characteristic of Z_{Tx} at different coupling coefficients. As the coupling coefficient k increased, indicating a decrease in the distance between Tx and Rx coils, the phenomenon of frequency splitting occurred. This phenomenon exhibited the single resonant peak of the system was split into two distinct peaks when the

coupling coefficient k was beyond a critical point, leading to variations in the resonant frequency and phase [216]. Frequency splitting affected the transmission distance and energy transfer efficiency of the system. In a WPT system, frequency splitting should be avoided through careful design, proper parameter selection, and advanced control algorithms in a WPT system [216, 220].

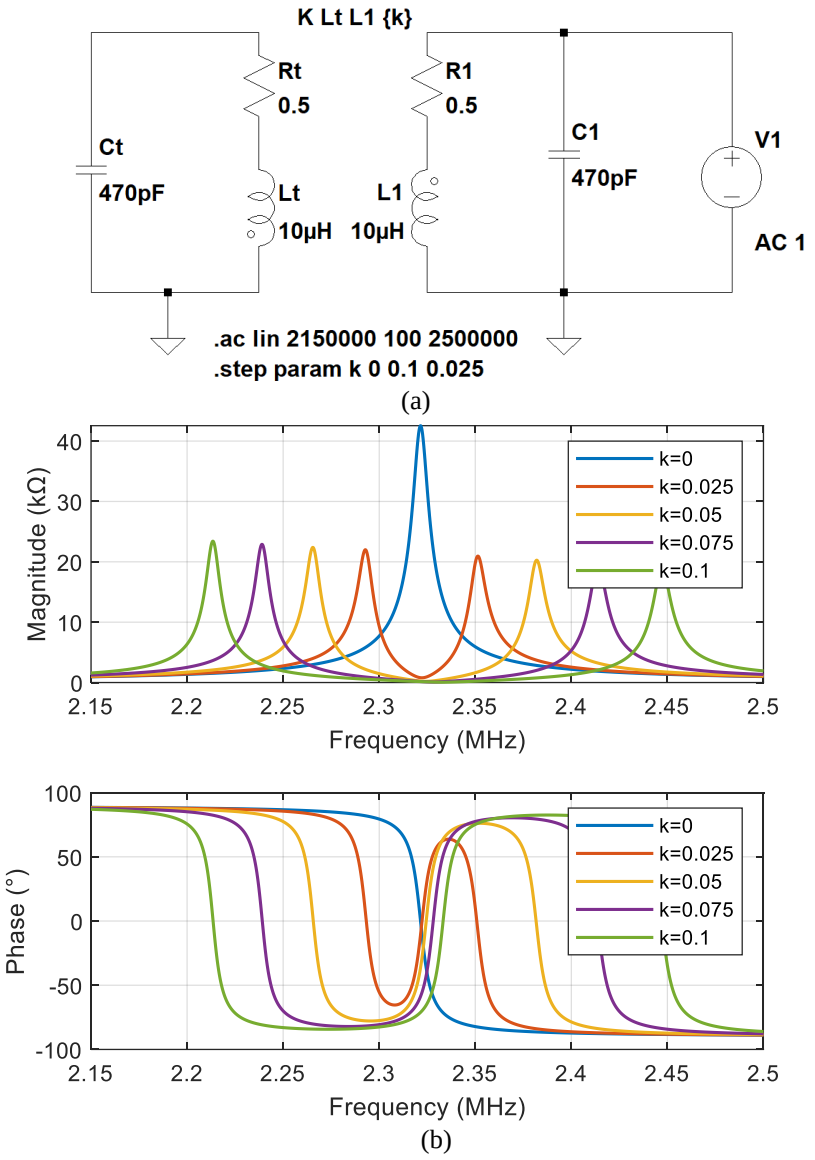

Figure 5.2 (a) MRC-WPT based circuit modelling without an SSG (b) Impedance of Tx without an SSG

5.3.2 PP/SP with SSG at Different Coupling Coefficients

Unlike Figure 5.2, which did not include an SSG, an SSG with a resistance of 350 Ω, denoted as R_{str}, was added to both the PP and SP topologies, as shown in Figure 5.3 (a) and (c). The coupling coefficients and frequency range remained the same as before. The simulation results are presented in Figure 5.3 (b) and (d). In contrast to Figure 5.2 (b), where frequency splitting

was observed, the setups here did not exhibit any frequency splitting. In the PP topology, the magnitude decreased as k increased because the increase in k caused R_{eq} to rise, which in turn lead to a decrease in R_{Peq}. The resonant frequency shifted to the right due to a decrease in L_{eq}. It can be explained by Equation (5.7) where L_{eq} was smaller than L_1 after the sweeping frequency exceeded the original resonant frequency $f_{res0} = 1/2\pi\sqrt{L_1C_1}$. A similar trend of magnitude was observed in the SP topology. Nevertheless, the resonant frequency remained unchanged, which can be attributed to the fact that L_{eq} in Equation (5.8) is equal to L_1 at f_{res0}. In both topologies, the phase curves gradually became flat as k continued to rise, and they passed through a common point at f_{res0}. That intersection point was similar to the lift-off point of intersection (LOI) in eddy current testing (ECT) [195].

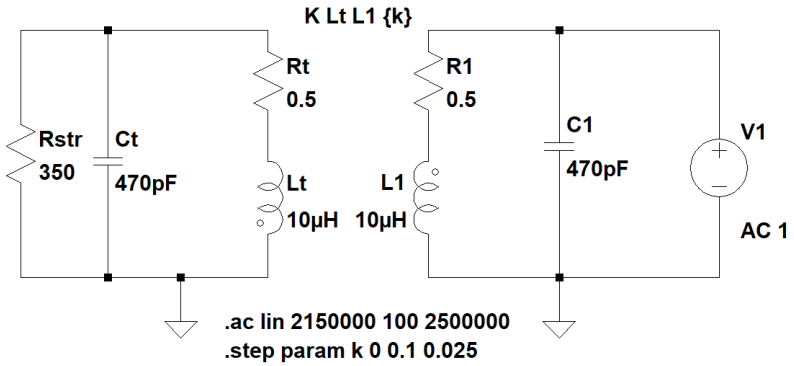

(a)

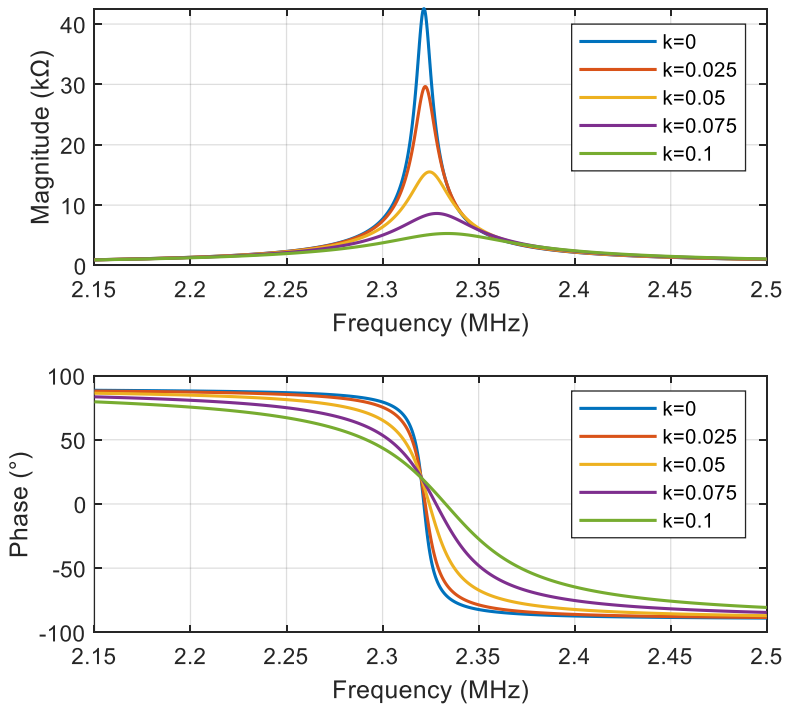

(b)

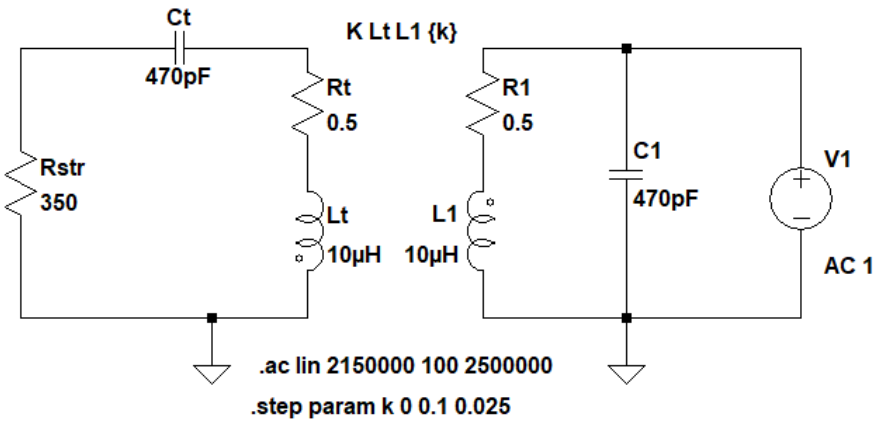

(c)

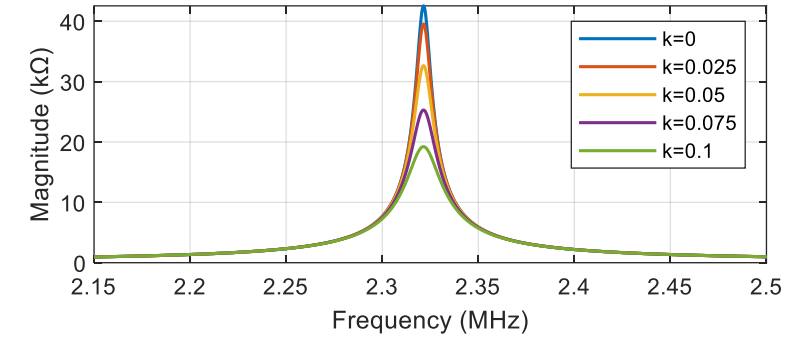

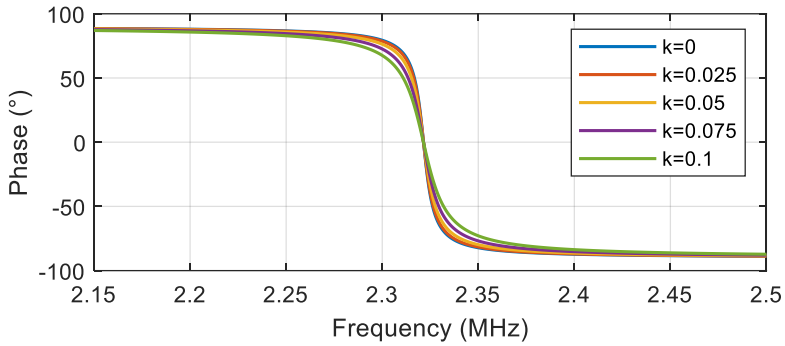

(d)

Figure 5.3 MRC-WPT-based circuit modelling for (a) PP topology (b) PP-Impedance of Z_{Tx} (c) SP topology (d) SP-Impedance of Z_{Tx}

5.3.3 Variation of SSG R_{str}

The simulation results in the previous sub-section demonstrated that frequency splitting did not occur at the designated coupling coefficients for both PP and SP topologies after adding the SSG. To understand the influence of the SSG on the Tx's impedance, the changes in SSG resistance for both topologies were simulated. Since the SSG resistance value was proportional to the force, R_{str} was set to vary from 350 Ω to 400 Ω with a step of 10 Ω, imitating that an increasing force was applied to the SSG. The coupling coefficient k was fixed at 0.1. Figures 5.4 (a) and (b) illustrate the change in the impedance of the Tx due to R_{str}. As the R_{str} increased, the magnitude decreased in the PP topology but increased in the SP topology. The maximum

value of the magnitude was extracted for both topologies. The resonant frequency corresponding to the maximum magnitude did not change because of the weak coupling with k of 0.1. In this coupling range, the contribution of the change in R_{str} for the imaginary part could be neglected.

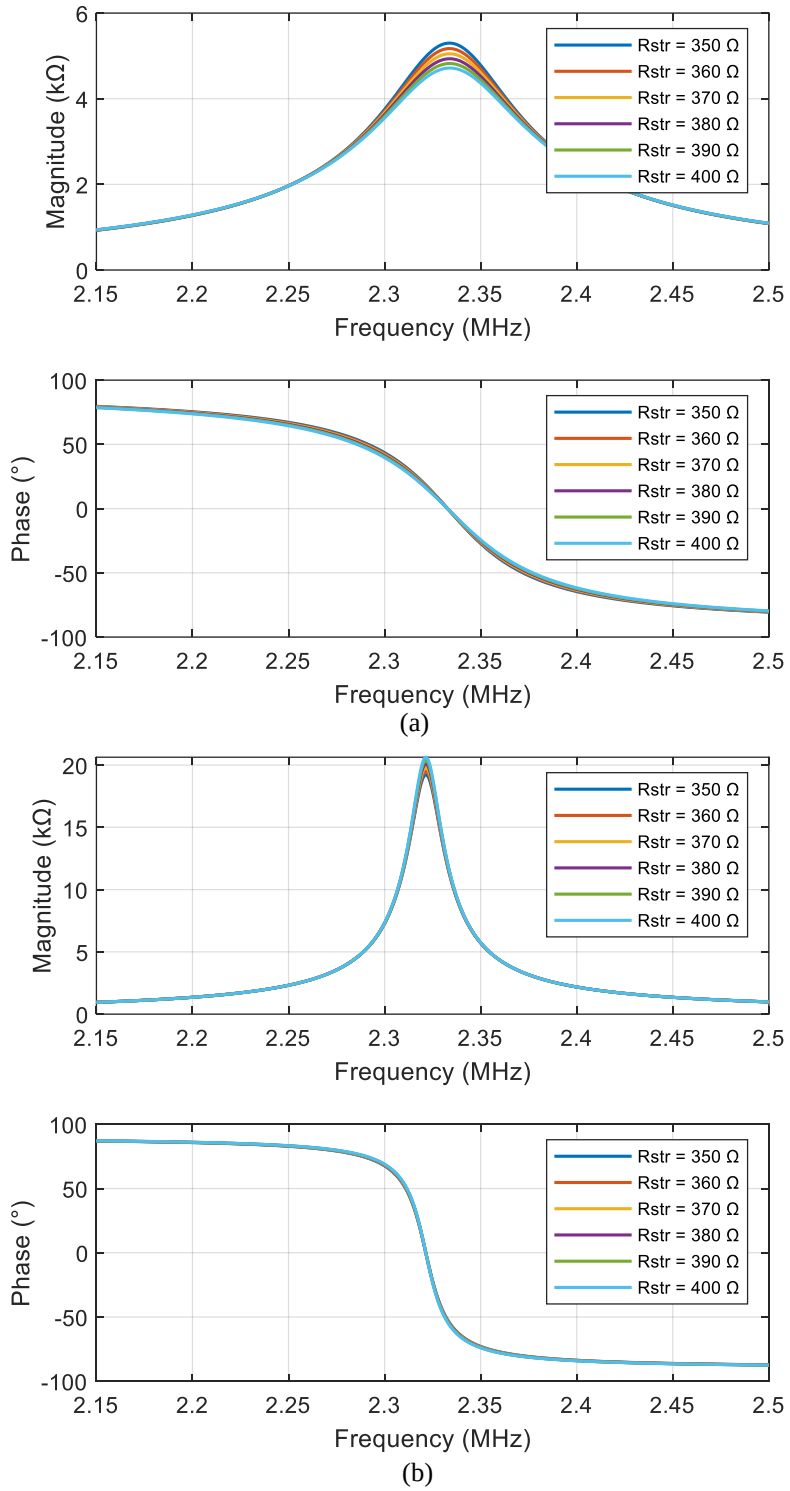

Figure 5.4 Variation of R_{str} for the influence of the Tx's impedance: (a) PP topology. (b) SP topology

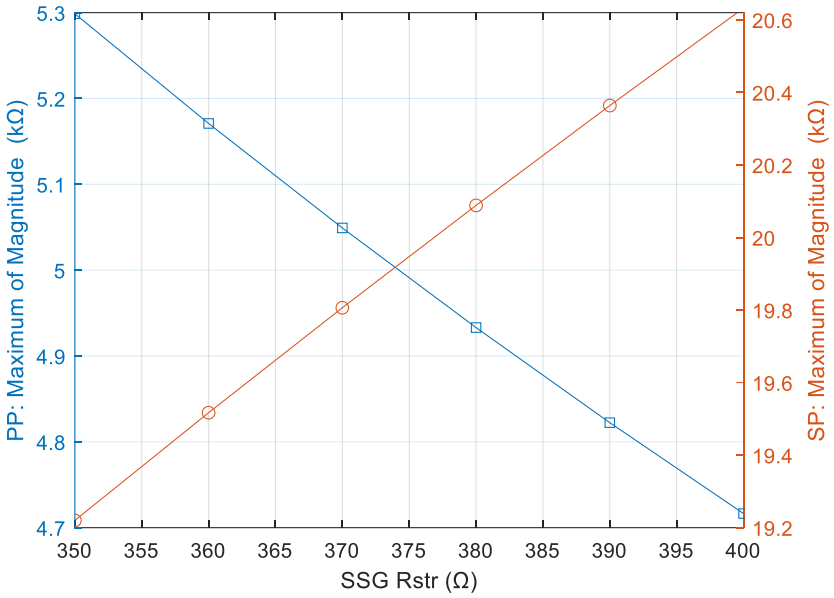

Figure 5.5 The extracted maximum of magnitude against SSG R_{str}

The phase information of both topologies remained almost unchanged with the variation of R_{str}. Figure 5.5 presents a linear relationship between the maximum of magnitude and the SSG in the PP and SP topologies, illustrating that employing an SSG coupled to MRC-WPT models for WFM is feasible.

5.4 Experimental Study and Results

This section describes the experimental study and results, including the experimental set-up, the measurement system based on LDC1101 and ESP32S3 for R_{Peq} and f_{res}, the SSG, MRC-WPT components, the comparison of a traditional SG and SSG, tensile testing results for PP/SP topologies with different SSGs and lift-offs, and a subsequent discussion.

5.4.1 Experimental Set-up

The experimental set-up included a testing machine INSTRON 3369, an LDC1101-ESP32S3 measurement system, an SSG, two MRC-WPT LC tanks, and a carbon steel C50 dog-bone specimen, as shown in Figure 5.6 (a) and (b). The testing machine was used to load the specimen in line with the pre-configuration. Here, a 2 kN pre-load was applied to remove any slack resulting from the grips, ensuring accurate and reliable measurements [221]. To implement repeatability tests, the loading force was kept within the elastic region. The loading then increased from 2 kN to 14 kN and was held for 30 seconds, followed by unloading from 14 kN back to 2 kN, as shown in Figure 5.6 (c). The speed of the crosshead was set at 0.5 mm/min.

Unlike simulations and most systems that rely on a bulky and expensive VNA to obtain the maximum of magnitude and resonant frequency through frequency sweeping [152, 153], our

system can directly measure the impedance characteristics in the resonant state, specifically R_{Peq} and f_{res}. It offered low-cost, portable, and time-saving benefits. The system consisted of an inductance-to-digital converter LDC1101 (Texas Instruments) [178], which supported an LC tank with a f_{res} range of 500 kHz to 10 MHz, an R_{Peq} range of 0.75 kΩ to 96 kΩ, and a 180 kSPS conversion rate. The LDC1101 was controlled by an IoT-level microcontroller, the ESP32S3 (Espressif Systems), via 4-wire SPI communications. Both R_{Peq} and f_{res} measurements achieved a 16-bit resolution. The mechanism of the readout system is the LDC-based system outputs a high-frequency pulse signal to drive the Tx, causing it to resonate at its resonant frequency. The resonant frequency f_{res} is then measured by counting the number of cycles of a reference frequency, similar to the principle of frequency meter. Meanwhile, R_{Peq} is measured by regulating the oscillation amplitude in a closed-loop configuration to a constant level while monitoring the energy dissipated by the Tx. Any change in R_{eq} and L_{eq} incurred by the SSG due to force will lead to a change in R_{Peq} and f_{res}.

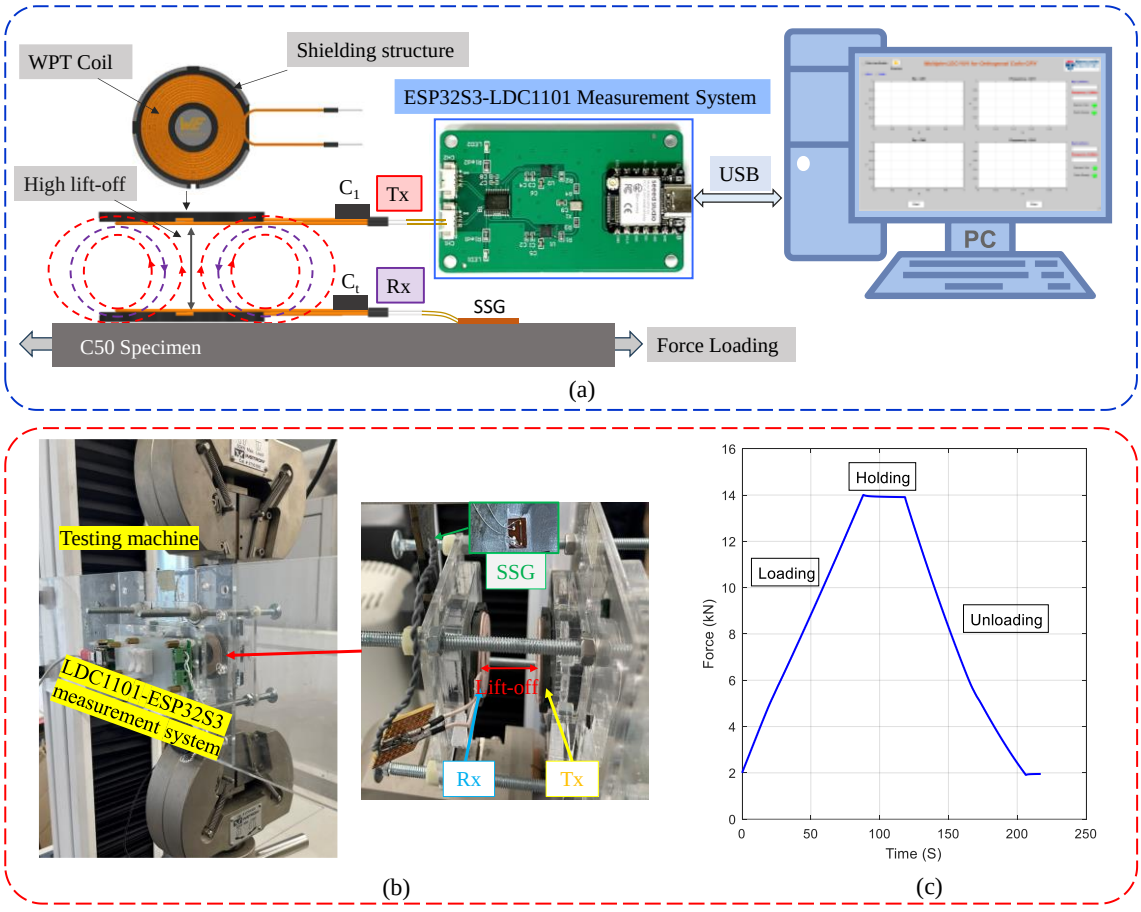

Figure 5.6 (a) System diagram of MRC-WPT-based impedance change for force measurement (b) Experimental set-up (c) Force loading, holding, and unloading curves

An SSG force sensor (5mm x 0.25 mm x 0.25 mm, manufactured by BENGBU KECHUANG SENSOR CO. LTD) with a nominal value of 350 Ω and a gauge factor of 130 was used, which is significantly higher than that of a traditional metal foil strain gauge. The two LC tanks had

identical circular coils and capacitors. Circular coils were selected for impedance sensing and transmission because they offered higher coupling efficiency, minor misalignment, less energy loss, and high Q factor compared with other types of coil shapes, such as rectangular, and hexagonal coils [222, 223]. The inductance of both Tx and Rx coils (Würth Elektronik, 760308100141) was 10 µH. The coil traces were made using Litz wires to reduce skin-depth effects at high frequencies, which generated a relatively small DC resistance, around 30 mΩ. The coils were wounded on a shielding structure to minimize EMI interference and to focus the magnetic field, thereby significantly enhancing the Q-factor (maximum 180) which extends the sensing and transmission distance. Two identical 470 pF capacitors were used with both coils, generating an initial resonant frequency of 2.3215 MHz in air. The SSG was bonded to the centre of the specimen using Cyanoacrylate adhesive after the surface of the specimen was cleaned. The wires from the SSG were then connected to the Rx in parallel or series to form PP or SP topologies. The LC tank in the Tx was in parallel to the inputs of LDC1101. Both LC tanks were aligned on a supporting plate, and the lift-off could be adjusted by screwing the nuts. The collected data were transmitted to the MATLAB-based GUI via USB from the ESP32S3, and the data were processed using MATLAB. Before testing, the specimen was pre-loaded, and then the system conducted the testing according to the settings.

5.4.2 Comparison of WFM using the traditional SG and SSG

A traditional metal foil strain gauge (SG) with a nominal value of 350 Ohm and gauge factor of 2 was used to compare with the SSG. The experimental set-up was the same for the two cases. The lift-off was set to 25 mm.

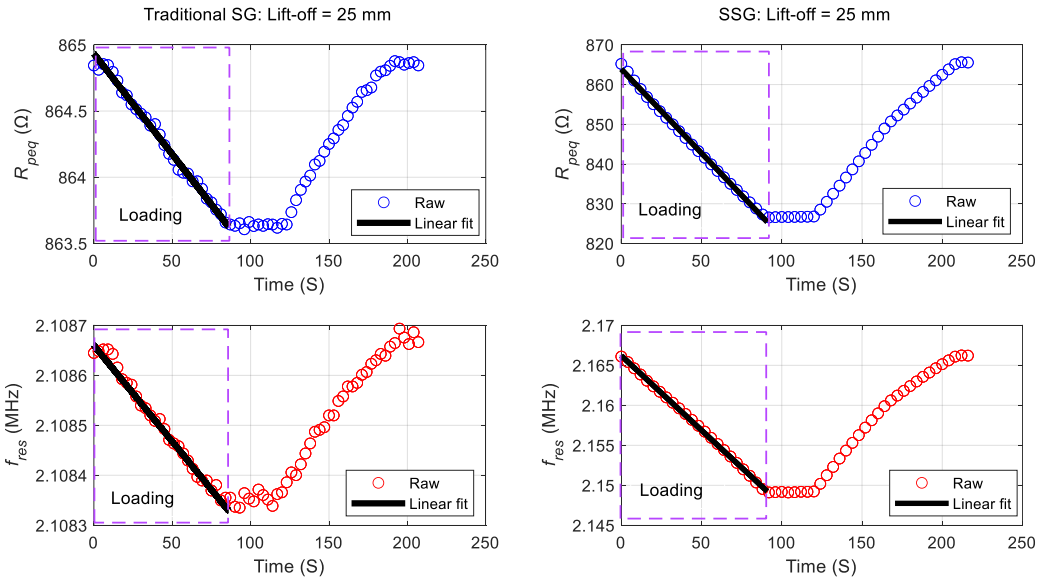

Figure 5.7 Experimental results of (a) traditional SG and (b) SSG

Figure 5.6 (c) presents the input force, and Figure 5.7 (a) and (b) show the sensing results for two types of SGs. The results at the loading stage were analyzed. Both exhibited an inverse proportional relationship with the input force. Table 5.2 provides a comparison of several key factors, including the variation in R_{Peq} and f_{res}, as well as the fitting factor R^2. The SSG exhibited a higher response than the traditional SG, approximately 32 times greater for ΔR_{Peq} and 59 times greater for Δf_{res}. Besides, R^2 for SSG was larger than the SG. In summary, the SSG demonstrates better sensitivity and linearity than the traditional SG due its larger gauge factor.

Table 5.2 Comparison of traditional SG and SSG at the loading stage

	Traditional SG	**SSG**
$\lvert\Delta R_{Peq}\rvert$	1.22 Ω	38.69 Ω
$\lvert\Delta f_{res}\rvert$	289.43 Hz	16988.72 Hz
R^2-R_{Peq}	0.9924	0.9982
R^2-f_{res}	0.9897	0.9992

5.4.3 PP/SP Topology with SSG for Force Measurement at Different Lift-offs

PP and SP topologies with a 350 Ω SSG were applied in the experiment respectively. Each was tested at a different lift-off. All tests were repeated three times to obtain the average of measurement values. Figure 5.8 shows the measured R_{Peq} and f_{res} of the PP topology during force loading, holding, and unloading, with the lift-off varying from 25 mm to 40 mm. It was observed that R_{Peq} decreased as the force increased, which aligned well with the simulation results. Furthermore, R_{Peq} remained almost constant during force holding and increased during the force unloading. The resonant frequency f_{res} also followed the R_{Peq} curves but tended to deteriorate when the lift-off exceeded 30 mm. The change of R_{Peq} and f_{res} with force was explained by Equations (5.7), (5.9), and (5.10), where R_{str} increased with the loading force, resulting in an increase in R_{eq} and L_{eq}, which in turn decreased R_{Peq} and f_{res}, and vice versa. R_{Peq} outperformed f_{res} because changes in SSG values primarily contributed to the real part of the impedance. R_{Peq} and f_{res}, along with the corresponding input force during the loading phase, were then extracted.

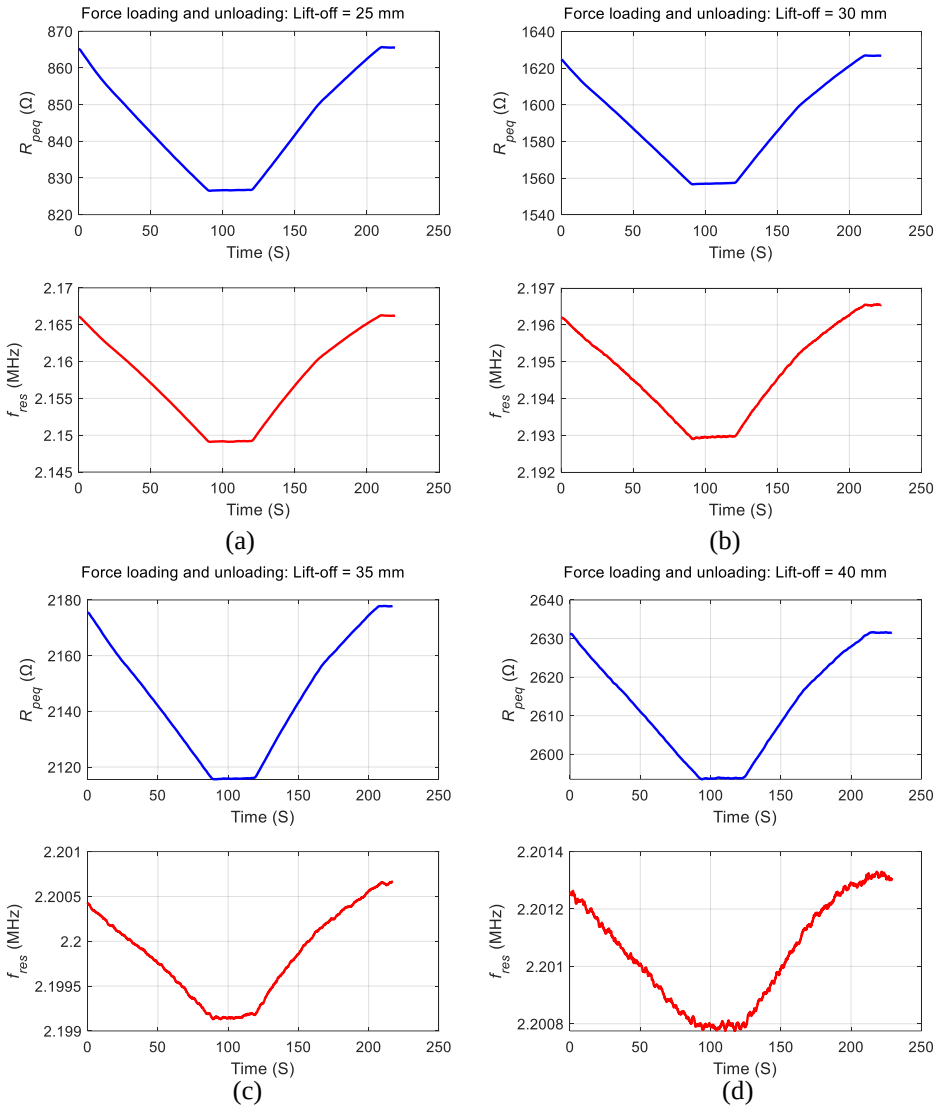

Figure 5.8 Experimental results of PP topology for force measurement at different lift-offs: (a) 25 mm (b) 30 mm (c) 35 mm (d) 40 mm

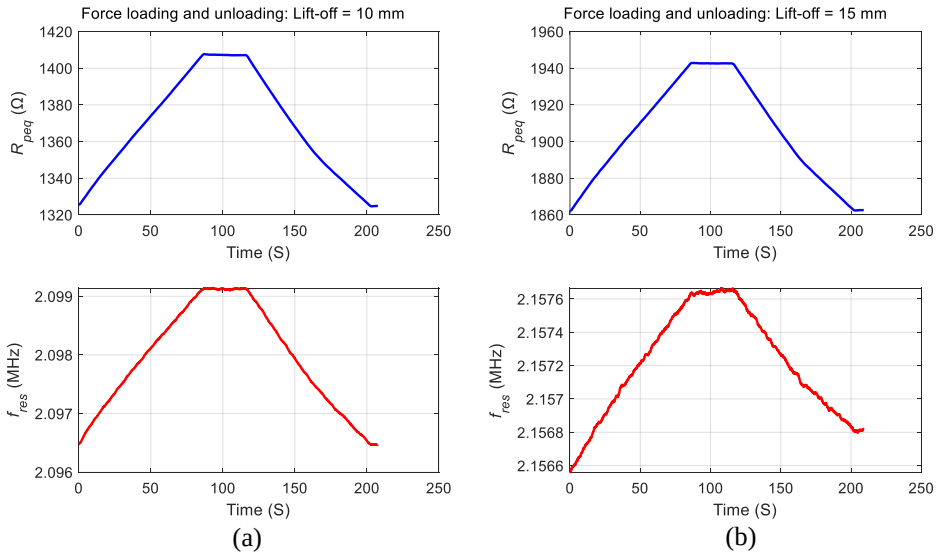

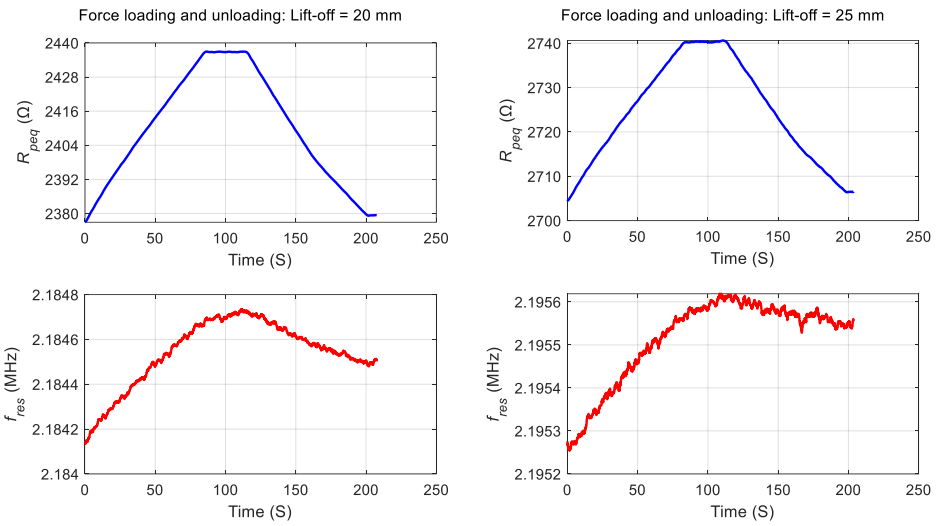

Figure 5.9 Experimental results of SP topology for force measurement at lift-offs: (a) 10 mm (b) 15 mm (c) 20 mm (d) 25 mm

Figure 5.10 (a) and (b) show the curves of R_{Peq} and f_{res} after subtracting the first measured value. A strong linear relationship was observed between them, particularly for R_{Peq}. The absolute sensitivity at various lift-offs is depicted in Figure 5.11 (a) and (b), indicated by the blue curve. The sensitivity of R_{Peq} differed from f_{res}, which decreased exponentially as the lift-off increased. The sensitivity in R_{Peq} exhibited a convex pattern, reaching a peak value of 5.5 Ω/kN when the lift-off was approximately 33 mm, indicating that the system was operating in the optimal coupling range due to critical coupling [152]. Furthermore, near the critical coupling region, the sensitivity tended to stabilize, which indicated that operating the Tx and Rx in this region can enhance robustness. In the PP topology with a 350 Ω SSG, it was noteworthy that the minimum lift-off was 25 mm because R_{Peq} approached the lower limit of the measurement system.

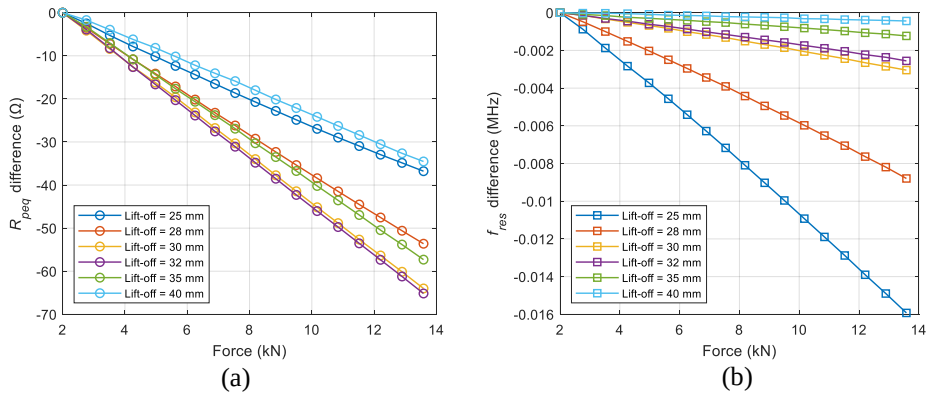

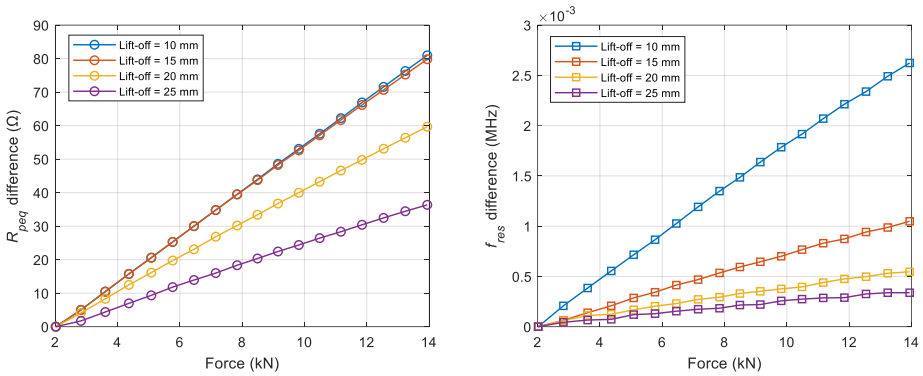

(c) (d)

Figure 5.10 Measurement parameters of PP/SP topology against loading forces: (a) PP: R_{Peq} difference versus loading force (b) PP: f_{res} difference versus loading force (c) SP: R_{Peq} difference versus loading force (d) SP: f_{res} difference versus loading force

For the SP topology with the same SSG, similar tests were conducted at lift-offs of 10 mm, 15 mm, 20 mm, and 25 mm. The lift-off configuration was different from that of the PP topology, as it was adjusted to consider the effective working range of the measurement system. Figure 5.9 shows the experimental results of SP topology for force measurement. The curves of the SP topology exhibited a reverse trend compared to the PP topology, which was consistent with the simulation results. Here, both R_{Peq} and f_{res} increased with the force, remained constant when the input force was steady, and decreased as the force decreased. This was explained by Equations (5.8), (5.9), and (5.10), where R_{str} increased with the loading force, leading to a decrease in R_{eq} and L_{eq}, which in turn increased R_{Peq} and f_{res}. Figure 5.10 (c) and (d) present the curves of R_{Peq} and f_{res} versus force during the loading stage. Similar to the PP topology, the sensitivity curves in Figure 5.11 (c) and (d), indicated by the blue curve, show that R_{Peq} reached a peak value of 6.9 Ω/kN at a lift-off of 10 mm, while f_{res} varied exponentially with the lift-off.

5.4.4 Influence of Different SSGs

The influence of different SSGs on the working range and sensitivity was investigated. An additional SSG with a resistance value of 120 Ω was adopted, and similar lift-off tests were carried out.

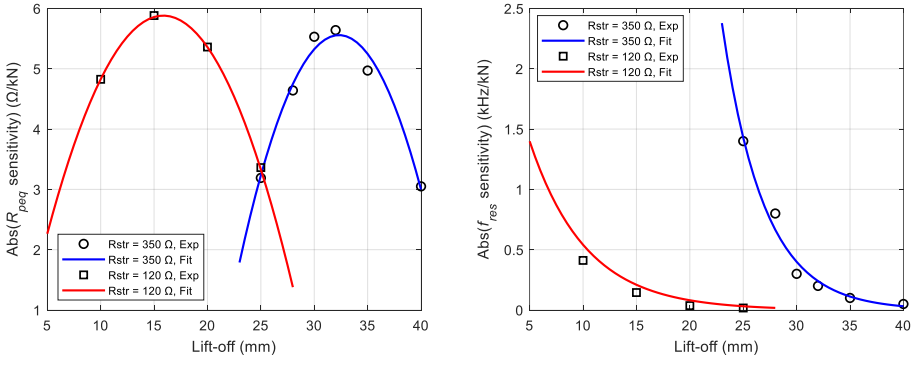

(a) (b)

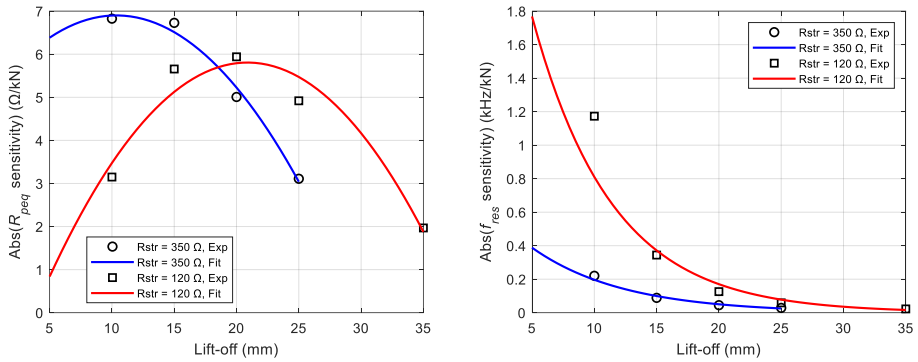

Figure 5.11 Absolute sensitivity against lift-off of PP/SP topologies with SSGs of 350 Ω and 120 Ω: (a) PP: R_{Peq} (b) PP: f_{res} (c) SP: R_{Peq} (d) SP: f_{res}

The sensitivity at each lift-off was obtained and plotted in Figure 5.11, shown by the red curves. It was observed that different SSGs corresponded to a different working range for R_{Peq} and f_{res}. Since the SSG was a resistive sensor, the sensitivity curve for R_{Peq} performed better compared to f_{res}. The latter was more susceptible to lift-off variations, showing better sensitivity at low lift-offs. However, the former was strongly dependent on the coupling range. In the PP topology, R_{Peq} reached optimal sensitivity at lift-off of 15 mm for a 120 Ω SSG, while for a 350 Ω SSG, its optimal sensitivity appeared at 33 mm. This was because the SSG changed the impedance of the entire system and altered the optimal working range. In the SP topology, a similar phenomenon was observed, but there was a wide overlap in the entire lift-off range for both R_{Peq} and f_{res}.

5.4.5 Discussion

The MRC-WPT-based impedance sensing for WFM utilizes the characteristics of MRC and high gauge factor of SSGs, as well as the integrated LDC-based measurement system. It transforms the change in SSG into the impedance of the Rx, and then into the impedance of the Tx by the reflected impedance. This approach fully combines the advantages of MRC-WPT and overcome the lift-off limitations, achieving the force measurement at high lift-offs. To some extent, the introduction of SSGs effectively avoids the occurrence of frequency splitting, which may have negative effects on measurement performance. Since the SSG is a resistive sensor, its primary impact is on the real part of the impedance, with minimal effect on the imaginary part, particularly at high lift-offs. This can be explained why R_{Peq} exhibited a good quality in contrast with f_{res} during the testing. SSGs in the PP and SP topologies demonstrate distinct influences, affecting the working range, optimal lift-off, and maximum sensitivity. Essentially, the proportion of SSGs in PP and SP topologies is closely associated with the original impedance without connecting any SSGs. When the SSG value is relatively small compared to the original

impedance, its impact is more pronounced in the PP topology rather than the SP topology, and vice versa. The LDC1101-based system is a miniaturized device which contains the function of driving Tx and detecting R_{Peq} and f_{res}. However, there are indeed some drawbacks, such as R_{Peq} needing to be greater than 750 Ω and the resonant frequency of the *LC* tank being limited to the range of 500 kHz to 10 MHz. These drawbacks potentially impact the optimal performance of the components. The Tx and Rx coils utilized in the work are ready-made products which can be specially designed to suit the application environment, including curved surfaces, by employing flexible PCB technology. The current method for WFM was affected by the lift-off interference and misalignment between the Rx and Tx coils, which vary coupling coefficients. There may be a method to compensate for these changes by adding an additional *LC* tank measure lift-off. There is always a trade-off between sensitivity, lift-off, topologies, SSG values, and coil shapes. These factors should be carefully selected to maximise the measurement performance.

5.5 Chapter Summary

In this chapter, a novel WFM approach based on impedance sensing using an SSG and MRC-WPT was proposed. This method leverages the high sensitivity of the SSG, the transmission characteristics of MRC-WPT, and the miniaturized LDC-based impedance measurement system to achieve WFM with enhanced sensitivity at high lift-offs. It offers the benefits of low cost, portability, and fast response, while also overcoming the lift-off limitations inherent in traditional LC resonance sensors that rely on eddy current effects.

A comparative study between a traditional SG and SSG for WFM was conducted, demonstrating that the SSG exhibited significantly higher sensitivity, with ΔR_{Peq} being 32 times greater and Δf_{res} being 59 times greater compared to the traditional SG. Both PP and SP topologies with different SSGs and lift-offs were studied through simulations and experiments. The results demonstrated both topologies were effective for WFM at high lift-offs. Specifically, for an SSG of 350 Ω, the PP topology achieved a maximum lift-off of 40 mm, while the SP topology achieved a maximum lift-off of 25 mm. Both R_{Peq} and f_{res} exhibited an excellent linear relationship with input force. It was found that the sensitivity in R_{Peq} exhibited a convex pattern, where it tended to stabilize near the critical coupling region, indicating that operating the Tx and Rx in this region can enhance robustness. In contrast, the sensitivity in f_{res} exhibited an exponential relationship. The SSG influenced the optimal lift-off for both PP and SP topologies. Overall, each topology has its advantages and disadvantages, allowing for customization based on specific application needs.

Although the proposed approach is influenced by lift-off interference, misalignment between the Rx and Tx coils, and inherent performance of the LDC-based system, it offers new insights into measuring forces on rotating mechanical components, such as wheel-rail contact force. By attaching an SSG and Rx to wheel areas most susceptible to external impacts, while using a Tx installed on the bearing box, wireless wheel-rail force measurement can be achieved. Additionally, its application can be extended to structural health monitoring of critical infrastructure such as bridges, pipeline, and buildings where power supply and cable connection are unavailable. Moreover, there is potential to integrate this technology with other types of sensors. For instance, SSG can be replaced with capacitive or inductive sensors to monitor various parameters, such as temperature, pressure, humidity, and structural defects. This integration could provide a comprehensive multi-sensor system capable of real-time environmental and structural health monitoring.

Previous studies were conducted using a uniaxial testing machine at a constant temperature on a relatively static platform. Nevertheless, real railway vehicles operate in dynamic environments, encountering factors such as temperature fluctuations and electromagnetic interference. Additionally, railway vehicles consist of rotating components. There remains a lack of studies on signal stability and testing of this technology on a rotating platform. The next chapter will concentrate on the stability study of WFM using differential LC resonators and software processing algorithms, as well as signal readout and analysis of signal characteristics on a rotating testing platform.

Chapter 6. Stability Study of MRC-based WFM and Signal Readout and Analysis under Rotating Test

This chapter describes the stability study MRC-based wireless force measurement (WFM) which is affected by temperature and electromagnetic interferences using differential configurations of LC resonators and signal processing algorithms including the moving average algorithm (MAA) and Kalman filter (KF). In addition, to realize the ultimate application of MRC-based WFM on practical wheels, a rotating testing platform in the lab was established to explore the signal readout and signal characteristics with varying lift-offs and variable resistors that represent the value change of a SSG in response to applied forces.

6.1 Introduction

WFM is promising for structural health monitoring, such as infrastructure deformation, wheel-rail contact force, as no cable connection and power supply are required [191]. Defect detection and force measurement in LC resonant sensors rely on the principle of eddy current effects. This occurs as defects or applied force alter the material's electromagnetic properties, affecting the intensity of eddy currents. These changes in eddy currents subsequently modify the equivalent parameters of LC resonant sensors, such as inductance and equivalent parallel impedance. Because of the characteristics of working in a resonant state, the current driving an LC sensor can be minimum which significantly reduces the power supply. However, the methods based on eddy currents is limited by lift-off which is the distance between the sensor and the specimen. Appling LC resonators based on magnetic resonant coupling (MRC) and a semiconductor strain gauge (SSG) opens a new approach to force or strain measurement, which overcomes the shortcoming of lift-off limitations. It utilizes the properties of high sensitivity of SSGs and mid-range communication of MRC between two LC resonators. A SSG varies the impedance in one LC resonator, and this variation is measured by the other LC resonator via magnetic field coupling. However, due to the interferences of external factors including temperature and electromagnetic noise [173, 224], the signal stability is subject to degradation. To compensate for this issue, some hardware and software measures can be adopted [173, 225, 226]. In terms of hardware measures, often a reference sensor is added into the measurement system where it undergoes the same conditions as the measurement sensor. The reference signal is then subtracted from the measured signal to reduce the noise interferences [224]. The MAA and KF algorithms are used for software processing [225].

Since the ultimate purpose is to apply MRC-based method on wheel-rail contact force measurement (WRCFM) which is a rotating system, preliminary exploration on a rotating

platform for signal readout and analysis is necessary. Rotating testing for LC sensors has been studied for in situ health monitoring of bearings, speed measurement, and pressure measurement [129, 141, 227]. After enhancing the signal stability of LC resonators using differential configurations, MAA and KF algorithms, rotating testing is performed to study the signal readout and analysis of signal characteristics.

6.2 Stability Study of WFM using Differential LC Resonant Sensors and Signal Processing

In this section, based on the high sensitivity of a SSG and the long-distance transmission characteristic of MRC, a differential LC resonant sensor using a customized two-channel inductance-to-digital converter (LDC)-based measurement system is proposed. This system is combined with MAA and KF algorithms to enhance the signal stability.

6.2.1 Experimental Set-up

To verify the stability and response of differential LC resonators against external interferences and force excitations, the experimental set-up was designed. Differential configuration of LC resonators and software processing were described. Two types of tests including the sensor outputs with and without force excitations were performed.

Figure 6.1 is the system diagram of applying differential LC resonators on WFM, where two channels of LDC1101 are included and connected to the ESP32S3. Two LC resonators are connected to the LDC1101s with a multiplexer which can be controlled by the ESP32S3. One LC resonator is aligned with Rx to get the readout of sensing signal while the other is acted as the reference. Besides, a temperature sensor is used to monitor the change in ambient temperature. The experimental set-up included a specimen, a SSG of 350 Ω, an LDC1101-ESP32S3 measurement system, a temperature module DHT22 with a temperature range: -40°C to 80°C and accuracy ±0.5°C, three identical LC resonators with the inductance coils of 10 μH and parallel capacitors of 470 pF, as shown in Figure 6.2. There were two LDC1101 channels in the measurement system, controlled by an ESP32S3 microcontroller via SPI communications. Tx_ref was connected to the LDC1101-CH2 and Tx to the LDC1101-CH1. The lift-off between Tx and Rx was set to 25 mm. When the specimen was suffering from a force excitation, the SSG would make response and change the impedance in Rx. This change was then magnetically coupled to Tx via the reflected impedance, varying its R_{peq} and f_{res}.

Figure 6.3 presents the software processing flowcharts with respect to R_{peq} and f_{res}, which contains pre-processing in ESP32S3 and post-processing in MATLAB. Based on the

characteristics of R_{peq} and f_{res}, the former is more susceptible to external interferences while the latter is relatively stable. The pre-processing involves a MAA algorithm applied to R_{peq} for Tx and Tx_ref, and a debounce algorithm by setting a threshold for f_{res} in two channels. After obtaining ΔR_{peq} and Δf_{res}, Δf_{res} becomes stable, and ΔR_{peq} is further processed through a KF algorithm to improve the signal-to-noise (SNR).

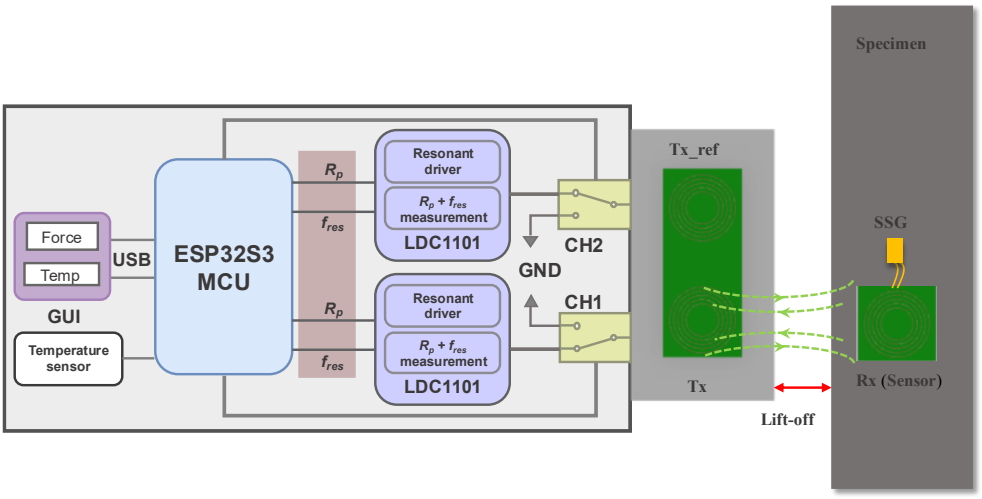

Figure 6.1 Differential LDC1101-ESP32S3 measurement system

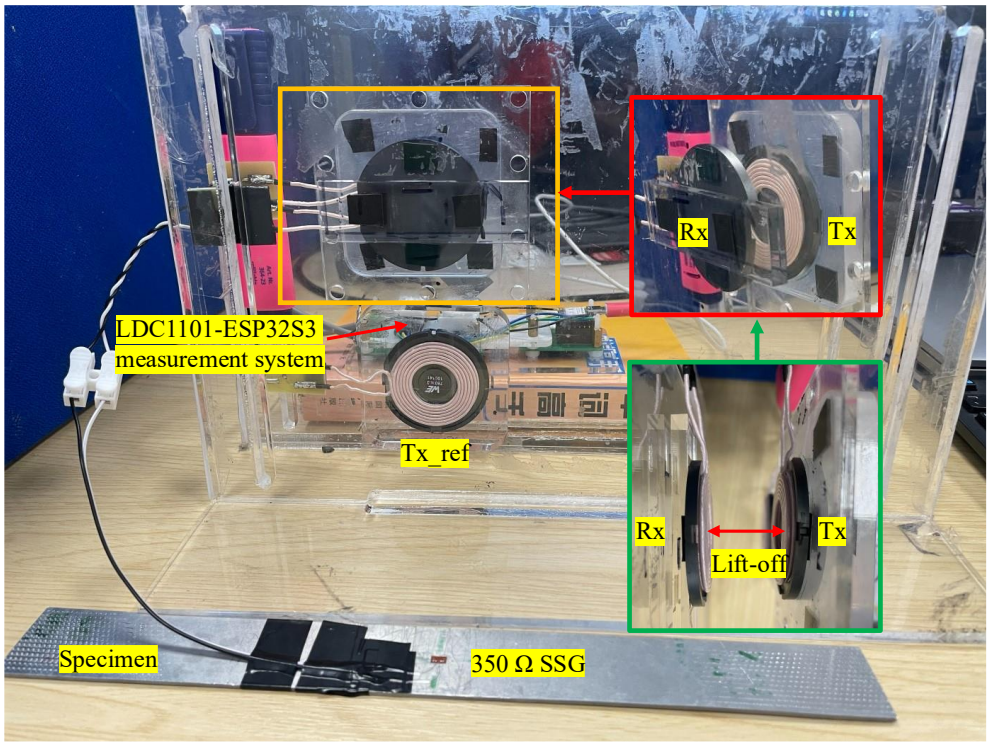

Figure 6.2 Experimental set-up of differential LC resonant sensors with LDC1101-ESP32S3 measurement system

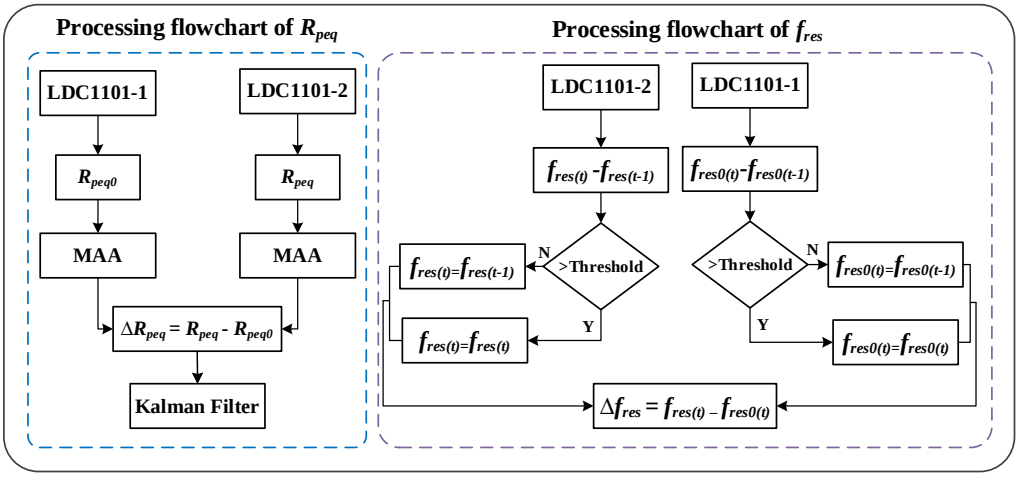

Figure 6.3 Software processing flowchart for R_{peq} and f_{res}

6.2.2 Sensor Output without Force Excitation

It is worthwhile determining the response of the differential *LC* resonant sensor when there is no force excitation, which can be regarded as a static response. The entire measurement system was placed in a room for around 4.5 hours where the temperature changed with the outside temperature. R_{peq} and f_{res} in two LDC1101 channels, and temperature signals were collected.

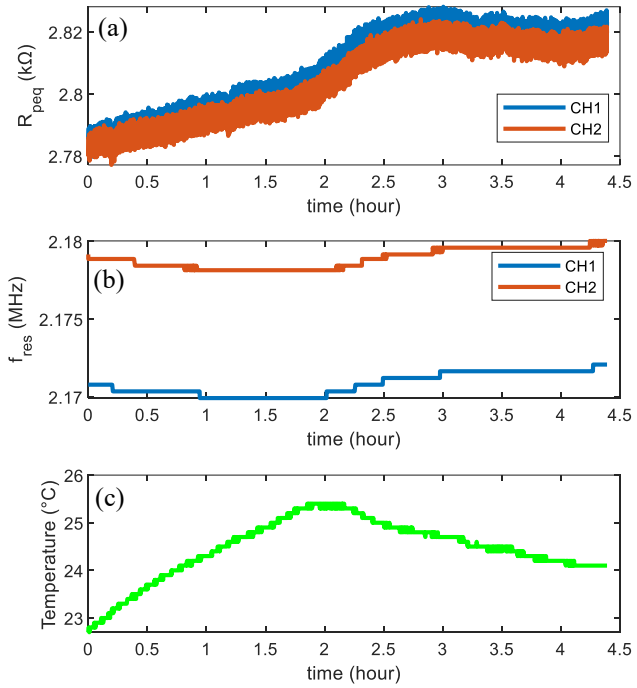

Figure 6.4 (a) R_{peq} and (b) f_{res} in 2 channels over 4.5 hours (c) Temperature variations over 4.5 hours

Figure 6.4 presents these three signals in response to external interferences including temperature variations and EMI noise. It is apparent that temperature causes both R_{peq} and f_{res} to drift, but the former is more serious than the latter, which was attributed to a higher

temperature coefficient in R_{peq}. From the trends of R_{peq} and f_{res} curves, it is not evident that temperature is proportional to them.

Figure 6.5 describes the differential signals ΔR_{peq} and Δf_{res} after signal processing. Both signals become less vulnerable to temperature variations. Since Δf_{res} exhibited a robust characteristic with the debounce algorithm in the whole period, the KF algorithm was only applied on ΔR_{peq}. Here, the same KF approach as described reference [225] was utilized. There were two key parameters in KF, the process variance constant Q and the measurement constant R, which must be chosen properly. Q was selected to 0.35 and R was 10. Therefore, the differential configuration and software processing effectively reduced the noise interference.

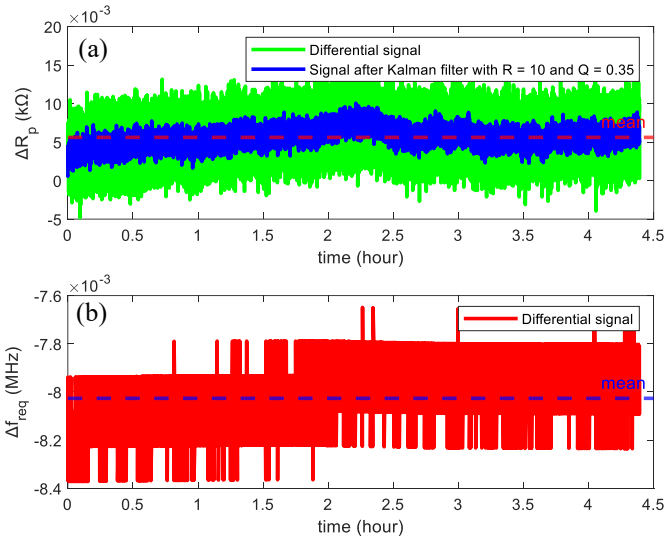

Figure 6.5 (a) ΔR_{peq} after processing over 4.5 hours (b) Δf_{res} after processing over 4.5 hours

6.2.3 Sensor Output with Force Excitation

To test the stability and dynamic response of the sensor, force excitation was applied randomly over time. The applied force was perpendicular to the central surface of the specimen, oriented inward or outward. That meant there were two forces, compression, and tension. In Figure 6.6 (a) and (b), ΔR_{peq} and Δf_{res} exhibit the static response and dynamic response over time. As the SSG was sensitive to the applied force, it caused the change in Rx's impedance, and then in Tx's R_{peq} and f_{res} via magnetic coupling. That enables wireless force measurement by impedance sensing. The sensor output in response to the force excitation is marked with black dash lines. Figure 6.6 (c) shows the temperature change with time. Overall, the minor temperature fluctuations exhibited the minimum impact on the stability of ΔR_{peq} and Δf_{res}. The dynamic response of the sensor resulting from the force excitation differed significantly from those responses observed without excitation. These findings demonstrate the sensor's robustness, stability, and high responsiveness.

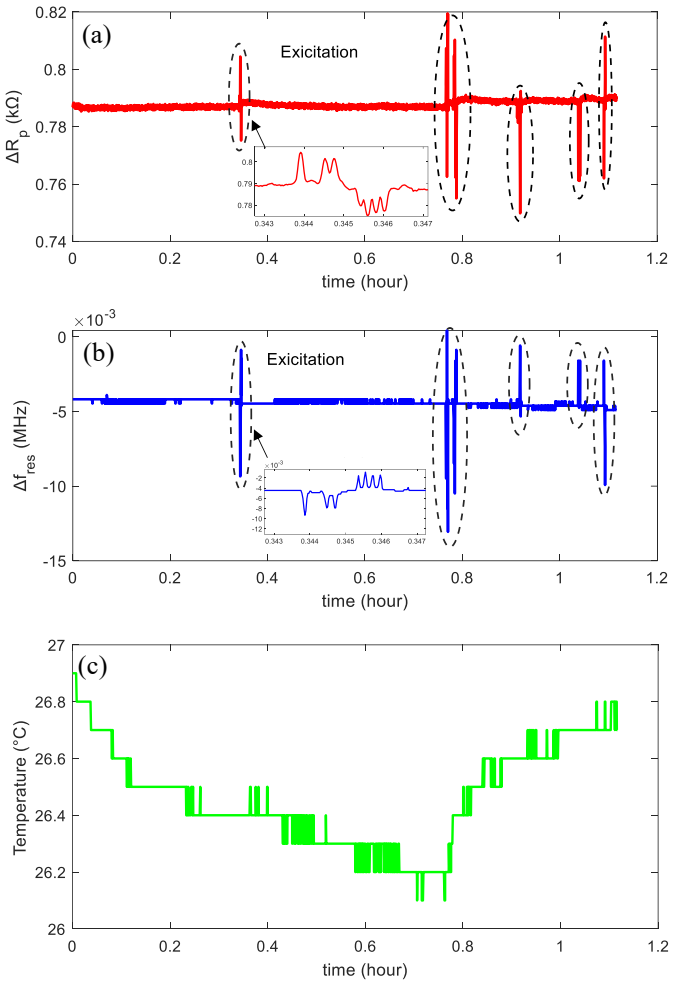

Figure 6.6 (a) ΔR_{peq} and (b) Δf_{res} with force excitation applied at random, and (c) Temperature variations over time

6.2.4 Summary

Based on the high sensitivity of a SSG, the mid-range transmission characteristic of MRC, and the fast response of LDC-based measurement system, a differential configuration of *LC* resonant sensors and software processing algorithms were combined to enhance the stability of the wireless force measurement against the external interferences including EMI noise and temperature fluctuations. Experiment study tested the static and dynamic responses of the sensor over time. The results indicate that differential configuration of *LC* resonators, MAA and KF algorithms facilitate the sensor's robustness, stability, and responsiveness. This method can be applied in areas where cable connections and power supplies are not available, such as structural state monitoring of bridges, railway tracks, and railway wheels.

6.3 Signal Readout and Analysis on Rotating Testing

This section presents the signal readout and analysis of signal characteristics for MRC-based sensing on a rotating testing platform, which lays the foundation for the future application on practical wheel rails.

6.3.1 Design of Circular LC Resonators

A pair of customized circular LC resonators was designed to fulfil the rotating platform, as shown in Figure 6.7. Table 6.1 presents the parameters of inductance coils with the outer diameter of 18.0 mm, the inner diameter of 6.4 mm, 19 turns per layer, 4 layers, track width of 6 mil, spacing between tracks of 6 mil, and the thickness of 1.6 mm. The COG/NPO capacitor with 270 pF was used due to its excellent stability and low losses. The circular inductance coils were fabricated by PCB technology. One LC resonator acted as the readout resonator Tx while the other as reference Tx_ref. The central distance between two circular coils was 25 mm. Another identical circular LC resonator operated as Rx where an SSG was connected to it in response to the change of force. To enhance the inductance value and Q factor, a ferrite sheet with high permeability was attached on the back of the circular resonators. After sticking a ferrite sheet, the inductance became from 66 μH to 108 μH and Q improved to 33 from initial 18. The DC resistance of each inductor coil was 21 Ω.

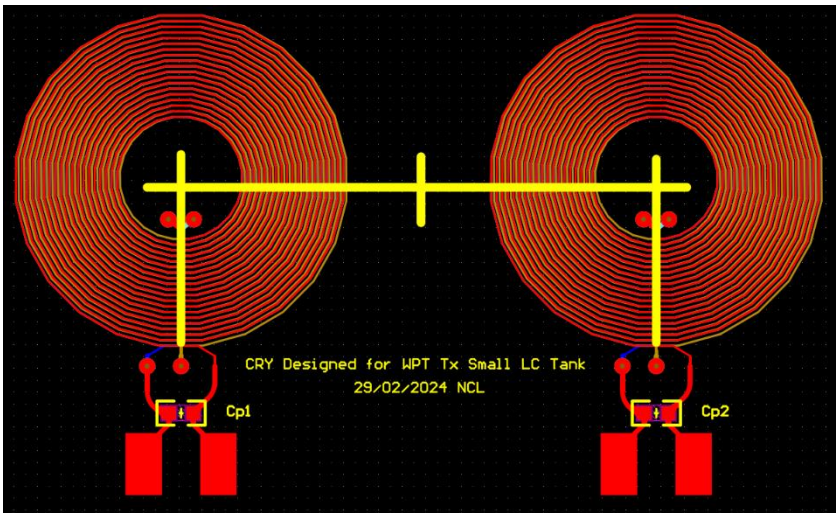

Figure 6.7 A pair of customized circular LC resonators

Table 6.1 Parameters of the circular LC resonator

Parameter	Value
Outer diameter	18.0 mm
Inner diameter	6.4 mm
Thickness	1.6 mm

Turns per layer	19.0
Layers	4.0
Trace width	6.0 mil
Spacing between traces	6.0 mil
Cp	270.0 pF

6.3.2 Development of LabView-based GUI

As a real wheel-rail system may rotate quickly and the previous MATLAB-based GUI was unable to capture the complete data under fast speed, an LabView-based GUI was developed which is based on consumer and producer loops to improve the sampling speed. Figure 6.8 shows the front panel of the LabView-based GUI which contains filename, baud rate, two visualisation windows for differential R_p and frequency. In Figure 6.9, there are two loops in which the producer loop is used for processing real-time incoming data and visualisation from the microcontroller based on serial communication while the consumer loop conducts data savings.

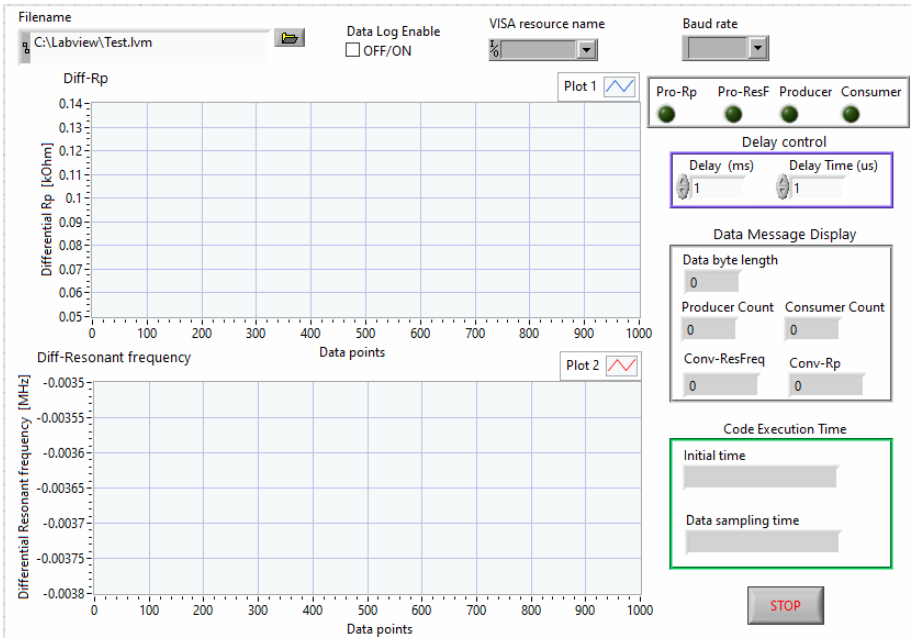

Figure 6.8 Front panel of LabView-based GUI for high-speed sampling

Communication between producer and consumer loops is completed by using queues. The incoming data which contain specific strings and numbers enter the producer loop though VISA, and then are added to the queue (called 'enqueue'). The consumer loop removes data from that queue (called 'dequeue'). Because queues are based on the first-in/first-out theory, the data will always be analysed by the consumer in the same order as they were placed into the queue by the producer. For both loops, the first letter of the incoming string data is extracted by string

subset for differentiating R_p and frequency in different processing case structures. Scan from string is then employed to extract the numeric information and display them in real time. The producer loop simultaneously displays the differential R_p and frequency while the consumer loop saves data into the assigned dynamic array. After the loops stop, the data will be saved into the designated file directory.

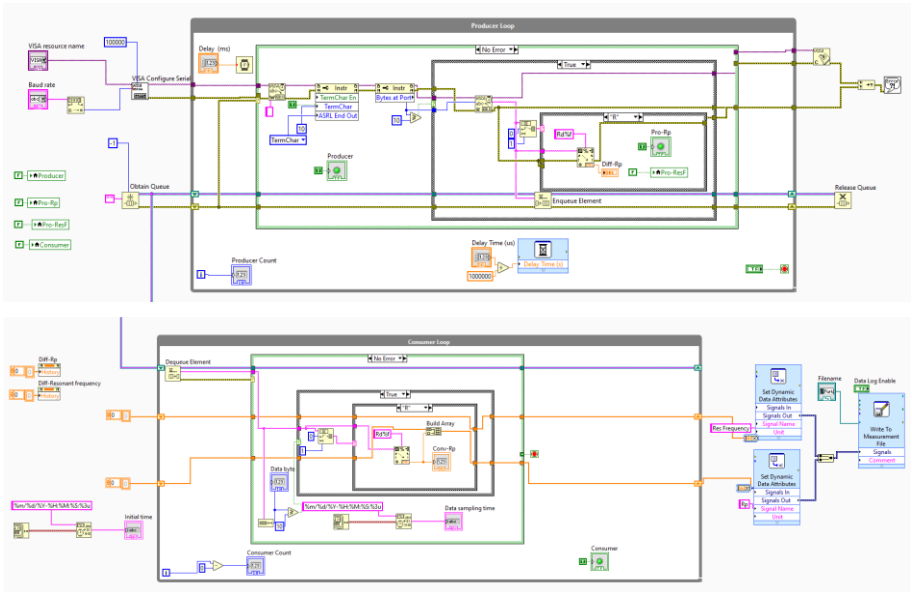

Figure 6.9 Back panel of LabView-based GUI with producer and consumer loops

6.3.3 Experimental Set-up

The experimental set-up continued the most configurations in Section 6.2, except for the LC resonators. Figures 6.10 and 6.11 show the diagram and photograph of the rotating testing platform based on differential LC resonators. A motor from Crouzet company (8983012) was used, with an adjustable speed controlled by varying the DC voltage, supporting a maximum of 3600 revolution per minute (rpm) at 24 VDC. A metal plate with a diameter of 150 mm was fabricated to install on the motor, which rotated as the motor to mimic the real rotating wheel. The Rx with a variable resistor R_{var} was attached to the plate and the variation in R_{var} represented the SSG in response to force. During the test, the distance between Rx and the readout part was fixed and the rotation speed of the motor remained constant. The LDC1101-ESP32S3 measurement system started to work once the motor was rotating. To reduce the interference between Tx and Tx_ref, a strategy similar to Section 4.5 was adopted where the measurement system controlled the multiplexer to switch the channel. When one was working, another one was grounded. The switching time was set to tiny, so data for Tx and Tx_ref were regarded simultaneously and synchronously. Tx and Tx_ref kept sampling data all the time, even though useful data containing the sensing information were only included when Rx was aligned with

Tx. The sampling data were then conveyed to the LabView-based GUI for further processing and saving.

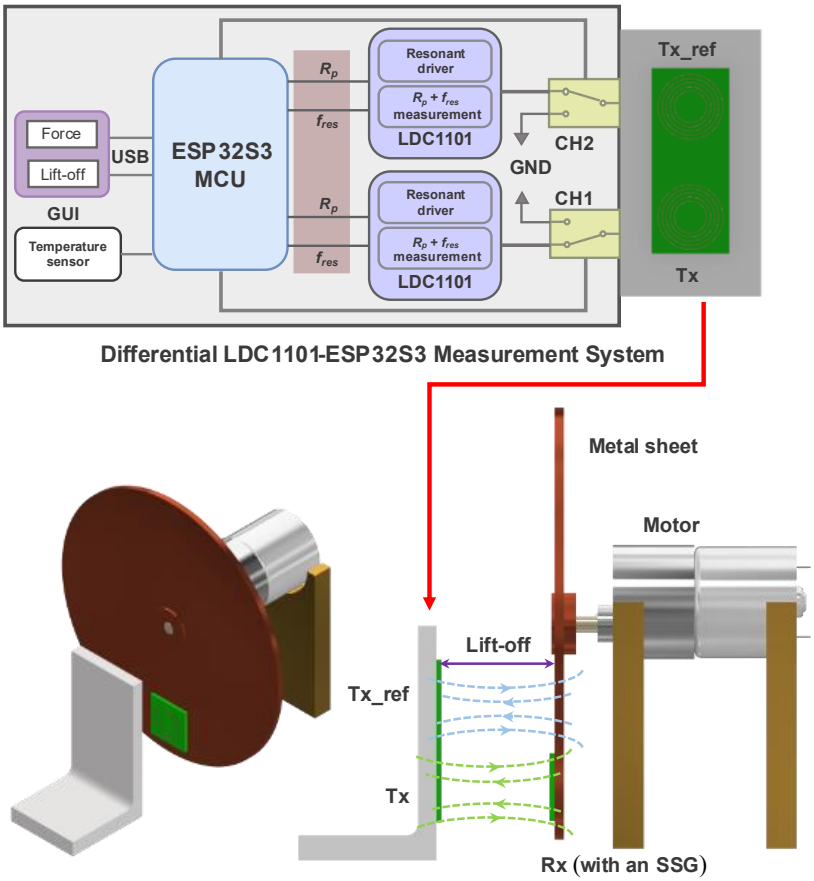

Figure 6.10 Rotating testing platform based on differential LDC1101-ESP32S3

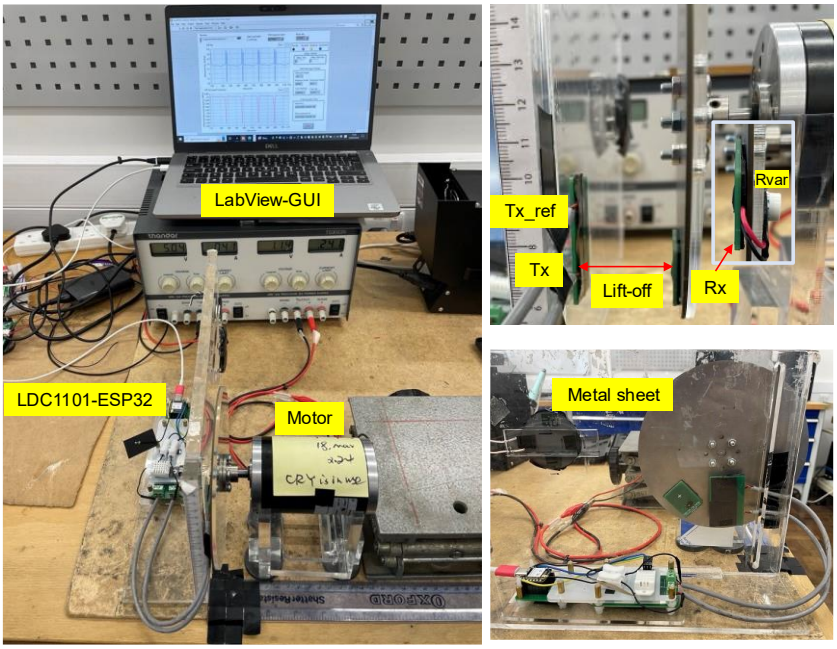

Figure 6.11 Practical photograph of rotating testing platform

6.3.4 Lift-off Variations

The rotating testing under lift-off variations was conducted to identify the response between Tx and Rx, Tx_ref and the metal plate. As the Tx_ref acted as the reference, it was subtracted from the values of Tx to attain differential values in terms of R_p and f_{res}, denoted as ΔR_p, and Δf_{res}, which can reduce the influence of common-mode interferences. R_{var} was not connected to Rx, only studying the lift-off influence for signal readout. Figure 6.12 shows ΔR_p and Δf_{res} against different lift-offs, from 5 mm to 15 mm with an interval of 2 mm. With respect to Δf_{res}, it exhibited a valley when Tx aligned Rx and maintained unchanged when Tx was not interacted to Rx. The valley value, minimum, decreased with the increase in lift-off due to the reduction in magnetic coupling between Tx and Rx. Rpm can also be derived based on the duration of the repeated valleys of Δf_{res}. ΔR_p described a distinguishing characteristic which included two spikes and one valley. The spikes were corresponding to that when Rx just started to enter and leave the magnetic field coupling area while the valley indicated that Rx was right in the middle of Tx. From 7 mm to 15 mm, a gradually decreasing trend was observed for ΔR_p. However, ΔR_p presented a phenomenon that spikes were larger than the valleys at the lift-off of 7 mm, which might be caused by the strong coupling between Tx and Rx. The results demonstrated that lift-off varied the response for ΔR_p and Δf_{res}.

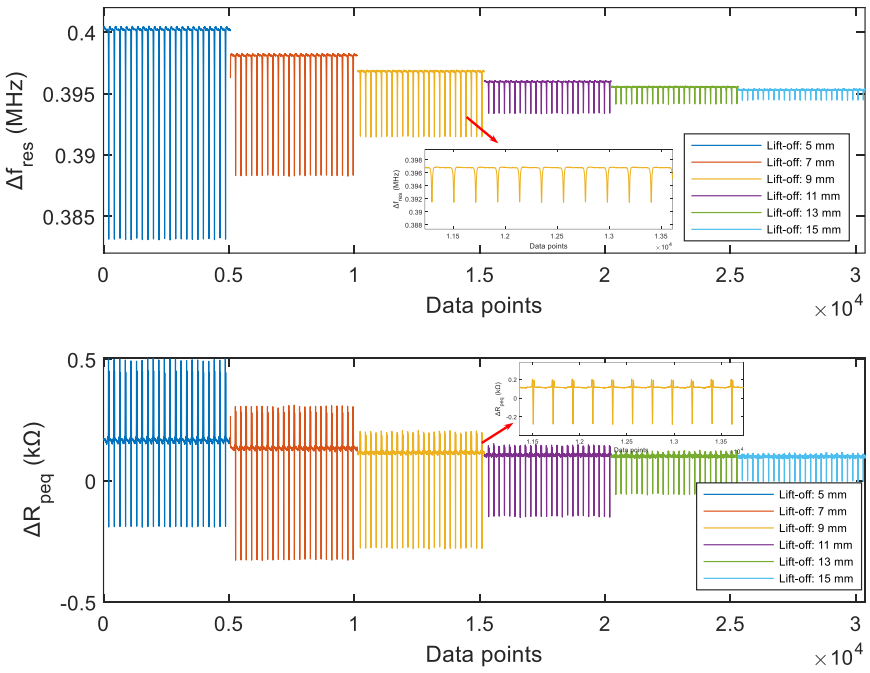

Figure 6.12 Practical photograph of rotating testing platform

6.3.5 Rotating Tests with Varying R_{var}

A variable resistor R_{var} installed on the metal plate was connected to Rx in parallel (PP topology in Figure 5.1 (b)) to mimic the change of SSG in response to wheel-rail contact force (WRCF).

R_{var} in Figure 6.11 was set to 49.6 Ω, 64.2 Ω, 79.2 Ω, 96.9 Ω, 116 Ω, and 131.6 Ω, respectively. The variation range in SSG was around 80 Ω, similar to that change of SSG against force presented in Chapter 5. The lift-off was set as 5 mm, 7mm, and 9 mm. Figure 6.13 shows the response of Δf_{res} against various R_{var} at lift-off 5 mm. Δf_{res} kept unchanged when R_{var} varied, which might be attributed to the small Q factor and weak coupling coefficient. However, the valley of ΔR_p increased inversely proportional to R_{var}. This tendency was consistent with the results in Section 5.4.3. This can be explained by Equation (5.7) where the increase of R_{var} resulted in an increase in R_{eq}, which in turn decreased R_{Peq}. Obviously, the change of R_{var} primarily affected the real part of the equivalent impedance while remained unchanged in Δf_{res}. This phenomenon was also seen in Figures 6.16, 6.17, 6.19, and 6.20 when lift-offs varied from 7 mm to 9 mm. Figures 6.15, 6.18, and 6.21 demonstrated the extracted negative peaks in ΔR_p and R_{var} at different lift-offs. Lift-off caused the variation in both ΔR_p and Δf_{res}, but R_{avr} only varied ΔR_p, indicating Δf_{res} can be harnessed to measure lift-off for compensating ΔR_p.

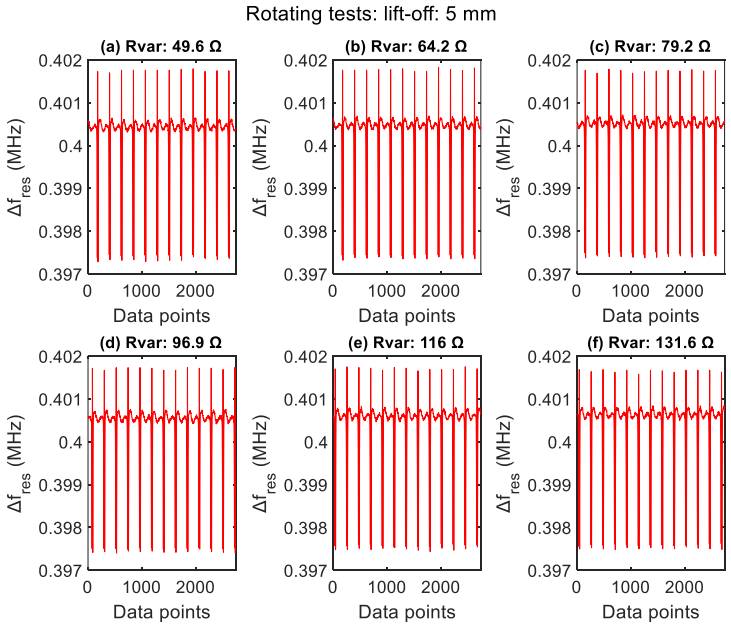

Figure 6.13 Δf_{res} against various R_{var} at lift-off 5 mm

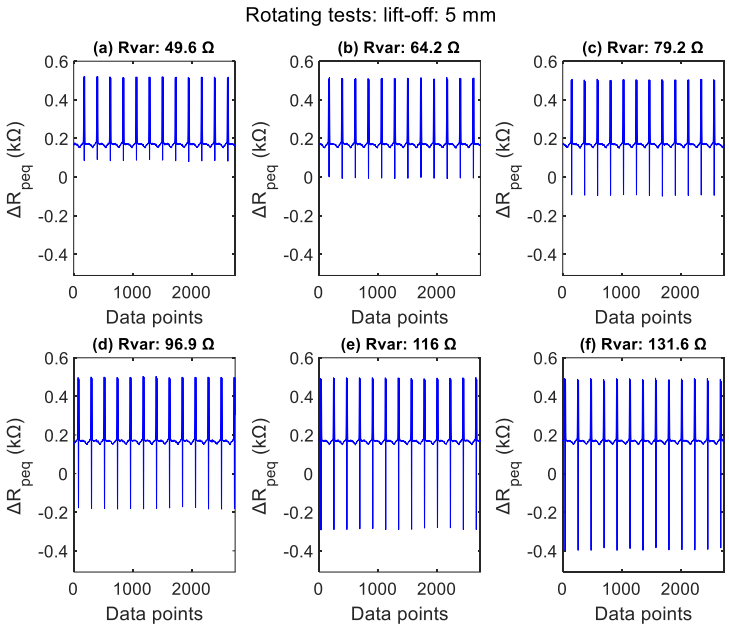

Figure 6.14 ΔR_p against various R_{var} at lift-off 5 mm

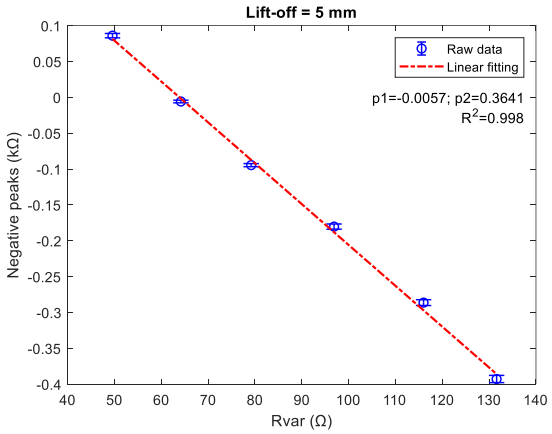

Figure 6.15 The extracted negative peak against various R_{var} at lift-off 5 mm

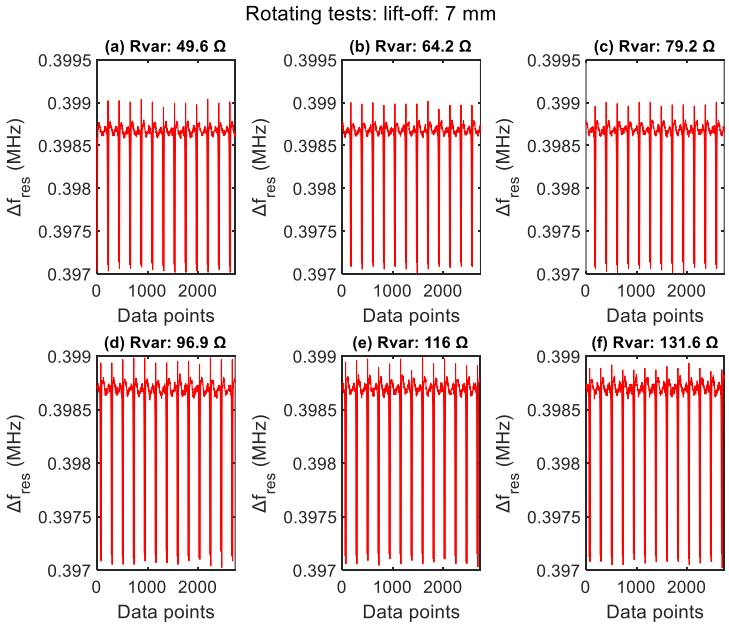

Figure 6.16 Δf_{res} against various R_{var} at lift-off 7 mm

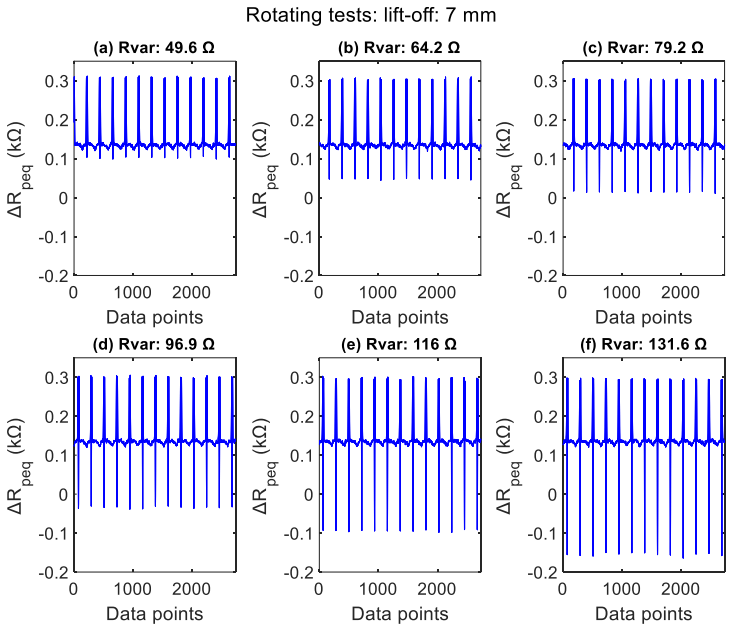

Figure 6.17 ΔR_p against various R_{var} at lift-off 7 mm

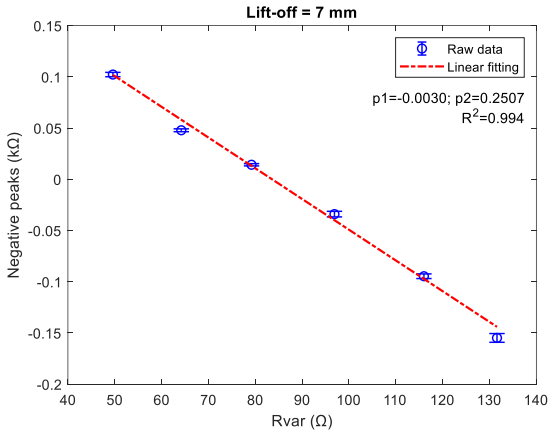

Figure 6.18 The extracted negative peak against various R_{var} at lift-off 7 mm

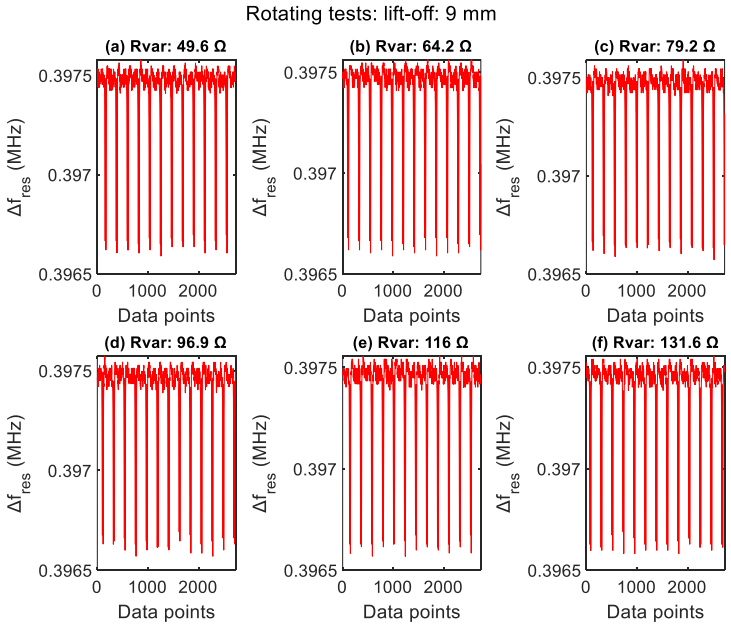

Figure 6.19 Δf_{res} against various R_{var} at lift-off 9 mm

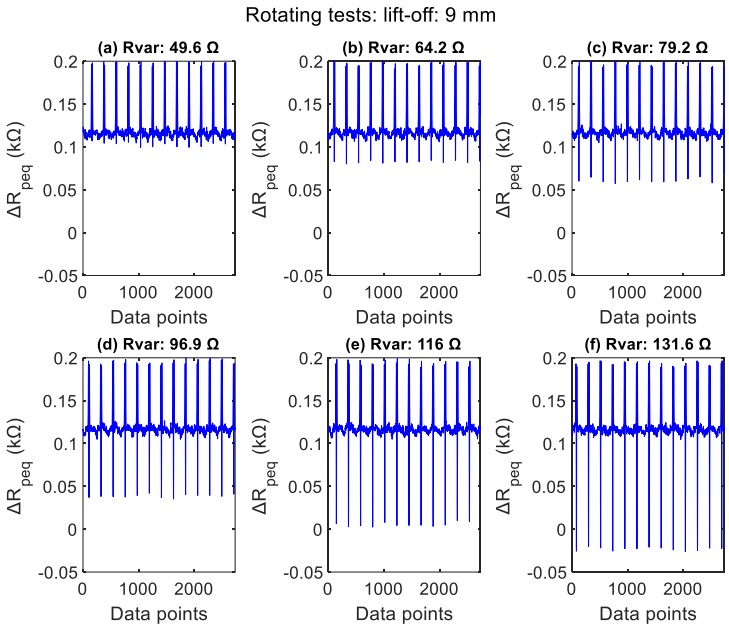

Figure 6.20 ΔR_p against various R_{var} at lift-off 9 mm

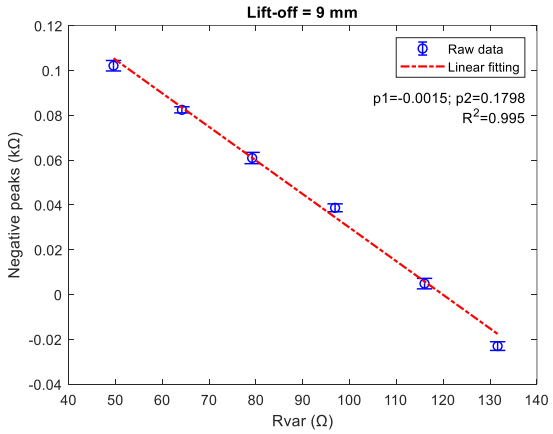

Figure 6.21 The extracted negative peak against various R_{var} at lift-off 9 mm

6.3.6 Summary

The rotating testing platform including differential configurations of customized LC resonators for Tx and Tx_ref, an LC resonator Rx with a variable resistor R_{var}, and the developed LabView-based GUI, was established to investigate the signal readout and analysis of signal characteristics. The variation of lift-off and R_{var} on the influence of ΔR_p and Δf_{res} was explored. The results revealed that lift-off varied both ΔR_p and Δf_{res}. However, the change in R_{var} only affected the valley signal of ΔR_p and it exhibited an inversely proportional relationship between the negative peak and R_{var}. This could be explained by the fact that R_{var} mainly made impact on the real part of the impedance in Tx. Due to the weak coupling coefficient and small Q factor of the LC resonator, the impact of R_{var} on Δf_{res} was nearly unchanged. According to this attribute, Δf_{res} can be applied to make compensation for ΔR_p against lift-off variations. As ΔR_p curves mainly responds the change in R_{var} on its negative peaks, real-time feature extraction is vital in

a field testing due to redundant and heavy data. Some advanced strategies can be adopted to assist signal processing such as machine learning and deep learning.

6.4 Chapter Summary

This chapter describes the investigation of stability of WFM using differential LC resonant sensors and software processing including KF and MMA algorithms, and signal readout and analysis on the rotating testing platform. The research results indicated that differential configurations of LC resonators, and KF and MMA significantly reduced the fluctuations of signal due to external factors, such as temperature drift, and EMI noise. Based on the improvement on hardware and software, a rotating testing was performed to study the signal readout and characteristics at varying lift-off and R_{var}. Results indicated that ΔR_p was in good response to the change of R_{var}, while Δf_{res} kept almost unchanged. Lift-off variations led to the changes in both ΔR_p and Δf_{res}, which meant that Δf_{res} can measure the lift-off and compensate the shift of ΔR_p caused by lift-off variations.

The next chapter will conclude the thesis and outline the future work.

Chapter 7. Conclusions and Future Work

7.1 Conclusions

Wheel-rail contact forces play a significant role in railway mechanical systems since they determine the running safety and stability. The traditional method is using strain gauges which are installed in wheel webs to conduct real-time measurement. Signals from strain gauges are transmitted from a rotating component to a static component through the slip ring that is based on electromagnetic induction. Although the way with strain gauges has high sensitivity, and reliable results, the strict requirements including installation of strain gauges, hole drilling, wired connection, complicated and expensive signal transmission systems restrict the popularization in railway vehicles. Some new methods have also been attempted to realize wireless WRCFM but there is still a need for seeking an alternative solution after taking the cost, signal processing, and system complexity. Therefore, the work in this thesis aims to investigate WFM based on LC resonance sensing whose goal is able to realize wireless WRCFM.

The work is divided into four parts. The first part is to investigate WFM using LC resonance sensing. It involves the design of LC resonance sensor, establishment of LDC1614-based system, experimental set-up, and signal analysis. A rectangular LC resonance sensor was designed to perform WFM on a C50 carbon steel using tensile testing machine. The measurement principle is based on eddy current effects where electromagnetic properties of materials, e.g. conductivity, and permeability, vary when under force. This variation in turn changes the intensity of eddy currents, subsequently changing the equivalent inductance and the resonant frequency. The relationship between the resonant frequency of the LC resonance sensor and applied force was studied. Due to the operation at high frequencies, MHz levels, the influence of permeability was ignored and only conductivity was used to analysed. The repeatability tests, comparative analysis with strain gauges, and the aspect ratio of inductance coil on the influence of sensitivity were conducted. Results showed that rectangular LC resonance had a linear relationship with applied force and the smaller the aspect ratio, the larger the measurement range, indicating the feasibility of using LC resonance sensing for WFM.

The second part is to separate the force and lift-off because both factors affect the output of the LC resonance sensors and there might be an overlap in certain points, leading to misinterpretation of the measured data. To address this issue, a multi-channel LDC1101-based measurement system was developed which gave multi-parameter outputs including resonant frequency and equivalent parallel resistance. Also, an orthogonal LC resonance sensor was

designed which consisted of two LC resonance sensors in perpendicular, with one being parallel while the other perpendicular to the specimen. Both were sensitive to lift-off but the one parallel to the specimen had more sensitivity compared to the other as the force was applied along the direction parallel to the specimen. The combination of the developed system and the orthogonal LC resonance sensor provided 4 outputs, *Frequency1*, R_{p1}, *Frequency2*, and R_{p2}. By observing these four outputs, it was found that *Frequency1- Frequency1*, R_{p1}-R_{p2} characteristic curves exhibited independence in lift-off and force changes. Specifically, the change in lift-off and force presented a reverse trend which can be used for separation. Therefore, an 8-node isoparametric coordinate transformation algorithm was proposed to perform lift-off and force separation. It was based on two assumptions. The first was when the force remained constant, regardless of the variation in lift-off, the force remained constant, and the second was when the lift-off remained constant, regardless of the variation in force, the lift-off remained constant. Results showed that the force and lift-off were separated effectively, with maximum relative error of 22.61% for forces and 1.66% for lift-offs.

The third part is to extend the preceding study and enhance the lift-off and sensitivity since the previous WFM was primarily based on eddy current effects in which the force was measured by indirectly sensing the change in electromagnetic properties of the material under force. The lift-off was limited within 2 mm. The combination of high sensitivity of semiconductor strain gauge, mid-range transmission characteristic of MRC, and LDC1101-based measurement system opened a novel path for WFM. This new method included two LC resonators with one connecting to a SSG and installed on the test piece for force sensing (Rx) while the other was connected to the LDC1101-based system for data transmission and measurement (Tx). When the SSG was under force and its resistance changed, the impedance of the connected LC resonator Rx changed. This change was coupled to the Tx via the reflected impedance, varying the real part and imaginary part of the equivalent impedance, which was then measured by resonant frequency and equivalent parallel resistance via the LDC1101-based system. Both parallel-parallel (PP) and series-parallel (SP) topologies in the Rx were investigated. The results presented that the sensitivity in R_p exhibited a convex pattern, reaching the maximum sensitivity 5.5 Ω/kN at a lift-off of 33 mm for the PP topology with a 350 Ω SSG, due to critical coupling. For the SP topology, this maximum sensitivity was observed at a lift-off of 10 mm. The sensitivity near the critical coupling region tended to stabilize, which meant that operating the Tx and Rx at this range can enhance robustness for R_p measurement. However, f_{res} showed exponential relationship as the lift-off. The proposed approach achieved WFM with improving sensitivity at much higher lift-offs, up to tens of mm.

The fourth part is to explore the signal stability against EMI and temperature interference and investigate the signal readout and characteristic analysis at a rotating platform. A differential configuration for LC resonators was proposed to reduce the influence of common disturbances, which was combined with signal processing algorithms for further improvement in signal quality. Results revealed that the LC resonators with the differential configuration and KF and MMA algorithms significantly minimize the influence from the temperature change and EMI noise. According to the enhancement in hardware and software, a rotating testing platform was established to perform the signal readout and characteristic analysis at various lift-offs and R_{var}. Results demonstrated that the change in lift-off led to the variations in both ΔR_p and Δf_{res}. However, R_{var} only altered ΔR_p, manifesting a proportional relation between the negative peak of R_{var} and ΔR_p, while Δf_{res} remained almost unchanged. The reason for unaltered Δf_{res} could be attributed to the small Q factor and high lift-offs as the LC resonators was customized in line with the rotating platform. The research outcome also meant that Δf_{res} can measure the lift-off and compensate the shift of ΔR_p caused by lift-off variations.

7.2 Future Work

Future work will move to the field testing for WRCFM. The proposed sensor and measurement system will be installed in practical wheels. The installation position of LC sensors (Rx) can be related to the simulation results showing in the Chapter 2, literature review of wheel-rail force mechanism, the stress distribution on the wheel due to lateral and vertical forces. The bogie frame will provide the installation positions for the measurement system and Tx. When Rx rotates to align with the Tx, because of the magnetic coupling, the sensing information in Rx is reflected to Tx. The force information can be decoupled according to the Tx signal, R_p and f_{res}. As lift-off is the primary challenge for the practical application of LC resonance sensors, future directions will be focused on compensation of the sensor output by adding one more lift-off measurement sensor. In addition, some advanced signal processing algorithms including machine learning and deep learning can be employed for feature extraction, force calibration, and auto-compensation for the lift-off and misalignment.

As this thesis investigates only a single LC resonance sensor or a single SSG that measures unidirectional forces, information regarding other directions is lacking, particularly for WRCF, which encompasses both lateral and vertical forces. Future studies will explore the use of multiple sensors or sensor arrays oriented in various directions to enhance the measurement of directional forces.

Since the LC resonance sensors used in Chapter 3 and 4 measures an area to present force information which could reduce force resolution and sensitivity, a double-D inductance coil structure with concentrated and uniform eddy currents will offer a novel approach to enhancing force measurement capability and directivity in future work.

The LC resonance sensors employed in this thesis are based on traditional PCB technology to fabricate, which has restrictions in operation range and sensitivity. New materials, such as nanotubes, graphene, and metamaterials, can be used in the fabrication of sensing elements, further increasing the coupling distance and measurement sensitivity. In addition to inductive or resistive sensors, capacitive sensors can be used to increase the diversity of sensor types.

Moreover, the LDC1101-ESP32S3 based measurement system owns a Wi-Fi module which can be connected to the internet, transmitting real-time data to an IoT platform, and offering visualization interfaces for running status of railway vehicles.

References

[1] G. Tao, Z. Wen, X. Jin, and X. Yang, "Polygonisation of railway wheels: a critical review," *Railway Engineering Science,* vol. 28, no. 4, pp. 317-345, 2020.

[2] K. Bollas, D. Papasalouros, D. Kourousis, and A. Anastasopoulos, "ACOUSTIC EMISSION INSPECTION OF RAIL WHEELS," *Journal of Acoustic Emission,* vol. 28, 2010.

[3] D. Barke and W. K. Chiu, "Structural health monitoring in the railway industry: a review," *Structural Health Monitoring,* vol. 4, no. 1, pp. 81-93, 2005.

[4] J. Peng *et al.*, "An ultrasonic technology study for subsurface defect in railway wheel tread," in *Proceedings of 11th European Conference on Non-Destructive Testing (ECNDT), Prague, Czech*, 2014.

[5] X. Zhao *et al.*, "Self-powered triboelectric nano vibration accelerometer based wireless sensor system for railway state health monitoring," *Nano Energy,* vol. 34, pp. 549-555, 2017.

[6] A. Alemi, F. Corman, and G. Lodewijks, "Condition monitoring approaches for the detection of railway wheel defects," *Proceedings of the Institution of Mechanical Engineers, Part F: Journal of Rail and Rapid Transit,* vol. 231, no. 8, pp. 961-981, 2016.

[7] P. Rolek, S. Bruni, and M. Carboni, "Condition monitoring of railway axles based on low frequency vibrations," *International Journal of Fatigue,* vol. 86, pp. 88-97, 2016.

[8] J. Wang, T. Wang, and Q. Luo, "A Practical Structural Health Monitoring System for High-Speed Train Car-Body," *IEEE Access,* vol. 7, pp. 168316-168326, 2019.

[9] Y. Cai, B. Chen, and C. Chang, "Research on the strain gauge mounting scheme of track wheel force measurement system based on high-speed wheel/rail relationship test rig," *Railway Sciences,* vol. 3, no. 4, pp. 503-513, 2024.

[10] A. Bracciali, F. Cavaliere, and M. Macherelli, "Review of instrumented wheelset technology and applications," in *The second international conference on railway technology: research, development and maintenance*, 2014, vol. 167, pp. 1-16.

[11] Y.-S. Ham, D.-H. Lee, S.-J. Kwon, W.-H. You, and T.-Y. Oh, "Continuous measurement of interaction forces between wheel and rail," *International Journal of Precision Engineering and Manufacturing,* vol. 10, no. 1, pp. 35-39, 2009.

[12] V. R. Bagheri, P. H. Tehrani, and D. Younesian, "Optimal strain gauge placement in instrumented wheelset for measuring wheel-rail contact forces," *International Journal of Precision Engineering and Manufacturing,* vol. 18, no. 11, pp. 1519-1527, 2017.

[13] S. Zhang, C. Koh, and K. Kuang, "Proposed rail pad sensor for wheel-rail contact force monitoring," *Smart Materials and Structures,* vol. 27, no. 11, p. 115041, 2018.

[14] F. Yu and M. T. Hendry, "A new strain gauge configuration on the rail web to decouple the wheel–rail lateral contact force from wayside measurement," *Proceedings of the Institution of Mechanical Engineers, Part F: Journal of Rail and Rapid Transit,* vol. 233, no. 9, pp. 951-960, 2019.

[15] X. Jin, "A measurement and evaluation method for wheel-rail contact forces and axle stresses of high-speed train," *Measurement,* vol. 149, p. 106983, 2020.

[16] A. Matsumoto *et al.*, "A new measuring method of wheel–rail contact forces and related considerations," *Wear,* vol. 265, no. 9-10, pp. 1518-1525, 2008.

[17] X. Wang, Z. Lu, J. Wei, and Y. He, "Wheel-Rail Contact Forces Monitoring Based on Space Fixed-Point Strain of Wheel Web and DIC Technology," in *Advances in Condition Monitoring and Structural Health Monitoring*, (Lecture Notes in Mechanical Engineering, 2021, ch. Chapter 27, pp. 295-304.

[18] P. Wu, F. Zhang, J. Wang, L. Wei, and W. Huo, "Review of wheel-rail forces measuring technology for railway vehicles," *Advances in Mechanical Engineering,* vol. 15, no. 3, 2023.

[19] R. Gadhave and N. S. Vyas, "Rail-wheel contact forces and track irregularity estimation from on-board accelerometer data," *Vehicle System Dynamics,* vol. 60, no. 6, pp. 2145-2166, 2022.

[20] Q. Wu, M. Spiryagin, I. Persson, C. Bosomworth, and C. Cole, "Parallel computing of wheel-rail contact," *Proceedings of the Institution of Mechanical Engineers, Part F: Journal of Rail and Rapid Transit,* vol. 234, no. 10, pp. 1109-1116, 2019.

[21] T. S. B. o. Canada. "Railway Investigation Report R16E0102." https://www.tsb.gc.ca/eng/rapports-reports/rail/2016/r16e0102/r16e0102.html (accessed 21/11, 2024).

[22] P. Urda, S. Muñoz, J. F. Aceituno, and J. L. Escalona, "Wheel-rail contact force measurement using strain gauges and distance lasers on a scaled railway vehicle," *Mechanical Systems and Signal Processing,* vol. 138, 2020.

[23] X. Jin, "Evaluation and analysis approach of wheel–rail contact force measurements through a high-speed instrumented wheelset and related considerations," *Vehicle System Dynamics,* vol. 58, no. 8, pp. 1189-1211, 2019.

[24] H. Kanehara and T. Fujioka, "Measuring rail/wheel contact points of running railway vehicles," *Wear,* vol. 253, no. 1-2, pp. 275-283, 2002.

[25] E. Gómez, A. Alonso, J. Giménez, and J. Vinolas, "Railway dynamometric wheelsets: a comparison of existing solutions and a proposal for the reduction of measurement errors," in *Proceedings of the 1st International Workshop on High-Speed and Intercity Railways: Volume 2*, 2012: Springer, pp. 261-284.

[26] E. Gomez, J. G. Giménez, and A. Alonso, "Method for the reduction of measurement errors associated to the wheel rotation in railway dynamometric wheelsets," *Mechanical Systems and Signal Processing,* vol. 25, no. 8, pp. 3062-3077, 2011.

[27] A. Matsumoto *et al.*, "A new measuring method of wheel–rail contact forces and related considerations," *Wear,* vol. 265, no. 9-10, pp. 1518-1525, 2008.

[28] S. Yoneyama and G. Murasawa, "Digital image correlation," *Experimental mechanics,* vol. 207, pp. 1-10, 2009.

[29] A. Matsumoto *et al.*, "Continuous observation of wheel/rail contact forces in curved track and theoretical considerations," *Vehicle System Dynamics,* vol. 50, no. sup1, pp. 349-364, 2012.

[30] A. Matsumoto *et al.*, "Actual states of wheel/rail contact forces and friction on sharp curves–continuous monitoring from in-service trains and numerical simulations," *Wear,* vol. 314, no. 1-2, pp. 189-197, 2014.

[31] P. Urda, S. Muñoz, J. F. Aceituno, and J. L. Escalona, "Wheel-rail contact force measurement using strain gauges and distance lasers on a scaled railway vehicle," *Mechanical Systems and Signal Processing,* vol. 138, p. 106555, 2020.

[32] J. Xu *et al.*, "The Principle, Methods and Recent Progress in RFID Positioning Techniques: A Review," *IEEE Journal of Radio Frequency Identification,* vol. 7, pp. 50-63, 2023.

[33] G. Liu *et al.*, "Review of Wireless RFID Strain Sensing Technology in Structural Health Monitoring," *Sensors (Basel),* vol. 23, no. 15, Aug 3 2023.

[34] Z. Ye, M. Yang, Y. Ren, C. H. Jonathan Hung, C. T. Michael Wu, and P. Y. Chen, "Review on Recent Advances and Applications of Passive Harmonic RFID Systems," *IEEE J Radio Freq Identif,* vol. 7, pp. 118-133, 2023.

[35] L. Cui, Z. Zhang, N. Gao, Z. Meng, and Z. Li, "Radio Frequency Identification and Sensing Techniques and Their Applications-A Review of the State-of-the-Art," *Sensors (Basel),* vol. 19, no. 18, Sep 17 2019.

[36] J. Zhang, G. Y. Tian, A. M. Marindra, A. I. Sunny, and A. B. Zhao, "A Review of Passive RFID Tag Antenna-Based Sensors and Systems for Structural Health Monitoring Applications," *Sensors (Basel),* vol. 17, no. 2, Jan 29 2017.

[37] R. Want, "An introduction to RFID technology," *IEEE pervasive computing,* vol. 5, no. 1, pp. 25-33, 2006.

[38] Z. Meng and Z. Li, "RFID Tag as a Sensor-a review on the innovative designs and applications," *Measurement science review,* vol. 16, no. 6, p. 305, 2016.

[39] E. M. Amin, J. K. Saha, and N. C. Karmakar, "Smart sensing materials for low-cost chipless RFID sensor," *IEEE Sensors Journal,* vol. 14, no. 7, pp. 2198-2207, 2014.

[40] S. C. Mohonta, L. Lasantha, M. Majumder, P. Aitchison, and N. C. Karmakar, "Chipless RFID strain sensors: A review and performance analysis," *Sensors and Actuators A: Physical,* vol. 376, 2024.

[41] A. Gregori, E. Di Giampaolo, A. Di Carlofelice, and C. Castoro, "Presenting a New Wireless Strain Method for Structural Monitoring: Experimental Validation," *Journal of Sensors,* vol. 2019, pp. 1-12, 2019.

[42] U. Tata, H. Huang, R. L. Carter, and J. C. Chiao, "Exploiting a patch antenna for strain measurements," *Measurement Science and Technology,* vol. 20, no. 1, 2009.

[43] X. Yi, C. Cho, J. Cooper, Y. Wang, M. M. Tentzeris, and R. T. Leon, "Passive wireless antenna sensor for strain and crack sensing—electromagnetic modeling, simulation, and testing," *Smart Materials and Structures,* vol. 22, no. 8, 2013.

[44] X. Yi, Y. Wang, M. M. Tentzeris, and R. T. Leon, "Multi-physics modeling and simulation of a slotted patch antenna for wireless strain sensing," *Structural Health Monitoring,* pp. 1857-1864, 2013.

[45] X. Yi, T. Wu, Y. Wang, and M. M. Tentzeris, "Sensitivity modeling of an RFID-based strain-sensing antenna with dielectric constant change," *IEEE Sensors Journal,* vol. 15, no. 11, pp. 6147-6155, 2015.

[46] D. Li, C. Cho, and Y. Wang, "Patch antenna sensor rosettes for surface strain measurement," *Proceedings of the Institution of Civil Engineers-Smart Infrastructure and Construction,* vol. 170, no. 2, pp. 39-49, 2017.

[47] M. F. Kuhn, G. P. Breier, A. R. Dias, and T. G. Clarke, "A novel RFID-based strain sensor for wireless structural health monitoring," *Journal of Nondestructive Evaluation,* vol. 37, no. 2, pp. 1-10, 2018.

[48] X. Cheng, Y. Yu, L. Wang, C. Sun, and G. Tian, "Wireless stress measurement on metal surface based on passive integrated RFID sensor tag," presented at the 2021 IEEE International Instrumentation and Measurement Technology Conference (I2MTC), 2021.

[49] I. Ibanez-Labiano, M. S. Ergoktas, C. Kocabas, A. Toomey, A. Alomainy, and E. Ozden-Yenigun, "Graphene-based soft wearable antennas," *Applied Materials Today,* vol. 20, p. 100727, 2020.

[50] N. Afsarimanesh, A. Nag, S. Sarkar, G. S. Sabet, T. Han, and S. C. Mukhopadhyay, "A review on fabrication, characterization and implementation of wearable strain sensors," *Sensors and Actuators A: Physical,* p. 112355, 2020.

[51] J. Kim, Z. Wang, and W. S. Kim, "Stretchable RFID for wireless strain sensing with silver nano ink," *IEEE Sensors Journal,* vol. 14, no. 12, pp. 4395-4401, 2014.

[52] K. Pan *et al.*, "Sustainable production of highly conductive multilayer graphene ink for wireless connectivity and IoT applications," *Nature communications,* vol. 9, no. 1, pp. 1-10, 2018.

[53] S. Niu *et al.*, "A wireless body area sensor network based on stretchable passive tags," *Nature Electronics,* vol. 2, no. 8, pp. 361-368, 2019.

[54] K. Omae, T. Yamazaki, C. Oka, J. Sakurai, and S. Hata, "Stress measurement based on magnetic Barkhausen noise for thin films," *Microelectronic Engineering,* vol. 279, 2023.

[55] N. Chukwuchekwa, "Investigation of magnetic properties and Barkhausen noise of electrical steel," Cardiff University, 2011.

[56] P. Fagan, B. Ducharne, L. Daniel, A. Skarlatos, M. Domenjoud, and C. Reboud, "Effect of stress on the magnetic Barkhausen noise energy cycles: A route for stress evaluation in ferromagnetic materials," *Materials Science and Engineering: B,* vol. 278, 2022.

[57] V. Vengrinovich, D. Vintov, A. Prudnikov, P. Podugolnikov, and V. Ryabtsev, "Magnetic Barkhausen Effect in Steel Under Biaxial Strain/Stress: Influence on Stress Measurement," *Journal of Nondestructive Evaluation,* vol. 38, no. 2, 2019.

[58] J. Wu, C. Liu, E. Li, J. Zhu, S. Ding, and Y. Wang, "Motion-Induced Magnetic Barkhausen Noise for Evaluating Applied Stress in Pipelines," *Journal of Nondestructive Evaluation,* vol. 39, no. 4, 2020.

[59] C. H. Gur, "Review of Residual Stress Measurement by Magnetic Barkhausen Noise Technique," *Materials Performance and Characterization,* vol. 7, no. 4, pp. 504-525, 2018.

[60] Y. Liu, Q. Liu, R. Gao, B. Gao, and G. Tian, "Stress Measurement of Ferromagnetic Materials Using Hybrid Magnetic Sensing," *IEEE Transactions on Instrumentation and Measurement,* vol. 72, pp. 1-13, 2023.

[61] D. BUTTLE, V. MOORTHY, and B. SHAW, "The measurement of Residual Stresses by Magnetic Methods–Maps and Barkhausen, A National Measurement Good Practice Guide n 88," *NPL, Inglaterra,* 2006.

[62] N. B. Ekreem, A. G. Olabi, T. Prescott, A. Rafferty, and M. S. J. Hashmi, "An overview of magnetostriction, its use and methods to measure these properties," *Journal of Materials Processing Technology,* vol. 191, no. 1-3, pp. 96-101, 2007.

[63] M. Maciusowicz and G. Psuj, "Use of Time-Dependent Multispectral Representation of Magnetic Barkhausen Noise Signals for the Needs of Non-Destructive Evaluation of Steel Materials," *Sensors (Basel),* vol. 19, no. 6, Mar 24 2019.

[64] B. Karpuschewski, O. Bleicher, and M. Beutner, "Surface Integrity Inspection on Gears Using Barkhausen Noise Analysis," *Procedia Engineering,* vol. 19, pp. 162-171, 2011.

[65] J. Liu, G. Y. Tian, B. Gao, K. Zeng, Y. Zheng, and J. Chen, "Micro-macro characteristics between domain wall motion and magnetic Barkhausen noise under tensile stress," *Journal of Magnetism and Magnetic Materials,* vol. 493, 2020.

[66] J. Liu, G. Tian, B. Gao, K. Zeng, Y. Xu, and Q. Liu, "Time-Response-Histogram-Based Feature of Magnetic Barkhausen Noise for Material Characterization Considering Influences of Grain and Grain Boundary under In Situ Tensile Test," *Sensors (Basel),* vol. 21, no. 7, Mar 28 2021.

[67] A. Sorsa, K. Leiviskä, S. Santa-aho, and T. Lepistö, "Quantitative prediction of residual stress and hardness in case-hardened steel based on the Barkhausen noise measurement," *NDT & E International,* vol. 46, pp. 100-106, 2012.

[68] P. G. Huray, *Maxwell's equations*. John Wiley & Sons, 2009.

[69] J. Garcia-Martin, J. Gomez-Gil, and E. Vazquez-Sanchez, "Non-destructive techniques based on eddy current testing," *Sensors (Basel),* vol. 11, no. 3, pp. 2525-65, 2011.

[70] K. Chen, B. Gao, G. Y. Tian, Y. Yang, C. Yang, and Q. Ma, "Differential Coupling Double-Layer Coil for Eddy Current Testing With High Lift-Off," *IEEE Sensors Journal,* vol. 21, no. 16, pp. 18146-18155, 2021.

[71] Y. Yang *et al.*, "Electromagnetic Pigging System Based on Sandwich Differential Planar Coil," *IEEE Sensors Journal,* vol. 22, no. 19, pp. 18903-18913, 2022.

[72] Y. He *et al.*, "Pulsed eddy current technique for defect detection in aircraft riveted structures," *NDT & E International,* vol. 43, no. 2, pp. 176-181, 2010.

[73] D. Placko and I. Dufour, "Eddy current sensors for nondestructive inspection of graphite composite materials," in *Conference record of the 1992 IEEE Industry applications society annual meeting*, 1992: IEEE, pp. 1676-1682.

[74] H. G. Ramos, O. Postolache, F. C. Alegria, and A. L. Ribeiro, "Using the skin effect to estimate cracks depths in mettalic structures," in *2009 IEEE instrumentation and measurement technology conference*, 2009: IEEE, pp. 1361-1366.

[75] H. Ma, D. Wang, Z. Zhang, W. Yin, H. Chen, and G. Zhou, "A simple conductivity measurement method using a peak-frequency feature of ferrite-cored eddy current sensor," *NDT & E International,* vol. 142, 2024.

[76] C. Ye, N. Zhang, L. Peng, and Y. Tao, "Flexible Array Probe With In-Plane Differential Multichannels for Inspection of Microdefects on Curved Surface," *IEEE Transactions on Industrial Electronics,* vol. 69, no. 1, pp. 900-910, 2022.

[77] W. Zhang, C. Wang, F. Xie, and H. Zhang, "Defect imaging curved surface based on flexible eddy current array sensor," *Measurement,* vol. 151, 2020.

[78] Q. Ma, B. Gao, G. Y. Tian, C. Yang, L. Xie, and K. Chen, "High sensitivity flexible double square winding eddy current array for surface micro-defects inspection," *Sensors and Actuators A: Physical,* vol. 309, 2020.

[79] H. E. Farag, E. Toyserkani, and M. B. Khamesee, "Non-Destructive Testing Using Eddy Current Sensors for Defect Detection in Additively Manufactured Titanium and Stainless-Steel Parts," *Sensors,* vol. 22, no. 14, 2022.

[80] Q. Ma, G. Y. Tian, B. Gao, X. Zhao, G. Ru, and H. Li, "Lift-off suppression based on combination of bridge and transformer signal conditionings of eddy current testing," *NDT & E International,* vol. 132, 2022.

[81] K. H. Ng, N. V. Venkatarayalu, V. P. Bui, and A. R. K. Rajkumar, "Design and characterization of PCB based planar coil Eddy current probes," in *2018 International Conference on Intelligent Rail Transportation (ICIRT)*, 2018: IEEE, pp. 1-4.

[82] L. Xie, B. Gao, G. Y. Tian, J. Tan, B. Feng, and Y. Yin, "Coupling pulse eddy current sensor for deeper defects NDT," *Sensors and Actuators A: Physical,* vol. 293, pp. 189-199, 2019.

[83] D. I. Ona, G. Y. Tian, R. Sutthaweekul, and S. M. Naqvi, "Design and optimisation of mutual inductance based pulsed eddy current probe," *Measurement,* vol. 144, pp. 402-409, 2019.

[84] L. S. Rosado, T. G. Santos, P. M. Ramos, P. Vilaça, and M. Piedade, "A differential planar eddy currents probe: Fundamentals, modeling and experimental evaluation," *NDT & E International,* vol. 51, pp. 85-93, 2012.

[85] OLYMPUS. "Eddy Current Probe Selection Information." OLYMPUS. https://www.olympus-ims.com/en/ec-probes/selection/ (accessed 02/10, 2024).

[86] C. Yang, B. Gao, Q. Ma, L. Xie, G. Y. Tian, and Y. Yin, "Multi-Layer Magnetic Focusing Sensor Structure for Pulsed Remote Field Eddy Current," *IEEE Sensors Journal,* vol. 19, no. 7, pp. 2490-2499, 2019.

[87] J. Ge, B. Hu, and C. Yang, "Investigation of the approximate decomposition of alternating current field measurement signals from crack colonies," *Mechanical Systems and Signal Processing,* vol. 160, 2021.

[88] G. Yang, G. Dib, L. Udpa, A. Tamburrino, and S. S. Udpa, "Rotating Field EC-GMR Sensor for Crack Detection at Fastener Site in Layered Structures," *IEEE Sensors Journal,* vol. 15, no. 1, pp. 463-470, 2015.

[89] J. Xin, N. Lei, L. Udpa, and S. S. Udpa, "Rotating field eddy current probe with bobbin pickup coil for steam generator tubes inspection," *NDT & E International,* vol. 54, pp. 45-55, 2013.

[90] L. Q. Trung, N. Kasai, K. Sekino, and S. Miyazaki, "Eddy current convergence probes with self-differential and self-nulling characteristics for detecting cracks in conductive materials," *Sensors and Actuators A: Physical,* vol. 349, 2023.

[91] Q. Ma, G. Tian, B. Gao, M. Robinson, C. Yang, and E. T. Ibrahim, "Novel Common-Differential Inductance Coils With Dual Signal Conditionings for Separation of Lift-Off and Defects," *IEEE Sensors Journal,* vol. 24, no. 2, pp. 2055-2065, 2024.

[92] Q. Xiao, J. Feng, Z. Xu, and H. Zhang, "Receiver Signal Analysis on Geometry and Excitation Parameters of Remote Field Eddy Current Probe," *IEEE Transactions on Industrial Electronics,* vol. 69, no. 3, pp. 3088-3098, 2022.

[93] J. Ge, C. Yang, F. Yu, and N. Yusa, "Transformation of the rotating eddy current testing signal at the desired eddy current orientation," *NDT & E International,* vol. 125, 2022.

[94] A. Sophian, G. Tian, D. Taylor, and J. Rudlin, "Electromagnetic and eddy current NDT: a review," *Insight,* vol. 43, no. 5, pp. 302-306, 2001.

[95] S. Huang, "New Technologies in Electromagnetic Non-destructive Testing," 2016.

[96] Z. Chen, J. R. Salas-Avlia, Y. Tao, W. Yin, Q. Zhao, and Z. Zhang, "A novel hybrid serial/parallel multi-frequency measurement method for impedance analysis in eddy current testing," *Rev Sci Instrum,* vol. 91, no. 2, p. 024703, Feb 1 2020.

[97] L. S. Rosado, P. M. Ramos, and M. Piedade, "Real-Time Processing of Multifrequency Eddy Currents Testing Signals: Design, Implementation, and Evaluation," *IEEE Transactions on Instrumentation and Measurement,* vol. 63, no. 5, pp. 1262-1271, 2014.

[98] A. Sophian, G. Tian, and M. Fan, "Pulsed Eddy Current Non-destructive

Testing and Evaluation: A Review," *Chinese Journal of Mechanical Engineering,* vol. 30, no. 3, pp. 500-514, 2017.

[99] L. Xiong *et al.*, "Through Thickness Inspection of Layered Magnetic Material Using Pulsed Eddy-Current Testing," *IEEE Transactions on Instrumentation and Measurement,* vol. 72, pp. 1-9, 2023.

[100] T. Chen, G. Y. Tian, A. Sophian, and P. W. Que, "Feature extraction and selection for defect classification of pulsed eddy current NDT," *NDT & E International,* vol. 41, no. 6, pp. 467-476, 2008.

[101] A. Sophian, G. Y. Tian, D. Taylor, and J. Rudlin, "A feature extraction technique based on principal component analysis for pulsed Eddy current NDT," *NDT & e International,* vol. 36, no. 1, pp. 37-41, 2003.

[102] Y. Li, B. Yan, D. Li, H. Jing, Y. Li, and Z. Chen, "Pulse-modulation eddy current inspection of subsurface corrosion in conductive structures," *NDT & E International,* vol. 79, pp. 142-149, 2016.

[103] G. Betta, L. Ferrigno, M. Laracca, P. Burrascano, M. Ricci, and G. Silipigni, "An experimental comparison of multi-frequency and chirp excitations for eddy current testing on thin defects," *Measurement,* vol. 63, pp. 207-220, 2015.

[104] Y. Yating, D. Pingan, and Y. Tuo, "Investigation on contribution of conductivity and permeability on electrical runout problem of eddy current displacement sensor," in *2011 IEEE International Instrumentation and Measurement Technology Conference*, 2011: IEEE, pp. 1-5.

[105] X. Ma, A. J. Peyton, and Y. Y. Zhao, "Eddy current measurements of electrical conductivity and magnetic permeability of porous metals," *NDT & E International,* vol. 39, no. 7, pp. 562-568, 2006.

[106] W. Ricken, H. C. Schoenekess, and W. J. Becker, "Improved multi-sensor for force measurement of pre-stressed steel cables by means of the eddy current technique," *Sensors and Actuators A: Physical,* vol. 129, no. 1-2, pp. 80-85, 2006.

[107] X. Chen and Y. Lei, "Electrical conductivity measurement of ferromagnetic metallic materials using pulsed eddy current method," *NDT & E International,* vol. 75, pp. 33-38, 2015.

[108] 3+, C. Wang, M. Fan, B. Cao, B. Ye, and W. Li, "Novel Noncontact Eddy Current Measurement of Electrical Conductivity," *IEEE Sensors Journal,* vol. 18, no. 22, pp. 9352-9359, 2018.

[109] W. Yin *et al.*, "Permeability invariance phenomenon and measurement of electrical conductivity for ferrite metallic plates," *Insight-Non-Destructive Testing and Condition Monitoring,* vol. 61, no. 8, pp. 472-479, 2019.

[110] M. Lu *et al.*, "Conductivity Lift-off Invariance and measurement of permeability for ferrite metallic plates," *NDT & E International,* vol. 95, pp. 36-44, 2018.

[111] I. D. Adewale and G. Y. Tian, "Decoupling the Influence of Permeability and Conductivity in Pulsed Eddy-Current Measurements," *IEEE Transactions on Magnetics,* vol. 49, no. 3, pp. 1119-1127, 2013.

[112] M. Morozov, G. Yun Tian, and P. J. Withers, "The pulsed eddy current response to applied loading of various aluminium alloys," *NDT & E International,* vol. 43, no. 6, pp. 493-500, 2010.

[113] M. Morozov, G. Y. Tian, and P. J. Withers, "Elastic and plastic strain effects on eddy current response of aluminium alloys," *Nondestructive Testing and Evaluation,* vol. 28, no. 4, pp. 300-312, 2013.

[114] K. Song, H. Sun, X. Cui, and L. Zhang, "Design and experimental research of stress measurement system for ferromagnetic components based on ACSM method," *The Journal of Strain Analysis for Engineering Design,* 2021.

[115] L. Bai and G. Y. Tian, "Stress measurement using pulsed eddy current thermography," in *Proceedings of the 51st Annual Conference of the British Institute of Non-Destructive Testing (BINDT 2012), Northamptonshire, UK*, 2012, pp. 11-13.

[116] J. Li *et al.*, "Estimation of stress distribution in ferromagnetic tensile specimens using low cost eddy current stress measurement system and BP neural network," *PLoS One,* vol. 12, no. 11, p. e0188197, 2017.

[117] H.-C. Schoenekess, W. Ricken, and W.-J. Becker, "Method to Determine Tensile Stress Alterations in Prestressing Steel Strands by Means of an Eddy-Current Technique," *IEEE Sensors Journal,* vol. 7, no. 8, pp. 1200-1205, 2007.

[118] J.-G. Liu and W.-J. Becker, "Force and stress measurements with eddy-current sensors," *Proceedings II of the SENSOR,* pp. 23-28, 2001.

[119] D. Zhou, M. Pan, Y. He, and B. Du, "Stress detection and measurement in ferromagnetic metals using pulse electromagnetic method with U-shaped sensor," *Measurement,* vol. 105, pp. 136-145, 2017.

[120] B. A. Abu-Nabah, F. Yu, W. T. Hassan, M. P. Blodgett, and P. B. Nagy, "Eddy current residual stress profiling in surface-treated engine alloys," *Nondestructive Testing and Evaluation,* vol. 24, no. 1-2, pp. 209-232, 2010.

[121] S.-a. Ji *et al.*, "Real-Time Strain Detection Technology for Steel Structures Based on Eddy Current Effect," *Journal of Sensors,* vol. 2023, pp. 1-9, 2023.

[122] R. Hughes and S. Dixon, "Developments in near electrical resonance signal enhancement (NERSE) eddy-current methods," 2015.

[123] R. Hughes, Y. Fan, and S. Dixon, "Near electrical resonance signal enhancement (NERSE) in eddy-current crack detection," *NDT & E International,* vol. 66, pp. 82-89, 2014.

[124] R. R. Hughes and S. Dixon, "Performance analysis of single-frequency near electrical resonance signal enhancement (SF-NERSE) defect detection," *NDT & E International,* vol. 102, pp. 96-103, 2019.

[125] C. Xiu, L. Ren, and H. Li, "Investigation on Eddy Current Sensor in Tension Measurement at a Resonant Frequency," *Applied Sciences,* vol. 7, no. 6, 2017.

[126] Q.-A. Huang, L. Dong, and L.-F. Wang, "LC Passive Wireless Sensors Toward a Wireless Sensing Platform: Status, Prospects, and Challenges," *Journal of Microelectromechanical Systems,* vol. 25, no. 5, pp. 822-841, 2016.

[127] M. Li *et al.*, "Wireless Passive Flexible Strain Sensor Based on Aluminium Nitride Film," *IEEE Sensors Journal,* vol. 22, no. 4, pp. 3074-3079, 2022.

[128] R. I. Rodriguez and Y. Jia, "A wireless inductive-capacitive (LC) sensor for rotating component temperature monitoring," *International journal on smart sensing and intelligent systems,* vol. 4, no. 2, pp. 325-337, 2011.

[129] Y. Zhou, L. Dong, C. Zhang, L. Wang, and Q. Huang, "Rotational Speed Measurement Based on LC Wireless Sensors," *Sensors,* vol. 21, no. 23, 2021.

[130] T. J. Harpster, B. Stark, and K. Najafi, "A passive wireless integrated humidity sensor," *Sensors and Actuators A: Physical,* vol. 95, no. 2-3, pp. 100-107, 2002.

[131] W.-J. Deng, L.-F. Wang, L. Dong, and Q.-A. Huang, "Symmetric LC Circuit Configurations for Passive Wireless Multifunctional Sensors," *Journal of Microelectromechanical Systems,* vol. 28, no. 3, pp. 344-350, 2019.

[132] Y. Wang, Q. Tan, L. Zhang, B. Lin, M. Li, and Z. Fan, "Wireless Passive LC Temperature and Strain Dual-Parameter Sensor," *Micromachines (Basel),* vol. 12, no. 1, Dec 30 2020.

[133] W. Lv, Q. Tan, H. Kou, W. Zhang, and J. Xiong, "MWCNTs/WS2 nanocomposite sensor realized by LC wireless method for humidity monitoring," *Sensors and Actuators A: Physical,* vol. 290, pp. 207-214, 2019.

[134] L. Dong, L.-F. Wang, C. Zhang, and Q.-A. Huang, "A Cyclic Scanning Repeater for Enhancing the Remote Distance of LC Passive Wireless Sensors," *IEEE Transactions on Circuits and Systems I: Regular Papers,* vol. 63, no. 9, pp. 1426-1433, 2016.

[135] C. Zhang, L.-F. Wang, J.-Q. Huang, and Q.-A. Huang, "An LC-Type Passive Wireless Humidity Sensor System With Portable Telemetry Unit," *Journal of Microelectromechanical Systems,* vol. 24, no. 3, pp. 575-581, 2015.

[136] P.-J. Chen, S. Saati, R. Varma, M. S. Humayun, and Y.-C. Tai, "Wireless Intraocular Pressure Sensing Using Microfabricated Minimally Invasive Flexible-Coiled LC Sensor Implant," *Journal of Microelectromechanical Systems,* vol. 19, no. 4, pp. 721-734, 2010.

[137] B. Xu *et al.*, "Radio Frequency Resonator-Based Flexible Wireless Pressure Sensor with MWCNT-PDMS Bilayer Microstructure," *Micromachines (Basel),* vol. 13, no. 3, Mar 1 2022.

[138] Q. Tan *et al.*, "A LC wireless passive temperature-pressure-humidity (TPH) sensor integrated on LTCC ceramic for harsh monitoring," *Sensors and Actuators B: Chemical,* vol. 270, pp. 433-442, 2018.

[139] Q. Tan, F. Lu, Y. Ji, H. Wang, W. Zhang, and J. Xiong, "LC temperature-pressure sensor based on HTCC with temperature compensation algorithm for extreme 1100 °C applications," *Sensors and Actuators A: Physical,* vol. 280, pp. 437-446, 2018.

[140] L. Dong, L.-F. Wang, and Q.-A. Huang, "An Passive Wireless Multifunctional Sensor Using a Relay Switch," *IEEE Sensors Journal,* vol. 16, no. 12, pp. 4968-4973, 2016.

[141] Q. Tan *et al.*, "Signal Readout of LC Pressure Sensor Operated in Multi-dimensional rotating Environment with Dual-inductance Resonator," *Sensors and Actuators A: Physical,* vol. 296, pp. 178-185, 2019.

[142] M. M. El Rayes, G. Nagib, and W. G. Ali Abdelaal, "A Review on Wireless Power Transfer," *International Journal of Engineering Trends and Technology,* vol. 40, no. 5, pp. 272-280, 2016.

[143] Z. Zhang, H. Pang, A. Georgiadis, and C. Cecati, "Wireless Power Transfer—An Overview," *IEEE Transactions on Industrial Electronics,* vol. 66, no. 2, pp. 1044-1058, 2019.

[144] M. Abou Houran, X. Yang, and W. Chen, "Magnetically Coupled Resonance WPT: Review of Compensation Topologies, Resonator Structures with Misalignment, and EMI Diagnostics," *Electronics,* vol. 7, no. 11, 2018.

[145] S. D. Barman, A. W. Reza, N. Kumar, M. E. Karim, and A. B. Munir, "Wireless powering by magnetic resonant coupling: Recent trends in wireless power transfer system and its applications," *Renewable and Sustainable Energy Reviews,* vol. 51, pp. 1525-1552, 2015.

[146] A. Kurs, A. Karalis, R. Moffatt, J. D. Joannopoulos, P. Fisher, and M. Soljacic, "Wireless power transfer via strongly coupled magnetic resonances," *science,* vol. 317, no. 5834, pp. 83-86, 2007.

[147] P. K. Sahu, S. Jena, S. Behera, M. M. Sahu, S. R. Prusty, and R. Dash, "Wireless power transfer topology analysis for inkjet-printed coil," *Open Engineering,* vol. 12, no. 1, pp. 373-380, 2022.

[148] J. W. M. L. E. G. L. Z. W. Y. Huang2, "Investigation of Magnetic Resonance Coupling Circuit Topologies for Wireless Power Transmission."

[149] W. Lee and Y.-K. Yoon, "Wireless Power Transfer Systems Using Metamaterials: A Review," *IEEE Access,* vol. 8, pp. 147930-147947, 2020.

[150] J. Wang, M. Leach, E. G. Lim, Z. Wang, and Y. Huang, "Investigation of magnetic resonance coupling circuit topologies for wireless power transmission," *Microwave and Optical Technology Letters,* vol. 61, no. 7, pp. 1755-1763, 2019.

[151] L. U. Daura, G. Tian, Q. Yi, and A. Sophian, "Wireless power transfer-based eddy current non-destructive testing using a flexible printed coil array," *Philos Trans A Math Phys Eng Sci,* vol. 378, no. 2182, p. 20190579, Oct 16 2020.

[152] C. T. Ertsgaard, M. Kim, J. Choi, and S. H. Oh, "Wireless dielectrophoresis trapping and remote impedance sensing via resonant wireless power transfer," *Nat Commun,* vol. 14, no. 1, p. 103, Jan 6 2023.

[153] L. U. Daura and G. Y. Tian, "Characterization of Angular RCF Cracks in a Railway Using Modified Topology of WPT-Based Eddy Current Testing," *IEEE Transactions on Industrial Informatics,* vol. 19, no. 4, pp. 5612-5622, 2023.

[154] L. U. Daura and G. Y. Tian, "Wireless Power Transfer Based Non-Destructive Evaluation of Cracks in Aluminum Material," *IEEE Sensors Journal,* vol. 19, no. 22, pp. 10529-10536, 2019.

[155] L. U. Daura and G. Y. Tian, "Characterization of Angular RCF Cracks in a Railway Using Modified Topology of WPT-Based Eddy Current Testing," *IEEE Transactions on Industrial Informatics,* pp. 1-11, 2022.

[156] C. Zhang *et al.*, "Conjunction of triboelectric nanogenerator with induction coils as wireless power sources and self-powered wireless sensors," *Nat Commun,* vol. 11, no. 1, p. 58, Jan 2 2020.

[157] C. Yang *et al.*, "Intelligent wireless theranostic contact lens for electrical sensing and regulation of intraocular pressure," *Nat Commun,* vol. 13, no. 1, p. 2556, May 17 2022.

[158] R. Lin *et al.*, "Wireless battery-free body sensor networks using near-field-enabled clothing," *Nat Commun,* vol. 11, no. 1, p. 444, Jan 23 2020.

[159] A. Device. "AD5933, 1 MSPS, 12-Bit Impedance Converter, Network Analyzer." https://www.analog.com/en/products/ad5933.html#part-details (accessed 24/10, 2024).

[160] A. Punapung and A. Kaewpoonsuk, "A design for a programmable swept frequency module for eddy current testing," in *2018 International Electrical Engineering Congress (iEECON)*, 2018: IEEE, pp. 1-4.

[161] P. Ibba *et al.*, "Design and Validation of a Portable AD5933–Based Impedance Analyzer for Smart Agriculture," *IEEE Access,* vol. 9, pp. 63656-63675, 2021.

[162] A. Devices. "AD698 Universal LVDT Signal Conditioner." https://www.analog.com/media/en/technical-documentation/data-sheets/ad698.pdf (accessed 24/10, 2024).

[163] TI. "LDC1612/4 Datasheet." https://www.ti.com/lit/ds/symlink/ldc1614.pdf (accessed.

[164] TI, "LDC1101, 1.8-V High-Resolution, inductance to digital converter for high speed applications," 2016.

[165] K.-Y. Koo, S. Park, J.-J. Lee, and C.-B. Yun, "Automated Impedance-based Structural Health Monitoring Incorporating Effective Frequency Shift for Compensating Temperature Effects," *Journal of Intelligent Material Systems and Structures,* vol. 20, no. 4, pp. 367-377, 2008.

[166] L. J. Koerner and T. W. Secord, "An embedded electrical impedance analyzer based on the AD5933 for the determination of voice coil motor mechanical properties," *Sensors and Actuators A: Physical,* vol. 295, pp. 99-112, 2019.

[167] J. D. Munoz, V. H. Mosquera, and C. F. Rengifo, "A low-cost, portable, two-dimensional bioimpedance distribution estimation system based on the AD5933 impedance converter," *HardwareX,* vol. 11, p. e00274, Apr 2022.

[168] P. Li, S. Xu, D. Xu, and C. Xu, "Structural Health Monitoring of an Aircraft Wing Using a Portable Wireless Electromechanical Impedance Analyzer," *IEEE Sensors Journal,* vol. 24, no. 14, pp. 22855-22866, 2024.

[169] Y. Liang, Z. Tan, and G. Zhai, "Development of a wireless multichannel miniature impedance measurement system and its application for bolt loosening detection," *NDT & E International,* vol. 148, 2024.

[170] J. Yuan, K. Wang, H. Lei, and B. Li, "An accurate modeling and design method of inductive displacement sensor," *Measurement,* vol. 219, 2023.

[171] X. Li, G. Tian, K. Li, H. Wang, and Q. Zhang, "Differential ECT Probe Design and Investigation for Detection of Rolling Contact Fatigue Cracks With Different Orientations," *IEEE Sensors Journal,* vol. 22, no. 12, pp. 11615-11625, 2022.

[172] W. Li, J. Hu, Z. Su, and D. Wang, "Radial and axial integrated inductive displacement sensor used for magnetic bearing system," *Transactions of the Institute of Measurement and Control,* 2024.

[173] X. Lu *et al.*, "Research on the Time Drift Stability of Differential Inductive Displacement Sensors with Frequency Output," *Sensors (Basel),* vol. 22, no. 16, Aug 19 2022.

[174] B. Kasemsadeh and L. LaPointe, "Inductive Sensing Touch-On-Metal Buttons Design Guide," *Application Report SNOA951,* 2016.

[175] H. Wang *et al.*, "Design and Characterization of Tri-Axis Soft Inductive Tactile Sensors," *IEEE Sensors Journal,* vol. 18, no. 19, pp. 7793-7801, 2018.

[176] A. Margarida, "IoT ready Eddy Current Testing Structural Health Monitor.pdf," *Master Thesis,* 2019.

[177] TI, "LDC1001 datasheet," 2019.

[178] T. Instruments, "LDC1101 1.8 V High-Resolution, High-Speed Inductance-to-Digital Converter," *LDC1101,* pp. 1-58, 2016.

[179] G. Tian, C. Yang, X. Lu, Z. Wang, Z. Liang, and X. Li, "Inductance-to-digital converters (LDC) based integrative multi-parameter eddy current testing sensors for NDT&E," *NDT & E International,* vol. 138, 2023.

[180] Z. Liang, Z. Wang, C. Yang, X. Lu, and G. Tian, "Investigating a defect width identification based on half-peak width for LDC-based eddy current testing," *Nondestructive Testing and Evaluation,* pp. 1-14, 2024.

[181] J. R. Feldkamp and S. Quirk, "Single-Coil Magnetic Induction Tomography Using the LDC-1101 Chip," *IEEE Sensors Journal,* vol. 21, no. 1, pp. 633-641, 2021.

[182] R. R. Hughes and S. Dixon, "Analysis of Electrical Resonance Distortion for Inductive Sensing Applications," *IEEE Sensors Journal,* vol. 18, no. 14, pp. 5818-5825, 2018.

[183] Y. Jia, K. Sun, F. J. Agosto, and M. T. Quiñones, "Design and characterization of a passive wireless strain sensor," *Measurement Science and Technology,* vol. 17, no. 11, pp. 2869-2876, 2006.

[184] H. Kou *et al.*, "Wireless flexible pressure sensor based on micro-patterned Graphene/PDMS composite," *Sensors and Actuators A: Physical,* vol. 277, pp. 150-156, 2018.

[185] L. Dong, L.-F. Wang, and Q.-A. Huang, "Effects of Metal Plane in LC Passive Wireless Sensors," *IEEE Sensors Letters,* vol. 2, no. 1, pp. 1-3, 2018.

[186] D. Chen *et al.*, "A Stress Measurement Method for Steel Strands Based on LC Oscillation," *Advances in Materials Science and Engineering,* vol. 2018, pp. 1-8, 2018.

[187] H. Cui, X. Li, B. Zhang, F. Yuan, and B. Chen, "Research on Inductance–capacitance electromagnetic resonance measurement of prestressed concrete beam," *Measurement,* vol. 189, 2022.

[188] H. Wang *et al.*, "Folding and Bending Planar Coils for Highly Precise Soft Angle Sensing," *Advanced Materials Technologies,* vol. 5, no. 11, 2020.

[189] H. Yim, H. Kang, S. Moon, Y. Kim, T. D. Nguyen, and H. R. Choi, "Multi-functional safety sensor coupling capacitive and inductive measurement for physical Human–Robot Interaction," *Sensors and Actuators A: Physical,* vol. 354, 2023.

[190] A. Barrancos, A. Silvestre, and L. S. Rosado, "Designing an Eddy Current Testing Structural Health Monitoring Instrument," presented at the 2021 Telecoms Conference (ConfTELE), 2021.

[191] C. Yang, G. Tian, M. Robinson, and E. T. Ibrahim, "Wheel-Rail Force Measurement Based on Wireless LC Resonance Sensing," *IEEE Sensors Journal,* vol. 23, no. 15, pp. 17470-17479, 2023.

[192] A. N. AbdAlla, M. A. Faraj, F. Samsuri, D. Rifai, K. Ali, and Y. Al-Douri, "Challenges in improving the performance of eddy current testing: Review," *Measurement and Control,* vol. 52, no. 1-2, pp. 46-64, 2018.

[193] L. Dziczkowski, "Elimination of Coil Liftoff From Eddy Current Measurements of Conductivity," *IEEE Transactions on Instrumentation and Measurement,* vol. 62, no. 12, pp. 3301-3307, 2013.

[194] G. Y. Tian, Y. Li, and C. Mandache, "Study of Lift-Off Invariance for Pulsed Eddy-Current Signals," *IEEE Transactions on Magnetics,* vol. 45, no. 1, pp. 184-191, 2009.

[195] M. Lu, X. Meng, R. Huang, L. Chen, A. Peyton, and W. Yin, "Lift-off invariant inductance of steels in multi-frequency eddy-current testing," *NDT & E International,* vol. 121, 2021.

[196] K. TASHIRO, H. WAKIWAKA, K. MINAKATA, T. KIMURA, and Y. NAKAMURA, "A novel eddy current method for magnetic plate identification with elimination of lift-off effect," *Journal of the Japan Society of Applied Electromagnetics and Mechanics,* vol. 27, no. 1, pp. 165-168, 2019.

[197] G. Y. Tian and A. Sophian, "Reduction of lift-off effects for pulsed eddy current NDT," *NDT & E International,* vol. 38, no. 4, pp. 319-324, 2005.

[198] M. Fan, B. Cao, P. Yang, W. Li, and G. Tian, "Elimination of liftoff effect using a model-based method for eddy current characterization of a plate," *NDT & E International,* vol. 74, pp. 66-71, 2015.

[199] W. Chen and D. Wu, "Resistance-frequency eddy current method for electrical conductivity measurement," *Measurement,* vol. 209, 2023.

[200] B. A. Abu-Nabah and P. B. Nagy, "Lift-off effect in high-frequency eddy current conductivity spectroscopy," *NDT & E International,* vol. 40, no. 8, pp. 555-565, 2007.

[201] B. A. Abu-Nabah, "Reduction of lift-off effect in high-frequency apparent eddy current conductivity spectroscopy," *Measurement Science and Technology,* vol. 28, no. 5, 2017.

[202] R. D. Cook, *Concepts and applications of finite element analysis*. John wiley & sons, 2007.

[203] Z. A. Ansari, B. A. Abu-Nabah, M. Alkhader, and A. Muhammed, "Experimental evaluation of nonmagnetic metal clad thicknesses over nonmagnetic metals using apparent eddy current conductivity spectroscopy," *Measurement,* vol. 164, 2020.

[204] T. Matsumoto *et al.*, "Investigation of electromagnetic nondestructive evaluation of residual strain in low carbon steels using the eddy current magnetic signature (EC-MS) method," *Journal of Magnetism and Magnetic Materials,* vol. 479, pp. 212-221, 2019.

[205] W. Chen, D. Wu, X. Wang, and T. Wang, "A self-frequency-conversion eddy current testing method," *Measurement,* vol. 195, 2022.

[206] J. H. Rose, C.-C. Tai, and J. C. Moulder, "Scaling relation for the inductance of a coil on a ferromagnetic half-space," *Journal of Applied Physics,* vol. 82, no. 9, pp. 4604-4610, 1997.

[207] Y. Cho *et al.*, "Thin Hybrid Metamaterial Slab With Negative and Zero Permeability for High Efficiency and Low Electromagnetic Field in Wireless Power Transfer Systems," *IEEE Transactions on Electromagnetic Compatibility,* vol. 60, no. 4, pp. 1001-1009, 2018.

[208] H. Nesser, H. A. Mahmoud, and G. Lubineau, "High-Sensitivity RFID Sensor for Structural Health Monitoring," *Adv Sci (Weinh),* p. e2301807, Jul 5 2023.

[209] K. J. Lee, N. Chou, and S. Kim, "A Batteryless, Wireless Strain Sensor Using Resonant Frequency Modulation," *Sensors (Basel),* vol. 18, no. 11, Nov 15 2018.

[210] M. Masud, P. Vazquez, M. R. U. Rehman, A. Elahi, W. Wijns, and A. Shahzad, "Measurement Techniques and Challenges of Wireless LC Resonant Sensors: A Review," *IEEE Access,* vol. 11, pp. 95235-95252, 2023.

[211] C. Yang *et al.*, "Measurement and separation of forces and lift-offs employing an inductance-to-digital converters (LDC)-based orthogonal LC resonance sensor," *NDT & E International,* vol. 144, 2024.

[212] W. Liu, K. T. Chau, X. Tian, H. Wang, and Z. Hua, "Smart wireless power transfer — opportunities and challenges," *Renewable and Sustainable Energy Reviews,* vol. 180, 2023.

[213] Y. Liu and H. Feng, "Maximum Efficiency Tracking Control Method for WPT System Based on Dynamic Coupling Coefficient Identification and Impedance Matching Network," *IEEE Journal of Emerging and Selected Topics in Power Electronics,* vol. 8, no. 4, pp. 3633-3643, 2020.

[214] J. P. W. Chow, N. Chen, H. S. H. Chung, and L. L. H. Chan, "An Investigation Into the Use of Orthogonal Winding in Loosely Coupled Link for Improving Power Transfer Efficiency Under Coil Misalignment," *IEEE Transactions on Power Electronics,* vol. 30, no. 10, pp. 5632-5649, 2015.

[215] M. Fu, T. Zhang, X. Zhu, P. C.-K. Luk, and C. Ma, "Compensation of Cross Coupling in Multiple-Receiver Wireless Power Transfer Systems," *IEEE Transactions on Industrial Informatics,* vol. 12, no. 2, pp. 474-482, 2016.

[216] J. Liu, C. Wang, X. Wang, and W. Ge, "Frequency Splitting and Transmission Characteristics of MCR-WPT System Considering Non-Linearities of Compensation Capacitors," *Electronics,* vol. 9, no. 1, 2020.

[217] Y.-J. Kim, D. Ha, W. J. Chappell, and P. P. Irazoqui, "Selective Wireless Power Transfer for Smart Power Distribution in a Miniature-Sized Multiple-Receiver System," *IEEE Transactions on Industrial Electronics,* vol. 63, no. 3, pp. 1853-1862, 2016.

[218] J. Kim *et al.*, "Coil Design and Shielding Methods for a Magnetic Resonant Wireless Power Transfer System," *Proceedings of the IEEE,* vol. 101, no. 6, pp. 1332-1342, 2013.

[219] B. Feng, S. Xie, L. Xie, K. Deng, S. Wang, and Y. Kang, "Analysis of the Lift-Off Effect in Motion-Induced Eddy Current Testing Based on Semi-Analytical Model," *IEEE Transactions on Instrumentation and Measurement,* vol. 73, pp. 1-8, 2024.

[220] Y.-L. Lyu *et al.*, "A Method of Using Nonidentical Resonant Coils for Frequency Splitting Elimination in Wireless Power Transfer," *IEEE Transactions on Power Electronics,* vol. 30, no. 11, pp. 6097-6107, 2015.

[221] A. Sharma, Y. Morisada, T. Nagaoka, and H. Fujii, "Influence of the number of FSP passes on the strength-ductility synergy of cold-rolled spark plasma sintered pure aluminum," *Journal of Manufacturing Processes,* vol. 79, pp. 296-304, 2022.

[222] J. M. Stankiewicz and A. Choroszucho, "Comparison of the Efficiency and Load Power in Periodic Wireless Power Transfer Systems with Circular and Square Planar Coils," *Energies,* vol. 14, no. 16, 2021.

[223] D. Ongayo and M. Hanif, "Comparison of circular and rectangular coil transformer parameters for wireless Power Transfer based on Finite Element Analysis," in *2015 IEEE 13th Brazilian Power Electronics Conference and 1st Southern Power Electronics Conference (COBEP/SPEC)*, 2015: IEEE, pp. 1-6.

[224] H. Wang and Z. Feng, "Ultrastable and highly sensitive eddy current displacement sensor using self-temperature compensation," *Sensors and Actuators A: Physical,* vol. 203, pp. 362-368, 2013.

[225] A. Ma'arif, I. Iswanto, A. A. Nuryono, and R. I. Alfian, "Kalman Filter for Noise Reducer on Sensor Readings," *Signal and Image Processing Letters,* vol. 1, no. 2, pp. 11-22, 2019.

[226] Y. Feng, X. Li, and X. Zhang, "An adaptive compensation algorithm for temperature drift of micro-electro-mechanical systems gyroscopes using a strong tracking Kalman filter," *Sensors (Basel),* vol. 15, no. 5, pp. 11222-38, May 13 2015.

[227] L. Wang, S. Zhang, L. Dong, and Q.-A. Huang, "Passive wireless multi-parameter LC sensing system for in situ health monitoring of bearings," *Sensors and Actuators A: Physical,* vol. 379, 2024.